Doctoral Dissertation
Doctoral Program in Materials Science and Technology (38th Cycle)

# Processing-driven structuring of melt compounded polymer-based systems

**Fulvia Cravero**

* * * * * *

**Supervisors**
Prof. Rossella Arrigo, Supervisor
Prof. Alberto Frache, Co-Supervisor

Politecnico di Torino
2026

I hereby declare that, the contents and organisation of this dissertation constitute my own original work and does not compromise in any way the rights of third parties, including those relating to the security of personal data.

Fulvia Cravero
Turin, 2026

# Summary

Polymer structuring is a valuable cost- and time-saving method for producing high-performance polymer-based materials. The main issue in the diffusion of this approach is the understanding of the relationship between the processing parameters, the microstructure and the resulting properties, which is crucial for the actual definition of the final features.

Therefore, the aim of this PhD dissertation is the study of the processing parameter-microstructure-property relationships in polymer blends-based materials with the purpouse of obtaining structured morphologies that can be opportunely tuned in the production step. In particular, after a detailed analysis of the state of the art and considering its importance at an industrial level, it was decided to investigate the solvent-free production of thermoplastic polymer blends by melt blending approach. Specifically, two homopolymer systems were selected. Namely, the first one is based on high-density polyethylene (HDPE) and the other one on polyamide 6 (PA6). With regard to the experimental trial, the role of both the material characteristics and the processing parameters was investigated. Specifically, the polarity of the polymer was considered along with the mono- or bimodality of the molecular weight (MW) in the blend. Various bimodal distributions were also investigated. From a processing point of view, both the HDPE and PA6 blends were obtained by corotating twin screw extrusion. Therefore, the effect of varying the screw rotation speed and the barrel temperature was evaluated.

Furthermore, the second step of the research focused on the role of the application of a non-isothermal uniaxial elongational flow at the exit of the die. In the case of PA6-based materials, the investigation was firstly performed on the polymeric systems. Then, the evaluation of the morphology of composites containing hydrotalcites (LDHs) characterized by two different surface areas were

studied. Thermal, rheological, morphological and mechanical investigations were performed and are reported and discussed in detail.

In addition, the innovative approach adopted in this PhD dissertation refers to the multivariate analysis employed for the interpretation of the results. In fact, this approach has allowed to highlight the impact of the simultaneous variation of two parameters on the resulting morphology, thus considering the role of the combination of two variables in the processing parameter-microstructure-property relationships and enriching the current knowledge available in the literature, which is mainly focused on the univariate analysis. Furthermore, the multivariate approach allows to obtain solutions that are often not obtained by considering the variation of a single parameter alone. This has been appreciated, for instance, in the study of the twin-screw extruded HDPE blends, where the full polymer miscibility was achieved when the highest values of shear stress and processing temperatures were simultaneously exploited. Also, from the analysis of the rheological characterization, the minor role of the screw speed and barrel temperature over the molecular weight was appreciated. In addition, the concurrent increase of the screw rotation speed and MW in PA6-based materials was found to promote the influence of the flow-induced crystallization (FIC) over the memory effect, resulting in the greater increase in final crystallinity and $\alpha/\gamma$ phase content when the high MW was considered instead of the low molecular weight.

Another novelty of the present PhD research is the extensive use of a simulation software to obtain information about the thermo-mechanical field inside the barrel during compounding. In particular, data on the actual shear rate, temperature and residence time were used to interpret the characterization results according to the processing parameters.

# Acknowledgment

First and foremost, I would like to thank RADICI Group for providing the polyamides, and Prolabin&Tefarm s.r.l. for the hydrotalcites that I used in my research.

Above all, I would like to thank my supervisor, Prof. Rossella Arrigo, who has been a key figure in the development of my professional growth. Through our conversations, I have deeply understood how curiosity, determination, and a solid grasp of scientific principles are essential in order to gain new knowledge in research. My deepest thanks also go to my co-supervisor, Prof. Alberto Frache, who has been a source of scientific insight and inspiration. His advices have encouraged me to think beyond conventional frameworks and to explore new approaches with confidence.

To Chiara and Giulia**.** Colleagues, desk mates, friends. What we have shared over these years cannot be summed up in a few lines. Thank you for everything.
I would also like to thank all the members of the All-Polymer research group, past and present, with whom I have shared experiments, data analysis, and team-building moments. Special thanks to Giusi, Ele and Giuseppe. And to Daniele, Diego, Fausto, James and Dario. For whom no technical challenge is ever too daunting.

My sincere thanks also go to the colleagues from the "research group next door". Thank you, Chiara, Lorenza, Massimo, Lorenzina, Enrica, Marta, Emir, Elisa, Valentina, and Tian, for sharing coffee, lunch, and conversations, both scientific and lighthearted. To the colleagues I met at Conferences and courses. Thank you, Debora, Francesca, Chiara, Edoardo, Marzia, Nicola, and all those I had the pleasure of meeting during these years of Congresses and Schools. Thank you for the scientific discussions and the existential musings shared over a beer.

I would also like to express my gratitude to those who, while not contributing scientifically to this work, have been equally important companions along the way.

Thank you, Dani, Matte, C, Romy, Giò, Ele, and Val. Whether in the kitchen or the eighteenth century, our laughter sounds the same. Thanks to Maria and Valentina, with whom I shared this engineering journey from our first days of university through its joys and challenges.
Thank you Marina and Federica, my North Poles, and Alby, my South one. Because waves are easier to face when you are not sailing alone. I am also grateful to Lucio and the Sangha. Multiform, ever-changing, multifaceted. Side by side, one step at a time.

Finally, I wish to thank my family, especially my parents and my brother Paolo, for their constant presence, encouragement, and unwavering support throughout these years.

*Come le nuvole in cielo*
*Hishiryo*

# Contents

# List of Tables

# List of Figures

# List of Abbreviations

The abbreviations are classified alphabetically

| | |
|---|---|
| $\alpha$ | Interfacial tension |
| Al | Aluminum |
| AFM | Atomic Force Microscopy |
| BSR | Breaking Stretching Ratio |
| CIM | Conventional injection molding |
| $\Delta H^0$ | Melting enthalpy of the 100 % crystalline polymer |
| $\Delta H_{calc}$ | Calculated melting enthalpy |
| $\Delta H_{Exper}$ | Experimental melting enthalpy recorded during the first heating cycle |
| $\Delta H_{Gap}$ | Difference between the experimental and the calculated melting enthalpies |
| $\Delta H_{HMW}$ | Melting enthalpy of the HMW pellet |
| $\Delta H_{LMW}$ | Melting enthalpy of the LMW pellet |
| $\Delta H_m$ | Melting enthalpy |
| D17 | Magnesium/Aluminum hydrotalcite having a surface area of 8.1 $m^2/g$ |
| D25 | Magnesium/Aluminum hydrotalcite having a surface area of 2.6 $m^2/g$ |
| $D_{Die}$ | Diameter of the extrudate in correspondance of the die |
| $D_{Fiber}$ | Diameter of the fiber after the drawing step |
| DoE | Design of Experiment |
| DR | Draw ratio |
| DSC | Differential Scanning Calorimetry |
| EPDM | Ethylene-propylene-diene rubber |
| EPR | Poly-ethylene rubber |
| $f_L$ | Lamellar orientation |
| FIC | Flow-induced crystallization |
| FICP | Flow-induced crystallization under pressure |

| | |
|---|---|
| $\eta^*$ | Complex viscosity |
| $\eta$” | Imaginary component of the complex viscosity |
| $\eta$’ | Real component of the complex viscosity |
| HDPE | High-density poly-ethylene |
| HMW | High molecular weight high density poly-ethylene |
| HV | High viscosity poly-amide 6 |
| IM | Injection molding |
| $L_{lateral}$ | Lamellar lateral size |
| LDH | Layered double hydrotalcites |
| LLDPE | Linear low density poly-ethylene |
| LMW | Low molecular weight high density poly-ethylene |
| LRT | Local Residence Time |
| LV | Low viscosity poly-amide 6 |
| MLR | Multilinear regression |
| MW | Molecular weight |
| Mg | Magnesium |
| NA | Nucleating agent |
| NR | Natural rubber |
| OTR | Oxygen transmission rate |
| OPIM | Oscillation Packing Injection Molding |
| PA6 | Poly-amide 6 |
| PA11 | Poly-amide 11 |
| PA12 | Poly-amide 12 |
| PA66 | Poly-amide 66 |
| PB | Poly-butene-1 |
| PBAT | Poly-butylene adipateterephthalate |
| PBS | Poly-butylene succinate |
| PC | Poly-carbonate |
| PCs | Principal components |
| PCA | Principal Component Analysis |
| PEG | Poly-ethylene glycol |
| PET | Poly-ethylene terephthalate |
| PHA | Poly-hydroxyalkanoate |
| PK | Poly-ketone |
| PLA | Poly-lactic acid |
| PLLA | Poly-L-lactic acid |
| PMMA | Poly-methyl methacrylate |
| POE | Poly-olefin elastomer |
| POM | Poly-oxymethylene |
| PP | Poly-propylene |
| PS | Poly-styrene |
| PTFE | Poly-tetrafluoroethylene |
| PVDF | Poly-vinylidene fluoride |
| $R_n$ | Number average radius |

| | |
|---|---|
| $R_v$ | Volume average radius |
| RSS | Rotational Shear System |
| SAXS | Small-angle X-ray scattering |
| SBR | Styrene-butadiene rubber |
| SCG | Slow Crack Growth |
| SCORIM | Shear Controlled Orientation in Injection Molding |
| SEM | Scanning Electron Microscopy |
| $T_{cryst}$ | Crystallization temperature |
| $T_m$ | Melting temperature |
| TRT | Total Residence Time |
| U | Ultra-high molecular weight polyethylene UTEC6540 |
| UHMWPE | Ultra-high molecular weight polyethylene |
| VIM | Vibration Assisted Injection Molding |
| $W_{rep}$ | Weissenberg number related to the longest relaxation time |
| $W_S$ | Weissenberg number related to the Rouse time |
| WAXD | Wide-angle X-ray diffraction |

# Chapter 1

# Introduction

## 1.1 The concept of polymer structuring

The term polymer structuring refers to the tailoring of the morphology in polymer-based materials by exploiting the relationship between the processing parameters and the microstructure, which ultimately determines the resulting properties [1–20,2,21,1,22,23]. Besides, when more than two levels of morphological organization are distinguished, the multiscale topology is addressed as hierarchical microstructure and the final performances are determined by the interactions that occur at the molecular, nano, micro, and macro scales [3,24–27]. In particular, hierarchical structures can be obtained in both single polymer and blend systems. In the first case, the multiscale morphology is achieved by organizing the crystalline phase into multilevel structures, such as the shish-kebab, characterized by a cylindrical central skeleton of aligned macromolecules from which epitaxial crystals of oriented lamellae grow at regular intervals [22,28–42]. On the other hand, when all-polymer blends are considered, the hierarchical structures are formed due to the mutual organization of the two polymer domains. For instance, this can be achieved by the formation of hybrid shish-kebab structures [25,43–53] or microfibrils [1,20,39,54–70]. The latter are anisotropic micrometer-sized morphologies that can be oriented and their density can be increased by adjusting the processing parameters. It is interesting to note that all of these was inspired by nature. In fact, tendons, bones, wood, grass, nacre, silk fibers, the paws of gecko, lotus leaves and intervertebral disks are good examples of how a proper microstructure allows to achieve superior mechanical properties and lightweight, outstanding adhesion characteristics or self-cleaning properties [3,4,21,23–25,71–78].

In fact, the ability to engineer the morphology and thus the final properties, creates significant opportunities for the application of such structured materials in high-performance technological areas [2,13,14,24], such as adhesive tapes [72], self-cleaning surfaces [71], coating applications and drug delivery [79,80]. On the

other hand, the hierarchically structured materials are particularly performant in terms of mechanical properties thanks to the efficient transfer of the loads, both in terms of tensile strength and energy adsorption during impact, which is related to the synergistic response of the entire material due to the multiscale design [3,20,22,39,81–84]. Thus, the interest in promoting the diffusion of hierarchically structured polymer-based materials seems clear. In the case of all-polymers and single-polymers, the processes that allow polymer structuring can be divided into two approaches, depending on the presence of a solvent. In particular, when solvent is present, they can be referred to as *solvent-assisted techniques,* while alternatively they can be called *solvent-free processes* [2,5,13,14,20,26,71,85–95].

In the first case, the structuring is mainly achieved by the self-assembly ability of the macromolecules, and microstructure tuning is primarily obtained by controlling the chain structure and the nature of the solvent [26,71,85–89,93–98]. Specifically, homopolymers or copolymers can be used. In the case of copolymers, an additional degree of freedom comes from the choice of monomer types and their order within the chains. In fact, the morphology of a two-component multiblock copolymer can be tailored by varying the block lengths and the stiffness of each section. This approach typically results in the formation of core-shell micelles or multilayer structures. In this context, solvent-assisted methods can be viewed as bottom-up design techniques, where the microstructure is shaped by first defining the macromolecular structure. Besides, the selectivity of the solvent towards a particular monomer can be used to manipulate the morphology. In fact, the solvo-phobic segments of the chains are induced to minimize their contact with the solvent by forming micellar structures, while the solvo-philic components remain exposed. Thus, by properly designing the chains with a solvo-phobic endblock or midblock, even layering is achieved [26,85,87,93,96,97].
Although the ability of macromolecules to self-assembly has long been known, the dynamics that govern the final morphology are still under debate [26,85,88]. Indeed, various theoretical approaches have been proposed over the years, but the complex multiscale relationship between composition and structure often requires molecular-level data that are typically not available. For this reason, simplified models have been developed [26,97,99–109].

On the other hand, in solvent-free processes, the microstructure is mostly determined by the balance between the orientation, relaxation and crystallization dynamics of the macromolecules through the selection of the right combination of materials, processing technique and parameters, and can therefore be considered as top-down approaches [5,13,110]. Besides, structuring is based on melt blending and consists of applying an external mechanical field to the material. For this reason, the microstructure can often be referred to as *external field determined morphology* [2,5,13,14,20,26,90–92].

In fact, considering the all-polymer materials containing semi-crystalline polymers, the morphology in the solid state can be initially distinguished into amorphous and crystalline phases. However, the separation between the two is not sharp and can be influenced by several factors such as the chain topology and the presence of a flow field [5,111–114]. Specifically, from the transformation of the

molten state into the solid state under quiescent conditions results in the formation of crystals and a three-dimensional spherulitic morphology of folded chains separated by the amorphous phase is obtained [5]. However, such a final microstructure can be properly modified by the application of a flow field, which interferes with the relaxation dynamics and thus affects the crystallization kinetics and the final crystallinity [2,5,13,40,110,110,115–121]. In particular, the main types of flow are the elongational and shear, which are distinguished according to the mutual direction between the flow of the material and the velocity gradient inside the molten state [115]. As a consequence, different results are obtained by applying one or the other. The elongational flow has the ability to promote the orientation and even stretching of the macromolecules in the direction parallel to the flow of the material, thus promoting the formation of an anisotropic morphology. On the other hand, such orienting ability is less effective for shear flow and the isotropy of the microstructure can be largely maintained in this second case [115,118,122–125].

In addition, the final morphology is also influenced by the isothermal or non-isothermal condition in which the material is processed. In fact, the application of a cooling rate to the material affects its rheological response and, as a consequence, the resulting effect of the flow field may be different from that expected under isothermal conditions. Furtherly, the formation of crystals may occur prematurely, taking into account both the contribution of the flow in promoting the crystallinity and the decreasing temperature [110,115,121,126].

All of this must be taken into account, especially in industrial-scale processing, where a non-isothermal step is often present. For instance, this can be referred to compounding and injection molding, which are widely used industrial techniques that are mainly characterized by the application of the shear flow. On the other hand, the role of the elongational flow is also appreciated when the melt enters the die section in compounding or the mold gate in injection molding [115,127–132]. Besides, external flow fields can also be introduced, as in the case of the application of the elongational flow in blow molding, film blowing, film casting and fiber spinning [17,92,133,115,134–156,5,121].

On the other hand, when focusing on the melt processing of polymer blends, the role of the materials becomes apparent. In fact, in most cases they are thermodynamically immiscible in the molten state, so a heterogenous morphology characterized by droplet-like domains of the second phase dispersed in the matrix is commonly observed [157,158]. As a result, the applied shear or elongational flow can deform, orient or even induce the breakup of such droplets, depending also on the rheological properties of the polymers and the blend composition. Thus, the final shape and size of the secondary domains and hence the resulting microstructure can be tuned by knowing the intrinsic characteristics of the system [115,118,122–124,159,160]. Specifically, the effect of shear or elongational flow in determining the final morphology has been related to two dimensionless parameters that depend on the blend in question. Namely, the *viscosity ratio* and the *capillary number*. The former is derived from the ratio between the viscosity of the dispersed phase and that of the matrix. The latter is calculated as the ratio between

the hydrodynamic stresses determining the elongation of the droplet and the interfacial stresses between the matrix and the dispersed phase [115,161]. As reported in Figure 1, the breakup of the dispersed droplet is obtained when a critical capillary number is reached and, considering a constant viscosity ratio, the value is determined by the type of flow applied. It was found that a lower capillary number is required in the presence of an elongational flow, because it is more effective in breaking the droplets. Also, in this case, it is possible to reduce the droplet size even for viscosity ratios higher than four, which, on the other hand, is a limitation that affects the shear flow [115,160–162].

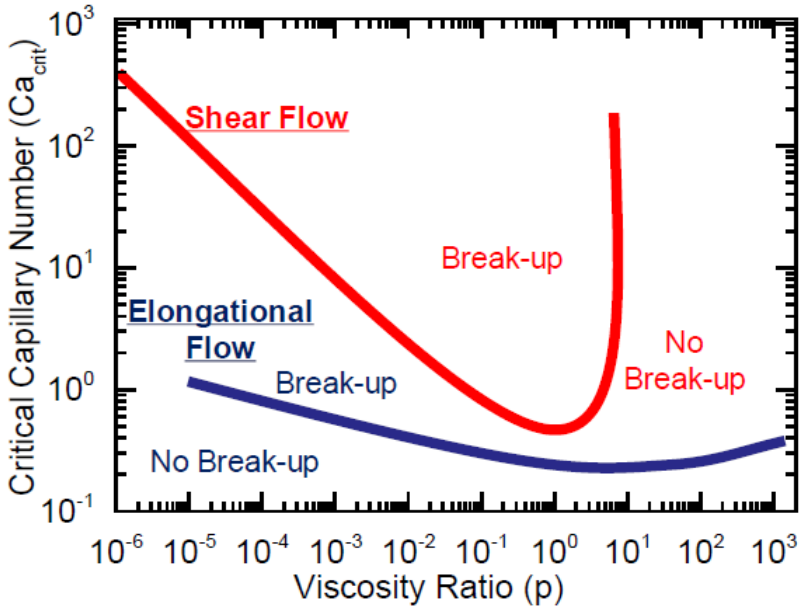


**Figure 1. Critical capillary number as a function of viscosity ratio in polymer blends, based on Grace's analysis [161]. Reprinted under CC BY 4.0 license.**

Considering the scenario described above, it seems clear that solvent-free structuring approaches are a valuable solution to tailor the performances of all-polymer systems exploiting melt-blending processing techniques and materials already used at industrial scale. Additionally, these techniques are less polluting for the environment and less hazardous for the specialized workers compared to the solvent-assisted ones due to the absence of the solvent. Nevertheless, the complexity of the relationship between processing parameters and microstructure has not yet been fully revealed due to the lack of knowledge on the evolution of macromolecular dynamics in the presence of an external field in real case scenarios and the lack of information on the actual thermo-mechanical field during melt blending, thus requiring further investigations in the coming years [110,163–168]. As summarized in Figure 2, a brief review of the topic has attempted to assess the current understanding of the relationship between processing parameters, microstructure and properties in extrusion and injection molding-based processes [169].

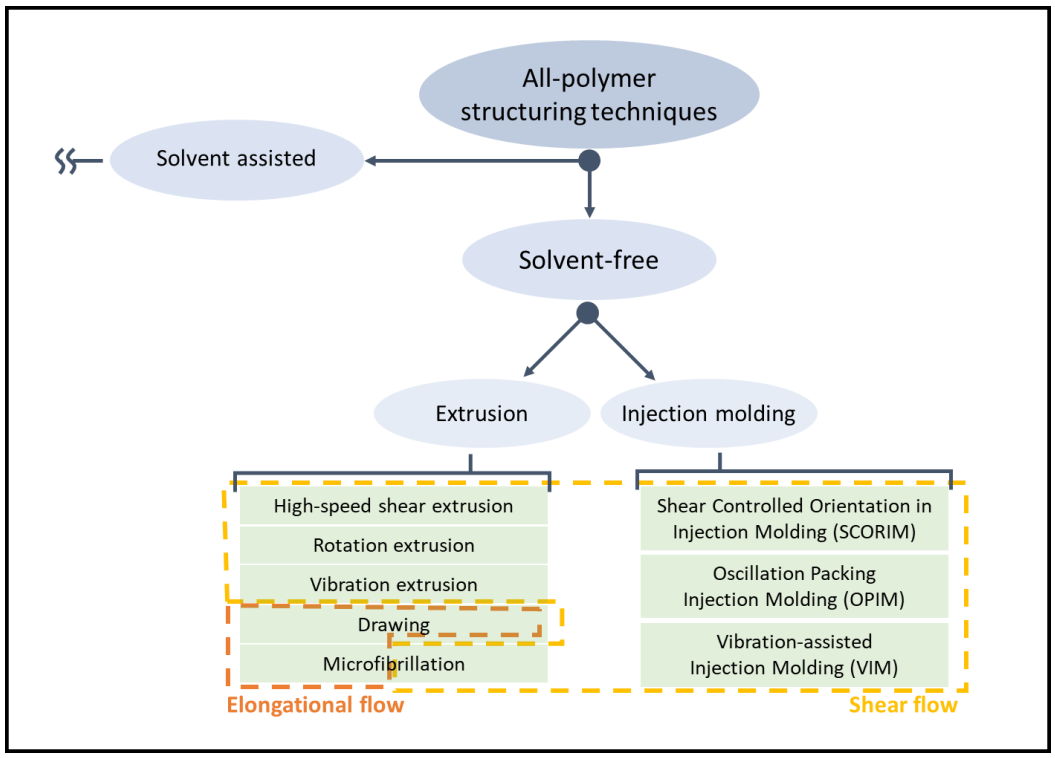


**Figure 2. Schematization of the major solvent-free all-polymer structuring techniques and the corresponding active flow fields [169]. Reprinted under CC BY 4.0 license.**

## 1.2 PhD Framework and objectives

The aim of the PhD dissertation is to produce microstructured polymer blends by exploiting the relationship between processing parameters and morphology, and to further extend the latter including the resulting properties.

This approach allows the production of high-performance polymer-based materials. However, poor knowledge of the relationship between the production variables and the microstructure does not allow tuning the final properties of the materials in an effective and satisfactory way. In this regard, the thesis focused on the study of the correlation between the variation of processing parameters and the resulting morphology in melt-blended materials. An apolar and a polar system were studied, also considering different reciprocal contents of high and low molecular weight polymer. In the first step, the effect of variation of screw speed and barrel temperature during twin-screw extrusion was evaluated, while in the second step the application of an additional elongational flow field was considered. In particular, LDHs were introduced in the polar systems as further degrees of freedom to tune the final morphology and resulting properties.

In particular, the thermal, rheological mechanical and morphological properties of the different systems were evaluated and discussed in relation to the processing parameters.

## 1.3 Thesis structure

The thesis is structured in the following chapters:

- Chapter 2 focuses on providing an overview of the melt blending approaches that can be used to microstructure polymer blends. In particular, it focuses on compounding and injection molding techniques
- From Chapter 3 to Chapter 6, the results of the experimental trials of the thesis are reported. In particular, Chapter 3 discusses the effect of the variation of the screw speed, barrel temperature and material composition on the microstructure of HDPE-based blends compounded by twin-screw extrusion.
- Chapter 4 focuses on the PA6 blends. The effect of different screw rotation speeds and material compositions on the final microstructure of the materials processed by twin screw extrusion has been studied in detail. In particular, the relative crystalline phase content and the overall crystallinity were considered.
- In Chapter 5, the results concerning the superposition of the thermo-mechanical field and elongational flow on PA6 materials was discussed. The relationship between the processing parameters, microstructure and properties has been studied, taking into account the mechanical and thermal performances and the corresponding crystallinity and crystalline phases present.
- In the Chapter 6, the role of hydrotalcite as a nanofiller in the preparation of PA6-based composites obtained by twin-screw extrusion and the application of an elongational flow was investigated. In particular, the effect of the aspect ratio of the LDH on the resulting mechanical and thermal properties was considered.

The materials, experimental equipment, and characterization techniques used are described in separate sections within Appendix A.

# Chapter 2

# State of the art on polymer structuring by solvent-free techniques

*Part of the work described in the Chapter 2 has been previously published in:*

*"Cravero, F.; Arrigo, R.; Frache, A. Processing-Driven Structuring of Polymer-Based Materials: A Brief Overview. Polymers 2025, 17, 76"* [169].

## 2.1 Extrusion-based techniques

### 2.1.1 High-speed shear extrusion

The present is a simple technique to improve the mechanical properties of single polymers. In fact, it requires an extruder with a suitable motor and no additional components. The tailoring of the morphology is achieved thanks to the application of a strong shear flow on the molten material, owing to the high screw rotation speed of the twin-screw extruder or internal mixer. Even if the structuring ability is observed starting from 400 – 600 rpm [170–176], the most typical value is around 1000 rpm [170–172,177] and can reach up to 4000 rpm [178–180].

The introduction of an overall self-reinforcing effect with increasing screw rotation speed can be seen from the study of Zhang et al. [174] on HDPE. The polymer was processed at 100, 500, 900 and 1200 rpm, respectively, and the corresponding increase in the tensile strength from 32.0 to 46.7 MPa was obtained when the value of 100 or 1200 rpm was used. Correspondingly, the elongation at break decreased from 562.8 to 29.9 %. This change in the mechanical properties was explained by considering the effect of the high shear imposed on the material by the high screw rotation speed. In fact, the increase in the collision probability

between the macromolecules, together with a short residence time, led to an increase in the entanglement density and the formation of a three-dimensional network of polymer chains. Ultimately, this resulted in the formation of packed oriented crystals, leading to smaller grains compared to those obtained in the HDPE processed at lower screw speeds. It was also found that the increase in the entanglement density had a negative effect on the crystallinity content. However, the anisotropic morphology had a dominant impact, resulting in an overall increase in tensile strength.

Besides, Zhang et al. [173] investigated the role of such oriented crystals in the formation of shish-kebab in HDPE homopolymer blends containing Ultra-High Molecular Weight Polyethylene (UHMWPE). In particular, from the comparison of materials containing 0.05, 0.1, 1 or 5 wt% of the latter, compounded at 100 or 500 rpm, it was appreciated that with a minimum content of 0.1 wt% of UHMWPE the formation of a three-dimensional network was achieved regardless of the screw speed. On the other hand, the rotation speed turns out to be a key parameter in determining the formation of the hierarchical structures. In fact, at 100 rpm only the preferential orientation of the HDPE crystals is obtained, while 500 rpm is required to observe the shish-kebabs. This phenomenon has been explained by considering that the shish is formed by the UHMWPE macromolecules, then coordinating the HDPE crystals as kebabs. Therefore, taking into account the high MW of the UHMWPE, it appears clear that the shear flow developed at 100 rpm is not intense enough to promote the alignment of the chains, which on the contrary is achieved at 500 rpm. In addition, the study confirms the high-speed shear extrusion is a viable alternative to solvent-assisted techniques to overcome the limitations in obtaining an effective compounding of the UHMWPE due to its high viscosity, as demonstrated by the good dispersion reported for the material containing 5 wt % and processed at 500 rpm.

Furthermore, the high compounding speed was found to promote homogeneous dispersion in immiscible polymer blends compared to lower screw speeds, by reducing the droplet size. As a consequence, improved ductility is achieved [170,171,177,180]. For instance this was observed by Teyssandier et al. [170] in their study of a 70 wt% polyamide 12 (PA12) with 30 wt% plasticized starch compounded at 50, 300, 600, 900 or 1200 rpm. Figure 3 shows the evolution of the number average radius ($R_n$) and volume average radius ($R_v$) with screw speeds. The result is a progressive reduction of the dimensions with the increase of the parameter, the higher and lower $R_n$ of 0.742 and 0.150 corresponding to 50 and 1200 rpm, respectively. Correspondingly, the increase in the specific contact area between PA12 and the plasticized starch favored the load transfer, improving, on the one hand, the deformation at break increasing from 80 % to 370 % and, on the other, the impact strength, which reached 7 kJ/m$^2$ when the material was processed at 1200 rpm, compared to a value of 4 kJ/m$^2$ for the screw speed of 300 rpm.

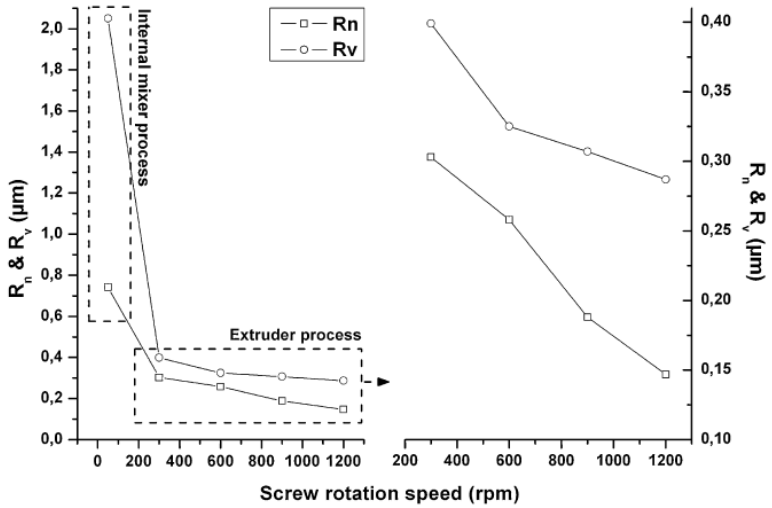


**Figure 3. The number-average and volume-average particle radii of plasticized starch as functions of screw speed [170]. Reproduced with permission from Elsevier Science Ltd., 2012.**

A similar behavior was reported in the work of Sui et al. [176] on 90 wt% polypropylene (PP)/10 wt% poly(lactic acid) (PLA) blends processed at 100, 500 or 900 rpm. In addition, the effect of 190 and 220 °C as processing temperatures was investigated and a minor influence on the size reduction was assessed. In fact, in both cases, the increase in the screw speed from 100 to 900 rpm corresponded to the significant decrease in droplet diameter. In particular, it was reduced form 1.09 mm to 0.68 mm at 190 °C and from 2.16 mm to 1.53 mm at 220 °C. Besides, the study pointed out that the high shear developed during compounding promotes the breakup of the dispersed domains and, at the same time, the low residence time prevents the coalescence of the droplets. However, the expected increase in mechanical properties in terms of yield and impact strength resulted to be poor or negligible regardless of the temperature considered.

On the contrary, the improvement in elongation at break corresponding to the reduction in droplet diameter, and therefore the increase in screw speed, has been confirmed by other studies [177,180]. In particular, for the two formulations containing 80 wt% of polyvinylidene fluoride (PVDF)/20 wt% of polyamide 11 (PA11) [177] or 80 wt% of polycarbonate (PC) and 20 wt% of polymethyl methacrylate (PMMA) [180], the achievement of the nanoscale size of the homogeneously dispersed phase in the blends processed at the highest screw speed corresponded to the increase in strain at break. In the first case, the improvement was from 50 % to more than 260 % for speeds of 100 or 1200 rpm [177], while in the second case the values were 22 % and 118 %, alternatively considering 300 or 2250 rpm [180]. This is consistent with the expected increase in ductility, considering the enhanced compatibility between the polymers, promoted by the increase in specific interfacial area resulting from the reduction in droplet size [171,176,180]. It is worth noting that an additional effect of the reduction of the second phase dimensions lies in the change of the optical properties, as observed by Li et al. [180] for the above mentioned 80 wt% PC/20 wt% PMMA blend. In particular, the UV-visible transmittance was improved from zero to 91 % by

increasing the screw speed from 300 to 2250 rpm, thanks to the decrease of the particles size from the range 2 mm - 200 nm to less than 50 nm.

Furthermore, some studies have highlighted a deviation from the previously described relationship between screw speed and particle size, possibly related to matrix degradation due to the excessive rotation speed [171,172] or to the reciprocal content of polymers in the formulation [175]. In fact, the morphology of the ternary blend containing 62 wt% PP/20 wt% polyethylene rubber (EPR)/18 wt% PE (PP/EPR/PE) and processed at 300, 600, 800 or 1200 rpm was in line with expectations at low screw speeds [171]. Specifically, the material compounded at 300 rpm showed coarse, irregular droplets with a strong tendency to coalesce, while improved sphericity and smaller second phase dimensions were obtained at 600 rpm. In addition, layered core-shell PE/EPR particles were observed, as shown in Figure 4. However, processing at 800 and 1200 rpm resulted in an undesired coarsening of the dispersed phase and a significant increase in the associated polydispersity index, which was related to the thermo-mechanical degradation of the polymers during processing due to the high rotation speed. This may be related to either the β-scissoring of the PP matrix or the crosslinking occurring between PE and EPR.

The ductile response of the material evolved consistently with these morphological changes [171]. In fact, the elongation at break increased from 200 % to 480 % when the blend was processed at 300 or 600 rpm, while it decreased to 310 and 170 % for the formulations compounded at 800 and 1200 rpm, respectively. Similar considerations can be applied to the impact strength, where the highest value was measured for the material obtained at 600 rpm. This last finding is particularly significant given that the size of the dispersed phase plays a role in the fracture mechanics of the component and, in particular, larger droplets promote crack coalescence and have a negative effect on impact strength [175].

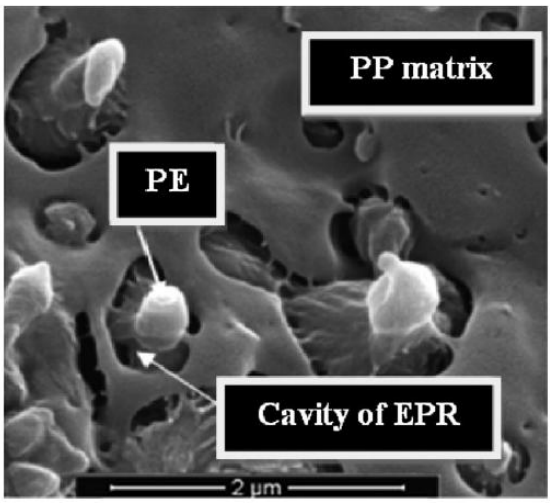


**Figure 4. SEM micrograph showing core–shell PE/EPR droplets within the PP/EPR/PE ternary blend processed at 600 rpm. [171]. Reprinted with permission from John Wiley and Sons, 2014.**

On the other hand, Raj et al. [172] verified the degradation of the PLA matrix with increasing screw speed in blends containing 30 wt% of PA12 by monitoring its crystallinity and viscosity after compounding at 200, 500, 800 or 1100 rpm. An abrupt increase in crystallinity was observed along with a decrease in viscosity in the formulation processed at 1100 rpm. At the same time, the coarsening that occurred at this speed ended up in polyamide domains with an average diameter of 1.1 mm, resulting in a morphology that was worse than that obtained at 200 rpm, where the value corresponded to 0.72 mm.
The tensile properties reflected the evolution of the microstructure. In fact, the strain at break first increased from 154.5 % to 224.2 % considering the material compounded at 200 and 800 rpm, but decreased to 18.1 % with the further enhancement of the screw speed to 1100 rpm.

An alternative explanation for the increase in dispersed phase size when the screw speed exceeds certain values has been identified by Yu et al. [175] in the reciprocal content of polymers in the blend. PE/PA12 materials containing polyamide in the range of 5 – 30 wt% were processed at 100 or 500 rpm and the average droplet diameter was evaluated. In fact, the decrease in the size of the dispersed phase with increasing screw speed was observed only in the blends characterized by 5 or 10 wt% of PA12, while no reduction in the diameter was detected for the ones containing 20 wt%. This behavior has been explained by the higher probability of collision between the domains in the presence of a greater content of polyamide, which promotes the coalescence of the droplets at the expense of the breakage driven by the shear applied. As a result, elongation at break and impact strength were favored by the increase in screw speed only in those materials where size reduction was observed. For instance, the strain improved from 90.5 % to 306.9 % in 95 wt% PE/5 wt% PA12 processed at 100 and 500 rpm, respectively, while it decreased from 64.6 % to 54.7 % for the blend containing 20 wt% of polyamide compounded under the same conditions. Likewise, the impact stress improved from 14.5 to 22 $kJ/m^2$ for the former material obtained at different rotation speeds, whereas no change was found for the latter.
Finally, considering the above considerations together with the findings of Raj et al. [172] on the PLA/PA12 blend discussed earlier, it is suggested that the polymers involved play a role in determining the evolution of the average dispersed phase droplet diameter with increasing screw speed when considering the effect of the reciprocal content of the two.

### 2.1.2 Rotation extrusion

With this technique, the orientation of the macromolecules is promoted according to a helical flow resulting from the superposition of two shear fields. The first, parallel to the direction of extrusion, is due to the flowing of the material, while the second acts perpendicularly and is generated in the die thanks to an annular rotating device with an external fixed casing and an internal rotating mandrel [45,181–183].
By exploiting the resulting structuring effect, hierarchical structures can be formed.

For instance, this is the case with HDPE and PP matrices, where the formation of shish-kebabs off the extrusion direction leads to important changes in the mechanical properties, which are particularly appreciated in the pipe production [184–188]. In fact, in traditional processing, the extruder is equipped with a fixed cylindrical annular die that forms the polymer and the final diameter is achieved by blowing air into the tube before the material solidifies. As a result, the macromolecules are preferentially aligned in the axial direction, where the best tensile properties are obtained. However, the main drawback is the low hoop tensile strength, which is related to the performance in the circumferential direction. This is particularly critical considering that the radial internal stress to which the pipes are subjected is twice as high as the axial stress, and therefore higher values of tensile strength would be preferred here in order to increase the operating pressure limit. In this term, rotation extrusion has proven to be a valuable solution [45,51,181–187,189]. In addition, another advantage of the technique was found to be the enhancement of heat resistance, which is also a decisive property that determines the operating conditions. For instance, pipes are commonly used to transport high-temperature fluids and this can determine the evolution of the microstructure towards a more isotropic organization, ultimately reducing the hoop strength over time [186].

The structuring effect of the helical flow generated in rotation extrusion is often studied using the Rotational Shear System (RSS), a batch thermostatic device that simulates the actual processing with good reliability [184,186]. It should be noted, however, that even if a single cooling system controls the temperature of both the inner and outer mandrel, some studies have reported a shift in the cooling rate of the two, with the latter being the lower, and this has implications for developing morphology through the thickness [182,186].

RSS was used by Yang et al. [186] for their study on the effect of the mandrel rotation speed on the morphology and final properties of a commercial bimodal molecular weight HDPE. The values of 5, 7.5, 10, 12.5 and 15 rpm were evaluated and the resulting microstructures through the thickness were investigated by Scanning Electron Microscopy (SEM). Figure 5 shows the corresponding micrographs. The terms inner layer and outer layer refer to the material in contact with the rotating mandrel and fixed mold, respectively, while the core layer refers to the section in between.

No shear has been applied to the material shown in the first row, so the final morphology is that typical of a polymer cooled under steady conditions. That is, an isotropic dispersion of spherulites. The effect of the different cooling rates is also clearly seen. In fact, both the inner and outer layers are characterized by smaller spherulites, while larger ones are detected in the core. This topology is related to the higher thermal conductivity of the metal walls with which the external layers are in contact, compared to that one of the polymer itself, on which the solidification of the core depends. On the other hand, Figure 5 rows 2 to 6 show the micrographs of the HDPE processed at increasing mandrel rotation speeds, and the morphology obtained is quite different from that described above. In fact, the formation of shish-kebabs and their orientation is clearly related to the imposed rotation speed.

Specifically, the higher the value, the greater the displacement of the shishs from the axial to the radial direction. However, as the mandrel rotation speed increases, the detrimental effect of excessive shear on the orientation and ultimately the formation of the hierarchical structures also becomes apparent. In fact, the anisotropy improved from 5 to 7.5 rpm (Figure 5, 2nd and 3rd rows), and the ordered lamellar structures seen in the inner and core layers of the HDPE processed in the former condition are organized in a homogeneous distribution of shish-kebabs in the latter case. Nevertheless, the microstructure of the polymer obtained at 10 rpm (Figure 5, 4th row) is very similar to that already observed obtained at 5 rpm, while the further increase of the mandrel rotation speed to 12.5 and 15 rpm (Figure 5, 5th and 6th rows) leads to a progressive loss of anisotropy. The shish-kebabs disappear in favor of ordered lamellae and finally spherulites.

The microstructural evolution can be elucidated by considering two primary mechanisms: the attainment of the critical strain rate in the molten polymer and the contribution of shear-induced thermal effects [182,186]. According to the "coil-stretch transition" theory, a minimum threshold strain rate must be exceeded to induce sufficient macromolecular stretching and orientation, which are prerequisites for the nucleation and growth of shish-kebab structures. In RSS, the deformation is imposed starting from the inner surface and propagates radially outward, resulting in a gradient of shear rate gradient that decreases through the thickness. At a mandrel speed of 5 rpm, the local strain rate in the outer layer remains below the critical threshold, inhibiting molecular orientation and leading to the development of an isotropic morphology in these regions. Conversely, at 7.5 rpm, the critical strain rate is exceeded across the entire pipe wall thickness, allowing the formation of a continuous hierarchical microstructure throughout the cross-section.

The second mechanism, referred to as shear heating, is responsible for the progressive transition of the microstructure to a less ordered configuration as the mandrel rotation speed increases. This phenomenon is attributed to the localized temperature rise in the polymer melt due to the elevated shear rate, which enhances macromolecular mobility and promotes chain relaxation [186,189]. As a result, a reduction in chain orientation and a shift towards a more isotropic morphology is observed. Nevertheless, the presence of residual shish-kebab structures in the inner layer of the sample processed at 12.5 rpm remains evident. This is attributed to the higher cooling rates experienced near the inner surface, which hinders the chain relaxation and partially maintains molecular orientation [186].

In light of the above considerations on microstructure, the evolution of the mechanical properties with increasing mandrel rotation speed is evident. The improvement in the hoop tensile strength is related to the presence and orientation of shish-kebabs. At the same time, the interlocking of these structures was found to play a role in preventing the chain slippage under tensile load. Therefore, the maximum value was obtained for the HDPE processed at 7.5 rpm, while it was negatively affected by the further increasing the mandrel rotation speed. Besides, the macromolecules stretched in the shishs greatly reduced the ductile deformation associated with the disentanglement and slippage of the chains. In fact, brittle

fracture behavior was observed and low values of elongation at break are usually associated with the increase in tensile strength obtained by rotation extrusion [186].

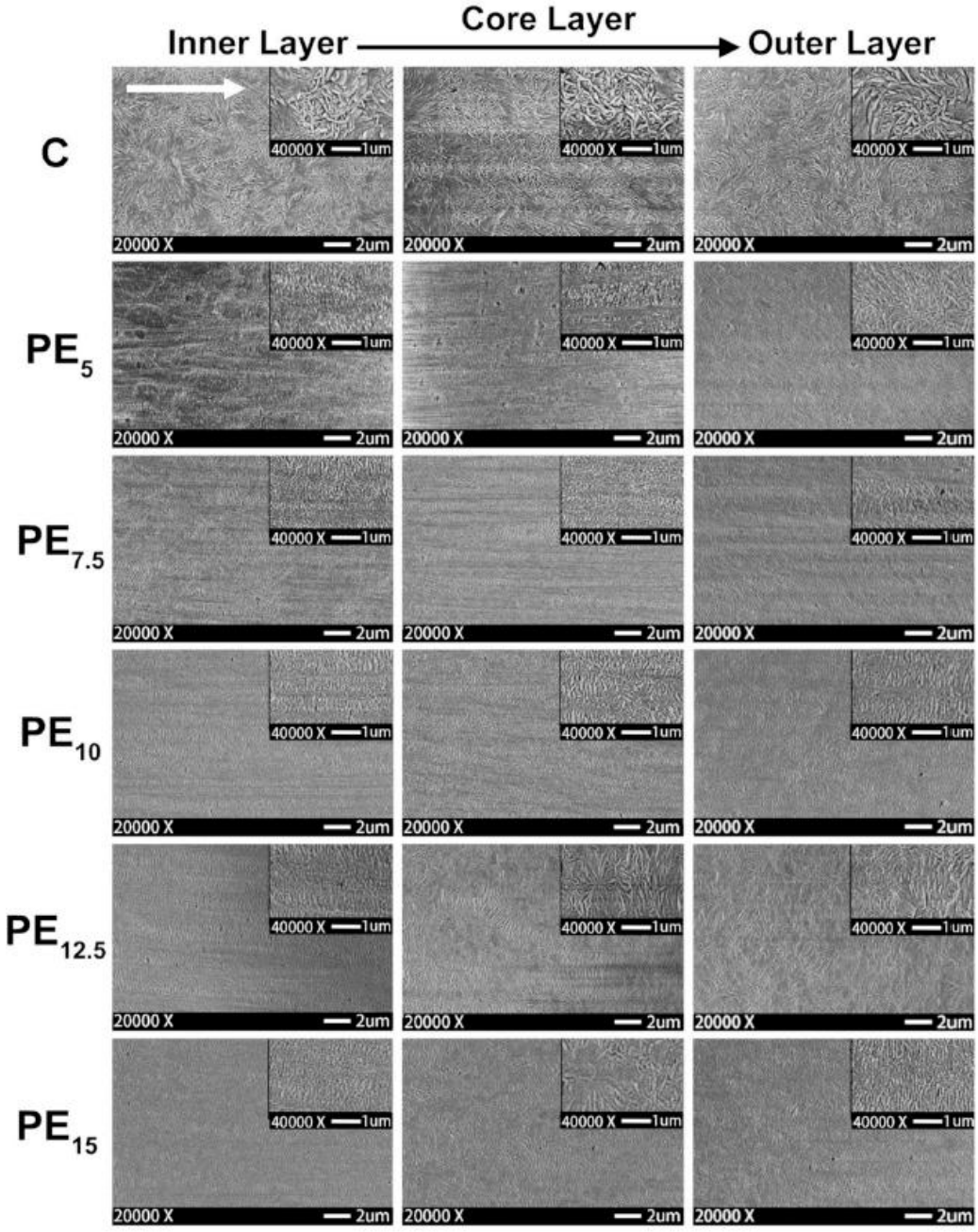


**Figure 5. SEM micrographs of the section of HDPE pipe processed with a mandrel rotating at 0 rpm (1st row), 5 rpm (2nd row), 7.5 rpm (3rd row); 10 rpm (4th row); 12.5 rpm (5th row); 15 rpm (6th row). The column refers to the material in contact with the mandrel (inner layer), the outer wall (outer layer) and the polymer in between (core layer). The white arrow indicates the direction of flow [186]. Reproduced with permission from Elsevier Science Ltd., 2019.**

The above analysis of the relationship between the mandrel rotation speed and the microstructure is consistent with the considerations of Nie et al. [182], explaining the behavior of HDPE pipes tested with the Slow Crack Growth (SCG) analysis, also known as the cone test. Crack initiation time and crack growth rate were evaluated for samples produced at 0, 5, 10 or 20 rpm. Comparing the two properties in the range 0 – 10 rpm, a positive effect of higher mandrel rotation speed

was observed. Specifically, the crack initiation time increased from 27 to 57 h, while the crack growth rate decreased significantly. As expected, the further intensification of the shear applied when the processing was performed at 20 rpm had a detrimental effect on the SCG. Again, the evolution of the mechanical properties was explained by considering the antagonistic role of the shear-induced orientation of the macromolecules and the shear heating developed with the increase of the mandrel rotation speed [182,188,190]. This was further confirmed by the hoop tensile tests where the stress increased from 17 MPa to 28 MPa when using 0 or 10 rpm as the mandrel speed, but decreased to 22 MPa for the samples produced at 20 rpm [182].

In addition, annealing can be used to manipulate the microstructure after processing and thus the resulting properties [184,191]. For instance, Chen et al. [184] compared the morphology of commercially available bimodal MW HDPE pipes, obtained at a mandrel rotation speed of 8 rpm, before and after annealing at 125 °C for 40 min. In Figure 6, the formation of oriented shish-kebabs is clearly seen throughout the section when the post-processing was not applied. On the other hand, after annealing, the hierarchical structures are retained only in the core layer, while the anisotropy has almost disappeared in the remaining thickness. This morphology was explained by considering the proximity of the post-processing temperature to the melting point of the polymer and the dimension of the lamellae in the different layers. In fact, under such conditions, the macromolecular relaxation tends to promote the melting of the thinner lamellae that form the shish-kebabs in the inner and outer layers of the pipe. On the contrary, the oriented hierarchical structures in the core layer are coarser and therefore more thermally stable. As a consequence, the orientation of the molten macromolecules is coordinated accordingly to the crystalline domains present, resulting in thicker and larger lamellae. The consequent advantage lies in the improved degree of interlocking between the kebabs and, in particular, the thermal properties are enhanced by the formation of such a network-like structure of oriented shish-kebabs. Besides, different thermal conductivity is obtained depending on the direction of measurement considered. In fact, the in-plane (perpendicular to the thickness) thermal conductivity was found to be greater than the out-of-plane (parallel to the thickness) thermal conductivity, and this was related to the microstructure. Specifically, the phonon transmission is maximized in the direction corresponding to the lower morphological discontinuity, and this condition is granted along the in-plane orientation, because that is where the stretched chains and shish are aligned, representing a preferential path for the transmission of the thermal energy.

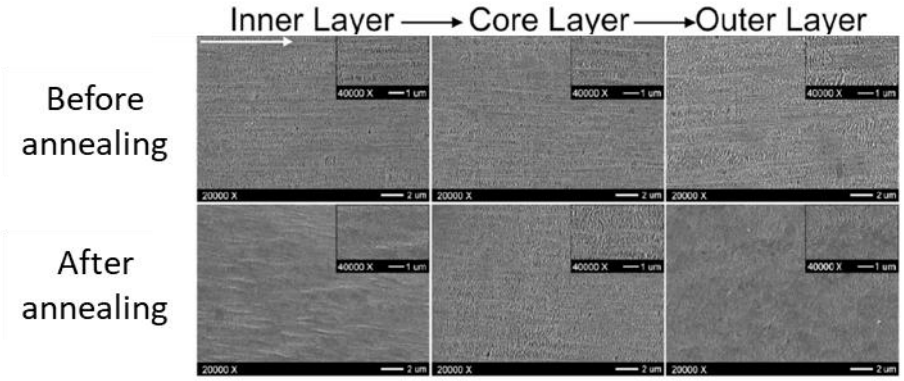


**Figure 6. SEM micrographs of HDPE pipes throughout the wall thickness. Comparison of the morphology before and after the annealing treatment at 125 °C for 40 min. Adapted from [184] with permission from Elsevier Science Ltd., 2020.**

Annealing also had an effect on the tensile properties, where the reduction in axial stress was related to the decrease in shish-kebabs content. However, no significant change was observed in the hoop tensile stress when compared to the performance of the samples before the treatment. In this case, the explanation was that the increase in crystallinity from 55.7 % to 60.7 % after annealing compensated for the decrease in anisotropy [184]. Whereas, the dependence of the hoop tensile stress from the die temperature has been shown by comparing the values of HDPE pipes processed at a mandrel rotation speed of 6 rpm and a temperature of 150, 170 or 210 °C [192]. The optimal value was found to be 170 °C, at which the oriented kebab-like lamellar structure allowed a hoop tensile stress of 31.8 MPa to be obtained. Further increase of the die temperature to 210 °C resulted in the formation of a random distribution of spherulites, favored by the macromolecular relaxation that prevents the orientation of the chains at high temperature. As a consequence, the value decreased to 24 MPa. Nevertheless, a comparable hoop tensile stress of 26 MPa was measured for the samples processed with a die temperature of 150 °C. The poor mechanical property was explained by the application of shear to the molten polymer at a temperature close to the melting point, resulting in the formation of deformed shish kebabs.

Finally, the effect of the introduction of 1 wt% UHMWPE on the morphology of HDPE pipe manufactured at a constant mandrel rotation speed was investigated [26]. The comparison of the two morphologies revealed an increase in the orientation degree of off- axis direction, from 0.26 in the matrix to 0.58 in the blend. Besides, the formation of shish-kebabs is promoted in the presence of UHMWPE (Figure 7b), while no such hierarchical structures are distinguished when the HDPE alone was processed under the same conditions (Figure 7a). This was related to the increase in the chain relaxation time in the blend due to the presence of the ultra-high MW polymer, which hindered the transition from oriented structures to random coil, resulting in the formation of a large number of folded lamellae, acting as shish nuclei and driving to denser kebabs. As a consequence, as revealed by the SCG analysis, the hoop tensile strength increased. In particular, the crack initiation time was enhanced from 43 to 92 h, while the crack growth rate decreased from 0.16 to 0.11 mm/h. This is in agreement with the previous observations [184], where

more packed kebabs were associated with the improvement of the tensile performance in the radial direction.

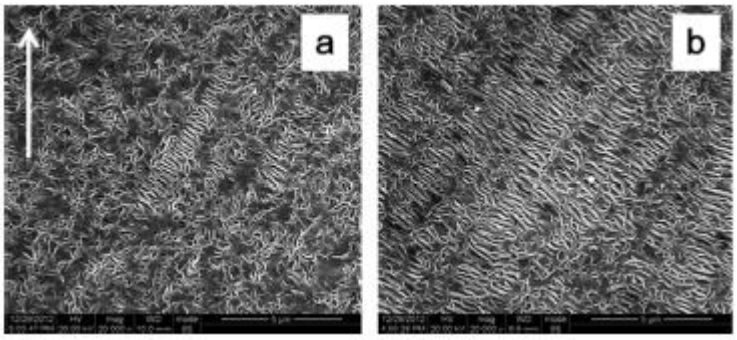


**Figure 7. SEM micrographs of the thickness of a a) HDPE and b) 99 wt% HDPE/1 wt% UHMWPE pipes. The white arrow indicates the axial direction. Adapted with permission from [193]. Copyright (C) 2014 American Chemical Society.**

In addition to HDPE, PP finds its place as polyolefin suitable for pipe production [45,51,181,185,194]. On the other hand, the formation of the α-spherulitic phase during conventional pipe extrusion poorly affects the impact toughness [185,195]. Typically, the problem is solved by using isotactic PP and a β nucleating agent (NA), which results in the formation of the metastable β phase in the final component. As a consequence, impact strength is improved because part of the energy is absorbed in the transformation to the stable α crystals. However, the resulting hoop strength decreases dramatically, and rotational extrusion has emerged as a viable method for improving material properties due to the formation of off-axis shish-kebabs. The morphology of the β-NAs has also been shown to play a role in their growth [15,195].

First, in their study, Nie et al. [45] clearly demonstrated the importance of the simultaneous presence of NA and mandrel rotation to obtain the desired microstructure. When neither mandrel rotation nor NA is present (Figure 8a), the isotropic distribution of α spherulites is observed. These structures are deformed by the action of the mandrel (Figure 8b), because even though β phase shish-kebabs may have been formed by the superposition of the axial and hoop drag flows, they tend to relax to a more stable conformation due to the high temperature in the absence of NA. In fact, the β phase was quantified as 6 % of the total crystalline content. On the other hand, due to the stabilization of the β phase by the introduction of the NA, shish-kebabs are obtained even in the absence of rotation (Figure 8c). However, the desired tilted orientation was achieved only with the mandrel in motion (Figure 8d). It is worth noting that the shish is made of the NA and the kebab are the folded lamellae of the β crystals. Besides, the final content of the metastable phase is influenced only by the presence of the NA, which is about 70 % in both cases. As expected, the impact strength increased in the presence of NA due to the high amount of β-crystalline phase. Most importantly, the effect of mandrel rotation on the hoop tensile strength was observed. In fact, the value was about 9 kJ when there was no rotation, despite the presence of NA, while the value increased to 13

and 15 kJ with the mandrel in motion, considering the presence or absence of NA, respectively.

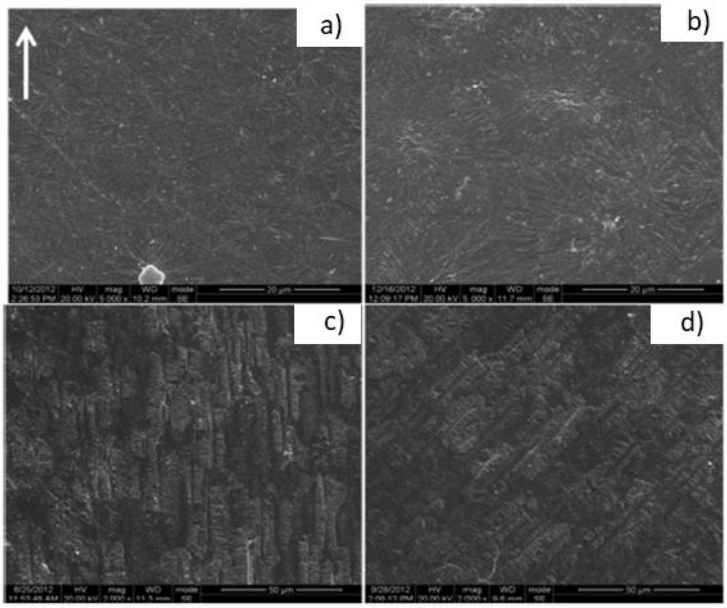


**Figure 8. SEM micrographs of isotactic PP produced under different conditions. a) no mandrel rotation and no NA; b) mandrel rotation, but no NA; c) no mandrel rotation, but NA present; d) both mandrel rotation and nucleating agent. The white arrow indicates the flow direction. Adapted with permission from [45]. Copyright (C) 2014, American Chemical Society.**

The effect of mandrel rotation speed on the hoop strength of isotactic PP pipes was examined, revealing a trend similar to that observed for HDPE [51]. As the rotation speed increased from 0 to 4 and 8 rpm, the hoop strength improved significantly, from 21.3 MPa to 30.0 MPa and 34.0 MPa, respectively. However, when the rotation speed was further raised to 12 rpm, a decline in tensile strength was observed, with values dropping to 26.7 MPa. This drop was related to flow instabilities at higher speeds, which led to the formation of microstructural defects that compromised the mechanical performance of the material. These results highlight the presence of an optimal rotation speed, beyond which the benefits are negated by structural irregularities.

Previously, the role of β-nucleating agent morphology in influencing the microstructure and enhancing the hoop tensile strength of isotactic PP was briefly introduced. A more detailed investigation by Pi et al. [181] addressed this aspect by employing 0.3 wt% of NA with different morphologies to evaluate their impact on structural development and mechanical performance. Specifically, a dot-like form and an irregular block-like form were considered.

Figure 9 provides clear insights into the microstructural evolution of the iPP samples, as revealed by 2D-WAXD analysis. When using the dot-like NA, both with and without mandrel rotation (Figure 9a and 9b), the diffraction rings corresponding to the β(300) plane appear perfectly circular. This indicates a homogeneous and isotropic distribution of the β crystalline phase, consistent with a spherulitic morphology evenly dispersed throughout the matrix. In contrast, samples incorporating the block-like NA exhibit arc-shaped β(300) diffraction

patterns (Figure 9c and 9d), which point to the development of a well-oriented microstructure. This structural ordering was further associated with hybrid shish-kebab formations. In these structures, the nucleating agent acts as the shish, while β-phase crystals grow epitaxially as kebabs, and that is consistent with earlier findings [45]. The study also revealed that the block-like NA transforms into fibrous nuclei prior to isotactic PP crystallization. This transformation is attributed to the dissolution of the NA in the polymer melt at elevated temperatures, followed by its self-assembly into fibrous structures.

Furtherly, in contrast to what was previously reported by Nie et al. [45], no noticeable orientation effect is observed when only spherulitic structures are present (Figure 9b). However, a distinct tilting of the hierarchical structure is evident when comparing Figure 9c and 9d. In the presence of mandrel rotation, the orientation angle of the resulting microstructure was calculated using the Herman equation and found to be approximately 25°.

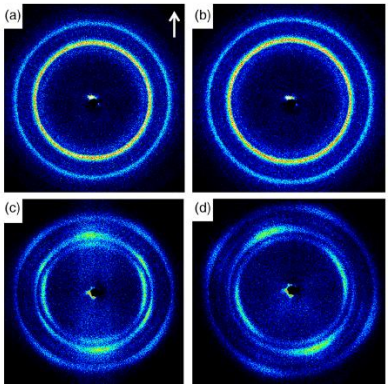


**Figure 9. 2D-WAXD of isotactic PP processed with a) dot-like NA and no mandrel rotation; b) dot-like NA and mandrel rotation; c) block-like NA and no mandrel rotation: d) block-like NA and mandrel rotation. The white arrow indicates the axial direction [181]. Reprinted with permission from John Wiley and Sons, 2019.**

As already emphasized, the presence of the β phase and the anisotropy of the morphology influenced the mechanical performance of the material. As previously discussed [51], the impact strength was primarily governed by the amount of metastable β phase, rather than by the mandrel rotation itself. The dot-like nucleating agent led to the formation of a higher content of β-phase crystals, with values of 89.3% and 92.8% for samples processed without and with mandrel rotation, respectively. In comparison, the block-like nucleating agent resulted in lower β-phase contents of 86.4% and 84.4% under the same conditions. This difference in phase content directly influenced the impact strength. Samples prepared with the dot-like nucleating agent exhibited an impact strength of 20 J, whereas those with the block-like agent reached 18 J. Additionally, the off-axis orientation in the microstructure was confirmed to be the best in terms of contribution to hoop strength. In samples with an isotropic spherulitic morphology, the hoop strength was measured at 24 MPa with a stationary mandrel and 23 MPa with mandrel rotation. However, when a helical flow induced the formation of

shish-kebab structures oriented off-axis, the hoop strength increased significantly to 34 MPa.

The off-axis orientation of shish-kebab structures was also observed in a polypropylene copolymer containing approximately 3.8 wt% of ethylene [194]. This effect became particularly evident with the addition of a NA and isotactic PP as a crystallization promoter. Under these conditions, the mesomorphic phase content increased significantly, from 0% to 51%. In addition, a comparison of the mechanical properties of pipes extruded with the mandrel rotating at 6 rpm revealed a notable improvement. The impact strength increased from 4 to 7 kJ/m², while the hoop strength rose from 23.7 to 28.9 MPa. These improvements were attributed to the combined action of isotactic PP and the nucleating agent. The mechanical performance declined when either of the two was used alone, which confirmed that the observed enhancement resulted from a synergistic interaction between them. In particular, in this mechanism the nucleating agent generates fibrous nuclei that serve as the shish, while the isotactic PP macromolecules crystallize on these structures, forming β-phase kebabs. These kebabs then act as scaffolds for further crystal growth by the copolymer, leading to the development of a complex, anisotropic hybrid shish-kebab microstructure. Finally, the orientation of the hierarchical structures is driven by the combined effect of axial and hoop drag flows, as their superposition induced by mandrel rotation promotes the off-axis alignment of the shish-kebab structures.

The preservation of an isotropic spherulitic microstructure in ethylene-containing polypropylene copolymers, in the absence of NA and isotactic polypropylene, was confirmed by Han et al. [196]. Their investigation focused on the effects of mandrel rotation speed and cooling rate on the morphology and mechanical properties of the neat copolymer. Across all processing conditions tested, no evidence of oriented crystalline structures was observed. On the other hand, the study did identify a degree of macromolecular orientation within the amorphous phase, which became apparent under mandrel rotation. Although no shish-kebab structures were formed, a slight improvement in mechanical performance was recorded. This enhancement was attributed to flow-induced orientation within the amorphous phase during processing.

Mandrel rotation also affected the amorphous phase orientation in polybutene-1 (PB) pipes, resulting in increased crystallinity and fewer crystal defects [183]. However, no shish-kebab structures were observed at any of the mandrel rotation speed, ranging from 2 to 12 rpm. This was attributed to the stronger steric hindrance to macromolecular orientation in PB compared to HDPE and PP, combined with the longer crystallization time of PB. Although a slight lamellar orientation was observed at the highest rotation speed, the microstructure remained predominantly spherulitic and isotropic. The orientation of macromolecules was, however, more easily maintained in the amorphous region [197]. This phenomenon was linked to the observed improvement in hoop tensile strength, which increased from 20 to 25 MPa as the mandrel speed rose from 0 to 8 rpm.

Finally, as with other materials, excessively high mandrel rotation speeds led to a decrease in mechanical properties. This decline was attributed to the formation of defects due to the high processing rates [51,183,189].

### 2.1.3 Vibration extrusion

Vibration extrusion is particularly effective for compounding polymers that are otherwise challenging to process using conventional solvent-free methods, primarily due to their high entanglement density. This technique operates by applying extra shear through an external vibrational field, which increases the energy transferred to the macromolecules. The added energy promotes greater conformational freedom for the macromolecules, ultimately reducing the density of molecular entanglements [14,198–201]. As a consequence, the process not only minimizes melt fracture and elastic turbulence but also enhances the overall throughput by 50 to 100% [202–210]. In addition, the final morphology, surface quality, and mechanical properties of the material are significantly influenced [198–200,202,205,206,208,209,211–214]. These outcomes are often described as the *physical effects* [205,207,215,216].

In addition to its physical effects, the application of an external vibrational field can also produce *chemical effects* as, for instance, polymer degradation, which results in a reduction of molecular weight, alters the molecular weight distribution and, ultimately, contribute to an overall decrease in melt viscosity [14,199,202,205,207,208,215–217]. However, the same chain scission events that lead to degradation may also generate long-chain radicals. These reactive species can promote in-situ copolymerization in immiscible polymer blends. Evidence of this mechanism was observed in atomic force microscopy (AFM) images, which revealed the formation of a transition layer at the interface between the matrix and the dispersed phase in samples processed with vibration extrusion. This interfacial layer was absent in samples produced without the vibrational field [205,217,218]. Further confirmation came from extraction experiments, which showed a higher residue in the blends treated with ultrasound. This residue was attributed to copolymers formed through reactions between the macromolecular chains of the two distinct polymers [217]. The formation of this interfacial transition layer enhances the compatibility between the polymer components. As a result, interfacial tension is reduced, and the size of the dispersed phase domains decreases significantly [205,217,218].

Several processing parameters must be taken into account when applying vibration extrusion. One key factor is the frequency of the vibrational field, which defines the specific variant of the technology. When the frequency exceeds 20 kHz, the process is referred to as *ultrasonic vibration extrusion* (named ultrasonic extrusion below). In contrast, frequencies ranging from 0 to 100 Hz characterize *mechanical* or *oscillation extrusion* (hereafter, oscillation extrusion) [14,198,202]. Another important consideration is the direction in which the vibrational field is applied. Vibrations can be introduced either longitudinally or transversally. Among

these, longitudinal vibration, where the shear field is aligned with the material flow direction, has been found to be more effective in promoting macromolecular orientation along the extrusion axis. This alignment leads to improved mechanical performance, particularly an increase in stress at break in the flow direction. In addition, the longitudinal vibration setup is particularly compatible with continuous manufacturing processes because it can be easily integrated into the extrusion of tubular products such as hoses and other cylindrical components [14,202–204] .

Various strategies can be adopted to apply the external vibrational field to the polymer during processing. In the case of oscillation extrusion, one approach involves vibrating the screw itself. This method produces a general plasticizing effect, which enhances melting efficiency and reduces the overall energy consumption of the extrusion process. In this configuration, the vibration is applied over a broader region and for a longer time compared to alternative setups [198,199,211,212,219,220]. A common alternative involves vibrating the die instead of the screw. Specifically, this is achieved using an annular die equipped with an internally vibrating cylinder. This configuration is widely adopted, partly because it allows the vibrational field to be applied in both longitudinal and transverse directions, depending on the specific processing requirement. However, for ultrasonic extrusion the vibrating die is the only viable option and in this case the field is applied in a direction parallel to the melt flow [198,205,206,215,221,222].

This section examines how variations in vibration frequency, intensity and amplitude influence the morphology and final properties of the processed polymers. Unless otherwise specified, the studies discussed here refer specifically to processes involving extrusion through a vibrating die.

First, the individual contributions of the physical and chemical effects of ultrasonic vibration were clarified through the processing of a single polymer system. In the study by Chen et al. [205], PP was extruded using ultrasonic vibration at a constant frequency of 20 kHz, while varying the intensity across five levels, which were 0, 50, 100, 150, and 200 W. In addition, the work provided further insight into how vibration intensity influences macromolecular orientation. To differentiate between the physical and chemical contributions, two successive extrusions were conducted for materials processed at each vibration intensity and apparent viscosity was measured after each step. In the first extrusion, the vibration field was applied, while the second extrusion was performed without it. As a result, the morphology of the materials after the first compounding step was influenced by both the physical and chemical effects of the vibration field, as well as by the thermo-mechanical impact of the extrusion process. In contrast, after the second step the materials were only affected by the melt blending and the chemical effect that persisted from the first compounding step, because the physical effect was no longer present due to the enhanced chain motion in the melting state along with the absence of the vibrational field [201,205].

First, the apparent viscosity values were normalized after the second extrusion step, in order to exclude the influence of the thermo-mechanical field. The reference for this normalization was the material processed entirely without vibration,

specifically at an ultrasonic intensity of 0 W. By comparing its viscosity after the first and second processing steps, it was found that the thermo-mechanical contribution accounted for 1.6% of the total value. Based on this result, all apparent viscosity values after the second extrusion were corrected accordingly (Figure 10a). Following this adjustment, the chemical effect was quantified for each sample. In particular, it was calculated as the difference in apparent viscosity between the material processed without vibration during the first step and the one processed with ultrasonic assistance. Once the chemical contribution was established, the physical effect was determined by subtracting the viscosity value after the first extrusion from that after the second. The analysis revealed that the chemical effect contributed approximately 35 to 40 % of the overall impact induced by the applied vibration field.

Besides, it was demonstrated that the overall reduction in viscosity, as well as the specific chemical contribution, increases with higher vibration intensity. To investigate this further, the molecular weight of the polymers after processing was analyzed. As shown in Figure 10b, increasing the vibration intensity led to a noticeable decrease in the overall MW and a narrowing of the molecular weight distribution. Both of these trends were attributed to the degradation of polymer chains induced by the vibrational field.

Finally, the influence of the external vibrational field on macromolecular orientation was examined, as shown in Figure 10c. The results indicated that chain orientation decreases as the vibration intensity increases, eventually stabilizing around an average value. This behavior was attributed to the greater molecular mobility induced by the energy input from the vibrations. As the number of entanglements and molecular interactions decreases, relaxation times are reduced. Consequently, when a high-intensity ultrasonic field is applied, the resulting morphology is expected to be more disordered [205,209].

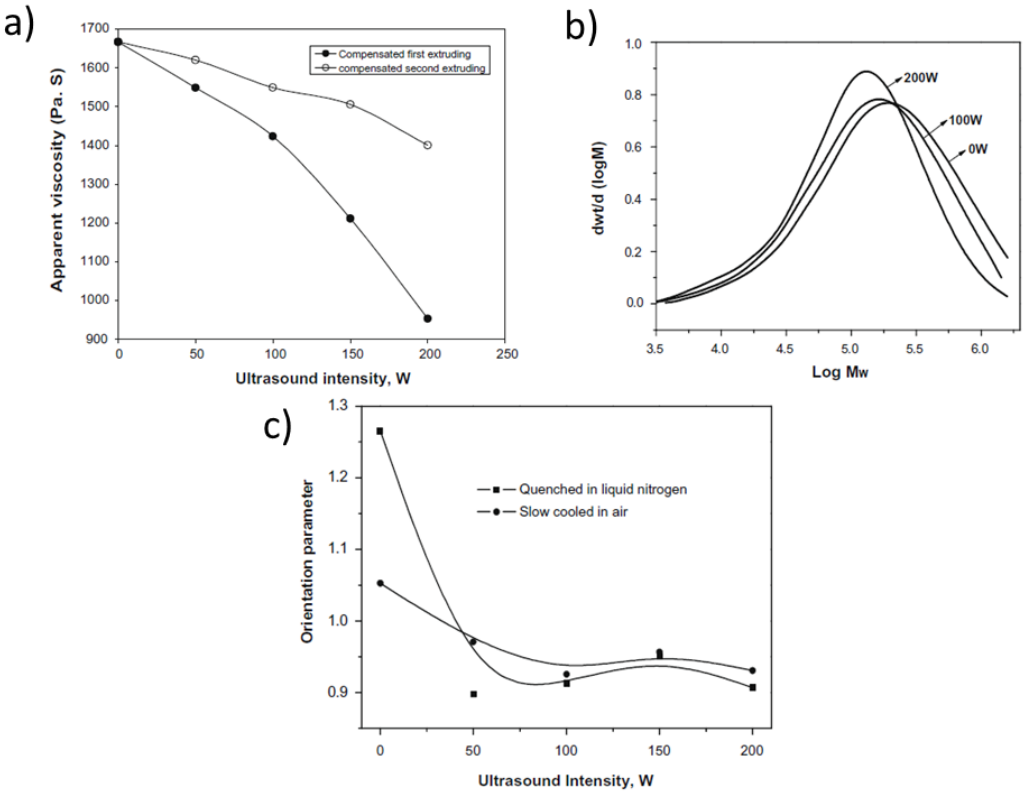


**Figure 10. a) Normalized apparent viscosity of PP after initial ultrasonic-assisted extrusion at varying intensities, compared to reprocessed material without vibration; b) Molecular weight distributions of PP processed at 0, 100, and 200 W; c) Orientation parameter as a function of ultrasonic intensity for quenched and air-cooled samples [205]. Adapted with permission from Elsevier Science Ltd., 2010.**

These findings align with the results reported by Guo et al. [206] on the ultrasonic extrusion of linear low-density polyethylene (LLDPE). The study demonstrated that the apparent viscosity decreased progressively with increasing ultrasonic vibration intensity, which was varied at 0, 50, 100, 150, 200, and 250 W. Additionally, a linear relationship between apparent viscosity and applied shear rate was observed across all intensities within the range of 30 to 100 $s^{-1}$. Besides, it was found that the sensitivity of apparent viscosity to shear rate depended on the vibration intensity. Specifically, at higher ultrasonic intensities, the apparent viscosity showed a more pronounced decrease with increasing shear rate compared to materials processed at lower intensities.

The relationship between the apparent viscosity sensitivity and the value of certain processing parameters was also observed by Gao et al. [213]. In their study, oscillation extrusion of HDPE was carried out with a frequency range between 0 and 93.3 Hz, while the screw rotation speed varied from 5.56 to 16.7 rpm. Figure 11a shows the property for HDPE processed at 5.56 rpm decreases from 950 Pa.s at 0 Hz to 600 Pa.s at 9.3 Hz. The value then increased to 700 Pa.s at 20 Hz before stabilizing at an almost constant level afterwards. This trend indicated that the sensitivity of the apparent viscosity was greatest at low vibration frequencies, while the contribution from higher frequencies became negligible. Then, considering the effect of the screw rotation speed (Figure 11b), it emerged the sensitivity of the apparent viscosity from the frequency to be suppressed also in the range of 0-20

HZ, when using values greater than 5.56 rpm.
Finally, the mechanical properties of the extruded HDPE were examined as a function of the applied vibration frequency. At a screw speed of 5.56 rpm, the longitudinal yield strength showed a sharp increase from 21.31 MPa under conventional extrusion to over 23 MPa once vibration was introduced. A similar trend was also observed in the transverse direction. The increase in longitudinal yield strength was expected, as the vibrational field promotes macromolecular disentanglement and alignment along the flow direction. However, the improvement in the transverse direction was less intuitive. To explain this behavior, the authors referred to the morphological and thermal analyses conducted on samples processed at 0, 5.6, and 9.3 Hz, respectively. The study revealed that increasing the vibration intensity led to greater overall anisotropy, promoting enhanced crystal orientation along the longitudinal direction. At the same time, samples processed at 5.6 and 9.3 Hz exhibited slightly higher crystallinity and the formation of smaller crystals with reduced lamellar thickness, when compared to those produced without vibration at 0 Hz. These structural changes were further amplified as vibration intensity increased from 5.6 to 9.3 Hz. As a result, the refinement of the crystalline structure contributed more significantly to improving the mechanical performance in the transverse direction than the loss caused by crystal alignment in the longitudinal axis. This balance confirmed the presence of a biaxial reinforcement effect induced by the application of oscillation during processing.

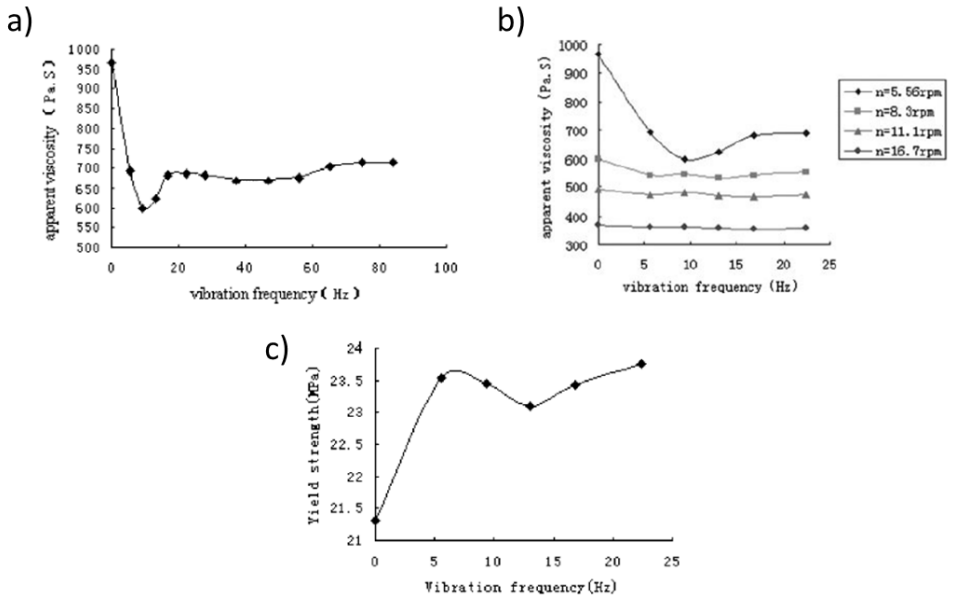


**Figure 11. a) Apparent viscosity as function of the oscillation frequency of the material produced at 5.56 rpm; b) Apparent viscosity as function of the vibration frequency for the HDPE produced at different screw speeds; c) Longitudinal yield strength of the material melt blended at 5.56 rpm as function of the oscillation frequency [213]. Adapted with permission from John Wiley and Sons, 2007.**

As previously discussed in Section 2.1.2 on rotational extrusion, techniques that enhance mechanical properties in both the longitudinal and transverse directions are particularly relevant for pipe production. To explore the benefits of screw

vibration during oscillation extrusion, Kaiyuan et al. [211] investigated the circumferential performance of HDPE pipes processed at frequencies ranging from 2 to 14 Hz, using vibration amplitudes of either 150 or 200 μm. The study revealed an overall positive impact of the vibrational field on mechanical properties. Specifically, analysis of the bursting pressure showed a non-linear response at both amplitudes. The pressure increased sharply from 3.3 MPa at 0 Hz to approximately 4.2 MPa within the 2 to 10 Hz range. At higher frequencies, the pressure remained stable when the amplitude was 200 μm, whereas it declined at 150 μm. Despite this variation, the bursting pressure under all vibration conditions exceeded that achieved through conventional extrusion, confirming the advantageous role of external vibration in enhancing the pipe's circumferential performance. Additionally, mechanical properties in the longitudinal direction were either preserved or further improved, demonstrating that the application of vibration contributes positively to both longitudinal and transverse performance in HDPE pipes.

Thermal analysis also revealed an improvement in both the crystallinity content and the perfection of the crystals with increasing oscillation frequency or amplitude. Specifically, the overall crystallinity rose from 57.61% at 0 Hz and 150 μm to 61.26% at 14 Hz, while the melting temperature increased from 133.7°C at 0 Hz and 200 μm to 135.6°C at 6 Hz. These improvements were attributed to the disentangling effect of the vibration on the macromolecules. In particular, as the entanglement density decreased, the macromolecules were able to nucleate at higher temperatures, forming more ordered and thermally stable crystals [68,211,213,223]. Furthermore, the combination of reduced entanglement density and the multiplex shear force created by the interaction of screw rotation and axial vibration facilitated the dragging and orientation of the chains in both the longitudinal and transversal directions, which in turn enhanced the mechanical properties, as observed also in other studies [200,211,213,214,220]. For instance, Qu et al. [220] investigated the tensile strength of isotactic PP films in both the machine and transverse directions, using vibration-assisted processing at frequencies ranging from 0 to 14 Hz and an amplitude of 80 μm. Their results showed that tensile strength in both directions increased as the vibration frequency rose, reaching a peak at 6 Hz, followed by a decline at higher frequencies. Although the overall trend was similar for both directions, the reduction in tensile strength at elevated frequencies was more pronounced in the machine direction.

Focusing on the blends, Liu et al. [233] investigated the influence of vibration intensity during ultrasonic extrusion of UHMWPE-PP blends containing 10, 20, or 30 wt% PP. As shown in Figure 12, the trend of the apparent viscosity is consistent with previous findings and decreased as vibration intensity increased. However, the rheological response varied with the PP content. Specifically, as the PP concentration increased, the sensitivity of the apparent viscosity to the shear rate was found to decrease. A distinctive trend emerges when comparing the apparent viscosity as a function of shear rate for blends processed at 200 and 250 W. In fact, the blend containing 10 wt% of PP displays a positive slope up to approximately 25 $s^{-1}$ (Figure 12a). However, this behavior becomes less pronounced as the PP content

increases. In the case of the 20 wt% blend (Figure 12b), the slope flattens, while a clear shear-thinning behavior at low shear rates is observed for the blend with 30 wt% PP (Figure 12c). This behavior was attributed to the characteristics of UHMWPE. In particular, blends with a higher UHMWPE content showed greater sensitivity at low shear rates. This was linked to the longer exposure of the extended polymer chains to high-intensity ultrasonic irradiation, which facilitates the disentanglement of the macromolecules but also increases the likelihood of chain scission. Both effects become more significant as the UHMWPE concentration and vibration intensity increase. However, at higher shear rates, the exposure time decreases, reducing the disentangling effect and leading to a rise in apparent viscosity.

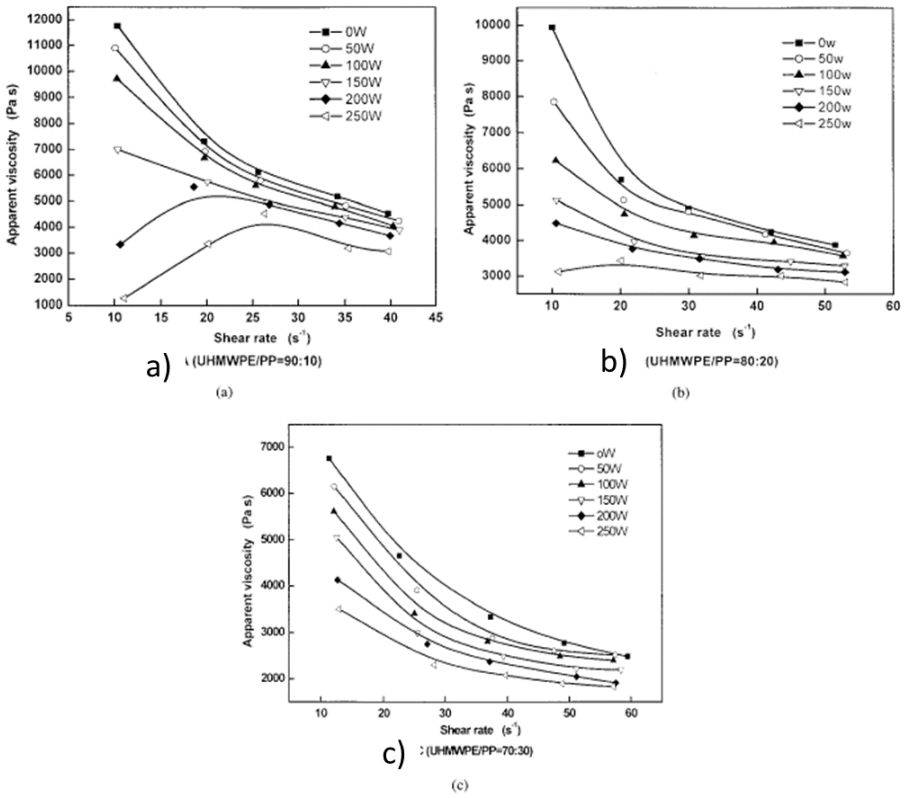


**Figure 12. Apparent viscosity of the UHMWPE-PP blends containing a) 10 wt%, b) 20 wt% and c) 30 wt% of PP under different ultrasonic intensities [208]. Adapted with permission from John Wiley and Sons, 2003.**

In contrast, the same study [208] reported that the application of the ultrasonic field had a limited or even negative effect on the mechanical properties when different screw rotation speeds were used (specifically 5, 10, and 15 rpm). For example, in the blend containing 20 wt% of PP, the yield strength remained unchanged up to an intensity of 150 W at both 10 and 15 rpm. However, when the intensity increased to 250 W, a noticeable decrease in yield strength was observed regardless of the screw speed. An even more critical outcome was observed when analyzing the Izod notched impact strength. The values remained stable only at a screw speed of 15 rpm, whereas a significant drop occurred at 5 and 10 rpm, where the impact strength fell from approximately 90 kJ/m² to below 40 kJ/m². This

reduction in mechanical performance was attributed to the detrimental effects caused by excessively high ultrasonic intensity or prolonged exposure time during processing.

On the other hand, notable findings on the enhancement of blend compatibility through the application of ultrasonic fields have been reported in the literature [216,218]. Chen et al. [216], for example, investigated HDPE– polystyrene (PS) blends containing 20 wt% PS. Using the emulsion-type model proposed by Palierne [224], they calculated the interfacial tension (α) and the volume-average particle radius. The blends were compounded either with or without the use of an ultrasonic field, employing either a single processing step (20 kHz and 200 W) or a double-step process (20 kHz and 100 W each). Subsequently, the rheological behavior was analyzed in terms of storage and loss moduli, using a parallel-plate rheometer. Then, the results were compared to those calculated using the Palierne model, and the ones that best matched were selected. Using these, the α and the $R_v$ of the dispersed phase were calculated with the Palierne relation. In the case of the single compounding step, a noticeable reduction in both α and $R_v$ was observed when the ultrasonic field was applied. Specifically, α decreased from 4.5 to 3.9 mN/m, and $R_v$ reduced from 1.14 to 0.83 mm. These reductions highlighted that the compatibility between HDPE and PS improved owing to the presence of the ultrasonic field. In the case of the double-step melt blending, similar results were observed when vibration was applied during extrusion, with both the interfacial tension and the volume-average particle radius decreasing from 5.2 to 1.53 mN/m and from 1.31 to 0.73 mm, respectively. This demonstrates the positive effect of the ultrasonic field on enhancing the compatibility in HDPE – PS blends, both in single and double-step compounding. Additionally, by comparing the α and $R_v$ values calculated for the materials processed with a single or double melt blending, the influence of vibration intensity can be clearly observed. In fact, when analyzing the interfacial tension, the two-step blend without the ultrasonic field showed a higher value (5.2 mN/m) compared to the single-step materials (4.5 and 3.9 mN/m for 0 and 200 W, respectively). This suggests that the double processing, in the absence of vibration, is less effective. In contrast, when vibration was applied, the final α value was the lowest (1.53 mN/m), even though the vibration intensity was only half of that used in the single extrusion. This indicates that a double extrusion at 100 W is more effective in improving the polymer compatibility than a single extrusion at 200 W.

Similarly, Oh et al. [218] reported an enhancement in the compatibility of a 50 wt% PP – 50 wt% natural rubber (NR) blend, as observed from the stress-strain curves obtained during ultrasonic vibration processing at an amplitude of 10 μm. Specifically, the maximum strain increased from 9 MPa to 12 MPa, while the strain at break showed a remarkable rise from approximately 25% to over 120%. In contrast, the study found significant improvement in impact resistance as measured by the probe penetration test. Specifically, the force, displacement and, thus, the resulting impact energy increased when the vibration was applied (Figure 13A). The value of 1.51 J, measured for the blend processed by the conventional approach improved to 3.32 and 4.72 J when one or two horns were used, respectively. In

addition, owing to the AFM analysis, the change in the impact behavior was explained with the formation of an interfacial transition layer between PP and NR. In fact, in the absence of vibration (Figure 13B1), sharp steps at the interface indicate poor adhesion between the polymers. On the other hand, when the ultrasonic field is applied, a more irregular transition zone is obtained (Figure 13B2 and B3), thus promoting compatibility between the two.

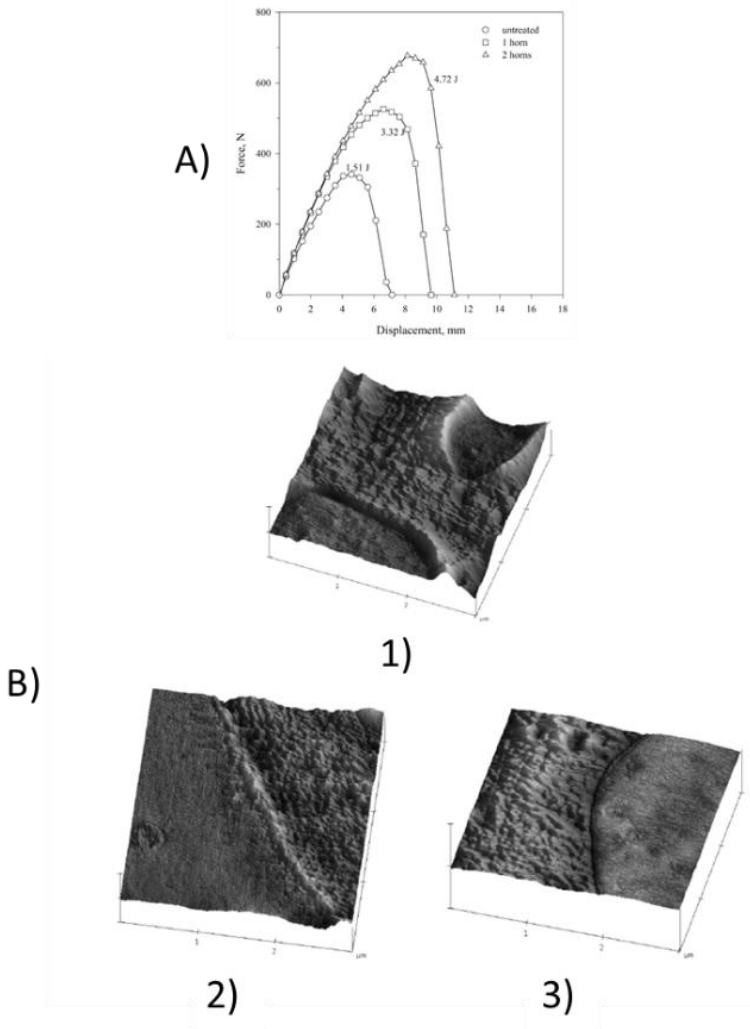


**Figure 13. A) Force as function of the displacement obtained from the probe impact test performed on the conventionally extruded and ultrasonic vibration-assisted blends. Next to each curve, the energy impact, calculated as the integral of the area below the curve, is shown. B) AFM surface profiles of PP/NR blends processed (1) without vibration or with (2) one horn or (3) two horns [218]. Adapted with permission from Elsevier Science Ltd., 2003.**

Finally, in-situ copolymerization in immiscible blends processed with ultrasonic vibration was observed also by Isayev et al. [217]. A PP or HDPE matrix were alternatively compounded with 50 wt% of NR, ethylene-propylene-diene rubber (EPDM) or styrene-butadiene rubber (SBR) and processed at a frequency of 20 kHz, power of 3 kW and amplitude of 6 or 10 mm. Also, conventional extrusion was performed as a reference.

Regardless of the polymer considered, the frequency amplitude turned out to be secondary to the presence or absence of vibration in improving the mechanical

properties. In fact, the chemical effect that leads to the formation of long-chain radicals that recombine at the interface to form a copolymer predominates, promoting adhesion and a more homogeneous dispersion of the second phase. As a result, the elongation at break and Young's modulus increased from 38.9 to 126.8% and from 191 to a maximum of 250 MPa, respectively, for the untreated or ultrasonically extruded PP/NR, while for HDPE/NR the elongation at break increased from 189.0% to 300.6% and the Young's modulus from 75.1 to 127.0 MPa. In addition, the impact energy calculated with the probe test increased from 2.75 to 5.89 J in PP/NR and from 6.09 to 8.12 J in HDPE/NR.

### 2.1.4 Drawing

The microstructural tailoring of polymers can be effectively achieved by introducing elongational flow through drawing aligned with the extrusion direction, a technique whose superior efficacy compared to shear flow has been consistently demonstrated in the literature [5,17,115,162,225]. In fact, this approach has been shown to enhance macromolecular orientation, modulate the amorphous-to-crystalline phase ratio, and facilitate the breakup and dispersion of the minor phase within polymer blends. Additionally, an increase in the intensity of elongational flow has been shown to induce progressive microstructural transitions, ranging from a homogeneous arrangement of spherulites to an anisotropic distribution of deformed spherulites and small lamellae, ultimately leading to a dispersion of well-oriented lamellar structures [5,143,226]. This capacity to modulate the morphology offers significant potential for the development of tunable final properties. Consequently, various production processes based on the exploitation of elongational flow have been established. Typical examples of such processes include film casting, film blowing, and melt spinning [5,17,115,144,227]. These techniques are widely employed at the industrial scale for applications in packaging [91,228,229], fishing nets [143,145], biomedical devices [92,146,148,230,231], and textiles [92,144,149], owing to their advantageous combination of high production rates, cost-effectiveness, favorable mechanical performance, and efficient barrier properties. The present analysis will concentrate on film casting and melt spinning, given the superior thickness uniformity achieved by the former compared to film blowing [232], and the high filament yield characteristic of the latter [144].

Both film casting and melt spinning require either a high degree of supercooling or the application of a strong flow field to effectively enhance material anisotropy and an annealing step may be incorporated in the process [5,233,234]. However, different equipment is used for the application of the elongational flow in each process. In film casting, the machinery is typically equipped with a center-fed "T" die, where elongational flow is applied during solidification under non-isothermal conditions in the air gap immediately following the extruder. Water-cooled or heated rollers maintained at a constant temperature are used to accomplish the drawing and to ensure complete cooling of the material [91,232]. Alternatively, a

precursor film may first be produced, with stretching applied at a later stage [5,235,236]. On the other hand, in melt spinning the filament is obtained by means of a spinneret, which is an ad-hoc die having a number of holes that can reach up to several hundred, thus allowing the production of a large quantity of fibers simultaneously. In addition, in this process a melt pump is often present to ensure a constant flow rate toward the die. Furthermore, the stretching step is performed inline using to a filament draw-down unit and wound onto a bobbin afterwards. Alternatively, offline drawing is usually exploited at industrial scale, because it is more compatible with the processing [144,237–239].

Regardless of the technique considered, the key parameters determining the microstructure are the draw ratio (DR) and roll temperature [11,18,143,151,152,226,240–252]. However, it is worth noting that in film casting, the DR is calculated as the ratio between the roller rotation speed and the extrusion velocity [253], while in melt spinning, it corresponds to the ratio between the square value of the diameter of the extrudate and the square of the diameter of the fiber [254].

The polymer microstructuring potential of drawing will be explored starting with the discussion of the effect of the variation of the latter parameter. The primary impact of increasing the DR lies in the ability to tune macromolecular orientation, crystallinity content, crystal morphology, and crystalline size, thus fostering the overall anisotropy [5,37,115,143,150–152,226,240–242,245–247,249,255–260]. The work of Xie et al. [245] on poly(butylene succinate) (PBS) films prepared at DR values of 25, 50, 75, 100, and 125 clearly demonstrates this phenomenon. In fact, as shown in Figure 14a, the deformed spherulites obtained at DR 50 progressively evolve into raw-nucleated oriented lamellar structures with increasing draw ratio. Additionally, the orientation improves from 0.46 at DR 25 to 0.73 and 0.80, for parameter values of 50 and 125, respectively. Therefore, it appears that the effect of increasing the DR on the macromolecular orientation is more accentuated in the range of low DR values. Besides, considering that PBS is a polymorphic material characterized by the α and β crystalline phases, the role of the draw ratio in promoting the formation of the former was investigated. This was related to the increase in chain orientation with DR, promoting the more stable α phase. Larger lateral dimensions of the lamellae were also obtained. On the other hand, there was no relationship between the crystallinity content and the draw ratio, presumably due to the low crystallization rate of PBS and the short time in which the drawing was applied [245].

The mechanical properties changed accordingly with the morphology. Noticeably, the tensile stress and elastic modulus improved with the increase of DR and, as shown in Figure 14b, a linear relationship was identified between the Young's modulus and lamellar orientation for draw ratios greater than 50, corresponding to conditions where spherulites are no longer present. Similar observations were reported by Deroiné et al [153] in their study on melt-spun PBS. Specifically, they found that as the DR increased, both the orientation and crystallinity of the fibers improved, leading to a progressive increase in tensile modulus and strength at break. At the same time, a reduction in elongation at break

was observed [143,152,153,226]. However, it is important to note that the increase in tensile strength with increasing DR was limited. In fact, while the application of elongation flow during the early stages of filament production promotes both molecular orientation and crystallinity, the subsequent alignment of the crystals along the drawing direction limits further gains in strength. Thus, once the crystals are sufficiently oriented, any additional increase in DR can lead to degradation of the crystal structures. This results in a decrease in the maximum tensile strength that the fiber can withstand [143,151,260].

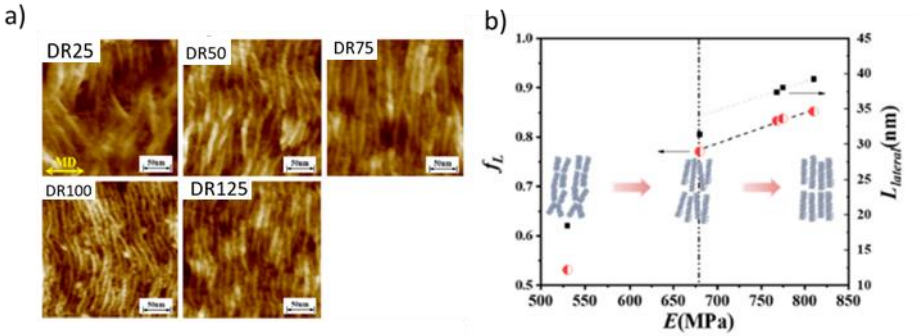


**Figure 14. a) AFM images of the PBS film casted at varying DR; b) lamellar orientation ($f_L$) and lateral size ($L_{lateral}$) expresses expressed as function of the elastic modulus [245]. Adapted under CC BY NC ND licence**

However, the relationship between DR and overall crystallinity remains debated. While some studies report negligible effects [245,255], others observe an initial increase followed by a sharp decrease at high draw ratios [150,250,251,259,261,262]. Besides, in melt spinning, the increase in DR consistently improves crystalline and amorphous orientation as well as anisotropy, with crystallinity content reported to increase steadily [151,152,226,240–242]. The divergence in crystallinity results can be attributed to the interaction between the crystallization kinetics of the polymer under study and the period during which drawing is applied prior to complete solidification. When considering the rate of film casting, a slow crystallization response implies that the application of strain has a negligible effect on the development of crystallinity, as the application interval is insufficient to allow significant crystal growth [251]. In contrast, when the solidification rate is sufficiently low, the application of drawing has a beneficial effect, promoting an increase in crystallinity. This enhancement results from the promotion of crystal nucleation and growth, enhanced by the orientation of the macromolecular chains induced by the elongational flow. Consequently, lamellar structures with reduced defect densities are more likely to form under these conditions. However, as the DR increases, a critical threshold may be reached where the solidification rate is insufficient to accommodate the crystallization kinetics. Under such circumstances, increasing the drawing speed results in the formation of lamellae with a high degree of structural imperfections, which prevents the formation of well-organized crystalline domains. This ultimately leads to a reduction in the overall crystallinity [250,251]. It should be noted that it is not possible to identify a single DR value beyond which crystallinity starts to decrease.

This threshold is inherently dependent on the specific polymer system and its associated crystallization behavior [150,250,251,262].

Furthermore, it is important to distinguish the effects of DR on the overall crystallinity content from those on the orientation of the crystalline structures. The latter effect, which consistently increases with higher draw ratios, has been well documented in the literature [150,245,246,250,262–264]. A good example of this phenomenon is the study of Xu et al. [255] on PP films processed at draw ratios of 40, 80, 120, 160, and 200. The corresponding differential scanning calorimetry (DSC) heating curves are shown in Figure 15. First, the crystallinity content was determined for all samples and found to be approximately 48%. However, significant differences in the melting temperatures and the shape of the DSC peaks allowed the identification of two distinct stages of microstructural evolution, depending on the DR applied. The first stage corresponds to draw ratio values between 40 and 120, where a decrease in melting temperature is observed, indicating changes in spherulite morphology. In particular, as the DR increases, the initially circular spherulites transition to ellipsoidal shapes and become smaller. Subsequently, randomly ordered lamellae begin to form at the expense of these ellipsoidal structures, culminating in a homogeneous distribution of oriented lamellar domains. This microstructural evolution is driven by the intensity of the elongational flow, which accelerates the crystallization rate and eventually exceeds the mean relaxation time of the polymer chains [235,252,255]. In contrast, the second stage is characterized by DR values above 120, where further increases in draw ratio no longer affect the melting temperature. However, the end point temperature of the melting peak increases and the intensity of the shoulder at higher temperatures also increases. These changes indicate a refinement of the oriented lamellar domains, suggesting the formation of larger and more perfect crystalline structures, and possibly the development of shish kebab [234,255].

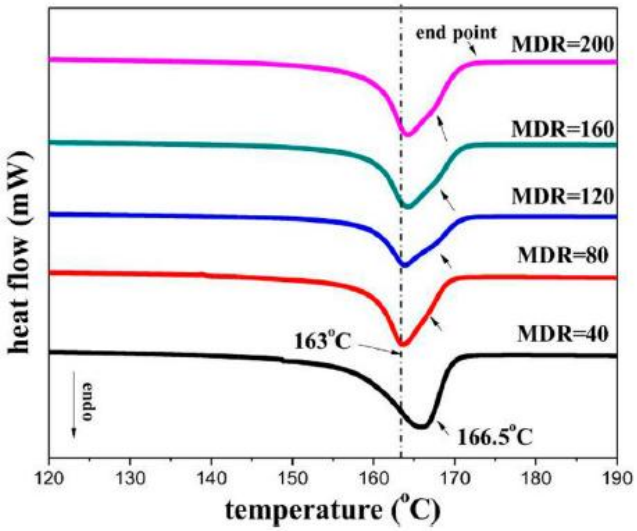


**Figure 15. DSC thermograms of PP films drawn at different draw ratio. Reprinted with permission from [255]. Copyright (C) 2015 American Chemical Society.**

As previously discussed, the increase in molecular orientation resulting from increased DR may ultimately facilitate the formation of shish-kebab structures

[234,250,251,255,265]. This phenomenon was demonstrated by Xu et al. [251] in their study of PLA films prepared at draw ratios of 80, 134, and 177. The corresponding small-angle X-ray scattering (SAXS) spectra are shown in Figure 16. X-ray analysis of the PLA sample processed at a DR of 80 shows an increase in anisotropy, a feature typically associated with the application of low draw ratios. The presence of oriented lamellae is clearly observed in this sample, while when the DR is increased to 134, the SAXS data indicate the appearance of shish structures oriented along the direction of the applied drawing force. A similar morphological configuration is also evident at a DR of 177. However, at the latter condition, the enhanced vertical orientation of the shish-related scattering signal suggests a higher degree of orientation with respect to the direction of elongation flow. Furthermore, at a DR of 177, the formation of kebab structures is confirmed by the appearance of equatorial scattering in the SAXS pattern. This equatorial signal results from the superposition of scattering contributions from both the oriented lamellae and the kebabs grown on the shish, indicating the development of a hierarchical, multilevel microstructure. Schematic representations of the microstructural arrangements corresponding to each DR condition are shown below the corresponding SAXS image (Figure 16).

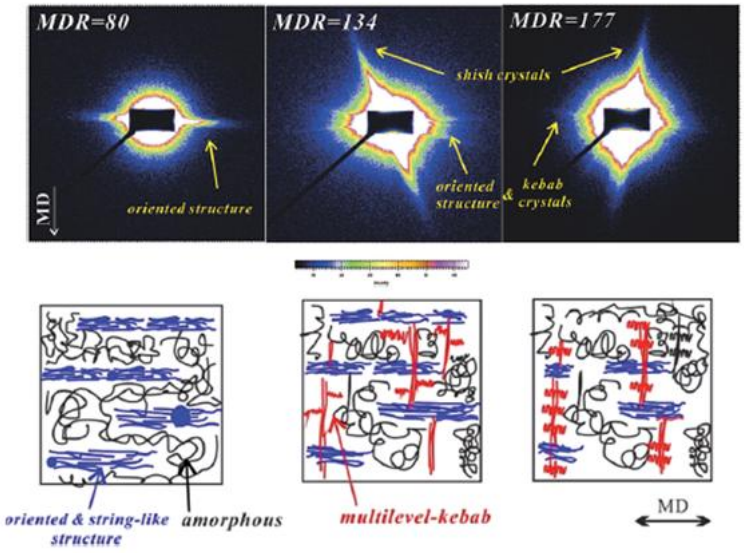


**Figure 16. SAXS spectra of samples extruded at different DR and schematic representations of their macromolecular organization (white arrows indicate direction) [251]. Adapted under CC BY 4.0 license.**

It is important to note that the elongation flow not only significantly affects the orientation of the crystalline phase, but also has a significant effect on the amorphous one [250,251,264,266]. As clearly shown in Figure 17, Xu et al. [251] followed the evolution of the orientation in both phases with increasing DR and found a similar trend of anisotropy enhancement for both crystalline and amorphous phases. In particular, the relative oriented content of each phase ($A_{oriented\ structure}/A_{amorphous}$) remained relatively constant with increasing DR. Furthermore,

although the orientation of the amorphous phase increases with DR, it does not promote the formation of new crystalline structures. This phenomenon can be explained by the higher entanglement density within the amorphous phase, which limits the mobility of the macromolecular chains. In contrast, the crystalline phase exhibits stronger intermolecular cohesion, requiring significant conformational ordering for crystal formation. Nevertheless, the increased orientation of the amorphous phase with DR has been proposed to facilitate the reorganization of the amorphous chains into lamellar structures growing as kebabs around the oriented shish [250].

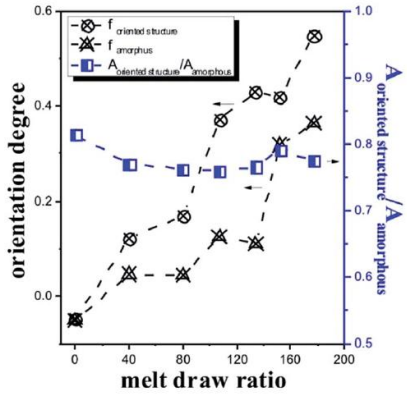


**Figure 17. Orientation degree of the amorphous ($f_{amorphous}$) and crystalline ($f_{oriented\ structure}$) phases at increasing DR and corresponding relative orientated content of the two ($A_{oriented\ structure}/A_{amorphous}$) [251]. Reprinted under CC BY 4.0 license.**

In fact, DR plays a critical role in determining the orientation of the amorphous phase, which directly affects the mobility of the macromolecules and, consequently, the final properties of the polymer films [251,264,266,267]. Among these properties, gas barrier performance is particularly sensitive to changes in chain mobility within the amorphous regions [264,267]. Reducing the mobility of these chains typically results in improved barrier properties by hindering the diffusion of gas molecules through the material. Higher DRs have been shown to increase the amount of rigid amorphous phase, thereby reducing chain mobility and improving barrier properties. This effect was observed by Tabatabaei et al. [264] in PP films prepared from different precursor morphologies and subjected to draw ratios ranging from 1 to 7.2. One type of precursor had a morphology composed exclusively of spherulites, while the other had a combination of spherulites and lamellae. The latter structure reflected a higher degree of initial molecular orientation. For instance, the oxygen transmission rate (OTR) of the samples was found to drop as the mobility of the amorphous chains decreased, which occurred with increasing draw ratio. This trend was consistent regardless of the initial microstructure of the precursor.

However, samples obtained from the more oriented precursor, which contained both spherulites and lamellae, exhibited lower OTR values at comparable draw ratios compared to those derived from the spherulitic precursor. This result suggests that a higher degree of initial molecular orientation contributes to a more restricted

amorphous phase mobility in the final film. As a result, improved barrier properties can be achieved at the same draw ratio.

In addition, the chill roll temperature has been identified as a key parameter influencing the microstructural development of cast polypropylene films. This temperature determines the time available for macromolecular rearrangement prior to complete solidification, thereby affecting not only the degree of crystallinity but also the specific polymorphic forms and resulting lamellar dimensions [11,18,244,248].

In the study by Di Sacco et al [11], the influence of three different cooling roll temperatures, namely 15, 40 and 70 °C, was investigated with respect to the resulting microstructure and properties of cast polypropylene films. Although variations in melt temperature and throughput were also considered, these factors had a limited effect and are not further discussed in the current analysis. According to the data presented in Figure 18a and 18b, a lower chilling roll temperature corresponded to an increased content of the mesomorphic phase at the expense of the stable α phase. This effect was particularly evident at 15 °C, where the rapid cooling limited the time available for molecular ordering and prevented the full development of the α form. These observations are consistent with the findings of Liu et al [248], who reported that the formation of crystalline phases in PP can be significantly suppressed depending on the chilling-roll temperature. In particular, mesomorphic structures were observed at temperatures below 40 °C, while only the α phase was present at processing temperatures above 80 °C.

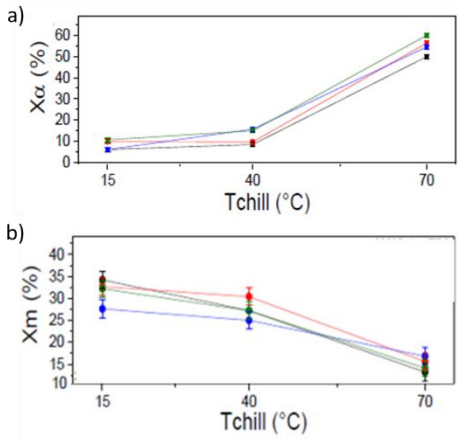


**Figure 18. Content of the a) α and b) mesomorphic crystalline phases in PP films at different chilling-roll temperature [11]. Adapted under CC BY 4.0 license.**

Both studies [11,248] demonstrated that the evolution of the α and mesomorphic phase contents, as influenced by the chilling-roll temperature, has a direct effect on the mechanical properties of cast polypropylene films. An increase in α-phase content, typically achieved by higher chilling-roll temperatures, was associated with an enhancement of the tensile modulus measured in the machine direction. This suggests that elevated chilling-roll temperatures promote the development of a stiffer crystalline structure, thereby improving rigidity. In addition, Di Sacco et al [11] observed that lower chilling-roll temperatures

contributed to a reduction in haze in the films. This reduction in haze was attributed to a decreased presence of the α crystalline phase, which otherwise acts as a barrier to light transmission, thereby reducing optical clarity. Since the crystalline phase interferes with light transmission, films with lower α content exhibited higher transparency. Optimizing the chilling-roll temperature is therefore a critical parameter as it determines the trade-off between transparency, ductility and tensile strength. These properties are particularly important in packaging applications, where both mechanical performance and visual clarity are essential. Consequently, the choice of chilling-roll temperature must be based on the specific performance requirements of the intended application.

In addition to its influence on the crystalline phase composition, the cooling roll temperature has also been shown to affect the size and thickness of the lamellae in cast polypropylene films [11,18]. Higher roll temperatures allow more time for molecular chains to undergo spatial rearrangement prior to solidification, facilitating the growth of larger and thicker lamellar structures. Tabatabaei et al [18], in their study on PP, further demonstrated that the roll temperature plays a critical role in determining the crystalline lamella size distribution. Their results indicated that when the cooling roll temperature reached or exceeded 110 °C, a bimodal size distribution developed. In contrast, lower temperatures consistently produced a monomodal distribution. This shift in morphological characteristics was attributed to the extended relaxation time available at elevated temperatures, which likely allows even the lower molecular weight chains to contribute to lamellar formation.

In the context of melt spinning, it refers to the drawing temperature rather than the chilling-roll temperature. As discussed above, this parameter affects the mobility of macromolecules, thereby altering properties such as entanglement density within the amorphous phase [143,153,268]. An increase in drawing temperature facilitates greater molecular orientation along the drawing direction and contributes to higher levels of crystallinity, ultimately increasing the anisotropy of the material [153,240,268]. At lower drawing temperatures, the formation of amorphous or mesomorphic phases is often favored over the development of well-ordered crystalline structures [155,156]. As a result, fibers processed at elevated temperatures exhibit a stiffer mechanical response characterized by increased tensile strength and Young's modulus and reduced elongation at break [156]. However, as shown in Figure 19, excessively high drawing temperatures can result in a decrease in mechanical performance due to enhanced ductility [153]. This behavior has been interpreted by considering the proximity of the drawing temperature to the melting temperature of the polymer. As the drawing temperature approaches the melting point, macromolecular relaxation and mobility are significantly increased. Under these conditions, the applied drawing force can facilitate chain slippage [143,153,156,240], and in some cases, partial remelting of the crystalline regions occurs [153,269].As a result, the fibers exhibit a reduction in ultimate tensile strength due to the disruption of the crystalline framework.

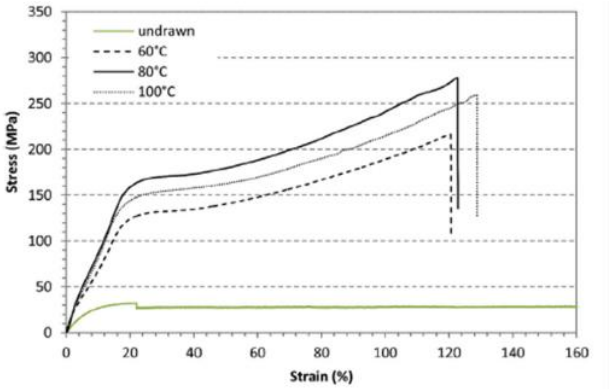


**Figure 19. Tensile behavior of the PBS fibers drawn DR 4 and different temperatures [153]. Adapted with permission from Elsevier Science Ltd., 2019.**

Finally, the effect of annealing on the microstructure of cast films is considered. This process is often introduced during film production to reduce residual stresses and promote reorganization of macromolecules [233,234,256,270–274]. It has been shown that thermal treatment, when applied at appropriate temperatures and durations, results in an increase in the crystallinity content of the film [250,263,273,274]. This increase is attributed to the rearrangement of amorphous chains near the crystalline regions, where they adopt an ordered structure corresponding to the crystalline phase present [250,270]. In addition, secondary crystallization within the amorphous phase is observed during annealing [233,234,270]. However, the formation of secondary lamellae is dependent on the presence of initial crystals that serve as a template for the crystallization of the surrounding amorphous macromolecules [250]. The application of external stress during the annealing process can further increase the overall anisotropy of the film, especially when compared to annealing without stress [263]. It is important to note that the temperature and time of the annealing process must be carefully optimized based on the specific polymer being treated. Excessively high temperatures or prolonged annealing times can result in an undesirable increase in crystallinity and a decrease in molecular orientation. Consequently, this may promote microstructural isotropy rather than the desired anisotropy [263].

## 2.1.5 Microfibrillation

Microfibrillation is the final extrusion-based microstructuring strategy discussed in this paper. Designed specifically for immiscible polymer blends, this technique allows for the generation of highly oriented dispersed second-phase fibrils within a continuous matrix, achieved by solid-state deformation of the minor component during processing [1,20,275–277]. The increased aspect ratio of these fibrils results in a larger interfacial area with the surrounding matrix, allowing more effective stress transfer to the high-strength oriented phase. As a result, microfibrillated blends exhibit significantly improved tensile strength and modulus compared to analogous unstructured systems [20,277–280,82,254]. Due to the mechanical improvements achieved, these systems are often referred to as *microfibrillar composites* (MFC) [278,279,281,282]. Their properties can be finely controlled by adjusting parameters such as fibril aspect ratio, morphology, spatial

distribution and orientation. These features, in turn, are determined by the choice of polymer components and the specific processing conditions applied [1,20,275–277].

Microfibrillation can be implemented via two main approaches: *single-step* and *two-step* processes, the latter commonly referred to as three-step. In the single-step configuration, fibrils are formed directly during compounding as the dispersed phase undergoes solid state deformation under the combined influence of shear and elongational flows within the extruder [70,283,284]. The more conventional three-step process, on the other hand, begins with melt blending of the constituent polymers. This is followed by a dedicated fibrillation step in which the elongational flow induce the formation of fibrils. A final stage, called isotropization, may be added to bring the material into its final shape by compression or injection molding. This stage involves a thermal treatment that typically results in a reduction in the fibril aspect ratio due to morphological relaxation [1,54,278,279,285–289]. Given the current focus on improving anisotropic properties, the isotropization stage will not be discussed further in this document.

It is important to note that microfibrillation is considered to be both versatile and cost-effective. Its implementation does not require specialized equipment, as it can be carried out using standard polymer processing machines already widely used in industry [54,281,290–292].

#### 2.1.5.1 One-step fibrillation

Two different approaches have been proposed for one-step fibrillation during compounding. One approach involves processing both the matrix and the dispersed phase in the molten state. Under these conditions, the formation of fibrillar structures is achieved by the combined effects of flow-induced crystallization and molecular orientation, both of which occur as the material passes through the slit die [292–298]. A critical factor in this process is the geometry of the die, which plays a central role in enabling effective polymer structuring. The die design facilitates the application of strong flow fields while extending the residence time of the material. This is achieved without the need for a significant increase in processing temperature, making the technique compatible even with relatively simple equipment such as single screw extruders [292–297]. After extrusion, the stability of the fibrils produced is largely maintained. This is ensured by two simultaneous mechanisms. First, immediate cooling after extrusion minimizes the potential for fibril relaxation. Second, the crystals formed under flow-induced conditions tend to have a higher degree of order and consequently a higher melting temperature. As a result, even if the material remains at elevated temperatures for a short time prior to complete solidification, the likelihood of fibril remelting is significantly reduced. This ensures that the aspect ratio of the fibrils is maintained throughout the process [292–295,298].

A representative example of the fibrillar morphology produced using this approach is provided in the work of Vozniak et al. [292]. In their study, a blend containing 3 wt% polyhydroxyalkanoate (PHA) dispersed within a PLA matrix

exhibited successful fibrillation, as evidenced by the micrograph taken in the transverse direction of the sample (Figure 20a). In addition to morphological characterization, rheological behavior was also investigated. Figure 20b presents a comparison of the time-dependent tensile stress growth coefficient for three systems: the pure matrix, the unfibrillated blend, and the microfibrillar composite. The results highlight a notable difference in rheological response. Specifically, the MFC demonstrates pronounced strain hardening, attributed to the formation of a continuous fibrillar network. This rheological feature is absent in both the matrix and the non-fibrillated blend, underlining the reinforcing effect of the fibrillar microstructure.

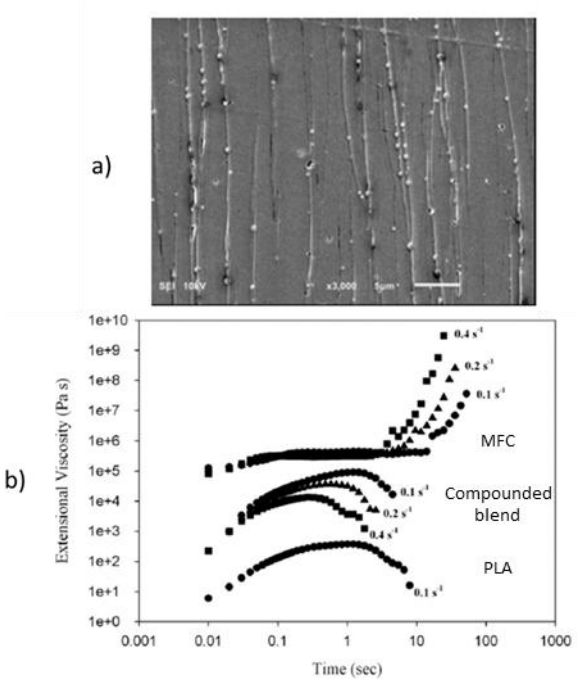


**Figure 20. a) SEM micrograph of the transverse direction of the MFC sample; b) time-dependence of the tensile stress growth coefficient of PLA, compounded blend and the MFC at different Hencky strain rates [292]. Adapted under CC BY 4.0 license.**

In addition to enhancing strain hardening, the presence of fibrils also contributes significantly to the overall mechanical performance of the composite. Due to their high aspect ratio, fibrils allow efficient stress transfer from the ductile matrix to the stiffer dispersed phase. This mechanism underlies the improved stiffness and strength observed in microfibrillated composites. For instance, in PLA/polybutylene adipate terephthalate (PBAT) blends, the development of a well-connected fibrillar network was identified as the key factor responsible for the observed increase in both Young's modulus and tensile strength. Notably, these improvements were achieved without compromising the strain at break, highlighting the ability of the fibrillar structure to reinforce the material while maintaining its deformability [294,296].

An alternative one-step microfibrillation strategy based on solid-state deformation has been proposed by Jurczuk et al. [299]. This method relies on the mechanical deformation of the crystalline dispersed phase during compounding,

which occurs when the stress transmitted from the molten matrix exceeds the critical shear stress of the crystal slip plane. The efficiency of this mechanism increases significantly under conditions characterized by a high capillary number, which enhances the stress transfer from the matrix to the dispersed phase. However, the successful application of this approach requires that the dispersed polymer meet certain criteria. Most importantly, its melting temperature must exceed that of the matrix to ensure that it remains in the solid state throughout the compounding process. It must also have high crystallinity and low entanglement density. These properties are critical to avoid premature fracture during deformation and to allow sufficient strain for fibril formation. As a consequence, materials such as nascent or as-polymerized UHMWPE and polytetrafluoroethylene (PTFE) are commonly used for this purpose [70,283,284,291,300–303].

Besides, the resulting fibrillar morphology can be tuned by varying processing parameters such as screw speed, processing temperature and time, and the relative content of matrix and dispersed phase [70,283,291,303]. Among these variables, screw speed plays a particularly important role. In fact, as it increases, so does the shear rate, which enhances the viscous drag force and leads to a higher capillary number. This results in the formation of fibrils that are not only thinner, but also mechanically stronger [17,70,283,291].

In addition, Hosseinnezhad et al. [291] investigated the effect of processing temperature and time on the fibrillation behavior of blends composed of 95 wt% polyolefin elastomer and 5 wt% UHMWPE. Compounding was performed at a fixed screw speed of 30 rpm, corresponding to a shear rate of 350 $s^{-1}$, while two processing temperatures, 75 °C and 115 °C, in combination with processing times of 10, 30 and 90 min, were investigated. The resulting morphologies are shown in Figure 21. First, a clear trend was observed with respect to processing time. As shown in the SEM images, an increase in processing time resulted in enhanced fibril formation. For instance, at 75 °C and 10 minutes (Figure 21a), the observed fibrils had an aspect ratio of approximately 70. This value then increased to 105 when the processing time was increased to 30 minutes (Figure 21b), and a further enhancement of the aspect ratio was achieved at 90 minutes (Figure 21c). Similar improvements were observed at the higher temperature of 115°C, where prolonged processing also resulted in greater fibril elongation and aspect ratio, as shown in Figure 21d and 21e for 10 and 30 minutes, respectively.

The study also highlighted the significant role of processing temperature in promoting fibril formation. In fact, when comparing blends processed at 75°C (Figure 21b) and 115°C (Figure 21e) for 30 minutes, the micrographs show a significantly more developed fibrillar network at the higher temperature. This enhanced fibrillation was attributed to the increased molecular mobility and deformation capacity under elevated thermal conditions, which allowed for both improved fibril aspect ratios and more uniform distribution within the matrix.

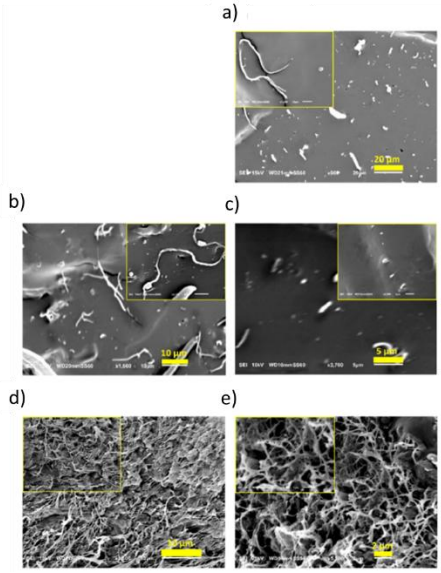


**Figure 21. SEM micrographs of the polyolefin elastomer/UHMWPE blends processed at the constant shear rate of 350 $s^{-1}$ an different combinations of temperatures and processing times: a) 75 °C for 10 min, b) 75 °C for 30 min, c) 75 °C for 90 min, d) 115 °C for 10 min, 115 °C for 30 min [291]. Adapted under CC BY 4.0 license.**

Lastly, Jurczuk et al. [303] carried out a rheological investigation on blends based on isotactic PP, PS, HDPE, and LDPE, incorporating varying contents of native PTFE at 1, 3, 5, and 7 wt%. Their findings revealed that a minimum PTFE content of 3 wt% was necessary for the development of fibrillar structures, regardless of the polymer matrix used. The influence of fibrillation on the rheological response was further demonstrated by the time-dependent tensile stress growth coefficient measured under uniaxial extensional deformation, where MFCs containing at least 3 wt% PTFE exhibited clear strain hardening behavior. In addition, increasing the PTFE content resulted in an earlier onset of strain hardening and the rheological response has been attributed to the presence of a fibrillar network formed by the dispersed phase [284,303]. Such a network plays a particularly beneficial role in polymer foaming processes because strain hardening improves foam quality by enhancing cell concentration, stabilizing cell size, and reducing coalescence when compared to foams produced from the matrix alone [70,284,301–306].

In addition, the fibrils were found to influence the crystallization behavior of the matrix. In particular, they acted as heterogeneous nucleation sites. The effectiveness of this nucleation depended on both the content and aspect ratio of the fibrils. A dense network of fine, elongated fibrils provided a greater number of nucleation sites than dispersed domains with lower aspect ratios. However, while the fibrillar network promoted nucleation, it also imposed physical constraints on crystal growth, resulting in smaller crystalline structures within the matrix. These were significantly smaller than those formed in systems containing spherical or droplet dispersed phases [283,300,302,304,307].

#### 2.1.5.2 Two-step fibrillation

This more conventional microfibrillation process begins with the melt blending of two immiscible polymers. The first step is aimed at achieving a homogeneous dispersion of the second phase within the matrix, typically resulting in spherical domains. The subsequent fibrillation step involves subjecting the compounded material to uniaxial stretching, which can be applied immediately after extrusion or at a later stage. In both configurations, stretching is typically performed using thermostatically controlled rollers. These not only facilitate stretching, but also define the orientation direction of the developing fibrils, thereby driving the morphological anisotropy in the material [1,12,20,287]. However, to ensure successful fibrillation, the selected polymers must meet specific requirements. First, they should have a melting temperature difference of at least 40°C, with the higher melting component acting as the dispersed phase responsible for fibril formation. In addition, the matrix must have sufficient thermal stability to withstand the temperatures required to process the dispersed phase, which in turn has to exhibit high elasticity to allow fibril development during the stretching phase [1,20,50,56,65,82,287,308–310].

It is important to note that both shear flow and uniaxial strain contribute to the formation of the fibrillar morphology. In fact, shear flow facilitates the breakdown of the dispersed phase into smaller domains, increases their dispersion within the matrix, and initiates the morphological transition from spherical to ellipsoidal shapes. Then, the application of uniaxial stretching to these preformed domains completes the fibrillation process, resulting in a well-oriented microstructure. Consequently, the final morphology results from the combined influence of both deformation mechanisms [1,311]. Therefore, the final microstructure and associated material properties are strongly influenced by the processing parameters chosen [1,20,57,287]. The following discussion addresses the role of several critical variables, including the relative content of matrix and dispersed phase, the viscosity ratio between the two components, the presence of compatibilizers, and the effect of draw ratio on the structuring of immiscible polymer blends.

First, the relative amounts of matrix and dispersed phase play a critical role in determining the initial sea-island morphology during melt compounding, which is essential for enabling fibril formation during the subsequent fibrillation step [57,280,308,312–320]. In the work of Kharghanian et al. [313], the microstructure of PP and polyethylene terephthalate (PET) blends was evaluated at PET concentrations of 10, 20 and 30 wt%. The material containing 10 wt% PET exhibited a clear sea-island morphology as shown in the SEM image (Figure 22aA). However, the corresponding rheological behavior was liquid-like and closely resembled that of the PP matrix (Figure 22b), which is unfavorable for effective fibrillation. A different result was observed at a PET content of 20 wt%. In fact, although a sea-island morphology was again visible in the micrograph (Figure 22aB), the increased concentration of dispersed domains, together with a viscoelastic liquid response (Figure 22b), provided the optimal rheological conditions for fibril development. In contrast, further increasing the PET content to

30 wt% led to the formation of a co-continuous phase, as shown in Figure 22aC, and the dispersed phase was no longer effective as a precursor for fibrils under these conditions, as indicated by the rheological behavior of a viscoelastic solid at low frequencies (Figure 22b). Based on these observations, the formulation containing 80 wt% PP and 20 wt% PET was identified as the most favorable composition for producing microfibrillar composites, providing a suitable balance between morphology and rheological behavior.

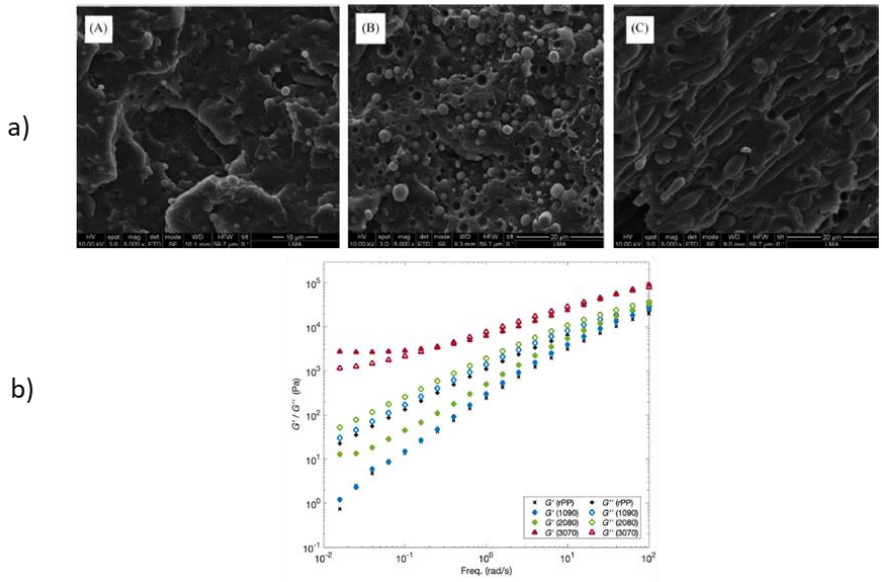


**Figure 22. a) SEM micrographs of the (A) 90:10 wt%, (B) 80:20 wt% and (C) 70:30 wt% PP/PET blends; b) Storage (G') and loss (G'') moduli as function of the frequency measured for the neat PP and the blends [313]. Adapted with permission from John Wiley and Sons, 2023.**

Other studies have supported the previously discussed relationship between second phase content and the resulting morphology, confirming that the increase in second phase leads to significant changes in mechanical properties [315–317,319,321]. For instance, Xie et al. [318] investigated the tensile properties of PLA blends containing 10, 20 and 40 wt% PBS. The results, presented in Figure 23A, show different combinations of yield strength and elongation at break depending on the PBS content. In all cases, an increase in yield strength was observed. However, in the 90 wt% PLA/10 wt% PBS and 80 wt% PLA/20 wt% PBS, this was accompanied by a reduction in elongation at break. In contrast, the material containing 40 wt% PBS showed a greater deformation at break. As shown in Figure 23B, the differences in mechanical behavior were related to the variations in microstructure. In fact, while microfibrillation was evident in all samples, the morphology varied with the amount of PBS present. In Figure 23B, PBS formed shish-like structures oriented along the stretching direction, which facilitated the formation of the kebabs of PLA lamellae. Consequently, the resulting shish kebab morphology inherently reinforced the blend. Notably, the morphology became more ordered as the PBS content increased, especially in the blend with 20 wt% PBS (Figure 23Bb) compared to that with 10 wt% PBS (Figure 23Ba). This change in microstructure had a positive effect on the mechanical properties, increasing both

yield strength and elastic modulus. However, when the PBS content was further increased to 40 wt%, the diameter of the PBS domains became larger and this resulted in a unique combination of higher yield strength and increased elongation at break. This increase in strength and stiffness compared to the PLA matrix was attributed to the presence of the oriented shish-kebab structures, while the increased ductility was due to the larger PBS domains. These larger domains were a result of the collision and agglomeration that occurred due to the high PBS content.

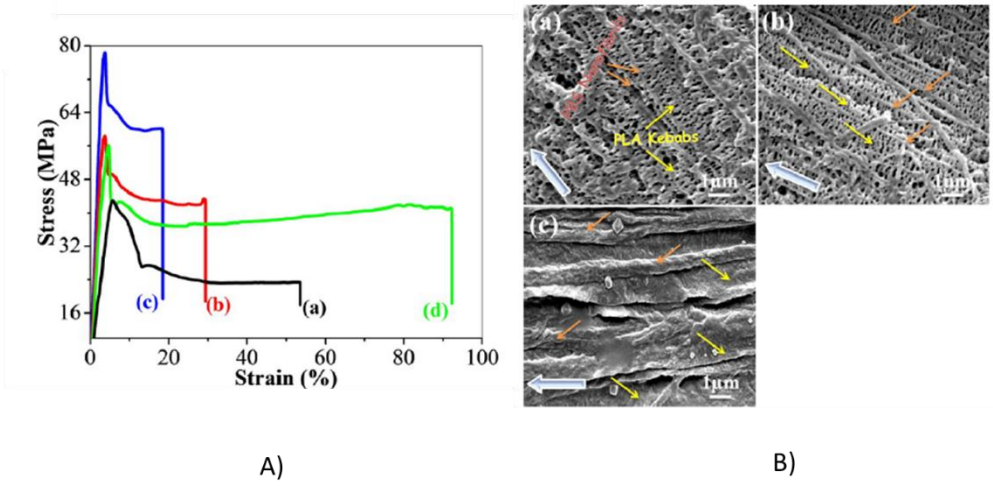


**Figure 23. A) Stress-strain curves for a) pure PLA and the PLA/PBS containing b) 10 wt%, c) 20 wt% and d) 40 wt% of second phase; B) SEM micrographs of the blends with a) 10 wt%, b) 20 wt% and c) 40 wt% of PBS. The light blue arrow indicates the stretching direction, while the orange identifies the PBS shish domains and the yellow highlights the lamellar kebab structures of PLA. Adapted with permission from [318]. Copyright (C) 2014 American Chemical Society.**

Several studies have confirmed the increase in both the diameter and diameter distribution of the microfibrils as the content of the second phase rises [312,314,315,320]. This phenomenon, together with coalescence during the drawing step, plays a crucial role in the development of the microstructure [50,312,314,320,322–324]. Huang et al. [312], in their study of PP/polyamide 66 (PA66) blends with 5, 10, 15, or 20 wt% PA66, observed the fibrillation regardless of the second phase content. However, as the polyamide concentration increased, so did the microfibril density. On the other hand, at a constant draw ratio, the diameter of the fibrils decreased from 10 μm to 4-5 μm, and the diameter distribution narrowed as the PA66 content increased from 5 to 15 wt%. Nevertheless, when the PA66 content reached 20 wt%, the average fibril diameter increased to 8 μm, and the diameter distribution broadened. This behavior can be explained by the deformation, breakup, and coalescence of second phase domains during the drawing step [50,312,314,323,325]. The first two phenomena are related to the capillary number of the system. When second phase concentrations are low, larger particles will deform and eventually break when subjected to elongational flow, while smaller particles retain their spherical shape. Thus, both thin fibrils and small droplet-like domains of the second phase are present in the final morphology. On the contrary, when the content of the second phase reaches a critical value, where particle collisions are more likely to occur, larger domains deform into fibrils

during drawing, while smaller particles collide, coalesce and, if they have grown large enough considering the capillary number of the system, finally deform. As a result, the final morphology is composed of two distinct populations of fibrils, the finer ones originating from the initial droplets with adequate diameters, and the coarser ones formed by the deformation of collided and coalesced particles. This explains both the observed increase in average diameter and the broadening of the diameter distribution. Therefore, based on the findings of Huang et al [312], it can be concluded that the PA66 content required for a high collision and coalescence probability is between 15 wt% and 20 wt%, as evidenced by the increase in fibril diameter at the higher concentration.

The mechanical properties were found to reflect the evolution of the morphology [312]. Tensile tests showed that the maximum strength increased with the PA66 content up to 15 wt%, followed by a decrease as the concentration was further increased. In contrast, the elastic modulus continued to rise until it reached a plateau at PA66 contents equal to or greater than 15 wt%. This behavior was explained by the higher intrinsic strength of PA66 compared to PP and by the occurrence of interfacial defects, which arise due to the limited compatibility between the two phases. At low PA66 contents, the increase in tensile strength was mainly due to the formation of fibrils from the dispersed phase. While as the concentration increased further, voids began to form at the interface during tensile deformation. These voids limited the stress transfer from the matrix to the fibrils and acted as stress concentrators, ultimately reducing the tensile strength. In contrast, the elastic modulus was not significantly affected by the presence of interfacial voids. Its behavior was governed by the number and aspect ratio of the fibrils, both of which increased with higher PA66 content. Also, the modulus reached a plateau when the fibril density within the matrix became sufficiently high, such that additional fibrils contributed little to further stiffening.

In addition to morphological and mechanical considerations, it has been found that coalescence is influenced not only by the concentration of the second phase, but also by the draw rate applied [314,323]. This relationship was highlighted in the study by Gonzales-Nunez et al. [314]. They investigated blends of HDPE and polyamide 6 (PA6) containing between 1 and 15 vol% of the latter. It was found that at low drawing speeds, the deformation behavior of the PA6 phase was largely unaffected by its content. Nevertheless, as the draw rate increased, a clear pattern emerged. For blends containing between 1 and 4 vol% PA6, the deformation behavior continued to appear independent of concentration. In contrast, when the PA6 content exceeded 5 vol%, coalescence became more pronounced with increasing concentration and drawing speed. This trend was attributed to the higher probability of collisions between dispersed domains under such processing conditions, which in turn facilitated coalescence.

An alternative mechanism to collision has been proposed to explain the coalescence phenomena that occur during drawing [275,324]. This mechanism involves the elongation of second phase domains that experience end-to-end contact facilitated by their mobility in the molten matrix. Such interactions lead to coalescence and consequently to the formation of extended fibrillar structures. The

validity of this mechanism has been investigated by incorporating a compatibilizer that enhances interfacial adhesion between the matrix and the dispersed phase while inhibiting coalescence by forming a thin interfacial film around the dispersed particles [20,275,322,326]. This approach was adopted by Friedrich et al [56], who studied the microstructure of 60:40 wt% PP/PET blends and incorporated 1 wt% compatibilizer, replacing an equivalent amount of matrix during compounding. As shown in Figure 24b, a significant reduction in the aspect ratio of the fibrils was observed in the presence of the compatibilizer when compared to the morphology of the drawn PP/PET blend without it (Figure 24a). This morphological change has been attributed to the inhibition of coalescence resulting from the compatibilizer film formed on the surface of the second phase domains [56,275,280,327].

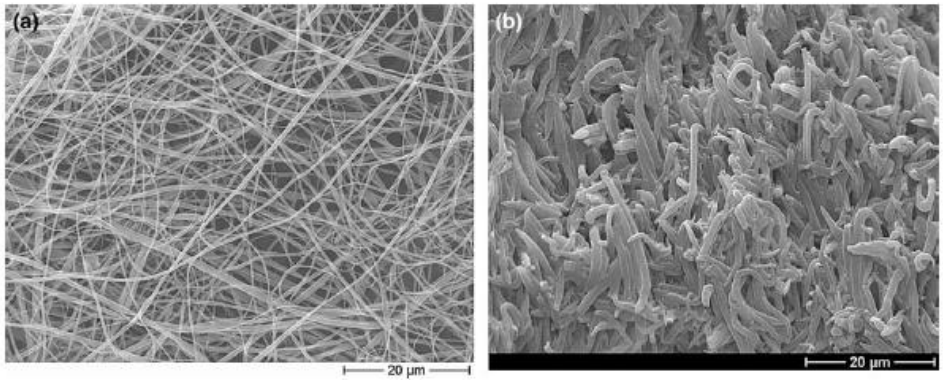


**Figure 24. SEM images of PP/PET blends a) without or b) with 1 wt% of compatibilizer [56]. Reprinted with permission from Elsevier Science Ltd., 2004.**

Accordingly, a consistent reduction in fibril aspect ratio following compatibilizer incorporation has been reported in other studies, with this effect attributed to the antagonistic influence of the compatibilizer on the coalescence of elongated domains [56,278,326,327]. At the same time, the combined presence of microfibrils and compatibilizer has been recognized for its beneficial effect on mechanical properties, which has been attributed to an increased interfacial compatibility between the matrix and the dispersed phase [20,82,278,279]. In this regard, Rosales et al. [279] investigated LDPE/PP blends containing 20 wt% polypropylene and 0, 1.4 or 3 wt% compatibilizer. As shown in Figure 25b-f, the drawing step promoted the formation of oriented microfibrils, and the compatibilizer-containing blends (Figure 25d, e) showed improved interfacial interaction between the two phases, accompanied by a significant reduction in the fibril aspect ratio.

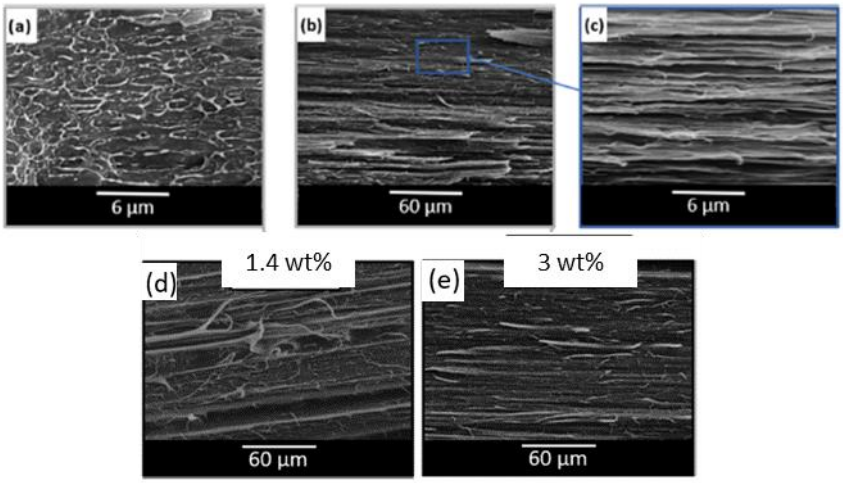


**Figure 25. SEM micrographs of LDPE/PP blends without compatibilizers and a) unstretched or b, c) stretched. Also shown are micrographs of MFC with d) 1.4 or e) 3 wt% compatibilizer. Adapted from [279] under CC BY 4.0 license.**

The evolution of the morphology has led to changes in mechanical properties, revealing a complex relationship between fibril aspect ratio and compatibilizer content, which influences both tensile strength and modulus [279,328,329]. In particular, the presence of fibrils, as opposed to droplets, provides a larger surface area for stress transfer, which is further enhanced by the compatibilizer at the interface between the matrix and the stiffer dispersed phase. However, a threshold level of additive was identified above which tensile properties deteriorated due to excessive reduction in fibril aspect ratio. Therefore, Kuzmanovic et al. [278] investigated the introduction of compatibilizer into 80 wt% PP/20 wt% PET blends during the isotropization step, rather than at the compounding stage, with the aim of keeping the fibril aspect ratio. Their results showed that introducing the compatibilizer after fibrillation resulted in an increase in the fibril aspect ratio. However, the mechanical properties, specifically impact strength, elongation at break and yield strength, were superior for the blends compatibilized during compounding, despite the observed reduction in fibril aspect ratio. This improvement was attributed to the superior interfacial adhesion achieved when the compatibilizer was added during compounding rather than during the isotropization step.

In addition, the viscosity ratio is a critical parameter influencing the resulting microstructure, as it controls fibril formation and directly affects their geometry and dimensions [1,20,330,331]. Specifically, a low viscosity ratio has been shown to facilitate the development of fibrils with high aspect ratios and narrow diameter distributions, ultimately favoring a more homogeneous dispersion of fibrils within the matrix. As a result, the corresponding MFCs exhibit improved mechanical properties, particularly in terms of strength and modulus, compared to those with a higher viscosity ratio [20,67,322,323,332,333].

Furthermore, the viscosity ratio also serves as a tunable parameter for tailoring the morphology of ternary polymer blends. This potential was investigated by Shi et al. [67], who examined blends composed of polyolefin elastomer (POE) and a binary mixture of PA6 and PLA. In the study, the PA6 to PLA ratio was kept

constant at 1:1, while the overall blend composition was maintained at a fixed POE to (PA6/PLA) ratio of 75:25 wt%. By systematically varying the viscosity ratio between PA6 and PLA, the resulting fibrillated structures were analyzed, as shown in the SEM micrographs in Figure 26. At the lowest viscosity ratio (Figure 26a), the fibrils exhibited alternating thick and thin sections along their length, producing a morphology described as “gourd-skewers-like.” As the viscosity ratio increased (Figure 26b, c), the diameter distribution along the fibrils became more uniform. At the highest viscosity ratio (Figure 26d), surface irregularities such as bumps became prominent, resulting in a morphology referred to as “trepang”.
Mechanical performance varied according to the different morphologies observed. Although all samples exhibited stress-strain behavior typical of elastomeric systems, there were notable differences in tensile strength and modulus. The most pronounced mechanical improvements were associated with the morphology characterized by the lowest viscosity ratio, where the gourd-skewer-like structure was observed. These improvements were attributed to the increased interfacial surface area inherent to this specific microstructural arrangement.

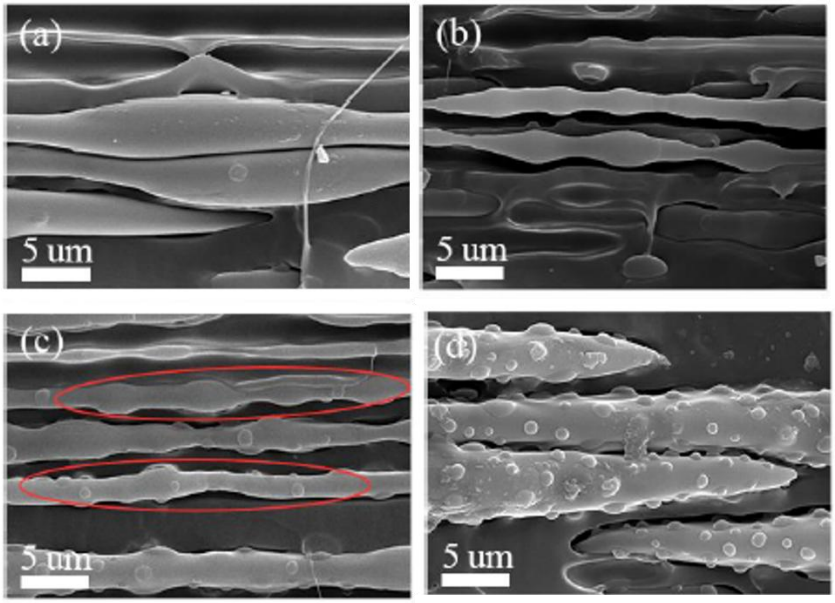


**Figure 26. SEM micrographs of PA6/PLA microfibrils having a viscosity ratio of a) 0.5, b) 2.2, c) 5.3 or d) 14.2. Adapted from [67] under CC BY 4.0 license.**

Besides, the formation of fibrils in PP/PET blends was shown to depend on the combined influence of the viscosity ratio and the concentration of the second phase [334]. In blends containing between 3 and 30 wt% PET, fibrillation and coalescence were observed even at high viscosity ratios when the PET content was low, resulting in effective dispersion and formation of high aspect ratio fibrils. Conversely, under conditions of lower viscosity ratio, a higher PET content was required to achieve coalescence and allow the development of elongated fibrils. These observations suggest that viscosity ratio and second phase content work together to define the critical concentration threshold for coalescence during the fibrillation step [314,334,335].

Additionally, the DR is a key parameter for tailoring the microfibrillation. Indeed, increasing the draw ratio induces the transformation of dispersed phase domains from spherulitic to ellipsoidal and finally to fibrils. This morphological evolution is accompanied by an increase in aspect ratio and a greater degree of alignment along the drawing direction. At the same time, the matrix undergoes an increased anisotropy, which is reflected in the improved orientation of both crystalline regions and amorphous polymer chains according to the applied drawing direction [1,20,55,69,161,254,288,289,321,336–339]. On the other hand, if the draw ratio is too high, the fibrils may break up, resulting in a decrease in both the aspect ratio and the orientation of the second phase domains. Under such conditions, the overall anisotropy of the material is reduced [288,337,338]. These structural changes have a direct effect on tensile properties. Higher DR typically results in increased tensile strength and modulus along with reduced elongation at break due to the formation of elongated fibrils and increased anisotropy. Conversely, when fibril breakage occurs, a reduction in tensile strength and a corresponding increase in elongation at break are observed [55,161,254,321,337,338,340].

Finally, the influence of fibrils on the nucleation behavior of the matrix deserves specific consideration [50,68,288,289,317,318,320,337,341–346]. As discussed previously in relation to one-step fibrillation, the formation of high aspect ratio fibrils increases the surface area available for the heterogeneous nucleation of the matrix. This morphological feature not only facilitates nucleation but also accelerates the crystallization kinetics of the matrix and improves the interfacial adhesion with the dispersed phase [275,286,288,289,317,318,337,342,344–347]. Furthermore, the growth direction of the crystals has been shown to align epitaxially with the fibril axis, leading to the development of shish-kebab structures and ultimately the formation of a network-like crystalline architecture [68,288,318,337,342–344,346,347]. Interestingly, in this case, the dimensions of the epitaxial crystals were observed to depend on the fibril content [343]. As shown in Figure 27, PLA/PA6 blends containing 6 wt% and 12 wt% PA6 exhibit shish-kebab morphologies, where PA6 fibrils act as the shish and PLA crystals as kebabs (Figure 27b, d). As the PA6 content increases, the density of the fibrils rises, which in turn reduces the length of the PLA kebabs. This effect is attributed to the spatial constraints imposed by the denser fibril network, which limits the growth of epitaxial crystals coordinated along the fibril surface.

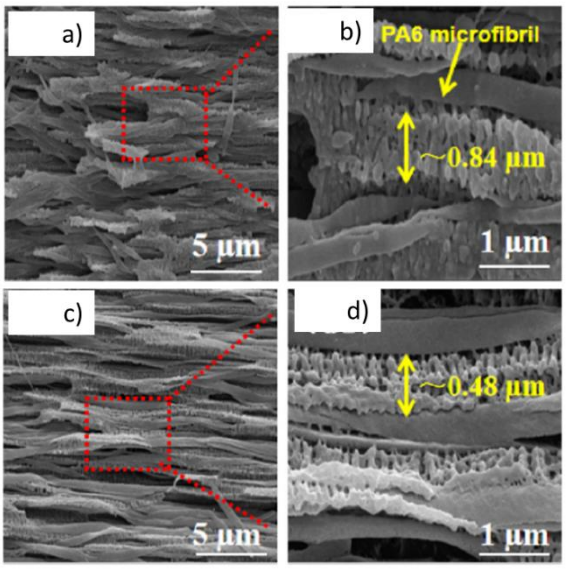


**Figure 27. SEM images of PLA/PA6 blends having relative weight content of (a, b) 94:6 and (c, d) 88:12. Adapted from [343] with permission from Elsevier Science Ltd., 2024.**

## 2.2 Injection molding-based techniques

Injection molding (IM) is one of the most widely used techniques for structuring polymer melts during processing [2,13,14]. The main advancement in this technology is the integration of an external field during the packing and solidification phases, which interferes with the relaxation behavior of the macromolecules in the core layer and induces repetitive flow in the mold. This process produces an anisotropic morphology characterized by a high degree of macromolecular orientation. To define the role of such flow conditions in enhancing both chain orientation and crystallinity, Zhong et al [2] introduced the term *flow-induced crystallization under pressure* (FICP), which includes all IM-based strategies that use externally applied forces to direct morphological development. These approaches serve as an alternative to the conventional use of nucleating agents, which are crucial for achieving microstructural control in standard IM processes [13,348–350]. Over the years, several technologies have been developed to exploit this principle. Shear Controlled Orientation in Injection Molding (SCORIM), for example, uses pistons within the injection barrel to introduce additional shear forces [8,14,351–362]. In Oscillation Packing Injection Molding (OPIM), these pistons are located at the mold cavity, allowing localized flow modulation [28–31,38,42,47,52,363–383]. Another technique, Vibration Assisted Injection Molding (VIM), uses the injection screw to deliver vibration pulses directly into the melt, thereby influencing molecular orientation and crystallization through dynamic mechanical input [32,34,35,384–393].

### 2.2.1 Shear Controlled Orientation in Injection Molding (SCORIM)

A key morphological outcome resulting from the use of out-of-phase pistons in SCORIM is the generation of a three-layer structure formed by the combined presence of shear and thermal gradients from the outer skin to the core [13,14,351]. These coupled gradients lead to the creation of an intermediate layer between the skin and the core, which modifies the typical morphology observed in conventional processes. This phenomenon has been clearly documented by Kalay et al [360] who studied a polymer blend consisting of 90 wt% PB and 10 wt% PP processed by both conventional injection molding (CIM) and SCORIM. Their morphological comparison, shown in Figure 28, shows that the CIM sample (Figure 28a) retains the expected structure with a highly oriented skin region, a spherulitic core and a transition zone separating the two. In contrast, the SCORIM processed specimen (Figure 28b) shows a complete suppression of spherulite formation in the core and instead exhibits a distinctly layered microstructure extending below the oriented skin. These microstructural changes were accompanied by significant mechanical improvements. Tensile strength increased from 36.8 MPa to 53.1 MPa and elastic modulus increased from 2083 MPa to 2894 MPa. However, the increased stiffness and strength came at the expense of ductility, as elongation at break decreased significantly from 195 to 21%.

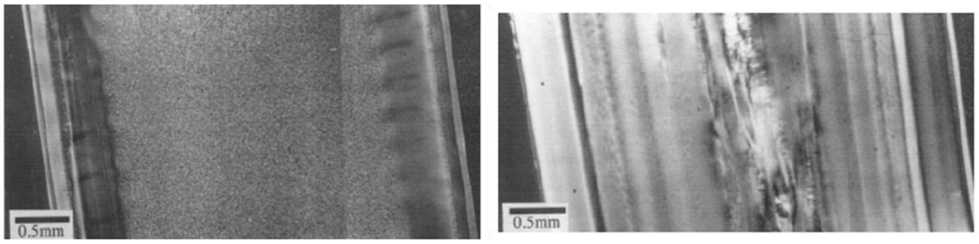


**Figure 28. Polarized light microscopy micrographs of the a) CIM and b) SCORIM 90 wt% PB/10 wt% PP blends [360]. Adapted with permission from John Wiley and Sons, 2003.**

Further insight into the influence of thermomechanical variables on morphology and properties was provided by Ghosh et al [361], who studied poly(L-lactic acid) (PLLA) under SCORIM conditions. Their experimental setup varied the mold temperature between 30 °C and 50 °C and applied shear for periods of 0, 3, 10, or 15 s. The results showed that lower mold temperatures allowed for greater core orientation, an effect that was enhanced by prolonged shear. Despite these differences in orientation, the elastic modulus remained relatively constant, indicating that stiffness was largely independent of molding conditions in this case. In contrast, significant improvements in tensile performance were observed. Samples molded with SCORIM showed higher strength and elongation at break than those molded with CIM, especially when longer shear times were applied at the elevated mold temperature.

Similar observations were reported by Kalay et al. [358] who investigated SCORIM processing of PP and aliphatic polyketone (PK). Their results support the conclusion that both strength and elongation at break are improved by this technique. In addition, in contrast to the results of Ghosh et al [361], their study showed a positive correlation between SCORIM and an increase in Young's modulus. This improvement was attributed to an enhanced macromolecular alignment and a higher degree of crystallinity. Previous research has shown that such orientation can lead to a shift in the crystalline structure, favoring the formation of the γ phase over the more commonly observed β phase in polypropylene, resulting in higher stiffness [353].

The ability of SCORIM to induce highly ordered morphologies is further confirmed by the frequent appearance of shish-kebab structures in semi-crystalline polymers such as PB, HDPE and PP [8,352,354–357,359,362]. Kalay et al. [8,359] observed these morphologies (Figure 29a) exclusively in SCORIM processed samples, while the CIM samples produced only isotropic scattering, a distinction clearly supported by X-ray Debye diffraction analysis as shown in Figure 29b A and B.

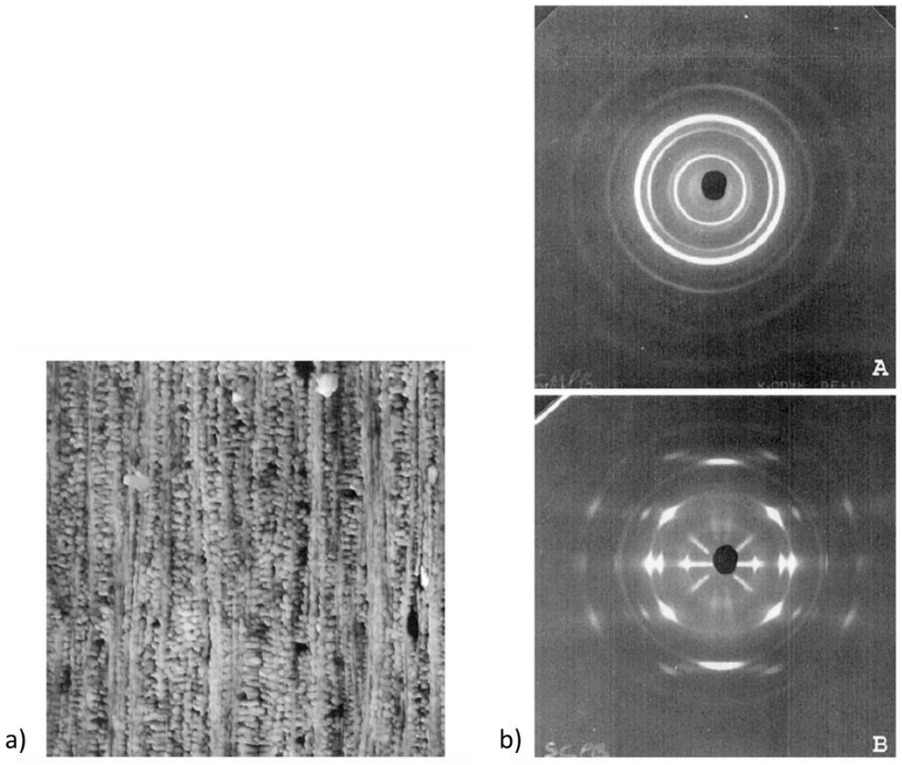


**Figure 29. a) Micrograph of the sample processed with SCORIM; b) X-ray Debye diffraction patterns of A) CIM and B) SCORIM PB [8]. Adapted with permission from John Wiley and Sons, 2003.**

Beyond its influence on tensile behavior, the formation of shish-kebab structures in SCORIM-processed samples has also been found to enhance wear resistance [8,352,354–357,359,362]. Zhang et al. [355] investigated the tribological performance of a polymer blend consisting of 95 wt% HDPE and 5 wt% UHMWPE, comparing specimens produced by CIM with those produced by

SCORIM. Their results showed a clear difference in the wear mechanisms between the two processing methods. While the CIM specimens exhibited wear primarily controlled by micro-fatigue, the SCORIM processed specimens exhibited a milder abrasive wear response. This variation in wear behavior was directly attributed to differences in microstructural organization. In the SCORIM specimens, the increased molecular orientation led to a reduction in the presence of micro-cavities and the propagation of micro-cracks. In addition, the improved resistance to cracking was closely related to the presence of shish-kebab structures and in-situ generated microfibrils, both of which contributed to the mechanical reinforcement of the surface under sliding conditions.

### 2.2.2 Oscillation Packing Injection Molding (OPIM)

This technique is sometimes referred to as Oscillation Shear Injection Molding (OSIM) or Dynamic Packing Injection Molding (DPIM) [2,13,14]. Similar to SCORIM, this process allows for the formation of a three-layer structure and the manipulation of phase separations within polymer blends [369–375,378,394–396]. In addition, this process has been found to be particularly useful for producing reinforced materials that exhibit shish-kebab structures [28–31,36,38,42–44,46,47,49,52,364–368,376,377,379,380,382,383,397]. These structures tend to be more pronounced in the core regions where, in contrast, less ordered morphologies are typically found [13,46,47,377,382]. Zhong et al [2] emphasized the versatility of this technique in generating shish-kebab morphologies regardless of the macromolecular properties of the polymer, such as chain stiffness and length. Nonetheless, their work also highlighted the critical role of flow duration and oscillation frequency in shaping the final microstructure.

For instance, Sang et al. [28] investigated the influence of oscillation frequency and time on the morphology of PLA rods. Their study included samples prepared at two different oscillation frequencies, 0.5 and 2 Hz, and subjected to five different oscillation durations of 6, 18, 30, 90, and 120 s. The samples prepared by CIM exhibited low crystallinity and poor orientation throughout the cross section. In contrast, the OPIM processed samples showed a well-defined structured layer. The thickness of this layer increased as either the exposure time or the oscillation frequency was raised. These findings were clearly illustrated in the SEM images shown in Figure 30, which were taken 800 μm from the surface of the samples under various processing conditions. The SEM micrographs showed that the spherulitic structure typical of CIM processing (Figure 30a) gradually changed to an oriented lamellar structure perpendicular to the flow direction with increasing oscillation time at a constant oscillation frequency (Figure 30b-e). Furthermore, shish-kebab structures oriented parallel to the flow direction were observed in the samples treated at 0.5 Hz for 6 and 18 s (Figure 30b and 30c). However, when the highest oscillation frequency and duration were applied (Figure 30f), distorted spherulites were observed instead.

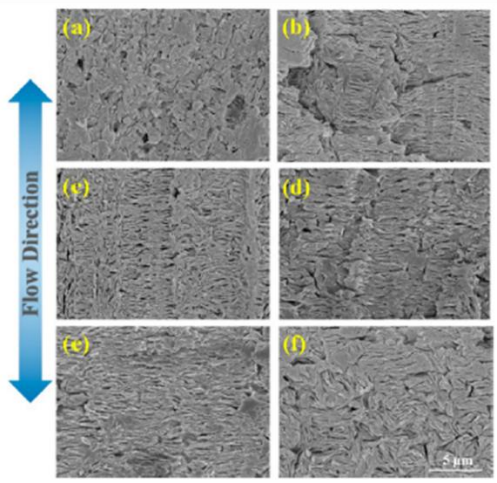


**Figure 30. SEM micrographs at 800 mm from the surface of PLA processed at different oscillation times and frequencies: a) CIM, b) 6 s at 0.5 Hz, c) 18 s at 0.5 Hz, d) 30 s at 0.5 Hz, e) 90 s at 0.5 Hz and f) 120 s at 2 Hz. Reprinted with permission from [28]. Copyright (C) 2017 American Chemical Society.**

The microstructural changes discussed above also affected the heat deflection temperature (HDT) of the materials, with orientation playing a significant role across the thickness of the samples [28]. Specifically, the HDT increased from 55.7 °C for the CIM sample to 76.5 °C when oscillation was applied for 18 seconds and the crystalline thickness reached 1200 µm, and the HDT remained nearly constant for longer oscillation times. When the oscillation frequency was increased from 0.5 Hz to 2 Hz, the HDT further improved, increasing from 78.9 °C to 96.6 °C, although the oriented film thickness remained the same at 2000 µm in both cases.

This improvement in material properties resulting from the structural changes during processing is often referred to as "self-reinforcement". OPIM has been shown to be particularly effective in achieving such results, which have also been observed in matrices like PP and HDPE [29–31,365,366]. Furthermore, other studies have consistently shown that mechanical properties significantly improve in presence of chain orientation and shish-kebab. As an example, Xie et al [38] studied a blend of 90 wt% PBS/10 wt% PLA processed via OPIM. The OPIM processed material showed significant increases in tensile strength, from 38 MPa to 49 MPa, and modulus, from 525 MPa to 634 MPa, compared to the CIM processed samples. These improvements were attributed to the interlayered shish kebab structures aligned parallel to the flow direction that formed under the influence of the external field. The improvements in tensile properties can be explained by the higher stress resistance of shish structures compared to isotropic crystals, together with the interlocking of the kebabs, which prevents the macromolecules from slipping. Additionally, the amorphous phase present between the lamellae plays an important role in transferring the applied load to the stiffer shish kebab structures.

The findings of Xu et al [42] on a 95 wt% PLA/5 wt% poly(ethylene glycol) (PEG) blend are consistent with the previous observations. While the OPIM processed samples showed improvements in mechanical properties, the reduction in ductility was less pronounced than in other cases. Specifically, the elongation at break for the CIM samples was 18.7%, while it was reduced to 11.3% for the OPIM

samples. On the other hand, a significant improvement in impact strength was observed, increasing from 5.0 KJ/m² to 10.6 KJ/m². This enhancement was attributed to the formation of a bamboo-like hierarchical morphology in the samples processed under the influence of the external field. The skin-core structure of these samples exhibited a crystalline skin layer densely populated with shish-kebab structures, while the core retained an isotropic spherulitic morphology. In this configuration, the highly oriented and anisotropic skin layer acts as a robust shell, while the softer core structure benefits from the enhanced ability to absorb impact energy in contrast to a more traditionally oriented morphology [42,397].

In fact, the shish-kebab itself can be further organized, resulting in additional hierarchical levels within the microstructure. Chen et al. [36] observed this phenomenon in OPIM processed isotactic PP. As shown in Figure 31b, both wide-angle X-ray diffraction (WAXD) and SAXS analyses revealed the emergence of branched lamellae representing a new structural level. These secondary lamellae are intercalated between the primary lamellae that form the shish kebabs (Figure 31c) and are essentially the result of branching within the kebabs themselves. A schematic representation of this hierarchical arrangement is shown in Figure 31a. The study also proposed a mechanism for their formation, which consists of the primary kebabs serving as nucleation sites for the secondary lamellae, which then orient themselves based on the angle of the α-phase monoclinic unit cells (99°80').

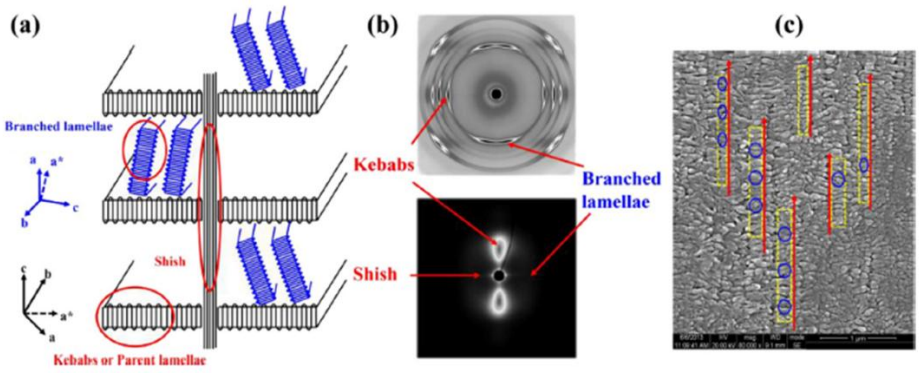


**Figure 31. a) Schematic illustration of the hierarchical structure, distinguishing the shish, the primary and branched kebab lamellae; b) WAXD and SAXS patterns of OPIM-produced isotactic PP samples; c) SEM micrograph with red arrows indicating the shish, yellow squares showing the outer perimeter provided by the kebabs, and blue circles highlighting the secondary lamellae. Adapted from [36] with permission from Elsevier Science Ltd., 2015.**

This morphology significantly influenced the mechanical properties, as tensile testing revealed a uniform deformation without necking, attributed to the presence of secondary branches [36]. Initially, the separation of the primary lamellae caused the secondary lamellae to rotate in the drawing direction, preventing lateral dimensional reduction by internal realignment. As axial deformation increased, both primary and secondary lamellae underwent disruption and reorganization, aligning macromolecules along the drawing direction and forming newly oriented crystals. This process, known as stress-induced crystal fragmentation and recrystallization, has been reported in several studies [36,398–403].

Furthermore, as shown by Wang et al. [44] for a 50 wt% PP/50 wt% LLDPE blend,

phase separation and shish-kebab can be induced. The AFM micrographs in Figure 32 show the OPIM sample at different depths from the skin, revealing different morphologies associated with specific combinations of cooling and shear rates. A co-continuous phase was observed when both cooling and shear rates were high (Figure 32a), while a decrease in the above promoted the formation and refinement of an island-sea structure (Figure 32b-e). In the core (Figure 32f), the morphology was attributed to the lower shear rate and increased heat received due to active shear flow. In addition, X-ray analysis revealed different chain organizations in the PP and LLDPE domains, with shish-kebab structures in PP and two orientations of lamellar structures in LLDPE. These lamellar orientations were observed both perpendicular to the flow direction and tilted at an angle of 45-50°, regardless of depth. As a result, the OPIM technique led to a refined structure with a complex organization at multiple scales.

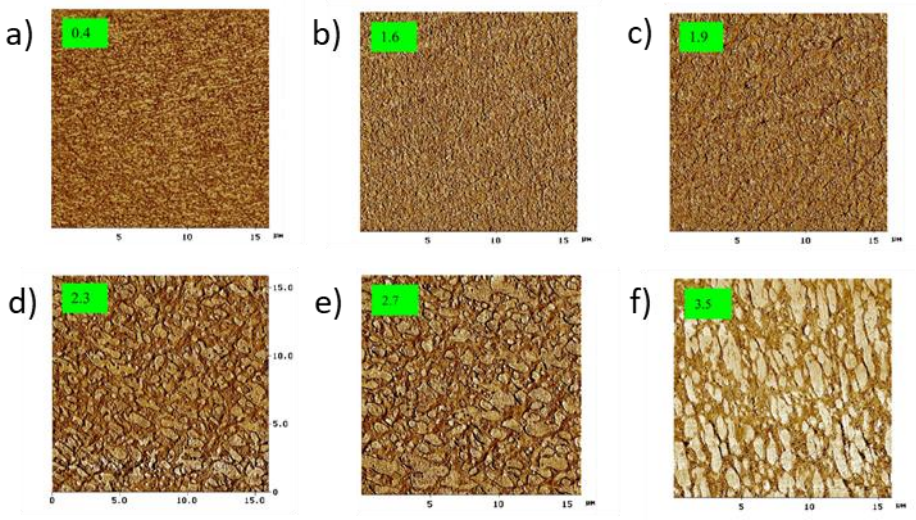


**Figure 32. AFM micrographs of OPIM 50 wt% PP/50 wt% LLDPE. Each photo reports a distance measured from the skin layer in mm. a) skin layer; b, c) sheared layer; d, e, f) core. Adapted from [44] with permission from Elsevier Science Ltd, 2003.**

The potential to achieve a complex hierarchical structure through the OPIM technique has been explored over the years to improve final properties. For instance, Zhou et al [49] proposed the use of OPIM on both pure PLA and a 90 wt% PLA/10 wt% PBAT blend to achieve higher strength and toughness. As shown in Figure 33a, OPIM PLA met the requirements if compared to CIM PLA, at the expense of the deformation at break. The latter was improved with the introduction of PBAT, but the detrimental reduction in stress and modulus ad to be overcome by processing the blend with OPIM. The resulting improvement in mechanical properties can be attributed to the refined microstructure, as shown in Figure 33b. In fact, PBAT nanofibrils formed at different depths from the skin in both CIM and OPIM samples, but the diameter was significantly reduced from 300 to 150 nm when the second technique was used, due to the intense shear flow present. In addition, PLA actively contributes to defining the hierarchical morphology of the blend. Oriented lamellae of the PLA matrix, epitaxially aligned with the PBAT fibrils, incorporate the second phase in both CIM and OPIM blends (Figure 33b A

and B). The combination of the second phase and the external field results in a synergistic effect that refines the microstructure, leading to the formation of structured shish-kebab throughout the thickness (Figure 33b B). As a result, the PBAT nanofibrils form the core of the shish, while the shear flow-induced stretching of the PLA macromolecules creates a surrounding layer of shish around it. The formation of the hierarchical structure is enabled by the low interfacial tension and large specific surface area between PLA and PBAT, which, together with their partial miscibility, stabilizes the PLA shish layer. The slow relaxation of the PBAT nanofibrils prevents the retraction of the stretched PLA chains and maintains their orientation after shear is stopped. This effect is confirmed by comparing the OPIM-processed PLA/PBAT blend (Figure 33bB) with pristine PLA (Figure 33bC), where the latter shows weaker shish-kebab orientation and anisotropy confined to the skin due to the reduced relaxation time provided to the macromolecules prior to solidification. These structural differences also explain the mechanical behavior reported in Figure 33a, where improved tensile strength results from higher shish-kebab density and alignment, while the ductile PBAT fibrils maintain toughness by allowing plastic deformation without loss of strength.

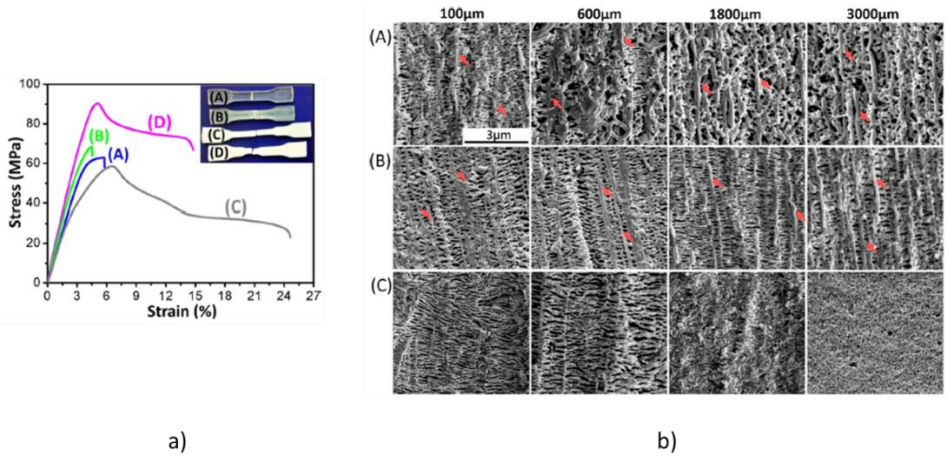


**Figure 33. a) Stress-strain curves and tested samples of A) CIM or B) OPIM PLA, C) CIM or D) OPIM 90 wt% PLA/10 wt% PBAT; b) Micrographs of selectively etched A) CIM or B) OPIM blend and C) OPIM PLA at different distances from the skin; the position of the PBAT nanofibrils is indicated by the red arrows. Adapted with permission from [49]. Copyright (C) 2017 American Chemical Society.**

The role of blending in stabilizing the morphology and refining the shish-kebab structures has been well documented [43,46,52,367,368,376,377,379,382,383]. The influence of the properties of the second polymer on the resulting microstructure has also been investigated. For example, Liang et al. [46,382] demonstrated that incorporating low MW HDPE instead of high MW HDPE into an LLDPE matrix improved shish kebab orientation and produced more compact kebab lamellae. This was attributed to increased chain mobility of the low MW HDPE and altered miscibility with the matrix, both of which contributed to improved anisotropy.

Finally, although shish-kebab structures are not always observed in OPIM-processed specimens, improvements in mechanical and impact properties compared to CIM counterparts are typically reported [369–375,378,394–396]. The application of an external field, though, does not prevent the decrease in tensile

properties with increasing minor phase content [374,375,378], as illustrated in the study by Su et al. [378] on polyoxymethylene (POM)/HDPE blends with polyethylene contents varying between 5 and 50 wt%. The SEM micrographs in Figure 34A show progressive phase coalescence and formation of a co-continuous HDPE phase at concentrations of 15 wt% and above, along with the presence of sub-inclusions of one phase within the other. The observed coalescence was attributed to the external field, which although promoting mixing, could not enhance domain orientation due to mutual hindrance between the immiscible polymers. As a result, even though OPIM samples exhibited higher tensile strength and modulus than CIM (Figure 34B), their mechanical performance decreased with increasing HDPE content.

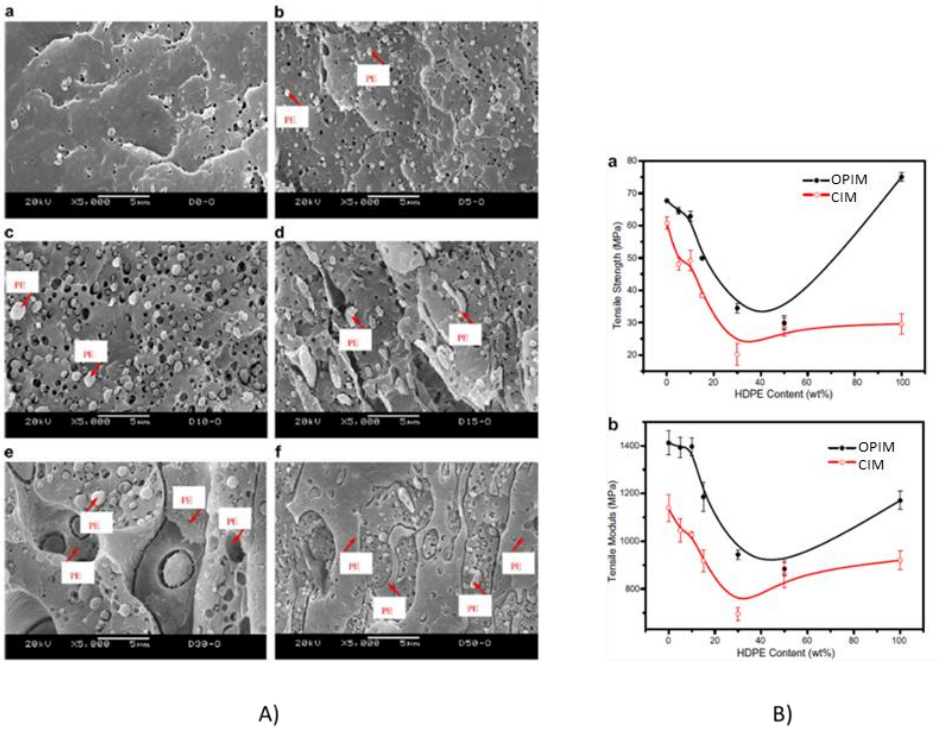


**Figure 34. A) SEM images of the section of OPIM-processed blends at increasing concentration of HDPE, specifically a) 0 wt%, b) 5 wt%, c) 10 wt%, d) 15 wt%, e) 30 wt% and f) 50 wt%; B) Tensile strength a) and modulus b) of the materials processed with OPIM or CIM. Adapted from [378] with permission from Elsevier Science Ltd., 2008.**

## 2.2.3 Vibration-assisted Injection Molding (VIM)

This technology is particularly efficient for the self-reinforcement of a single polymer by forming layers and shish-kebab structures [2,13,14,32,34,35,381,385–389,391–393,404]. Yang et al. [34] provided an interesting example by studying the effects of different vibration frequencies on PVDF. As can be seen in Figure 35 from the morphologies of samples processed at frequencies of 0, 12, and 30 $s^{-1}$, there is a progressive increase in anisotropy as the vibration frequency rises. While the CIM processed sample remains isotropic, the 12 $s^{-1}$ sample shows improved orientation and the 30 $s^{-1}$ sample exhibits shish-kebab structures aligned with the flow direction. In addition, the polymorphism of PVDF changes with the variation

of the vibration frequency. In particular, the CIM sample contains only the α phase, while the 12 $s^{-1}$ sample shows both α and β phases, and the 30 $s^{-1}$ sample contains the α, β, and γ phases.

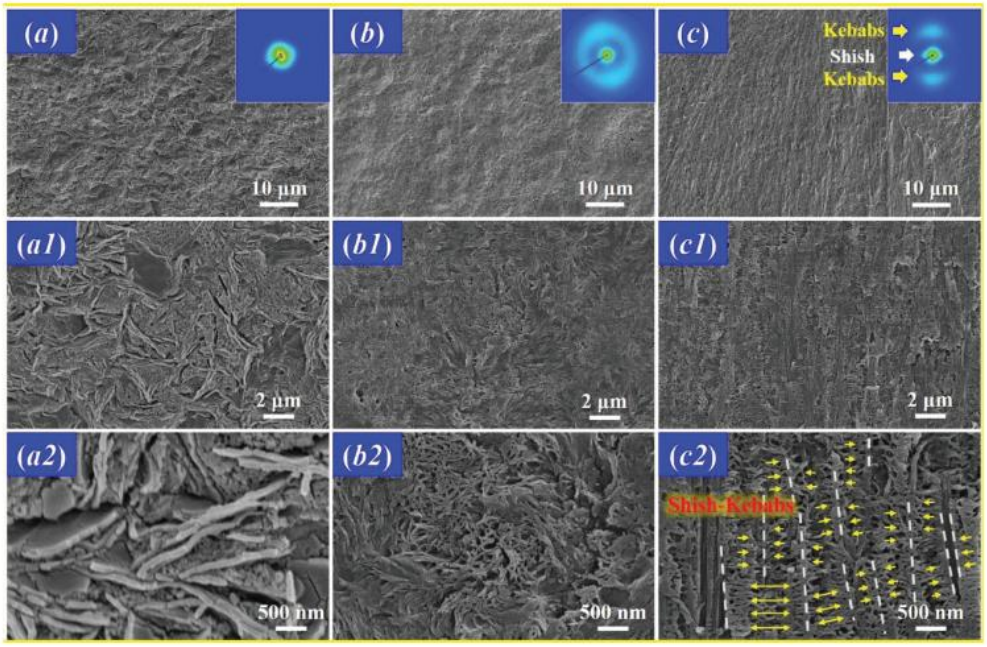


**Figure 35. SEM images of samples obtained with a vibration frequency of a) 0, b) 12 and c) 30 $s^{-1}$ and corresponding magnitudes (a1, a2, b1, b2, c1 and c2). SAXS are also reported. The flow is aligned to the vertical direction, while the white lines represent the shish [34]. Adapted with permission from John Wiley and Sons, 2018.**

Besides, the VIM technique allows the formation of a layered morphology consisting of shear and spherulitic layers, which improves crack deflection and impact strength, as demonstrated by Hou et al. [32,381] for PP. In contrast to CIM, where a skin-core structure with a thin shear layer is observed (Figure 36a), VIM processing produces tunable microstructures with alternating shear and spherulitic layers, as shown in Figure 36b and c. This is obtained by controlling the duration of the static and vibrational conditions in the cavity. For instance, the absence of spherulites in the core in one case results from a reduced static cooling time. Additionally, considering the skin and shear layer as a whole ($R_s$), it corresponds to the 16% of the overall thickness, while when the vibration is applied, the final value is about 40 % and comparable regardless the processing conditions. Thus, a hierarchical tunable microstructure with a quite constant crystalline content was obtained.

Furthermore, shish-kebab structures aligned with the shear flow appear in the shear layers, with their density and size influenced by the cooling rate and, in particular, a lower density of shish characterized by larger kebabs was obtained in correspondence with the mold walls, while a higher density of thinner shish-kebabs was reached in the inner shear layer.

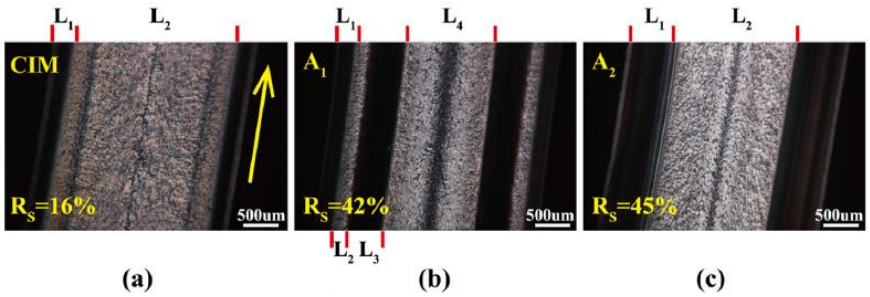


**Figure 36. Micrographs of samples obtained with a) CIM and b, c) OPIM. The resulting of b) long and c) short static interval are shown. Also, represents the ratio between the shear layer and the overall section thickness ($R_s$) is reported. The flow direction is indicated by the arrow [381]. Reprinted with permis-sion from Elsevier Science Ltd., 2017.**

The resulting VIM specimens showed greater plastic deformation in the spherulitic layers after impact tests when compared to CIM samples [381]. Considering the rough fracture surfaces and the greater plastic deformation observed in the shear layer, the effect of shish kebabs in increasing impact strength was highlighted. Specifically, their role in transferring impact energy to the surrounding material, thereby enhancing energy absorption and plastic deformation, was revealed. As a result, it seems clear that the impact behavior of two OPIM samples is different due to the different distributions of oriented and isotropic layers [381,405]. For instance, referring to the microstructures reported in Figure 36, the one having the better efficiency in crack deflection is the one in Figure 36b. Despite this, microstructural tuning had little effect on other mechanical properties, as tensile strength was primarily determined by the overall crystallinity rather than the layered structure [32,381].

VIM also allowed for more complex morphologies, such as shish-kebab-like cylindrulites in PP [35,391], as observed by Zhou et al. [35]. In fact, in the samples processed at 1.10 Hz an additional fourth layer of shish-kebab-like cylindrulites is observed (Figure 37b D) in addition to the expected skin (A), core (C) and transition layers (B) obtained in the CIM sample (Figure 37a). Besides, the morphology of the cylindrulite depends from the distance from the surface, with the ones closer to the core characterized by a single-fibril shish and smaller dimensions. On the other hand, the ones next to the surface are multi-fibrillar (Figure 37c). This variation was explained by the lower shear stress during solidification from the skin to the core, resulting in multifibrillar shish near the surface and single fibrillar shish near the core. Therefore, more vibrations are transferred in the first case ad a larger number of macromolecules are oriented closer to the surface, resulting in multi-fibrillar shish (Figure 37d). In both cases, oriented macromolecules acted as nucleation sites for epitaxial lamellae formation.

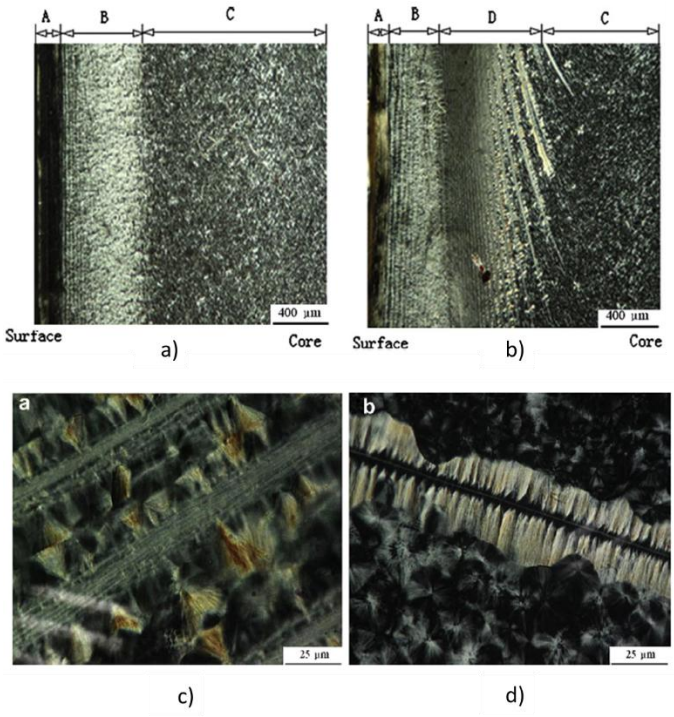


**Figure 37. Micrographs of the cross-section of the samples prepared with a) CIM and b) VIM, and corresponding magnification of the c) multi-fibrillar and d) single-fibril shish. A is the skin layer, B the transition one, C the core and D the shish-kebab-like cylindrulite region [35]. Adapted with permission from Elsevier Science Ltd., 2011.**

# Chapter 3

# Compounding of HDPE homopolymer blends

*Part of the work described in the Chapter 3 has been previously published in:*

"Cravero, F.; Cavallini, N.; Arrigo, R.; Savorani, F.; Frache, A. The Effect of Processing Conditions on the Microstructure of Homopolymer High-Density Polyethylene Blends: A Multivariate Approach. *Polymers* **2024**, *16*, doi:10.3390/polym16070870" [406]

## Abstract

In the present Chapter, a multivariate approach was utilized for gaining some insights into the processing–structure–properties relationships in polyethylene-based blends. In particular, two HDPEs with different molecular weights were melt-compounded using a twin-screw extruder, and the effects of the screw speed, processing temperature and composition on the microstructure of the blends were evaluated based on a Design of Experiment–multilinear regression approach. The results of the thermal characterization, interpreted trough the multilinear regression response surfaces, demonstrated that the composition of the blends and the screw rotation speed are the two most important parameters in determining the crystallinity of the materials. Furthermore, the rheological data were examined using a Principal Component Analysis multivariate approach, highlighting also in this case the most prominent effect of the weight ratio of the two base polymers and the screw rotation speed.

## 3.1 Introduction

The first polymeric system considered is based on HDPE. The material was selected for its cost-effectiveness, ease of processing, and excellent mechanical and chemical resistance properties, making it one of the most widely used thermoplastic polymers in the industry [407–409]. In fact, the global quantity of PE required on an annual basis corresponds to approximately 30% of the total amount of plastic produced. It is estimated that the range for this amount was between 114 and 154 million tons for the years 2022 and 2023 [408,410]. The markets of greatest use are packaging, automotive, cable, and plumbing industries [407,409,411–413]. Besides, it is important to note that about 70% of the polyethylene used is mixed with other polymers, and this has an impact on the microstructure of the final material and, ultimately, on its properties. Consequently, in recent years there has been an increase in the studies of the relationship between the microstructure of PE-containing blends and the resulting characteristics. The works mainly focus on binary blends involving HDPE, LDPE, and LLDPE. The primary objective is to evaluate miscibility in both the solid and molten states [414–423]. One of the main issues in this area is the discrepancy among various studies regarding actual miscibility. This is due to the characterization techniques used to assess this property, as well as the different behaviors observed among the blend constituents in liquid or solid states [414–416,422,424–427]. On the other hand, since the final characteristics of the materials are strongly related to macromolecular architecture, molecular weight, and molecular weight distribution, most studies have focused on these aspects, while paying less attention to the effects of processing parameters [158,414–416,418,419,421–423,428–433]. In fact, only a few studies have explored the effect of the operative conditions of the melt blending, even though the process is a crucial step in producing polymer blends [415,422,434–439].
Additionally, even if a lack of studies affects the field, HDPE/HDPE binary blends offer unique opportunities for the formation of shish-kebab-like crystal structures, making them particularly intriguing in the field of self-reinforcing composites [13,83,84,415,434,437,438,440,441]. In fact, it has been shown that by selecting the MW of the chains in PE blends provides a higher degree of freedom in tuning the processability and final properties of the resulting material [442]. In recent years, an increasing number of studies have investigated the effect of molecular weight distribution on the final morphology of blends, highlighting its significant impact on crystallization kinetics [440–443]. For instance, a bimodal MW distribution was found to negatively impact the crystallization rate while promoting the overall crystallinity content compared to a unimodal MW distribution system [443].

Due to the possibility to select the final properties of the blend through an appropriate distribution of molecular weights, as well as the extensive use of polyethylene-based blends in various fields, this study aimed to investigate how to customize the final properties of the material by blending two commercially available HDPE matrices with different MW. The work primarily focused on studying the relationship between processing parameters, microstructure, and

properties when melt blending with twin screw extrusion was considered. In this regard, the materials were processed using a Design of Experiments (DoE) approach ($2^3$ full factorial design), in which the relative content of high-to-low molecular weight matrix, the compounding temperature profile, and the screw speed were selected as variable parameters [444]. In the first case, the two high molecular weight (HMW) and low molecular weight (LMW) matrices were considered both independently and in blends having reciprocal weight combination of 30:70, 50:50 and 70:30, respectively. In addition, two temperature profiles constant from hopper to die were exploited, the lower corresponding to 175 °C and the higher to 190 °C. Besides, two different screw rotation speeds of 150 and 400 rpm were considered, respectively. On the other hand, the screw profile was maintained constant, in accordance with the description provided in in Section A.2.1 (see Figure 98 and Table 15). Table 1 summarizes constant and variable parameters, along with their corresponding values.

**Table 1. Variable and constant factors used for the production and characterization of the HDPE homopolymer blends.**

| | Factor | Levels | | | | |
|---|---|---|---|---|---|---|
| Variables | Screw speed [rpm] | 150 | | | 400 | |
| | MW distribution | Monomodal | | | Bimodal | |
| | HMW:LMW content [wt% of HMW] | 0 | 30 | 50 | 70 | 100 |
| | Temperature [°C] (constant profile) | 175 | | | 190 | |
| | Rheological analysis temperature [°C] | 175 | | | 190 | |
| Constant | Feed rate [g/h] | 270 | | | | |

Subsequently, the materials were characterized on a thermal and rheological point of view. This provided important information regarding the microstructure, which was then related to the process parameters adopted, exploiting two different mathematical models. In particular, the thermal analyses were analyzed using the response surfaces of a multilinear regression (MLR) model, while the study of rheological behavior involved the use of a Principal Component Analysis (PCA) multivariate approach [445]. Furthermore, the discussion considered the miscibility of the two HDPEs, evaluating three different rheological models. It is important to note that two different analysis temperatures were also used in the case of the rheological behavior study. These temperatures corresponded to the two values that were used for the compounding step (see Table 1).

Considering all the above parameters, the materials in the present study were named after the values of the factors used for their production. For instance, 50HMW_190C_400 refers to the blend containing 50 wt% of the high molecular weight matrix, compounded at 190 °C and 400 rpm.

## 3.2 Data analysis

### 3.2.1 DSC results

Firstly, willing to evaluate the effect of the processing parameters on an experimental point of view, a reference system comparing the actual melting enthalpy values with the theoretically expected ones has been introduced. Specifically, the melting enthalpy of each blend was expressed referring to the second heating melting enthalpy of the commercial HMW and LMW pellets. This means that the $\Delta H_m$ of the as-received pellets of HMW and LMW were firstly obtained. Then, the expected values for the blends were calculated according to Eq. 3.1.

$$\Delta H_{calc} = m * \Delta H_{HMW} + (1 - m) * \Delta H_{LMW} \quad \text{Eq. 3.1}$$

where $\Delta H_{calc}$ is the calculated melting enthalpy, m is the concentration of HMW in the blend, $\Delta H_{HMW}$ is the melting enthalpy of the HMW pellet, and $\Delta H_{LMW}$ is the melting enthalpy of the LMW pellet. The experimental metling enthalpies of the pellets of HMW and LWM along with the values calculated for the blends in accordance to Eq. 3.1 and the corresponding crystallinity (see Eq. A.4) are reported in Table 2.

**Table 2. Melting enthalpy (ΔH) and crystallinity of the LMW and HMW of the pellets recorded during the second heating cycle; Melting enthalpy (ΔH) of the blends calculated according to Eq. 1 and corresponding crystallinity.**

| Material | ΔH [J/g] | Crystallinity [%] |
|---|---|---|
| LMW pellet 2nd heating | 231 | 80 |
| HMW pellet 2nd heating | 187 | 64 |
| 30HMW calculated value | 218 | 75 |
| 50HMW calculated value | 209 | 72 |
| 70HMW calculated value | 200 | 69 |

In addition, in order to evaluate the difference between the theoretical and experimental data, the latter were determined with DSC analyses and the corresponding results are reported in Table 3. In addition, the crystallinity content and the melting temperature are listed.

**Table 3. Melting enthalpy ($\Delta H_m$), crystallinity content and melting temperature ($T_m$) of the investigated materials.**

| Material | $\Delta H_m$ [J/g] | Crystallinity [%] | $T_m$ [°C] |
|---|---|---|---|
| 100LMW_175C_400rpm | 208 | 72 | 139 |
| 30HMW_175C_400rpm | 172 | 59 | 136 |
| 50HMW_175C_400rpm | 171 | 59 | 136 |
| 70HMW_175C_400rpm | 164 | 57 | 135 |
| 100HMW_175C_400rpm | 151 | 52 | 133 |
| 100LMW_190C_400rpm | 189 | 65 | 136 |
| 30HMW_190C_400rpm | 177 | 61 | 137 |
| 50HMW_190C_400rpm | 174 | 60 | 136 |
| 70HMW_190C_400rpm | 167 | 58 | 134 |
| 100HMW_190C_400rpm | 157 | 54 | 131 |
| 100LMW_175C_150rpm | 177 | 61 | 136 |
| 30HMW_175C_150rpm | 173 | 60 | 135 |
| 50HMW_175C_150rpm | 182 | 63 | 135 |
| 70HMW_175C_150rpm | 170 | 59 | 134 |
| 100HMW_175C_150rpm | 160 | 55 | 132 |
| 100LMW_190C_150rpm | 180 | 62 | 136 |
| 30HMW_190C_150rpm | 167 | 58 | 136 |
| 50HMW_190C_150rpm | 167 | 58 | 134 |
| 70HMW_190C_150rpm | 166 | 57 | 133 |
| 100HMW_190C_150rpm | 168 | 58 | 132 |

Then, the difference between the expected melting enthalpies and the actual values was obtained according to Eq. 3.2:

$$\Delta H_{Gap} = \frac{\Delta H_{Exper} - \Delta H_{calc}}{\Delta H_{Exper}} * 100 \qquad \text{Eq 3.2}$$

where $\Delta H_{Gap}$ refers to the difference between the experimental and the calculated melting enthalpy, $\Delta H_{Exper}$ is the experimental melting enthalpy recorded during the first heating cycle of the compounded material reported in Table 3, and $\Delta H_{calc}$ is the melting enthalpy calculated according to Eq. 3.1. It is wort nothing that, considering Eq. 3.2, the value of $\Delta H_{Gap}$ will be positive if the experimental enthalpy (and thus, the crystallinity) is greater than the calculated value. On the

other hand, if the experimental value is smaller than the calculated one, the final value will be negative. Lastly, if the two values match, $\Delta H_{Gap}$ will be equal to zero. The interpretation of the data was performed using the DoE approach described in Section 3.2.2.

### 3.2.2 Design of Experiment

In accordance with the DoE method, the ranges of values of interest of the factors (corresponding to the variable parameters) are first required to be defined. From these, the specific values (or levels) to be used to define the combinations of factors are then determined. Typically, the minimum and maximum levels correspond to the boundary values of range of interest. Furthermore, additional levels are selected within the interval to ensure equidistance between subsequent levels. Consequently, fixed levels are defined for every factor, resulting in a set of combinations for each processing parameter corresponding to the experiments to be performed [444]. This approach enables the effective evaluation of the potential effects of individual factors on the morphology of the blends. Besides, it is important to note that defining the ranges of variation for each factor delimits the so-called experimental domain. It is important to note that defining the ranges of variation for each factor establishes the so-called experimental domain. Consequently, the experimental conditions within this domain can be explored and modeled, even if the trials were not performed in practice, and by systematically varying all the factors across their levels, the behavior of a specific response across the domain itself can be modeled. Most importantly, an estimation of the response can also be obtained in the points of the experimental domain for which no experimental value was measured.

In the present study, three factors were considered. Specifically, the relative content of the HMW and LMW matrices, the compounding temperature and screw speed. For the first parameter, five levels were established with decreasing weight percentages of HMW in the blend. In particular, 100%, 70%, 50%, 30% and 0%. Also, two levels were defined for the other two factors, corresponding to 175 and 190 °C for the melt blending temperature, and to 150 and 400 rpm in the case of the screw rotation speed. As summarized in Table 4, the DoE required twenty compounding processes to be performed (5 x 2 x 2 = 20). Besides, for the rheological characterizations, a further factor corresponding to the analysis temperature was required. The two levels that were considered in this case were 175 and 190°C.

**Table 4. Factors, variable values, and corresponding levels used to define the DoE. The "code" column refers to the abbreviations used to label the factors in the results section.**

| Factors | Code | Levels | | | | |
|---|---|---|---|---|---|---|
| | | − 1 | − 0.5 | 0 | 0.5 | 1 |
| HMW:LMW content [wt% of HMW] | HMW content | 0 | 30 | 50 | 70 | 100 |
| Compounding temperature [°C] | T | | 175 | | 190 | |
| Screw rotation speed [rpm] | rpm | | 150 | | 400 | |
| Rheology analysis temperature [°C] | / | | 175 | | 190 | |

As previously stated, determining the experimental domain is essential for estimating responses in experimental conditions where data is not available, even if the factor values are within the range of the minimum and maximum experimental levels. Therefore, a mathematical function is necessary to model the domain, which describes the experimental data acquired in accordance with the DoE scheme. Among the different approaches that can be exploited, the most common and flexible method is based on multilinear regression [446]. In fact, given the factors under examination, MLR allows for the inclusion of additional terms in the equation of the constituent model. Each term in the equation describes an effect that a particular factor has on the response. Therefore, defining the experimental domain through the factors and their levels is strictly connected to the postulated MLR model, determining the terms that should be included in the mathematical model. Besides, it is important to note that when factors with two levels are studied, only the linear and interaction terms of these factors can be modeled. If more than two levels are present, however, the quadratic terms can also be included. Thus, considering the DoE scheme used in the present study (Table 4), Eq. 3.3 describes the MLR model for modeling the response (y). The open-access software Chemometric Agile Tool was used to perform all DoE modeling using MLR [447].

$$y = b_0 + b_{p_{wt}} \cdot X_{p_{wt}} + b_T \cdot X_T + b_{rpm} \cdot X_{rpm} + b_{p\_wt,T} \cdot X_{p\_wt} \cdot X_T + b_{p\_wt,rpm} \cdot X_{p\_wt} \cdot X_{rpm} + b_{T,rpm} \cdot X_T \cdot X_{rpm} + b_{p^2_{wt}} \cdot X^2_{p\_wt} \quad \text{Eq. 3.3}$$

Where, $b_{pwt}$, $b_T$ and $b_{rpm}$ are the three linear terms, $b_{p\_wt,T}$, $b_{p\_wt,rpm}$ and $b_{T,rpm}$ are the three interaction terms, and $b_{p2wt}$ is the quadratic term. Additionally, the b terms represent the regression coefficients, which allow us to interpret the actual effect of each factor on the response y based on their values.

### 3.2.3 Rheological results

In order to evaluate the miscibility of the HMW and LMW in their molten state, the rheological experimental data were compared with the trends of the complex viscosities obtained considering three different additive rules. In particular, the logarithmic rule (Eq. 3.4) and the linear rule (Eq. 3.5) predicting the behavior of miscible blends [448] were used, as was the diluted emulsion of the Newtonian liquid model (Eq 3.6) [449]:

$$\ln \eta_B = W_{HMW} * \ln \eta_{HMW} + (1 - W_{HMW}) * \ln \eta_{LMW} \quad \text{Eq 3.4}$$

$$\eta_B = W_{HMW} * \eta_{HMW} + (1 - W_{HMW}) * \eta_{HMW} \quad \text{Eq 3.5}$$

$$\eta_B = \eta_m * \left(1 + \frac{5\varphi+2}{2\varphi+2} * n\right) \quad \text{Eq 3.6}$$

where $\eta_B$ is the viscosity of the blend, $W_{HMW}$ is the weight fraction of HMW, $\eta_{HMW}$ and $\eta_{LMW}$ are the viscosities of HMW and LMW, respectively, $\eta_m$ is the viscosity of the matrix, φ is the viscosity ratio between the dispersed phase and the matrix, and n is the volume fraction of the dispersed phase. In all cases, the viscosity values of the matrices refer to LMW and HMW being compounded and analyzed in the same conditions as those of the blend.

### 3.2.4 Principal Component Analysis

Principal Component Analysis [450] is an exploratory data analysis method that is used to facilitate the interpretation of multivariate data. In fact, it reduces the data dimensions and removes the noise owing to the projection of the data onto a space of fewer dimensions. In particular, this space is defined by the so-called Principal Components (PCs), which are linear combinations of the original variables. Each Principal Component describes a portion of the information that is contained in the modeled data, and the PCs are ordered by decreasing the amount of explained variance. Thus, by properly selecting the number of PCs, it is possible to model the actual information of the data and exclude the noise [445].

In the present study, PCA is applied to the rheology data with the aim of inspecting whether the screw speed, the temperature profile, the blend composition and the temperature of the rheological measurement have any effects on the rheological curves. In PCA, the factors' levels (as discussed in Section 3.2.2) can be used as "class information", i.e., the PCA results can be colored according to the different levels to spot possible groupings and tendencies in the so-called score plots. These scatter plots, in which pairs of PCs are plotted against the other, are one of the two main outputs of PCA, and each point on a score plot corresponds to one sample (i.e., one individual experimental rheological run). This means that samples that are close to each other will share similar features, while distant ones will have different results.

In accordance with the literature, it seems that the application of PCA analysis to the study of the rheology of polymer blends is an innovative approach. In fact, only few works concerning PCA analysis of rheological data of asphalts [451] or bitumen [452], aqueous dispersions for cosmetic use [453], wheat-based doughs [454,455] and drug-delivering polymer systems [456] are available in the literature. Nevertheless, in all these studies, a PCA approach is applied to experimentally measured parameters (such as a cross-over modulus, zero-shear viscosity or phase angle), while in this work, the overall dependency of the complex viscosity on the frequency will be analyzed.

In this study, the PCA toolbox for MATLAB [445], developed by the Milano Chemometrics and QSAR Research Group, was used. The toolbox is freely downloadable from the group's website [457].

## 3.3 Results and Discussion

### 3.3.1 Rheological behavior

Figure 38 presents the complex viscosity curves for HMW, LMW and their blends processed at 190 °C and 400 rpm. As expected, the rheological behaviors of the two pristine polymers strongly differ, according to their different molecular weights. In particular, LMW shows a pronounced Newtonian behavior, with a Newtonian plateau developing in the low-intermediate frequency range and mild shear thinning in the high-frequency region. Otherwise, HMW exhibits a shear-thinning behavior throughout the whole investigated frequency interval, which is likely due to the high molecular weight of the samples, implying the formation of a dense network of entanglements which hinders the full relaxation of the macromolecular chains in the tested time interval [458]. The blends exhibit a rheological behavior that is intermediate between those of the two HDPE samples, with complex viscosity values accounting for the relative content of HMW and LMW. Nevertheless, it should be noticed that the low-frequency behavior of all the investigated blends is strongly affected by the presence of HMW; in fact, regardless of the content of the high-molecular weight HDPE, all the blends exhibit a prominent non-Newtonian behavior at the lowest investigated frequencies.

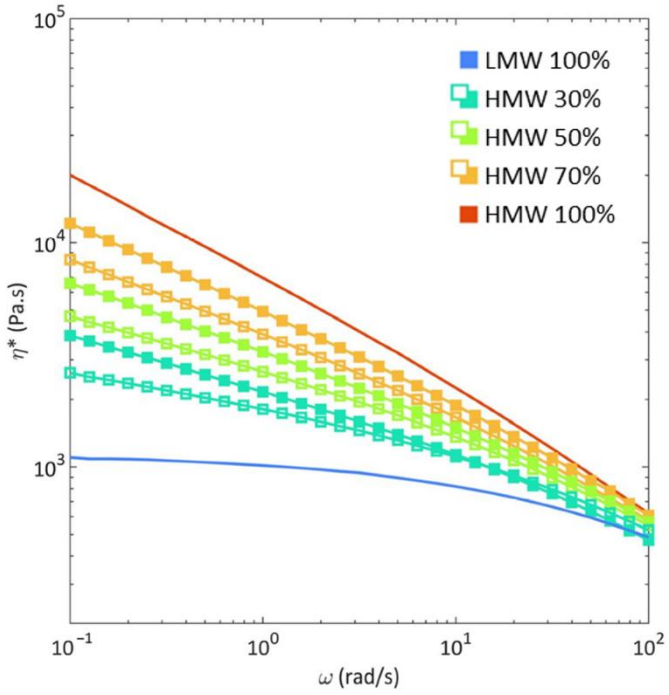


**Figure 38. Complex viscosity (η*) as a function of the frequency (ω) for HMW (high molecular weight) and LMW (low molecular weight) (continuous lines) and blends (solid symbols), processed at 190 ◦C, 400 rpm, and analyzed at 175 ◦C. The values calculated through the logarithmic additive rule (hollow symbols) are also reported [406]. Reprinted under CC BY 4.0 license.**

From the comparison of the experimental data with the calculated values (Eqs. 3.4, 3.5, 3.6), it emerged that, irrespectively of the blend' s composition and of the adopted processing conditions, the diluted emulsion model is the worst-fitting one, as it does not predict reliable values, neither in the low-frequency or in the high-frequency region. On the other hand, the linear and logarithmic models perform better. In particular, both models accurately predict the rheological behavior in the shear-thinning region, especially for frequencies above 10 rad/s, while they overestimate the experimental values in the low-frequency region, as can be appreciated in Figure 38 for the blends compounded at 190 °C, 400 rpm and analyzed at 175 °C. In Figure 39 and Figure 40 are reported the comparisons for all the other materials studied.

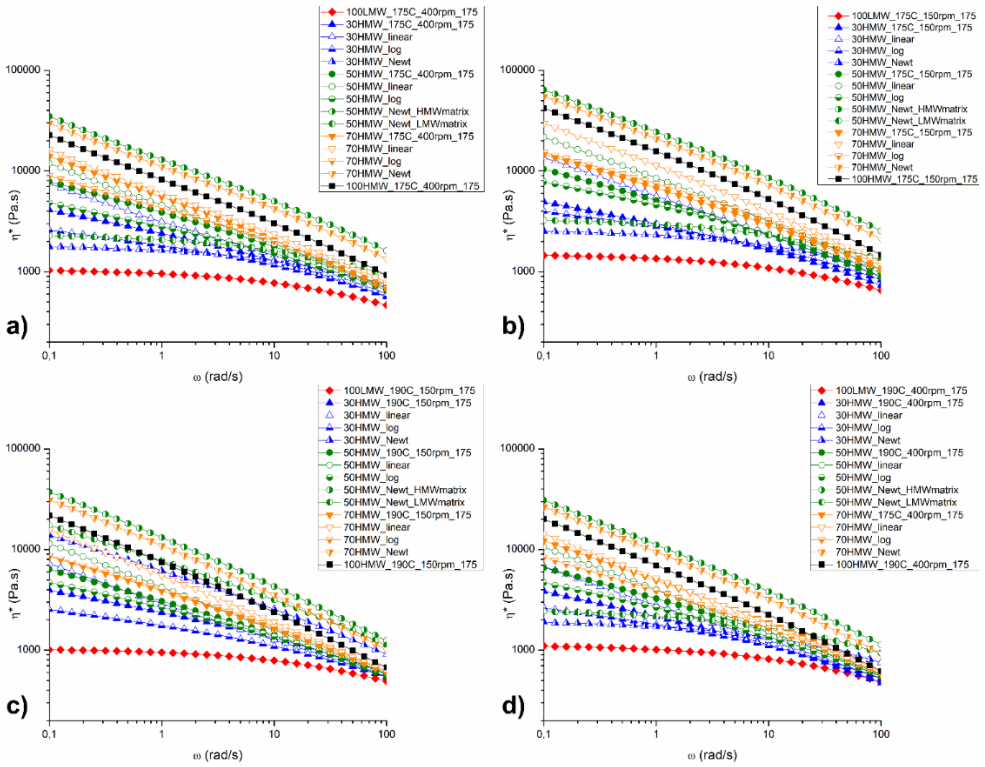


**Figure 39. Comparison between the experimental data (obtained by performing frequency sweep tests at 175 °C) and the curves obtained by applying additive rules showed in Eqs 3.4-3.6 [406]. Reprinted under CC BY 4.0 license.**

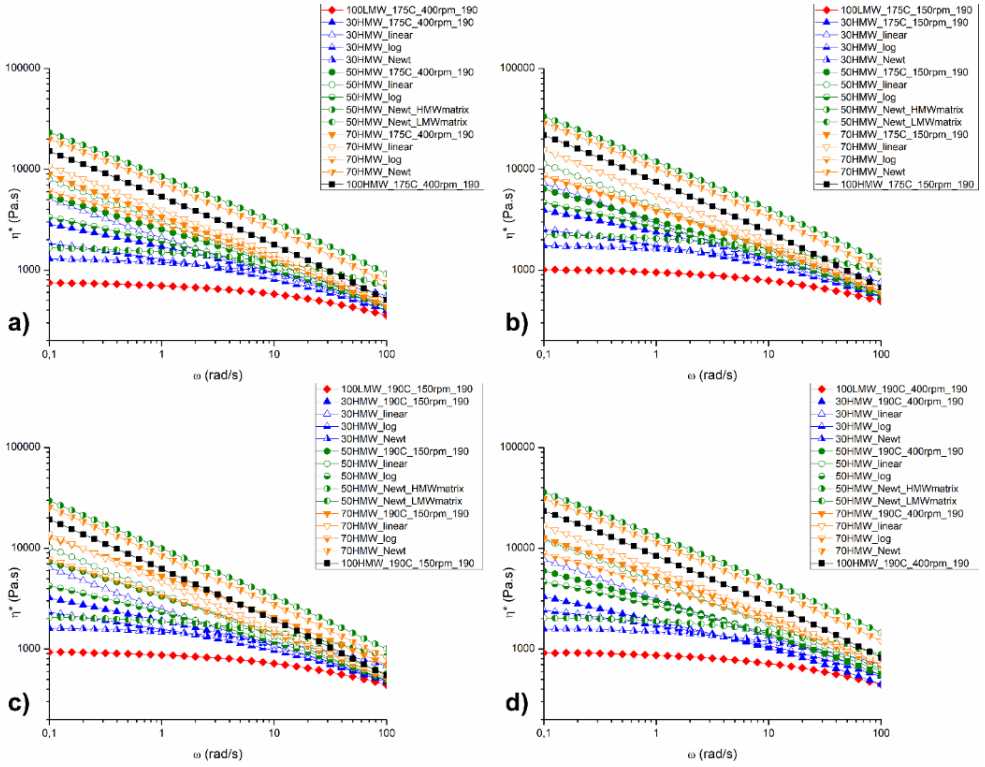


**Figure 40. Comparison between the experimental data (obtained by performing frequency sweep tests at 190 °C) and the curves obtained by applying additive rules showed in Eqs 3.4-3.6 [406]. Reprinted under CC BY 4.0 license.**

In order to gain further insights into the miscibility of the two matrices in the molten state, the Cole-Cole plots of all the investigated materials were analyzed. In fact, through this representation, the relaxation behavior of the blends can be assessed, allowing obtaining important information about the miscibility of the polymers. In particular, the shape and smoothness of the plot of the imaginary part of the viscosity (η") versus the real part (η') is evaluated [416,459–461]. According to the literature, homogeneous polymeric materials with a single-phase microstructure are characterized by a smooth and semicircular arc, indicating the presence of a single dynamic population relaxing in a single time interval. Conversely, more complex shapes (involving the appearance of a second arc or of a linear tail) are expected for systems presenting distinct relaxation times resulting from the presence of different phases.

The representative Cole-Cole plots of the blends processed at 190 °C and 400 rpm (whose complex viscosity curves are presented in Figure 38) are reported in Figure 41. In addition, the curves for all the other blends investigated are plotted in Figure 42 and Figure 43 for the material analyzed at 175 or 190 °C, respectively.

Firstly, focusing on Figure 41 and as already discussed for the complex viscosity, the two base HDPEs show a very dissimilar behavior, according to their different molecular weights. More specifically, the plot for LMW has a semicircular shape, indicating the complete relaxation of the macromolecules of this sample in the tested time interval. In contrast, the high molecular weight of the HMW macromolecules involves the obtainment of longer relaxation times compared to LMW, and the polymer is not able to fully relax in the same time domain. Once again, it can be observed that the behavior of the blends is intermediate between those of the two matrices. In all cases, the curves are smooth and do not show deviations from the full arc shape, indicating the presence of a unique relaxation mechanism. This result indicates the achievement of a uniform and homogeneous morphology in the molten state for all the explored HMW/LMW compositions. As already inferred from the analysis of the complex viscosity curves, the presence of HMW strongly influences the relaxation dynamics of the blends; in fact, the blend containing the lowest amount of HMW (i.e., 30 wt%) also shows a significantly higher relaxation time compared to LMW.

In addition, the same considerations can be referred to the Cole-Cole plots of the materials obtained with the other processing parameters combinations (see Figure 42 and Figure 43). This confirms that, in all cases investigated, the HMW and LMW achieved homogeneous and uniform morphology in the molten state.

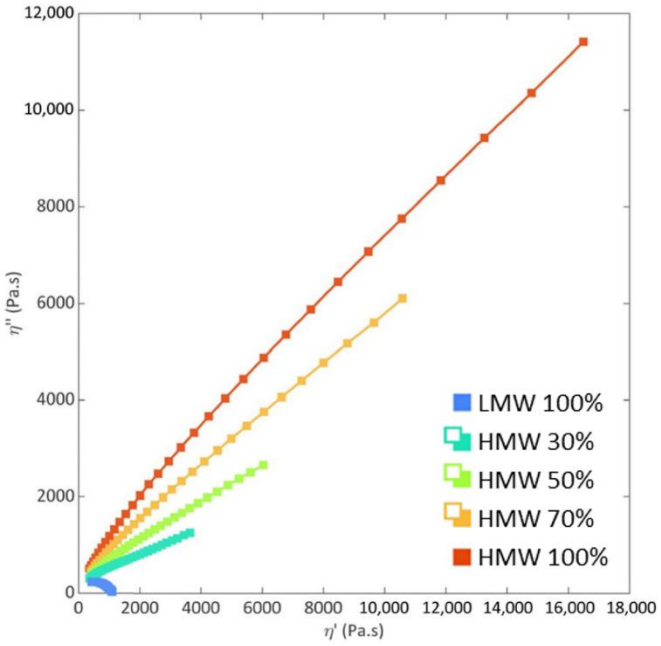


**Figure 41. Cole–Cole plot for HMW (high molecular weight), LMW (low molecular weight) and blends, compounded at 190 ˚C, 400 rpm, and tested at 175 ˚C [406]. Reprinted under CC BY 4.0 license.**

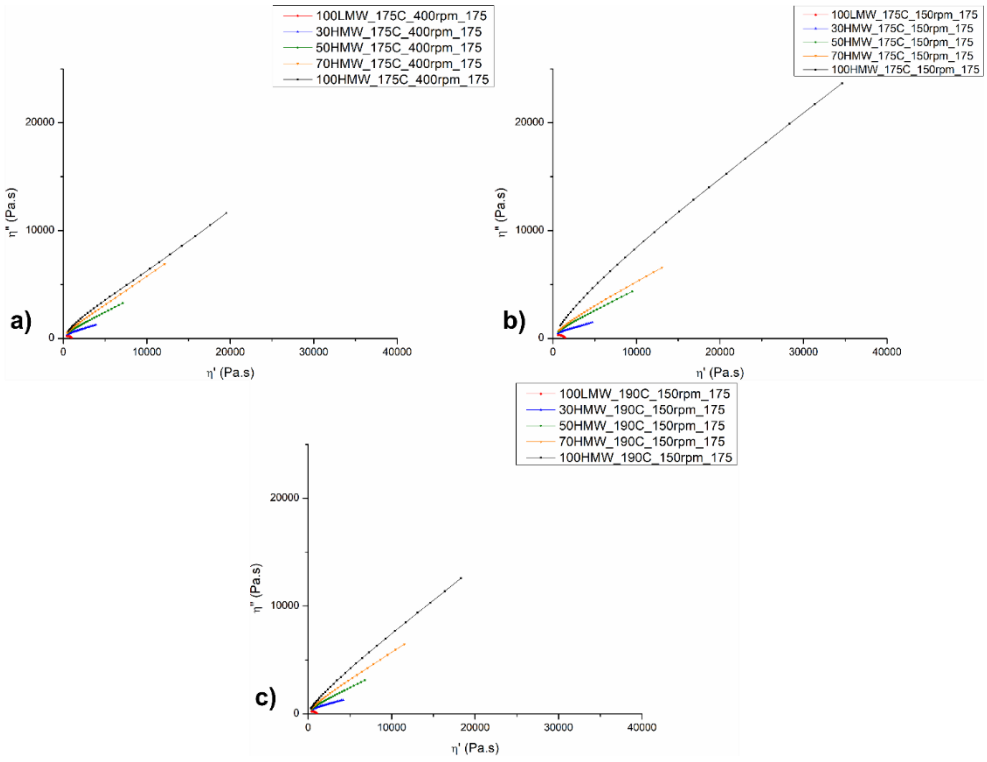


**Figure 42. Cole-Cole plots for the materials analyzed at 175 °C [406]. Reprinted under CC BY 4.0 license.**

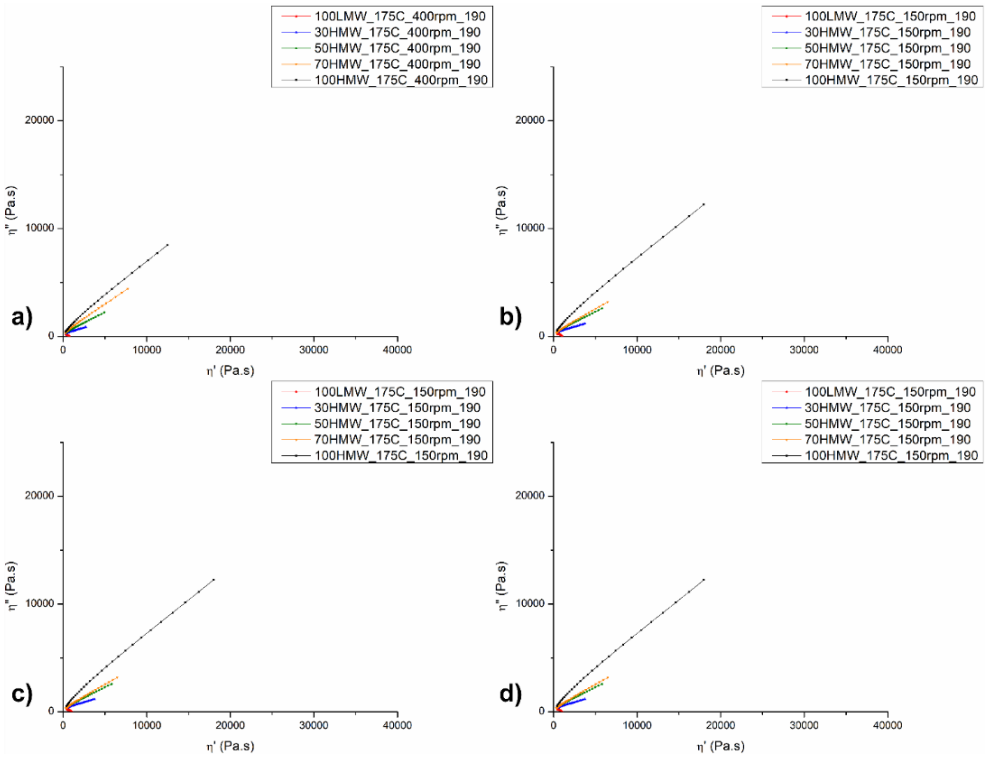


**Figure 43. Cole-Cole plots for the materials analyzed at 190 °C [406]. Reprinted under CC BY 4.0 license.**

Finally, the effects of the other three parameters (screw rotation speed, processing temperature and analysis temperature) were investigated. Figure 44 presents the comparison of the complex viscosity curves for the blends compounded at different screw speeds, maintaining a constant processing temperature and analysis temperature, while the graphs reporting the comparison of the other parameters are reported in Figure 45 and Figure 46. Firstly, from a general point of view, when considering the materials that were compounded under the same screw speed and processing temperature conditions, an amplification of the non-Newtonian behavior (i.e., a decrease in the Newtonian behavior and intensification of the shear thinning) from increasing the content of HMW can be observed. However, some differences emerge for the behavior of the 70HMW and 50HMW blends processed at 150 rpm and analyzed at 175 °C: both systems show a more pronounced shear thinning when compounded at 190 °C.

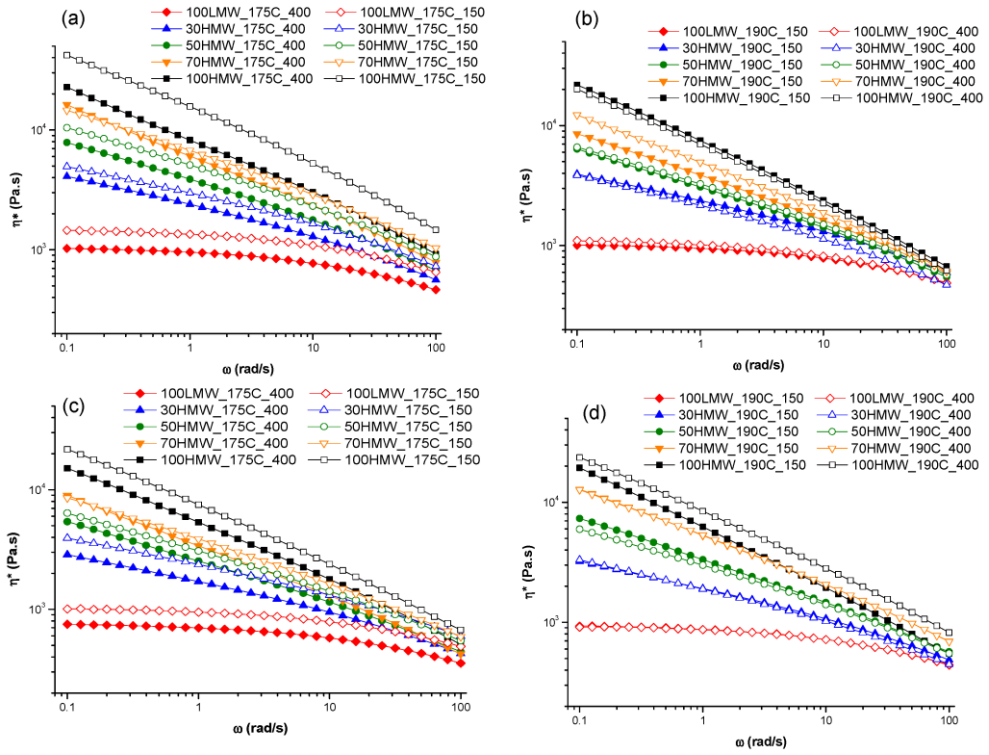


**Figure 44. Comparison of the complex viscosity curves depending on the variation in the screw rotation speed, with a constant processing temperature and analysis temperature. (a) Processing temperature = 175 °C and analysis temperature = 175 °C; (b) processing temperature = 190 °C and analysis temperature = 175 °C; (c) processing temperature = 175 °C and analysis temperature = 190 °C; (d) processing temperature = 190 °C and analysis temperature = 190 °C [406]. Reprinted under CC BY 4.0 license.**

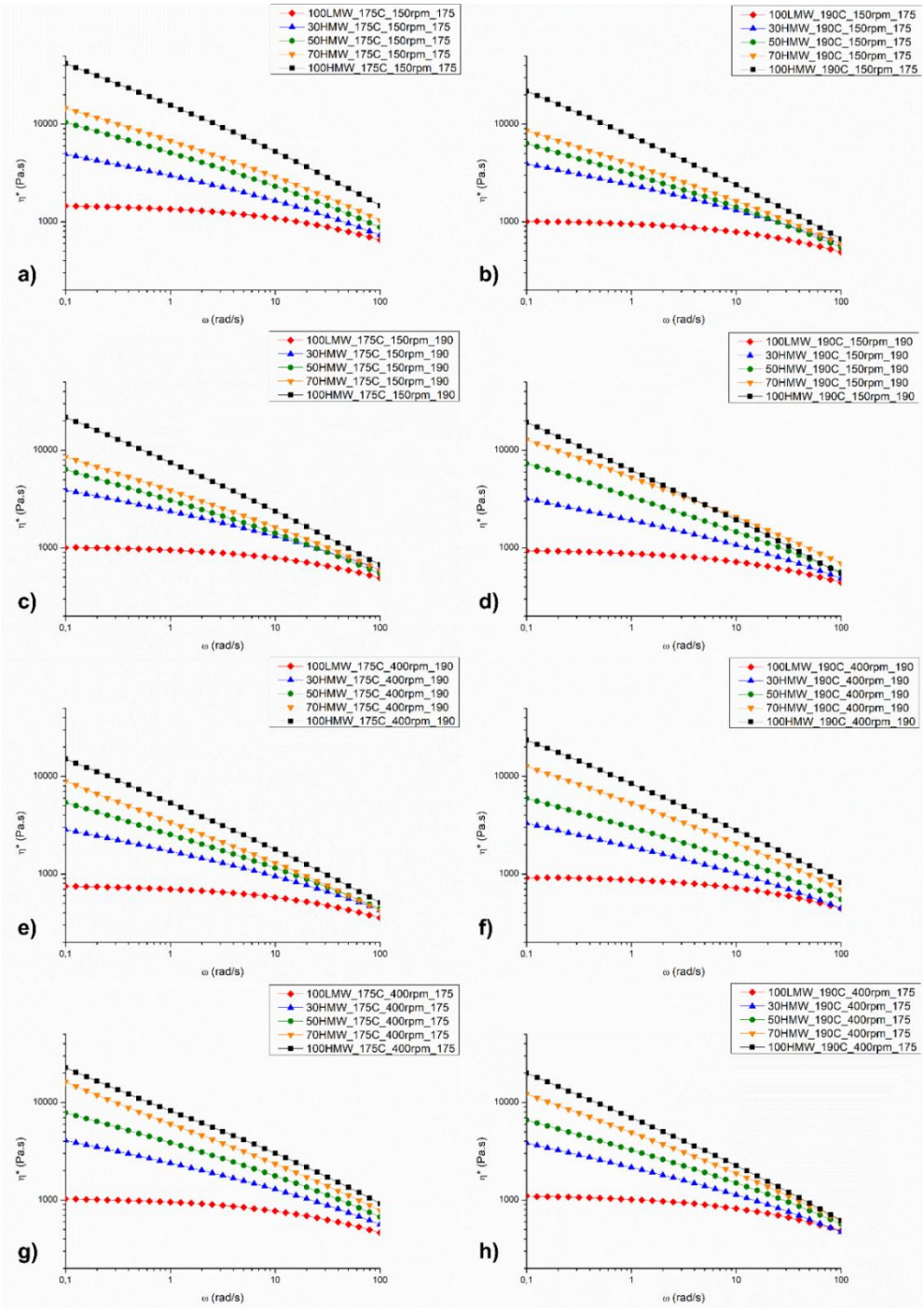


**Figure 45. Comparison of the complex viscosity curves for the materials having different HMW content [406]. Reprinted under CC BY 4.0 license.**

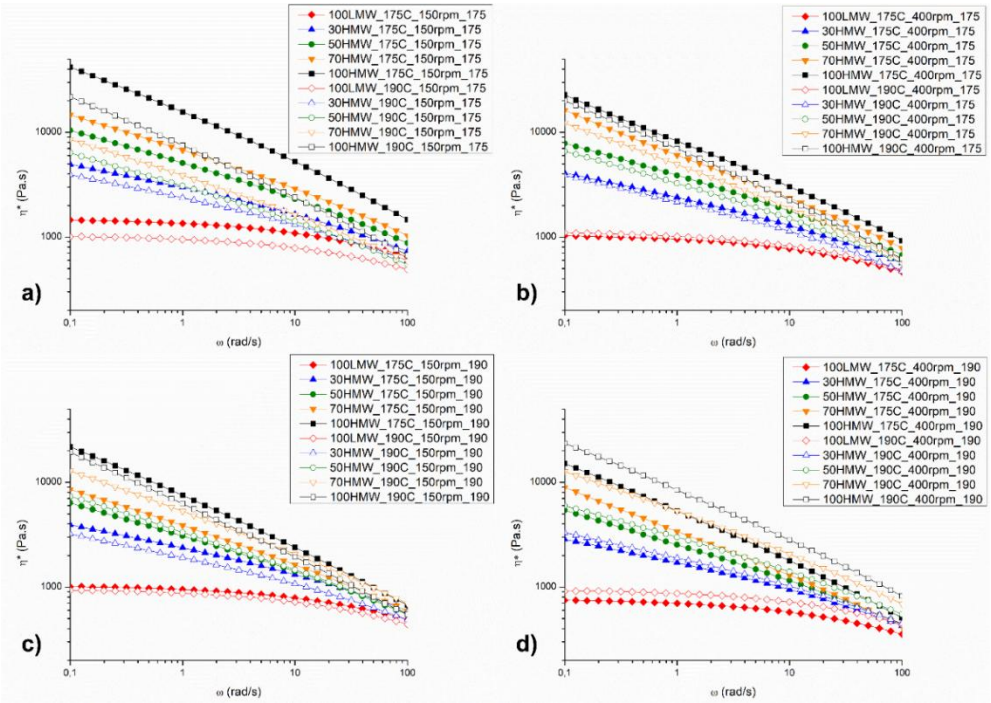


**Figure 46. Comparison of the complex viscosity curves depending on the variation of the processing temperature [406]. Reprinted under CC BY 4.0 license.**

As far as the screw rotation speed is concerned (Figure 44), the effect of this parameter is almost negligible for the blends processed at 175 °C. In contrast, for the systems compounded at 190 °C, higher values of the complex viscosity were obtained at a low screw speed.

Additionally, the processing temperature seems to only have an effect in a few cases. More specifically, for the blend compounded at 150 rpm and analyzed at 175 °C, the blends compounded at a processing temperature of 175 °C showed a higher viscosity than the one compounded at 190 °C. Also, HMW and 70HMW compounded at 400 rpm and analyzed at 190 °C showed a higher viscosity when compounded at 190 °C. The same was the case for the 70HMW compounded at 150 rpm and analyzed at 190 °C.

## 3.3.2 PCA analysis

To investigate the effects of the processing parameters on the rheological behavior of the blends more deeply, the results from the rheological characterization were analyzed using PCA. As a first step, PCA requires the selection of the number of PCs to be modeled [445] or, in other words, to define the dimension of the model. In our case, the selection was made on the basis of the variance that is explained by each component, but also considering the information that is displayed by each component. Some clear trends were found in PC1, while the information related to PC2 and PC3 (the next PCs of interest) were deemed too weak to be interpreted clearly. Furthermore, PC1 describes 99.56% of the total variance, leaving PC2 (0.43%) and PC3 (0.01%) with just the crumbs. So, only the

information that is described by PC1 was inspected and will be commented on in the following. The information about the polymer concentrations was used to color the PCA scores that are depicted in Figure 47b. Additionally, Figure 47a presents the viscosity curves for all the samples obtained with different compositions (0, 30, 50, 70, and 100 wt% of HMW), extrusion temperatures (175 or 190 °C), screw rotation speeds (150 or 400 rpm) and testing temperatures (175 or 190 °C). It is important to highlight that, for the curves presented in Figure 47a, each color refers to the samples containing the same amount of HMW (irrespectively of the other considered parameters).

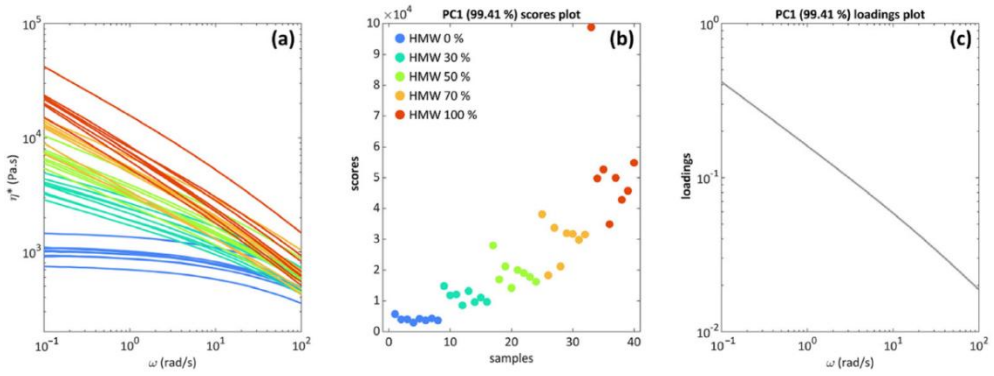


**Figure 47. (a) Viscosity curves (raw data), colored according to polymer concentrations; (b) PCA (Principal Component Analysis) score plot of PC1, colored according to polymer concentrations ("samples" refers to all blends compounded in different conditions); (c) PCA (Principal Component Analysis) loadings of PC1 [406]. Reprinted under CC BY 4.0 license.**

The most significant results are related to the blend concentration, and this can be clearly seen in the case of PC1, presented in Figure 47b. As the percentage of HMW increases, the differences between the blends become larger, along with the internal variability of each blend: the pure LMW (0% HMW) samples appear to be much more similar to each other than the 70% and 100% HMW blends. This difference can be noticed because with an increasing concentration of HMW, the blends become much more vertically scattered in Figure 47b: the experiments become "less reproducible", so the factors that were varied in the DoE scheme have an enhanced influence on the blend's properties, as will be discussed below.

The interpretation of the differences between the blends is carried out by inspecting the loading plot in Figure 47c. All the experiments consisted of a curve with decreasing values of complex viscosity as the frequency increases, which is expected considering the pseudo-plastic rheological behavior of the investigated materials. The blends appear to be mostly distinguished in the low-frequency region, which is a confirmation of the fact that the value of the zero-shear viscosity and the low-frequency behavior are crucial in determining the blends' properties. The fact that only one Principal Component is able to describe basically all the information that is present in the data (over 99.4% of the total variance) confirms that also from a multivariate and holistic point of view, the curves under examination follow the same viscosity changes that are described by the loadings of Figure 47c. It is very important to consider that this approach (PCA modeling of

the data) did not require postulating an a priori model, so what is described in Figure 47 is the actual information that is contained in the data, but represented in a clearer way, especially regarding the within-blend variability (Figure 47b). Therefore, PCA and similar multivariate approaches, based on mathematical decomposition, allow us to retrieve the relative and absolute measurements of the differences between samples directly from the data.

The distribution depicted in Figure 47b relating to the HMW content is in accordance with the expected behavior of the viscosity when considering polymers with different MWs [415]. Moreover, the fact that the viscosities of the blends are always located between the one of LMW and that of HMW and progressively increase with the HMW content is further proof of the miscibility of the two HDPEs [462].

### 3.3.3 DSC characterization

Multilinear regression was applied to model the DoE experimental results, in which the displacement ($\Delta H_{Gap}$) between the experimental ($\Delta H_{Exper}$) and the calculated ($\Delta H_{calc}$) melting enthalpy was determined for each performed experiment and thus used as the response variable y. According to the postulated model described in Eq. 3.3, three linear terms (one for each factor), three interaction terms and one quadratic term were included. The resulting coefficients are visually depicted in Figure 48a, together with their confidence interval and significance. Only two terms resulted in relevant (based on the coefficient's value) and significant (please note the asterisks in Figure 48a, which correspond to different significance levels) results: the linear term of the concentration of HMW (*HMW content*) and the interaction term between the concentration and the screw rotation speed (*HMW content · rpm*). All other terms resulted in non-statistically significant results, and their relevance was also significantly reduced compared to the abovementioned interesting terms. For these reasons, only *HMW content* and *rpm* will be discussed. The experimental domain portion represented in Figure 48 corresponds to these two factors.

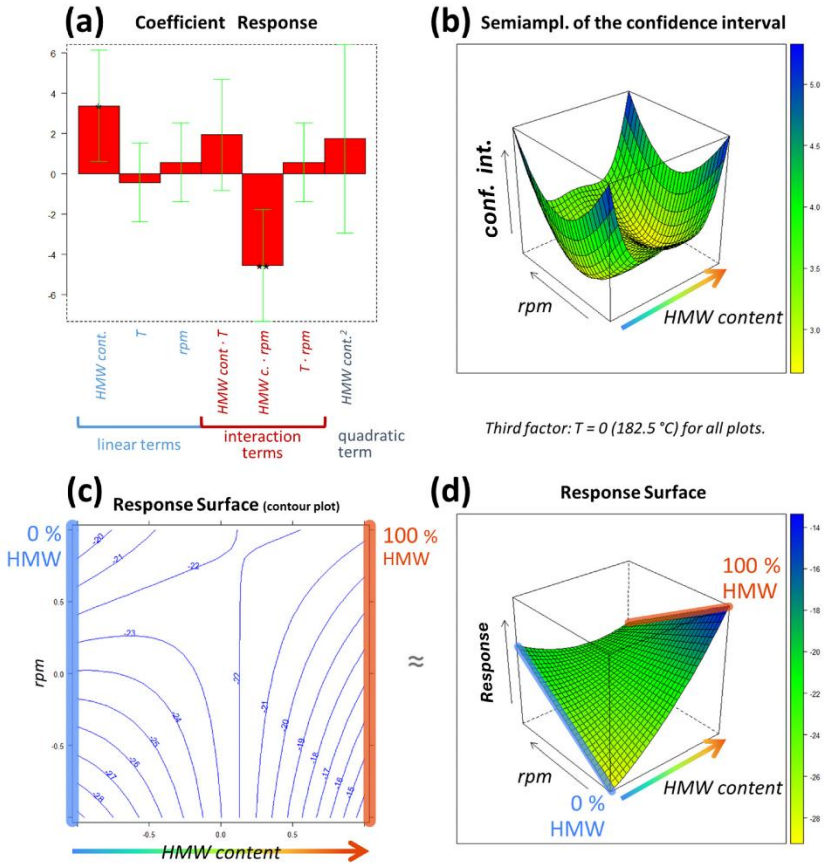


**Figure 48. The results of modeling the DoE (Design of Experiments) with MLR (multilinear regression). The experimental domain portion inspected in the figures corresponds to the only factors for which the coefficients resulted in significant results *(HMW content* and *rpm*), while the remaining one (T) was set to its central level (T = 182.5 °C). The regression coefficients are represented in (a), and the response surface is depicted in two dimensions ((c) a contour plot) and three dimensions (d). The confidence interval values corresponding to the response surface are reported in (b) [406]. Reprinted under CC BY 4.0 license.**

Starting from HMW content, the positive value of its linear term indicates that, from a general point of view, the response increases as the percentage of HMW increases (or as the content of LMW decreases). Thus, taking Eq. 3.2 into consideration, this means that, in general, the greater the quantity of HMW is, the closer the experimental enthalpy is to the calculated one. However, the interaction with *rpm* is also relevant, and this causes a distortion of the response surface across the experimental domain (Figure 48d), so the interpretation of the linear term of *HMW content* alone can be misleading.

To interpret these two effects together, an inspection of the response surface reported in Figure 48d is required. As can be observed, there are two extreme situations between which the surface develops: 0% HMW (pure LMW, in blue) on the left and 100% HMW on the right (in red). The effect of the interaction between the blends (*HMW content*) and the screw rotation speed (*rpm*) can be clearly seen at these two extremes. The maximum and minimum response values that are obtained within the experimental domain can be found at low *rpm* (level of −1 = 150 rpm), with the maximum response at 100% HMW (level of +1 of *HMW content*) and the minimum response at 0% HMW (level of −1 of *HMW content*). Thus, the lowest enthalpy is obtained for pure LMW processed at low rpm, while

the highest enthalpy is obtained for pure HMW that is melt-compounded at low rpm. Moving to higher *rpm* values, the situation becomes practically unrelated to the content of HMW, since the response values that are obtained at the two *HMW content* extremes (0% and 100%) are essentially the same, especially considering the associated error. This effect can be more clearly observed in Figure 48c: by moving horizontally along the top part of the contour plot, the response does not vary significantly, from about −20 to about −21. Considering that the minimum error associated to the response surface values is about ±2.6 (bottom part of the color bar of Figure 48b), the difference between these two values is not significant, so they can be considered virtually equal. The visual description of the error (i.e., the confidence intervals) is provided in Figure 48b, whose dimensions correspond to the response surface of Figure 48d and the contour plot of Figure 48c: they must be interpreted jointly, as they both describe two quantities within the same portion of the experimental domain. For instance, an error of about ±5.4 is associated with both the minimum and maximum response values, which are, respectively, −29 ± 5.4 and −14 ± 5.4. This difference appears to be significant. In between the two extreme percentages (the two pure polymers) are the blends. The response surface in Figure 48d (which is the graphical representation of the MLR mathematical function) allows us to have an estimate of the response also in relation to blends that were not tested experimentally.

Furthermore, DSC is a well-known indirect technique to evaluate the miscibility of blends, although there is a lack of research on HDPE/HDPE blends when considering the effect of the processing parameters [414]. In this context, Bai et al. [415] investigated the miscibility of two HDPEs with different MWs through DSC, demonstrating the presence of a single melting peak for all the blends, along with a decrease in the melting temperature with the increase in the HMW content. Also, it was observed that the crystallinity of the materials followed a linear additivity rule. In the present study, either the thermograms that were collected during the first (Figure 49) or the second (Figure 50) heating scan show the presence of a single endothermic peak, associable with melting phenomena.

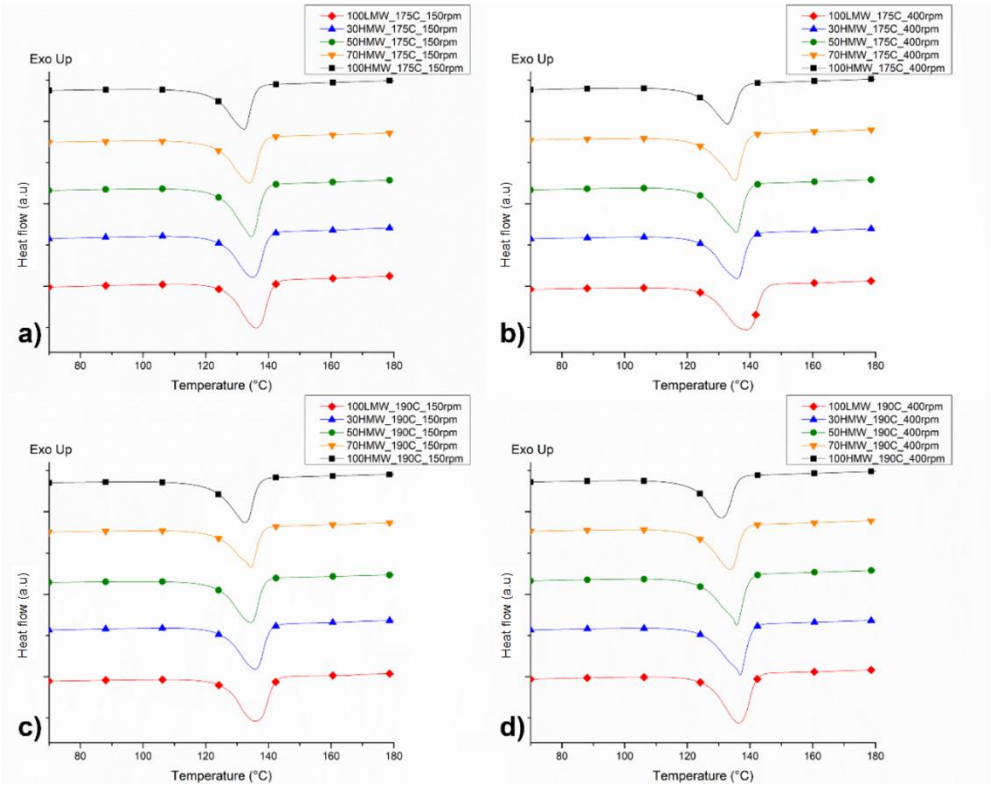


**Figure 49. Thermograms recorded during the first heating scans [406]. Reprinted under CC BY 4.0 license.**

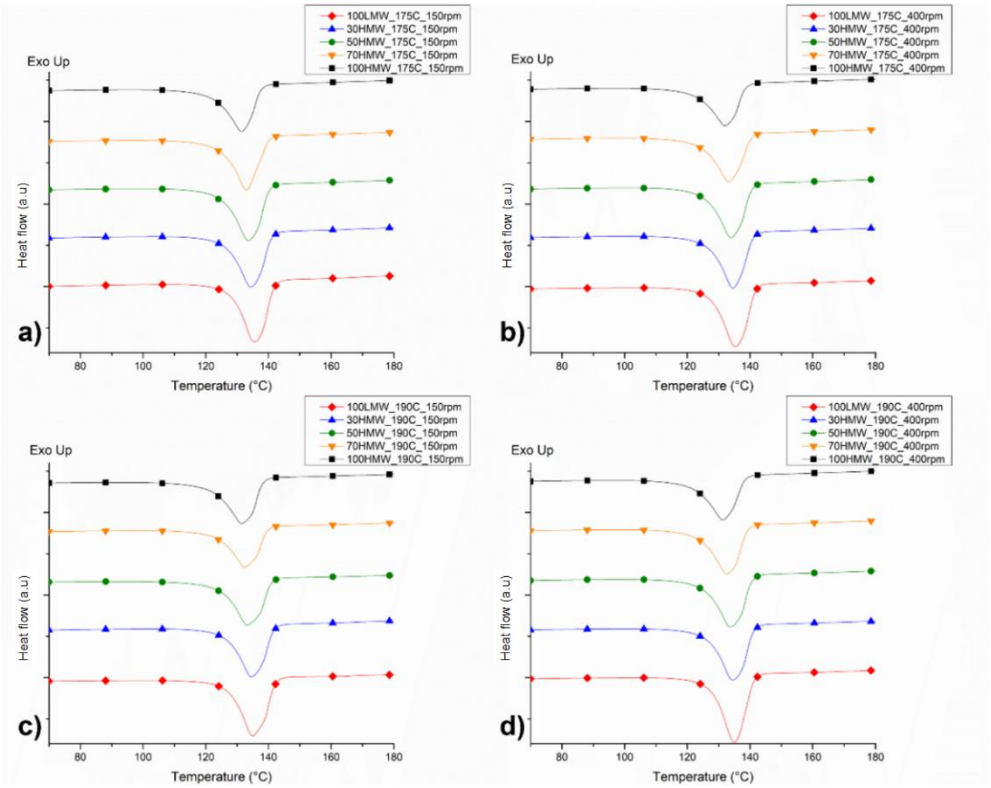


**Figure 50. Thermograms recorded during the second heating scans [406]. Reprinted under CC BY 4.0 license.**

Additionally, important considerations are addressed regarding the second heating cycle. As is observable in Figure 51a, all the blends that were processed with the different combinations of processing parameters exhibit a decreasing trend of the melting temperature as a function of the HMW content, although the linear additivity rule applies exclusively for the materials processed at 175 °C and 150 rpm ($R^2$ = 0.996). A similar behavior was noticed as far as the crystallinity of the materials is concerned. In fact, looking at the data reported in Figure 51b, the values of the crystallinity degree for the blends are intermediate (apart from 50HMW_175C_150 and 70HMW_190C_150) between those of the two starting HDPEs. Furthermore, the crystallinities of the systems processed at 190 °C and 400 rpm follow a linear additivity rule ($R^2$ = 0.995), suggesting the achievement of a fully miscible blend [415]. This result can be explained when considering that the higher processing temperature, causing a decrease in the polymer viscosity, induces a more effective disentanglement of the polymer chains, promoting the achievement of a miscible blend.

Furthermore, from a practical point of view, this refers to the possibility of tuning the crystallinity of the blends by selecting a specific HMW content and proper processing conditions [417].

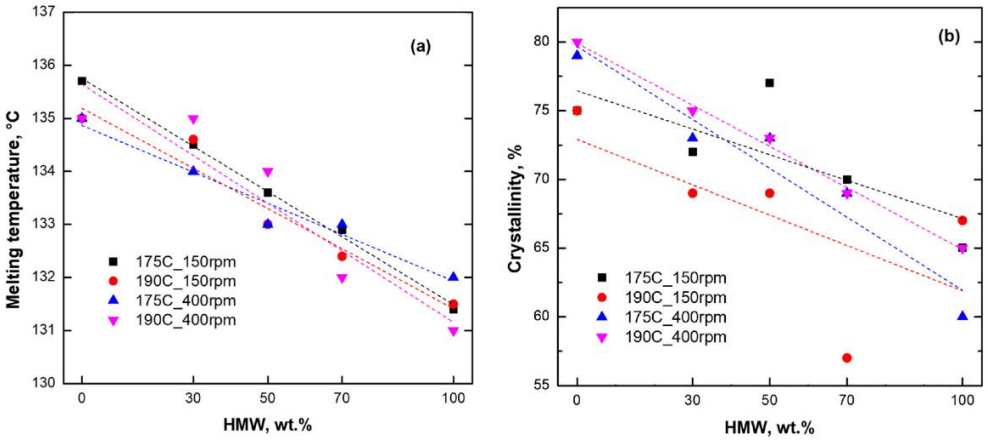


**Figure 51. (a) Melting temperature and (b) crystallinity degree for all investigated materials as a function of HMW (high molecular weight) content. Dashed lines refer to trend of linear additivity rule [406]. Reprinted under CC BY 4.0 license.**

## 3.4 Concluding remarks

The present study aimed at deepening our knowledge of the effect of the processing parameters (relative concentration, processing temperature, compounding screw speed) on the rheological and thermal behavior, as well as on the crystallinity, of homopolymer blends that were obtained through the melt compounding of two HDPEs with different molecular weights. The blends were processed according to a DoE approach, considering two levels of processing temperature and screw rotation speed and five levels of composition of the polymer blend. Then, the obtained materials were characterized using DSC and rheological measurements. The results of the thermal analysis were investigated by using the response surfaces of the MLR model, in which the displacement of the experimental melting enthalpy from the calculated one was used as the response variable. In this study, two factors were influential: the reciprocal matrix concentration and the screw speed. Furthermore, the DSC characterization indicated that high shear stresses and high processing temperatures promote the achievement of fully miscible materials. Additionally, the rheological behavior was investigated using PCA, a multivariate approach. In this case, the HMW composition was also found to be the most impacting parameter. Nevertheless, with a higher HMW content, an increase in the data dispersion in the score spaces was observed, indicating that the results are also affected by the processing temperature and the screw speed, whose effect, however, cannot be detected in the score plot. Overall, the proposed approach demonstrated that the multivariate analysis allowed us to achieve useful information about the processing/microstructure relationships in polymer-based blends, opening up new perspectives towards the application of this strategy in the study of the effect of the processing conditions on the final morphology of polymer-based complex systems, such as blended nanocomposites or hierarchically structured materials.

# Chapter 4

# Compounding of PA6 homopolymer blends

*Part of the work described in the Chapter 4 has been previously published in:*

*"Cravero, F.; Arrigo, R.; Frache, A. Processing/Microstructure Relationships in Melt Compounded Polyamide 6 with Different Molecular Weights: Effect of Screw Speed and Viscosity Ratio. Polym. Eng. Sci.* ***2025****, 65, 2525–2538, doi:10.1002/pen.27165"* [163]

## Abstract

In the present Chapter, the relationships between the processing parameters and the microstructure in melt-compounded PA6 are investigated. To this aim, two PA6 having different viscosities are processed in a twin-screw extruder at two different screw speeds (150 or 300 rpm) and characterized through rheological and thermal analyses. Furthermore, the thermomechanical field along the screw is simulated using Ludovic® software, and the obtained results in terms of shear rate, residence time, and actual temperature are exploited to disclose interesting processing/microstructure relationships. In particular, the antagonistic role of the flow-induced crystallization and memory effect in governing the final microstructure is assessed. Specifically, for high screw speed and viscosity, FIC outweighs the memory effect due to the higher shear rate and temperature experienced by the material during processing. Besides, the dominant influence of FIC over the memory effect is found to be responsible for the higher overall crystallinity and α/γ content observed for the materials processed at 300 rpm. Finally, the same analyses are performed on blends containing different relative contents of the two PA6, demonstrating the interdependency of the screw speed and viscosity effects on the resulting microstructure.

## 4.1 Introduction

Aliphatic polyamides are key engineering polymers in fields such as automotive, aerospace, sports equipment and healthcare due to their valuable thermo-mechanical performance [463–468]. However, despite extensive research and application, the influence of processing parameters on the resulting microstructure remains poorly understood. This is due to the fact that several complex phenomena occur simultaneously during solidification, determining the final microstructure. These phenomena are influenced by the thermo-mechanical field experienced by the material during melt processing [463,464].

First, the presence of the intermolecular H-bonding between the amide groups of the chains causes the so-called memory effect, whereby the macromolecular organization of the solid state is partially retained upon melting [164,463,464,469–475]. Although the interaction weakens with increasing temperature, the hydrogen bonds are in a dynamic, temperature-dependent equilibrium in the molten state, meaning they are statistically bonded and broken at every instant. Thus, a constant average number of free amide groups is maintained, and the complete breakage of the intermolecular bonds requires specific conditions [464,470,476,477]. It is important to note that the presence of entanglement has also been found to play a significant role in promoting the memory effect [478]. Additionally, hydrogen bonds in molten PAs cooperate to achieve shear-induced crystallization, which is a multi-order coupling process determined by the flow of the molten material [110,464,469,479]. The final morphology is the result of the competition between chain relaxation and crystallization kinetics, and even hierarchical crystalline structures may be formed. This non-equilibrium phase transition depends on intrachain conformation, interchain orientation, and density fluctuations in the melt [110,480,481]. Theories such as the "flow-induced coil-helix transition" [482], the "conformation-density coupling for phase separation" [483], “isotropic-nematic transition” [484,485], and the “entropic reduction-energy change model” [116] have been used to describe the evolution of the system by coupling the two phenomena. However, due to the lack of description of the thermodynamically determined intermediate morphologies induced by the flow, none of these theories is exhaustive in modeling the final microstructure [110].

Besides, when both FIC and memory effect were present, their interplay appeared to determine the resulting macromolecular arrangement, with hydrogen bonding responsible for the formation of ordered clusters and flow determining the size distribution [486–488]. Consequently, the influence of the thermo-mechanical field applied during processing on the resulting microstructure of PAs is evident.

Finally, polyamides are polymorphic materials [164,463,469,471,489–491]. In PA6, the two most common crystalline phases are the monoclinic α and γ, which differ in the rotation angle of the amide groups involved in the intermolecular hydrogen bonding. As a result, the melting temperatures differ, corresponding to 223 °C for α and 215 °C for γ [464,489,492–496]. In fact, the poor knowledge of the dynamics involving hydrogen bonds is the main reason for the limited understanding of the relationships between processing parameters and the

microstructure of polyamides. This results in poor control over the tunability of the final properties [164–167].

Studies have investigated the effect of thermal or mechanical fields on the memory effect, FIC, and polymorphism. However, these phenomena have been considered separately, and the effect of thermo-mechanical fields on melt-processed PAs remains unclear [469,472,476,490,493]. The impact of temperature and cooling rates on crystallization is typically evaluated by DSC [489,492–494,497], and the effect of shear is monitored through isothermal rheological tests [479,498]. On the other hand, research is now focusing on real processing equipment to consider actual manufacturing conditions. For instance, Skorupska et al. [499,500] found that increasing the extrusion pressure during cold hydrostatic extrusion of PA6 promoted chain orientation and increased the α crystalline phase content. The enhancement in tensile strength was also appreciated, in accordance with the expectations of increasing the α over γ crystalline phase ratio [471,501–503].

Additionally, the final morphology depends on the macromolecular properties of the material. For instance, crystallinity is affected by MW and its distribution. To overcome limitations and achieve high crystallinity contents, ad hoc chains are usually synthesized [504,505]. A more flexible and scalable alternative is melt blending polymers with different molecular weights and MW distributions, which allows for microstructure tailoring. However, this approach has not been extensively investigated for polyamides, for which existing studies typically examine the impact of copolymers in blends [406,504,506–509].

For the aforementioned reasons, this study investigated the relationship between processing conditions and the resulting microstructure of twin-screw extrusion melt-compounded commercial PA6s with two different MW, and consequently, viscosities, in order to replicate a monomodal or bimodal molecular weight distribution. The two materials were evaluated separately or blended in weight ratios of 30:70, 50:50, or 70:30 of high to low MW. Ludovic ® software was used to simulate the thermo-mechanical fields during compounding with the different combination of processing conditions. In particular, key process parameters such as the actual temperature, shear rate, and residence time, were modeled. This detailed information enabled a more accurate interpretation of the results in terms of how the actual processing conditions influenced hydrogen bonding and entanglement density in the polymer melt during compounding. Consequently, the use of Ludovic® allowed a deeper understanding of the mechanisms of competition between FIC and the memory effect in determining the final microstructure.

It is important to note that, although Ludovic® has already been used in the literature to simulate compounding processes, this study represents a novelty because it exploits the software to investigate the relationship between the actual process parameter values and the microstructure. In particular, the tailoring of polymorphism through compounding is a topic that has not yet been explored in the PA6 literature, and this study has highlighted the role of the actual values of the process parameters in balancing the FIC and memory effect and consequently determining the microstructure.

## 4.2 Ludovic® simulations

This software uses a localized, one-dimensional modeling approach to simulate melt flow along the axis of a co-rotating, intermeshing twin-screw extruder under steady-state conditions. Besides, it is particularly adequate for applications like the present one, in which the focus is on studying the thermo-mechanical field inside the barrel of a twin-screw extruder. The inputs required to run the simulations are numerous but easily accessible and include the screw profiles (see Figure 98 and Table 15), set temperature profile, feed rate, screw speed, and the thermal and rheological properties of the materials. Key process parameters were determined through these simulations. Specifically, shear rate, actual temperature, and residence time [168,510–514].

In the study, the screw speed and HV to LV weight content ratio were selected as the primary variable factors, while the set temperature profile and feed rate were held constant. The values considered for each parameter are summarized in Table 5. It is worth noting that the temperature profile adopted for the compounding of the PA6-based systems was defined by considering both the values reported in the literature for twin-screw extrusion [515–518] and the specific characteristics of the experimental equipment. In particular, the torque limit of the extruder used and the viscosities of the polymer matrices were taken into account to ensure stable processing conditions.

To facilitate identification, each sample was labeled according to its composition and processing conditions. For instance, the designation “30HV_150rpm” indicates a blend that contains 30 wt% HV and was processed at a screw speed of 150 rpm.

**Table 5. Variables and constant factors used in the Ludovic® simulations.**

| | Factor | Levels | | | | |
|---|---|---|---|---|---|---|
| Variables | Screw speed [rpm] | 150 | | | 300 | |
| | MW distribution | Monomodal | | | Bimodal | |
| | HV:LV content [wt% of HV] | 0 | 30 | 50 | 70 | 100 |
| Constants | Feed rate [g/h] | 290 | | | | |
| | Temperature [°C] - from hopper to die | 220\220\225\230\230\230\230\230 | | | | |

First, the shear rate and residence time were examined. As can be appreciated in Figure 52, no variation related to the MW or MW distribution was observed for either parameter. Consequently, the reported curves are representative of all the material processed at the corresponding screw rate. Specifically, the shear rate

shows a distinctive trend, exhibiting maximums in correspondence with the kneading zones and minimums in the conveying sections. The corresponding values are 76 and 40 $s^{-1}$ at 150 rpm, and 152 and 80 $s^{-1}$ at 300 rpm. Therefore, the role of screw elements and screw speed in determining the final shear rate was emphasized. Similar considerations can be applied to the residence time. A reduction of approximately 25% in the Total Residence Time (TRT), defined as the period during which the material moves from the hopper to the die, has been observed when comparing the results of the simulations relative to the processing performed at 300 or 150 rpm (Figure 52). In addition, a clear distinction emerges in comparing the Local Residence Time (LRT) values reported in Table 6, highlighting the impact of screw geometry on the residence time. Furthermore, the impact of the geometry of the screw element clearly emerges from the comparison of the Local Residence Time (LRT) values reported in Table 6 (see Section A.2.1 for the screw element code). In fact, when considering the time spent by the material in each screw section separately, it was appreciated that the decrease in the TRT is due to the lower LRT in the conveying sections when the higher screw speed is considered, while no role is attributed to the kneading zones. Consequently, the simulations demonstrated that MW and MW distribution do not significantly influence the final residence time.

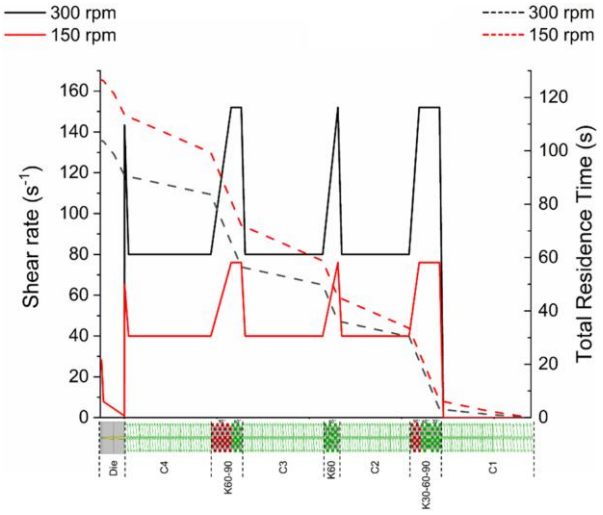


**Figure 52. Shear rate and TRT along the screw profile [163]. Reprinted under CC BY 4.0 license.**

**Table 6. LRT and TRT calculated for the compounding performed at 150 and 300 rpm.**

| Screw element | LRT [s] | |
|---|---|---|
| | 150 rpm | 300 rpm |
| C1 | 6.35 | 3.17 |
| K30-60-90 | 27.18 | 27.18 |
| C2 | 11.66 | 5.84 |
| K60 | 13.00 | 13.00 |
| C3 | 14.10 | 7.40 |
| K60-90 | 27.18 | 27.18 |
| C4 | 13.85 | 6.98 |
| TRT [s] | 126 | 104 |

Different considerations emerged from the investigation of the actual temperature along the screw profile. In fact, Figure 53 shows that temperature peaks occurred in correspondence with the kneading elements, and that higher values were associated with increased stagger angles. This indicates intensified shear and viscous dissipation. In all cases, the highest temperature was found at the end of the K60-90 section (see Table 15 for the coding details). In contrast, a consistent decrease in the actual temperature was recorded in the conveying zones. Besides, the temperatures at 300 rpm were consistently higher than those at 150 rpm for a specific formulation and the further enhancing of the HV content at a constant screw speed led to an increase in the actual parameter.

These results emphasized the significant influence of the screw configuration, screw speed, and material viscosity on the thermal profile. Specifically, an increase in either HV content or screw speed results in a more pronounced temperature increment along the screw profile. Table 7 shows the minimum and maximum temperatures for each screw section at 150 and 300 rpm for all materials.

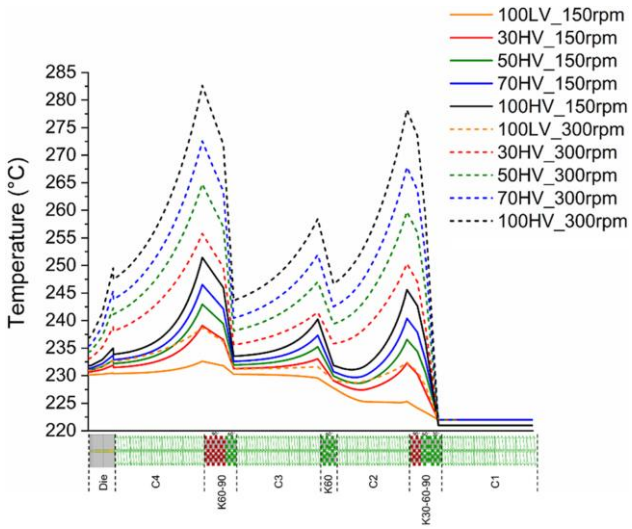


**Figure 53. Actual temperature profiles along the screw for the different samples [163]. Reprinted under CC BY 4.0 license.**

**Table 7. Maximum and minimum actual temperature in each screw element for a screw speed of 150 or 300 rpm.**

| Screw element | 150 rpm | | | | | | | | | |
|---|---|---|---|---|---|---|---|---|---|---|
| | 100HV_150 rpm | | 70HV_150rpm | | 50HV_150rpm | | 30HV_150rpm | | 100LV_150rpm | |
| | [°C] | [°C] | [°C] | [°C] | [°C] | [°C] | [°C] | [°C] | [°C] | [°C] |
| C1 | 221 | 221 | 222 | 222 | 222 | 222 | 222 | 222 | 222 | 222 |
| K30-60-90 | 221 | 246 | 222 | 240 | 222 | 237 | 222 | 232 | 222 | 225 |
| C2 | 246 | 231 | 240 | 230 | 237 | 229 | 232 | 227 | 225 | 225 |
| K60 | 232 | 240 | 231 | 237 | 230 | 235 | 229 | 233 | 228 | 230 |
| C3 | 240 | 234 | 237 | 233 | 235 | 232 | 233 | 231 | 230 | 230 |
| K60-90 | 234 | 251 | 233 | 247 | 232 | 243 | 231 | 239 | 230 | 233 |
| C4 | 251 | 234 | 247 | 233 | 243 | 232 | 239 | 231 | 233 | 230 |
| | 300rpm | | | | | | | | | |
| Screw element | 100HV_300 rpm | | 70HV_300 rpm | | 50HV_300 rpm | | 30HV_300 rpm | | 100LV_300rpm | |
| | [°C] | [°C] | [°C] | [°C] | [°C] | [°C] | [°C] | [°C] | [°C] | [°C] |
| C1 | 221 | 221 | 222 | 222 | 222 | 222 | 222 | 222 | 222 | 222 |
| K30-60-90 | 221 | 278 | 222 | 268 | 222 | 260 | 222 | 250 | 222 | 232 |
| C2 | 278 | 247 | 268 | 243 | 260 | 239 | 250 | 236 | 232 | 229 |
| K60 | 247 | 258 | 243 | 252 | 239 | 247 | 236 | 241 | 229 | 232 |
| C3 | 258 | 244 | 252 | 241 | 247 | 238 | 241 | 236 | 232 | 231 |
| K60-90 | 244 | 283 | 241 | 273 | 238 | 265 | 236 | 256 | 231 | 239 |
| C4 | 283 | 247 | 273 | 244 | 265 | 241 | 256 | 238 | 239 | 233 |

# 4.3 Characterization

## 4.3.1 Rheology

As illustrated in Figure 54, the complex viscosity ($\eta^*$) of the materials varies with frequency. As expected, given the difference in molecular weight, 100HV exhibits higher $\eta^*$ values than 100LV [67,519–521]. Also, both matrices present a non-Newtonian behavior in the low-frequency region, likely due to the presence of hydrogen bonds. In fact, these interactions have been shown to restrict the complete relaxation of macromolecular chains [463,464,469,470,496,521,522]. Additionally, comparing the complex viscosities of matrices processed at 150 and 300 rpm reveals similar rheological behavior at both screw speeds. This suggests that, for neat matrices, screw speed has a negligible effect on the overall rheological response.

In the case of the blends, the complex viscosities are distributed between those of the two matrices, and the values increase with higher HV content. A slight non-Newtonian behavior is also evident at low frequencies. This phenomenon, previously discussed for neat matrices, can be attributed to the intermolecular hydrogen bonds. Besides, the effect of screw speed on the $\eta^*$ of the blends is also negligible. These findings suggest that the blend composition, particularly the HV

to LV ratio, dominates over screw speed in determining the rheological characteristics of the system.

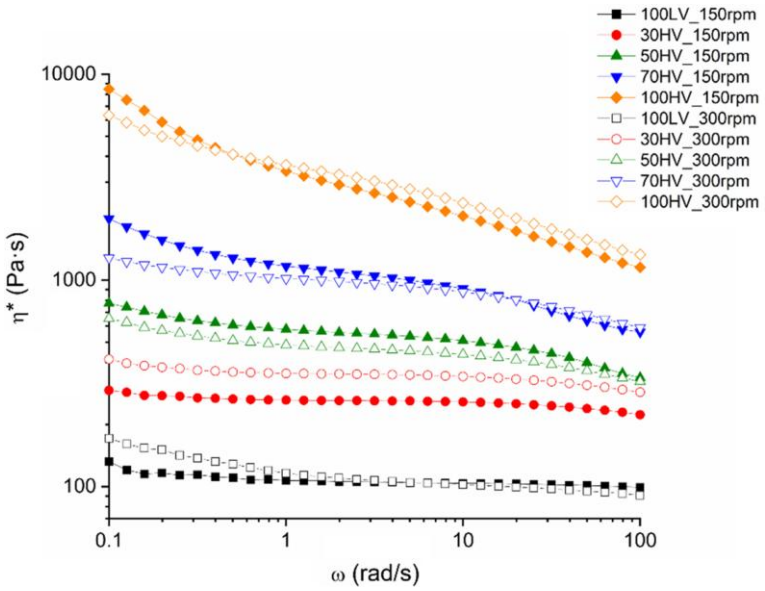


**Figure 54. Complex viscosities of the materials processed at different processing conditions [163]. Reprinted under CC BY 4.0 license.**

## 4.3.2 DSC

The thermograms presented in Figure 55A–C were obtained during the second heating scan of calorimetric analyses. The unprocessed materials (Figure 55A) exhibit a distinct melting peak at 222 °C for both LV and HV, indicative of the presence of the α crystalline phase [489]. It is also worth noting that the 100HV sample also exhibits a subtle shoulder at lower temperatures, which suggests the presence of a small amount of the γ phase [500,523]. As reported by Cavallo et al. [492], the appearance of the latter exclusively in the high molecular weight polymer can be attributed to the MW dependence of the γ phase stability in PA6. Specifically, the stability range has been shown to widen as the MW increases.
Furthermore, the thermal response of the materials changes upon processing at either 150 or 300 rpm. As demonstrated in Figure 55B and 41C, both screw speeds give rise to a multiple melting peak. Deconvolution analyses revealed two distinct thermal transitions, attributed to the γ and α crystalline phases, respectively. The corresponding melting temperatures are summarized in Table 8. A comparable melting profile was observed across all blend compositions, indicating that the compounding process consistently promotes γ phase formation. This effect appears to be largely unaffected by variations in screw speed, HV content, or molecular weight distribution. Additionally, when focusing on the cooling thermograms (see Figure 55D and 41E), a single peak emerges, regardless of the processing speed or formulation. The corresponding crystallization temperatures ($T_{cryst}$) are reported in Table 8.

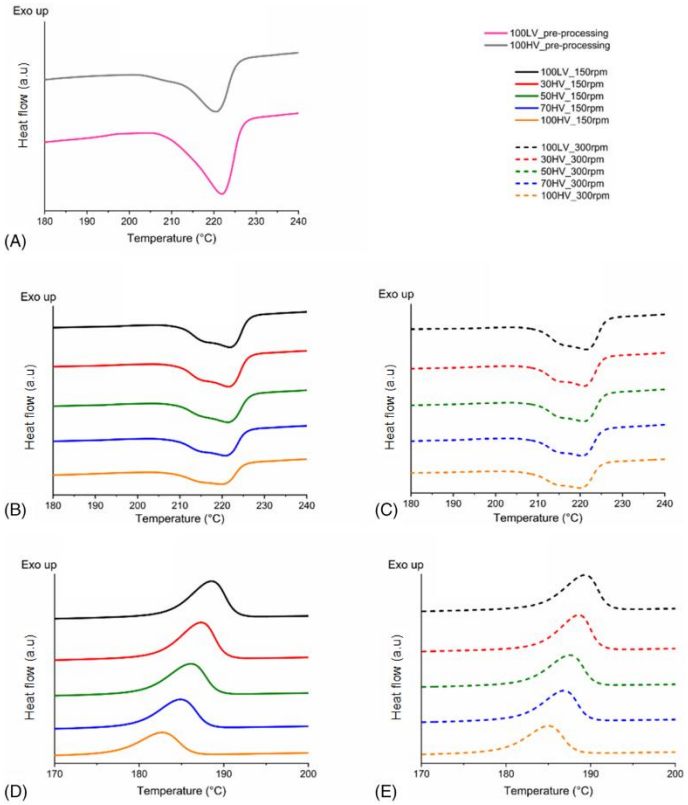


**Figure 55. Thermograms of the second heating scan of the A) pre-processing 100HV and 100LV, and the materials compounded at B) 150 or C) 300 rpm. In addition, the corresponding cooling ramps are reported for a screw speed of D) 150 and E) 300 rpm, respectively [163]. Reprinted under CC BY 4.0 license.**

**Table 8. Melting temperatures of the γ and α phases measured during the second heating scan and crystallization temperatures of the materials processed at 150 or 300 rpm [163]. Reprinted under CC BY 4.0 license.**

| Material | Melting temperature [°C] | | Crystallization temperature [°C] |
|---|---|---|---|
| | γ | α | |
| 100LV_150rpm | 215 | 222 | 189 |
| 30HV_150rpm | 215 | 222 | 187 |
| 50HV_150rpm | 215 | 221 | 186 |
| 70HV_150rpm | 215 | 221 | 185 |
| 100HV_150rpm | 214 | 220 | 183 |
| 100LV_300rpm | 215 | 221 | 189 |
| 30HV_300rpm | 215 | 221 | 189 |
| 50HV_300rpm | 215 | 221 | 188 |
| 70HV_300rpm | 214 | 220 | 187 |
| 100HV_300rpm | 214 | 220 | 185 |

As expected, the melting enthalpy ($\Delta H_m$) calculated for all the materials from the second heating ramp, decreases with increasing MW [524]. As can be seen in Figure 56A, this trend is evident for both the matrices, regardless of screw speed. However, it has also been observed that enhancing the latter parameter can increase the $\Delta H_m$ for a specific material, and the effect is more pronounced for HV than for LV.

Different behaviors emerge in the blends depending on the combination of HV content and screw speed (Figure 56A). Specifically, the resulting melting enthalpies decrease as the HV content increases when processed at 150 rpm. At the same time, the $\Delta H_m$ of the blends are higher than expected based on the linear combination of the values obtained from the matrices compounded at the same screw speed. On the other hand, when 300 rpm was used, the resulting melting enthalpies appeared independent from the HV content. In addition, when taking into account the linear combination of the values of the two matrices, the $\Delta H_m$ of the blends are lower. Additionally, further considerations can be addressed by comparing the data for the blends compounded at different screw speeds. Higher $\Delta H_m$ values were indeed recorded for materials processed at 150 rpm than at 300 rpm. However, the difference in the corresponding system values decreases as the HV content increases. Therefore, if the screw speed and MW have an independent effect on the final crystallinity content of the matrices, this feature is no longer true for the blends. The crystallinity contents of all materials, calculated from the second heating ramp for the compounded and pre-processed polymers according to Eq. A.4, are reported in Table 9.

Lastly, Figure 56B shows the crystallization temperatures. According to the literature [471,525], the $T_{cryst}$ of the matrices decreases with increasing HV content. It is worth noting that the current study revealed that this trend is also independent from the screw speed. The same behavior is observed in the blends. In fact, regardless of the screw speed, the experimental $T_{cryst}$ is consistent with the linear combination of the crystallization temperatures of the matrices, and the values are slightly higher than the calculated ones. Additionally, by comparing the ones for a single material compounded at two different screw speeds emerges that a higher $T_{cryst}$ is associated with the blend processed at 300 rpm. These findings suggest a positive correlation between the parameter and crystallization temperature independent from the HV content.

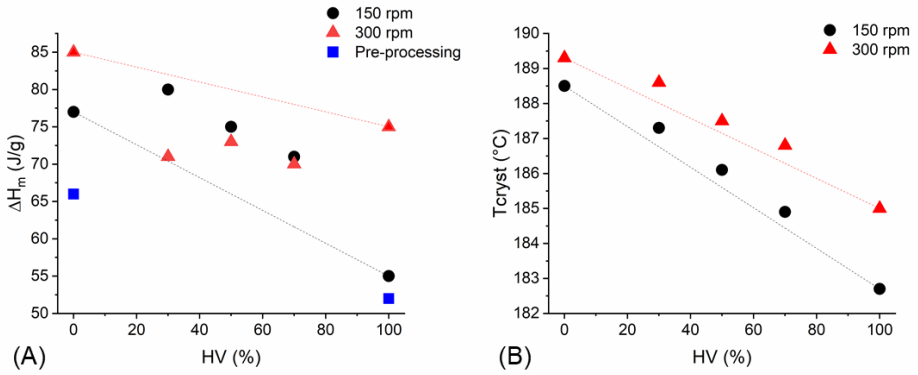


**Figure 56. A) Melting enthalpy calculated for all the materials from the second heating ramps; the linear combination of the $\Delta H_m$ of the two matrices is indicated at the two different screw speed by dotted lines. B) Crystallization temperatures of the materials processed in different conditions; the dotted lines represent the linear combination of the $T_{cryst}$ of the two matrices [163]. Reprinted under CC BY 4.0 license.**

**Table 9. Crystallinity content of the pre-processing matrices and compounded materials at 150 and 300 rpm.**

| Material | Crystallinity content [%] |
|---|---|
| 100LV_pre-processing | 29 |
| 100HV_pre-processing | 23 |
| 100LV_150rpm | 33 |
| 30HV_150rpm | 35 |
| 50HV_150rpm | 33 |
| 70HV_150rpm | 31 |
| 100HV_150rpm | 24 |
| 100LV_300rpm | 37 |
| 30HV_300rpm | 31 |
| 50HV_300rpm | 32 |
| 70HV_300rpm | 30 |
| 100HV_300rpm | 33 |

The relative content of the α and γ crystalline phases was assessed through a deconvolution procedure. As shown in Figure 57A and B, both phases are present in materials compounded at 150 or 300 rpm. Additionally, the α phase is more abundant in the matrices regardless of the screw speed, and the relative content is higher in 100LV than in 100HV.

Comparing the processed and pre-processing matrices provides additional insights. In the case of 100LV, the α phase content decreases with compounding, independently from the applied screw speed. In contrast, it remains relatively unchanged in 100HV following processing at 300 rpm, when compared to the unprocessed sample. Regarding the γ phase, its content in the pre-processed HV sample is lower than in the two processed counterparts (100HV_150rpm and 100HV_300rpm), thereby supporting earlier observations (Figure 55) that compounding enhances γ crystalline formation. A similar trend is observed in the blends (Figure 57A and B). In fact, the α phase is more abundant than the γ phase across all compositions. Additionally, as HV content increased, a general decrease in both crystalline phases was observed, indicating a reduction in the overall crystallinity.

A more detailed understanding of the interaction between processing conditions and crystalline structure is provided by analyzing the α/γ phase ratio, as reported in Figure 57C. The highest α/γ ratios for 100LV and 100HV are achieved at 300 rpm, suggesting that elevated screw speeds favor the formation of the α crystalline phase in the neat materials. However, among the blends, only 70HV exhibits a trend similar to that of the matrices, while 30HV and 50HV display higher α/γ ratios when processed at 150 rpm.

These results highlight the complex interplay between screw speed and molecular weight in determining phase distribution. The α/γ ratio does not depend exclusively on a single parameter; rather, it is determined by the interplay of processing and compositional variables. It is noteworthy that comparable α/γ ratios can be attained through various processing conditions. For instance, 30HV_150rpm, 50HV_300rpm, and 70HV_300rpm all exhibit comparable α/γ

values, despite differences in HV content and screw speed exploited for their compounding.

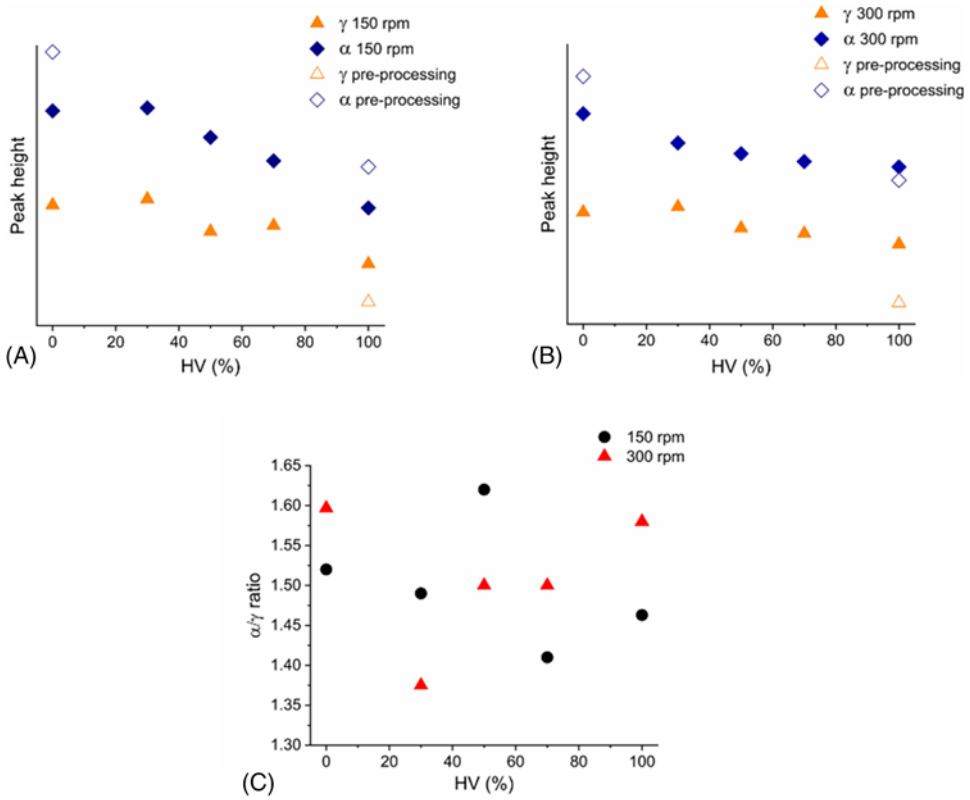


**Figure 57. Height of the α and γ peaks, obtained by deconvolution of the melting peaks detected by the second heating ramp at A) 150 or B) 300 rpm; C) α/γ height ratio of the materials compounded at the two screw speeds [163]. Reprinted under CC BY 4.0 license.**

## 4.4 Discussion

In order to understand the relationship between processing parameters and microstructure, simulations performed with Ludovic® were crucial to interpreting the results of characterization techniques. First, the simulations provided actual information on temperature, shear rate, and residence time as a function of the selected processing conditions. Second, considering the role of these parameters in primarily affecting H-bonding stability and entanglement density, the evolution of macromolecular dynamics could be evaluated more accurately. Consequently, the simulations provided further insight into the effect of the thermo-mechanical field on the final microstructure, highlighting the crucial role of the memory effect and FIC.

### 4.4.1 Matrices

A systematic investigation was conducted to evaluate the influence of screw speed and molecular weight on the thermal and structural characteristics of the materials under study. DSC analyses revealed an increase in the post-processing

melting enthalpy values, which indicates a higher degree of crystalline order within the polymer matrices. This finding was primarily attributed to the shear-induced alignment of the macromolecules occurring during the melt compounding process, a finding that is in agreement with existing literature on the subject. In particular, the flow-induced crystallization and the presence of hydrogen bonds have been shown to promote an increase in the degree of molecular ordering [110,469,479,488,526,527]. The results of numerical simulations performed using Ludovic® software (Figure 52) further confirmed the hypothesis that elevated screw speeds correspond to higher shear rates within the extrusion system, with the increase of the values from 76 and 40 $s^{-1}$ at 150 rpm to 152 and 80 $s^{-1}$ at 300 rpm, respectively. Concurrently, the DSC results showed that the values of $\Delta H_m$ of the matrices processed at 300 rpm were higher compared to those processed at 150 rpm (Figure 56A), and this is indicative of a higher crystallinity. The observed correlation between an increased shear rate and the final crystalline content is consistent with previous findings and reinforces the critical role of processing parameters in determining the thermal and structural characteristics of polymeric materials [528].

A more in-depth analysis of the effect of the compounding process on crystallinity was conducted, taking into account that different shear-induced crystallization regimes are promoted depending on the applied shear rate and the intrinsic characteristics of the polymer chains. Consequently, this results in the production of different morphologies [110,498,527,529]. The assessment of the active crystallization regime was performed by calculating two dimensionless parameters, the Weissenberg numbers, which are defined as the product of the applied shear rate and the longest relaxation time ($W_{rep}$) or the Rouse time ($W_s$), respectively [498]. A $W_{rep}$ value greater than one indicates chain orientation promoted by processing. Furthermore, a $W_s$ value that exceeds one denotes the occurrence of macromolecular stretching. Consequently, at low shear rates, where both $W_{rep}$ and $W_s$ are lower than one, the effect of shear-induced crystallization is negligible, and the final morphology resembles that of the polymer in a quiescent state. Subsequently, at elevated shear rates, enhancements in chain orientation and elevated crystallization kinetics are obtained when $W_{rep}$ exceeds one and $W_s$ remains less than one, resulting in the formation of fine spherulites with more ordered macromolecular chains. Finally, at even greater shear rates, both $W_{rep}$ and $W_s$ exceed one, indicating a regime where the chains are not only oriented but also stretched, allowing even the formation of highly ordered, shish-kebab-like structures.

To evaluate the Weissenberg numbers for the 100HV and 100LV matrices processed at two different screw speeds, the shear rates obtained from Ludovic® simulations were employed. In addition, the longest relaxation time and the Rouse time, as calculated by Massaro et al. [498], were utilized. As shown in Table 10, the resulting values of $W_{rep}$ and $W_s$ indicate that, for all materials, the first parameter is greater than one, while the second is lower. Consequently, the expected microstructure consists in all cases of spherulites containing ordered macromolecules, with no shish kebabs present.

**Table 10. $W_{rep}$ and $W_s$ for 100HV and 100LV compounded at 150 and 300 rpm. The maximum and minimum values of shear rate are reported between branches for the two screw speeds.**

| Material | $W_{rep}$ | | $W_s$ | |
|---|---|---|---|---|
| | 150 rpm ($40\ s^{-1}$ – $76\ s^{-1}$) | 300 rpm ($80\ s^{-1}$ – $152\ s^{-1}$) | 150 rpm ($40\ s^{-1}$ – $76\ s^{-1}$) | 300 rpm ($80\ s^{-1}$ – $152\ s^{-1}$) |
| 100LV | 1.60 – 3.04 | 3.20 – 6.08 | $3.99 \cdot 10^{-2}$ – $7.58 \cdot 10^{-2}$ | $7.98 \cdot 10^{-2}$ – $1.52 \cdot 10^{-1}$ |
| 100HV | 5.60 – 10.64 | 11.20 – 21.28 | $7.00 \cdot 10^{-2}$ – $1.33 \cdot 10^{-1}$ | $1.40 \cdot 10^{-1}$ – $2.66\ 10^{-1}$ |

The results can be interpreted in light of the role of the memory effect related to the presence of H-bonding and entanglements, as well as the FIC due to the shear rate applied to the materials. A comparison of 100HV and 100LV reveals that the former exhibits a greater content of intermolecular hydrogen bonds and entanglement, attributable to its larger molecular weight. Consequently, the molecular friction in the molten state is greater, which limits the motion of the chains and results in a lower crystallinity content compared to the low MW matrix [464,478,530].

Furthermore, additional considerations regarding the relationship between the compounding parameters and the crystallinity emerged when examining the temperature trend along the screw profile modeled with Ludovic® (Figure 53 and Table 7). Specifically, the high molecular weight polymer is subjected to elevated temperatures in comparison to the low MW one, despite both being processed at the same screw speed. Furthermore, larger differences from the set temperatures are achieved at 300 rpm.

The observed discrepancies in the $\Delta H_m$ with respect to MW and temperature variation can be attributed to the temperature dependence of entanglement and hydrogen bonding densities in polyamides. In particular, it is well known that a dynamic, temperature-dependent equilibrium of hydrogen bonding density occurs in the molten state of PAs. Additionally, although the phenomenon is less intense at higher temperatures, data relative to the actual temperature and TRT modeled with Ludovic® suggest that the parameters are conservative compared to the conditions reported in the literature when considering the erasure of the memory effect. The reference values are 270°C for 10 min or 280°C for 90 min [464,470,474,476]. According to the results discussed in Section 4.2, the 100HV scenario requires the most attention. In fact, the material is exposed to the highest temperature peaks (251 and 283 °C at 150 and 300 rpm, respectively). However, these values are outliers when considering the entire temperature profile along the screws. Additionally, the corresponding TRTs of 126 and 104 s at 150 and 300 rpm, respectively, are much shorter than the reference times reported in literature. Therefore, the memory effect is always an active mechanism in the current study.

In consideration of these findings, the smaller difference in the melting enthalpy between 100LV_300rpm and 100HV_300rpm, as compared to the corresponding materials processed at 150 rpm, is explained by the decreased memory effect intensity resulting from the higher temperatures reached at 300 rpm. Reducing intermolecular hydrogen bonding density leads to diminished molecular friction

and increased macromolecular mobility [464]. At the same time, entanglements are less abundant at higher screw speeds than at lower ones [478]. Consequently, the memory effect is likely weaker compared to the FIC active under the same processing conditions.

Furthermore, the aforementioned considerations offer a potential explanation for the observed variations in the α/γ ratios. As illustrated in Figure 57C, a comparison of the values for the two matrices that were compounded at the same screw speed reveals that the α/γ contents are greater for the materials that were processed at the highest screw speed. Additionally, the results are more similar for the 100HV and 100LV produced at 300 rpm. These results can be attributed to the decreased density of molecular constraints caused by the effect of the applied shear rate and temperature, which likely results in a more similar effect of shear on chain orientation and a greater α phase content. Specifically, as the screw speed increases, the FIC effect becomes dominant over the memory effect. As discussed above, however, the latter remains active due to the contribution of hydrogen bonds, considering the actual temperature and residence time [464,470,474,476,478]. Furthermore, the non-Newtonian behavior observed in the low-frequency region of the complex viscosity in Figure 54 confirms the presence of entanglement which, in turn, further promotes the memory effect.

On the other hand, it is also to be taken into account that the decrease in H-bonding density caused by an increase in temperature not only weakens the memory effect, but it may also negatively impact the FIC. However, the latter phenomenon is promoted by the higher shear rate faced by the material at 300 rpm (Figure 52). This is particularly evident from the rise in $W_{rep}$ promoted by the increase of the screw speed, as reported in Table 10. Further confirmation emerges from comparing the crystallization temperatures measured in the different cases (Figure 56B). Indeed, for a given matrix, higher $T_{cryst}$ values correspond to the material processed at the highest screw speed and, as known from the literature, this is associated with faster crystallization kinetics [110,471,526,531]. In addition, the predominant role of the FIC over the memory effect at the highest screw speed is assumed to be the basis of the larger difference between the $T_{cryst}$ of the high MW matrix processed at 150 or 300 rpm, when compared to the smaller difference observed for 100LV in the two cases.

Subsequently, a comparison of the α and γ content in the pre-processed and compounded matrices gave rise to additional considerations. As illustrated in Figure 55 and Figure 57, the latter crystalline phase is more abundant after processing, at the expense of α. This indicates that the processing significantly impacts the final morphology. Indeed, the α crystalline phase is the more stable of the two [489], thus its decrease during the compounding step suggests that extrusion promotes macromolecular disorder. However, an increase in the α/γ content is observed when comparing values calculated for the same material processed at 150 or 300 rpm (Figure 57C). This behavior is consistent with previous observations that high shear rates promote the formation of α in PA66 while having a negligible effect on γ [528]. Consequently, the occurrence of the γ phase post-processing can be ascribed to the interplay between memory effects and FIC, both of which are active in the

processing under investigation. Specifically, at 150 rpm, the molecular constraints hinder chain mobility, preventing the α phase formation. At 300 rpm, the higher screw speed reduces H-bonding and entanglement density, which in turn favors the formation of the more stable phase due to enhanced chain mobility.

Therefore, it can be concluded that the final crystallinity and α/γ content are improved in the matrices processed at higher screw speed, while the role of the molecular weight appears to depend on the screw speed selected.

### 4.4.2 Blends

In the case of blends, the decreasing trend of the $\Delta H_m$ with increasing HV content that can be observed in Figure 56A for the materials compounded at 150 rpm, has been explained by considering the antagonism of the memory effect and the FIC. Indeed, the higher HV content in the formulation leads to an increase in macromolecular constraints, both in terms of H-bonding and entanglement densities, due to the greater MW chain content. This is consistent with earlier considerations regarding matrices, in which the increase in MW and screw speed was related to an improvement in chain order owing to an intensification of FIC and weakening of the memory effect. However, a positive deviation is observed when comparing the experimental values with the modeled ones, derived from the linear combination of the melting enthalpy of the matrices. This observation indicates the occurrence of a cooperative mechanism that is active in the presence of a bimodal molecular weight distribution, thereby promoting crystallinity. By contrast, no such considerations can be applied to the melting enthalpies of the blends processed at 300 rpm (Figure 56A). In this case, the $\Delta H_m$ appears to be independent from the high MW content, and the experimental values are lower than the ones derived from the linear combination of the melting enthalpies of the matrices. In this regard, an increase in screw speed appears to be disadvantageous for the overall crystallinity content in the presence of a bimodal MW distribution. Furthermore, a comparison of the α/γ ratio of a specific blend processed at 150 or 300 rpm reveals a general increase in the less stable phase, promoted by the higher screw speed (Figure 57C).

Additionally, the comparison of the $T_{cryst}$ (Figure 56B) reveals that the values of the blends processed at 300 rpm exceed those measured for the materials compounded at 150 rpm. This finding suggests that the crystallization kinetics in the former case are expected to be higher [110,471,526,531].

## 4.5 Concluding remarks

The present Chapter investigated the relationship between processing parameters and microstructural evolution in melt-compounded PA6, focusing on the effects of screw speed and viscosity. For this prupose, the use of Ludovic® software was crucial to obtain the actual values of the temperature, shear rate and residence time faced by the different materials along the barrel during compounding. In particular, this study represented a novelty because it specifically

focused on tailoring the microstructure of PA6 homopolymer blends using twin screw extrusion. Besides, it clearly highlighted the impact of the actual values of the processing parameters on the balance between the FIC and memory effect which, in turn, was identified and discussed as fundamental for microstructure tailoring.

In particular, a series of simulations of the thermo-mechanical fields present were performed, and it was assessed that increasing the screw speed results in an enhancement of the shear rate and a reduction of the TRT, thereby altering the thermal and rheological conditions during extrusion. Additionally, higher MW and screw speed resulted in increased temperatures along the screw profile. Furthermore, thermal analysis revealed that the overall crystallinity and the α/γ ratio increased with screw speed. This behavior was attributed to the antagonistic effects of FIC and the thermal memory effect. Specifically, elevated shear rates reduced chain entanglement, and higher temperatures decreased hydrogen bonding density. Consequently, this results in a reduction of macromolecular constraints, thus allowing FIC to increase overall crystallinity and α phase formation.

Furthermore, blends with varying HV/LV PA6 ratios were characterized to evaluate the combined influence of bimodal molecular weight distribution, viscosity, and screw speed. While clear correlations were identified for the matrices, the blend behavior exhibited a higher degree of complexity. Specifically, the simultaneous presence of LV and HV has been observed to affect the mechanism by which the applied shear rate promotes macromolecular orientation. Furthermore, existent FIC models do not adequately account for transient morphologies or the role of the amorphous phase in achieving final structure formation. Therefore, it is unclear whether the crystalline structures observed in the blends after processing are stable configurations or transitional states.

# Chapter 5

# Effect of elongational flow on PA6 homopolymer blends


## Abstract

The present Chapter investigated the effect of the superposition of shear and non-isothermal uniaxial elongational flows on the processing parameters-microstructure-properties relationship in melt-compounded PA6 homopolymer systems. In particular, given the conclusions of Chapter 4, the role of compounding screw speed (150 or 300 rpm), the intensity of the elongational flow, the average MW (high and low viscosity), and the MW distribution (mono- and bimodal) were analyzed. Subsequently, the materials were subjected to thermal and tensile testing to assess their properties. Additionally, the drawability in the molten state was evaluated.

The average molecular weight and elongational flow were found to play a primary role in determining deformability and mechanical properties due to their effects on entanglement density and chain orientation, respectively. Furthermore, the MW distribution was found to play a secondary role in relation to the applied shear rate and was particularly significant in stabilizing the melt and enhancing drawability.

In particular, the elongational flow was assessed to promote chain orientation and the formation of the more stable α crystalline phase in monomodal systems. Its intensity was directly related to increased strength and strain hardening. Conversely, a more complex evolution of the crystallinity emerged when considering the bimodal MW distribution. Finally, despite the variations in the content of the α and γ crystalline phases, an overall negligible effect of the polymorphism on the mechanical behavior was observed.

# 5.1 Introduction

As detailed in Chapter 2, the application of uniaxial elongational flow to the extruded material right after the die promotes chain orientation, leading to effective macromolecular structuring. Furthermore, the final morphology is influenced by the isothermal or non-isothermal condition under which the drawing is performed [5,110,115,118,121–124,126,143,161]. This technique is widely used in industry to produce fibers, wires and films for various applications [5,91,92,143,145,146,148,228,230,231]. As a result, the study of the impact of the application of uniaxial elongational flow on the processing parameters-microstructure-properties relationship is not merely of academic interest.

Considering polymer blends, the literature mostly focuses on immiscible systems (see Section 2.1.4), highlighting the improved breakup and dispersion of the minor phase when the field is applied, along with the progressive evolution of the microstructural arrangement from homogeneous spherulites to well-oriented lamellar structures. In addition, as reviewed by Arrigo et al. [115], when homogeneous polymers are considered, the progressive alignment of the macromolecules according to the flow direction is assessed. Therefore, the application of a uniaxial elongational field to semicrystalline polymers results in the closer arrangement of macromolecules, leading to a reduction in the energy barrier for the crystallization and an enhancement in the crystallization kinetics and orientation of the resulting crystalline phases [242,532–535]. The main outcome is an improvement in tensile properties with an increase in draw ratio. Thus, higher stiffness and lower ductility are expected from the material after drawing [115,254,536–543].

The present study investigated the impact of elongational flow on the microstructure and properties of melt compounded PA6 homopolymer systems. The uniaxial field was applied right after the die of the twin screw extruder used for processing the materials, thereby corresponding to a non-isothermal drawing condition. Additionally, the simultaneous variation of screw speed was taken into account. Such experimental design allowed to evaluate the effect of the superposition of the shear and elongational flows on the microstructure of the processed materials.

Considering the conclusions of Chapter 4, relative to the analysis of the effect of the thermo-mechanical field applied during compounding onto the polyamide matrices and blends, three materials were selected. Specifically, the two high MW and low MW matrices, and the blend containing 30 wt% of the former. The selection was made taking into consideration the microstructure obtained in the blend. In fact, the chosen material exhibits an opposite trend compared to the individual matrices in terms of the $\alpha/\gamma$ phase ratio and melting enthalpy. For the matrices, these two parameters increase with screw rotation speed. However, for the blend containing 30 wt% of HV, the values are maximized at lower speeds (Figure 56A and Figure 57C).

Elongational flow was applied using an ad hoc apparatus equipped with a series of rotating pulleys that caught the filament and drew it at an increasing speed. The

resulting microstructure, in terms of crystallinity content and α/γ ratio was analyzed with DSC analyses, while the final mechanical properties of the fibers were evaluated through tensile tests as function of the DR, which was calculated in accordance with Eq. A.2. Furthermore, the data were interpreted by taking into consideration the relationship between processing parameters, microstructure, and properties, following the approach used in the previous Chapters.

An overview of the variables and constant factors used in the production of the fibers discussed in this Chapter is provided in Table 11.

**Table 11. Variables and constant factors used for the production of the PA6 homopolymer fibers.**

| | Factor | Levels | | |
|---|---|---|---|---|
| Variables | Screw speed [rpm] | 150 | | 300 |
| | MW distribution | Monomodal | | Bimodal |
| | HV:LV content [wt% of HV] | 0 | 30 | 100 |
| | Stretching speed [rpm] | From 0 to 1000 or to filament breakage - Acceleration mode | | |
| Constants | Feed rate [g/h] | 290 | | |
| | Temperature [°C] - from hopper to die | 220\220\225\230\230\230\230\230 | | |

In the present section, the materials are identified with a code that includes the reciprocal content of the HV and LV matrices expressed as a percentage, the screw speed in rpm, and, in the case of the fibers, the value of the calculated DR. For instance, "30HV_150rpm_DR200" denotes a fiber obtained from the blend containing 30 wt% of HV, with a screw speed of 150 rpm and characterized by a DR of 200. It is worth noting that the code "DR1" corresponds to materials for which no drawing was applied (see Eq. A.3).

# 5.2 Characterization

## 5.2.1 Drawability

The ability of the materials to withstand stretching in the molten state was evaluated through the BSR (see Eq. A.2). The corresponding data are reported in Figure 58. Focusing on the matrices processed at 150 rpm, the increase of the MW corresponds to the lowering of the drawability. This behavior is in accordance with the expectations, considering the higher entanglement density in the 100HV in comparison to the 100LV, when processed in the same conditions [198,544]. As a consequence, the first material is expected to have a greater extent of elastic response between the two, leading to more pronounced instabilities in the melt and in lower drawability prior to melt fracture [545–547]. When considering the blend, the BSR is between those of the two matrices. This behavior is explained

considering the role of the average molecular weight on the drawability along with the bimodal MW distribution. In fact, the average MW is related to the entanglement density in the material; thus for the blend, having an in-between average molecular weight, the drawability is expected to be between that of the two matrices [548,549].

Furthermore, in Figure 58 the BSRs calculated for the materials processed at 300 rpm are reported. In such operative conditions, it was not possible to obtain the fibers from the 100LV_300rpm. On the other hand, the elongational flow was successfully applied to both 100HV_300rpm and 30HV_300rpm. For the high molecular weight matrix, the BSR reached a value of 410, which is higher than that obtained for the same material processed at 150 rpm. Furthermore, a significant increase in BSR is appreciated for the blend. In fact, at the highest screw speed the material was not subject to breakage even at the highest applied stretching speed. This improvement in polymer deformability can be explained considering the results of the Ludovic® simulations provided in Section 4.2. In particular, as highlighted in Figure 52, the increase of the screw rotation speed corresponds to a higher shear rate applied. Thus, an increased detangling effect is expected on the polymer processed at 300 instead of 150 rpm. Therefore, the ability to withstand drawing is improved [163,198,478,550]. Besides, a further effect of the increase of the intensity of the shear flow at the higher screw speed lies in the dynamics occurring at the entrance of the capillary die. In fact, in this part of the extruder the flow field imposes a uniaxial stretching to the macromolecules, which increases accordingly to the screw rotation speed and furtherly promotes their orientation [549,551,552].

Lastly, a synergistic role of the MW distribution and the screw rotation speed may be considered. In particular, from the comparison of the BSR values reported in Figure 58, it can be appreciated that the increase in the drawability of 30HV in correspondence to the higher shear rate applied is considerably greater than the one obtained for 100HV. These evidences can be explained considering the known effects of the MW distribution of polymeric materials on the melt instabilities. In fact, it has been reported that the latter occur under more demanding processing conditions in the presence of a bimodal MW distribution than in a monomodal MW distribution matrix [545,553,554].

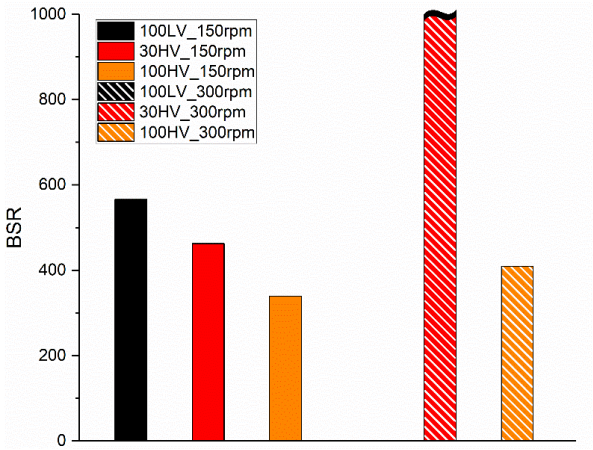


**Figure 58. BSR of the materials processed at 150 and 300 rpm. The "~" indicates that no rupture was observed under the experimental conditions used. Also, no data are reported for the 100LV_300rpm because it was not possible to obtain the fibers in such operative conditions.**

## 5.2.2 DSC

For the thermal analyses, the materials obtained at the same extent of the uniaxial elongational field were considered in order to investigate the effect of the applied flow. Thus, all the data reported for the drawn materials in the present section refer to a DR of 350.

Willing to investigate the structuring impact of the processing step, in Figure 59A and B are shown the thermograms of the first heating ramps of the fibers obtained from the polymers compounded at 150 or 300 rpm, respectively. Considering the materials produced at the lowest screw speed (Figure 59A), the peak at about 222 °C (see Table 12) attesting the presence of the α phase [489] is appreciated in all cases, regardless the MW and MW distribution considered. However, it is important to note that the 100HV_150rpm_DR350 exibits a second peak at 215 °C related to the γ phase [500,523].

On the other hand, when considering those processed at 300 rpm, differences in the crystalline structures obtained after the application of the elonational flow clearly emerge. In this second case, the high viscosity matrix showed a single peak at 221 °C, corresponding to the melting of the α phase, while no signal related to the γ can be detected [489]. On the contrary, the presence of the latter crystalline phase is suggested in the 30HV_300rpm_DR350 by the subtile shoulder at 212 °C [500,523].

Besides, the cooling thermograms of the fibers are shown in Figure 59C and D for the polymer compounded at 150 or 300 rpm, respectively. What emerges is that in all cases a single crystallization peak is present. Thus, independently of the material or the screw speed considered.

Lastly, in Table 12 are reported the values of melting temperatures relative to the first heating ramp along with the crystallization temperature relative to the thermograms shown in Figure 59.

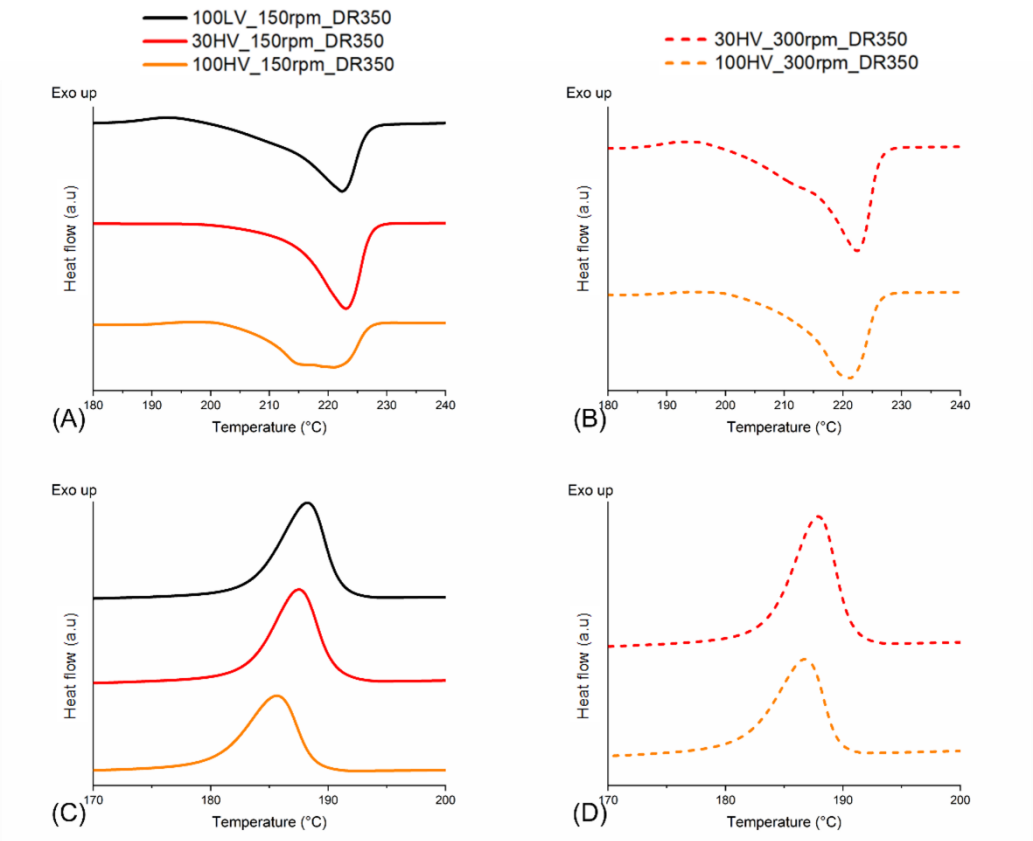


**Figure 59. Thermogram of the first heating scan of the fibers having DR of 350 and compounding screw speed of (A) 150 and (B) 300 rpm; corresponding cooling ramps for the materials processed at (C) 150 and (D) 300 rpm.**

**Table 12. Melting temperatures of the γ and α phases measured during the first heating scan and crystallization temperatures of the fibers having DR of 350 and processed at 150 or 300 rpm.**

| Material | Melting temperature [°C] | | Crystallization temperature [°C] |
|---|---|---|---|
| | γ | α | |
| 100LV_150rpm_DR350 | - | 222 | 188 |
| 30HV_150rpm_DR350 | - | 223 | 188 |
| 100HV_150rpm_DR350 | 215 | 221 | 186 |
| 30HV_300rpm_DR350 | 212 | 222 | 188 |
| 100HV_300rpm_DR350 | - | 221 | 187 |

Furthermore, in order to highlight the different thermal behavior assessed above, in Figure 60A and B are reported the comparisons between the heating thermograms of the fibers of 100HV and 30HV, respectively. For the matrix (Figure 60A), the disappearance of the γ phase with the increase of the screw speed can be attributed to the improved macromolecular order promoted by the higher shear rate applied at 300 rpm if compared to those at 150 rpm. As extensively discussed in the previous Chapter 4 (see Section 4.4), the increase of the macromolecular order is promoted by the higher shear rate and actual temperatures applied to the material during processing. Therefore, the disentanglement of the chains is promoted and the predominance of the FIC over the memory effect is achieved. As a consequence, the formation of the more stable α crystals is favored over the γ phase

[163,464,470,474,476,478]. On the other hand, for 30HV (Figure 60B), the opposite behavior emerges. The formation of the γ crystalline phase promoted by the increase of the applied shear rate is in accordance with the observations reported in Chapter 4. The evolution of the microstructure as function of the screw speed was there related to the bimodal MW distribution affecting the relaxation dynamics involved in the chain orientation, as a consequence of the increase of the appied shear rate [163].

Considering the above discussion, a dominant role of the shear over the elongational flow in tailoring the microstructure may be suggested. However, a deeper investigation on the melting enthalpies and α/γ contents of the fibers led to different findings.

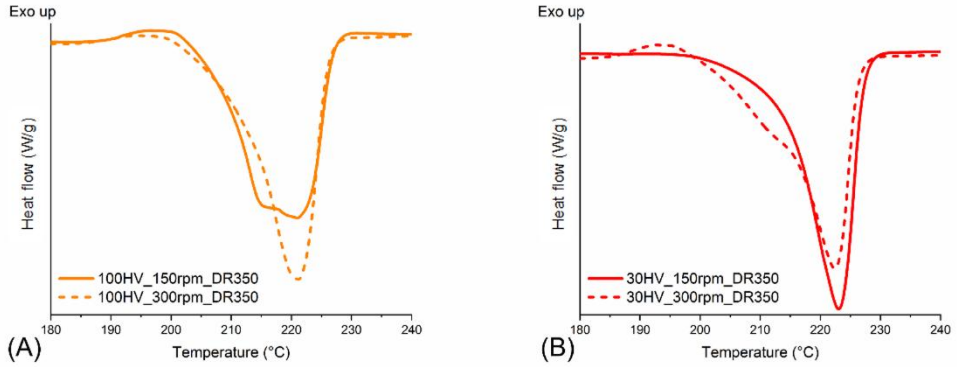


**Figure 60. Comparison of the first heating scan of the fibers having DR of 350 and processed at 150 and 300 rpm in the case of (A) 100HV and (B) 30HV.**

In Figure 61A, the melting enthalpies calculated from the first heating ramps of the fibers are compared with those of the second heating ramps of the corresponding isotropic materials, as discussed in Chapter 4.

Firstly, let's focus on the $\Delta H_m$ of the fibers. When the two matrices are processed at 150 rpm, the melting enthalpy lowers with the increase in the MW, thus showing an inversely proportional trend with the chain length. Additionally, the $\Delta H_m$ of the blend is consistent with the theoretical value predicted by the linear combination of the melting enthalpies of the two individual matrices. Besides, from the comparison of the data with those calculated for the fibers obtained at 300 rpm, it emerges that the $\Delta H_m$ of the 100HV matrix is comparable, regardless the screw speed considered. On the other hand, only a slight increase is obtained for the blend processed at 300 rpm. These observations suggest that the effect of the intensity of the shear rate in determining the melting enthalpy of a specific material is negligible when elongational flow is applied.

In addition, from the comparison of the $\Delta H_m$ of the fibers with those of the corresponding isotropic materials compounded at the same screw speed (Figure 61A), the impact of the application of the elongational flow can be appreciated. For the samples processed at 150 rpm, a negligible effect emerges for 100LV. In contrast, for the 100HV, the drawing appears to increase $\Delta H_m$, while an opposite trend is observed for the 30HV blend, where elongational flow leads to a slight

decrease of the value. Furthermore, also for the materials processed at 300 rpm, the impact of elongational flow on $\Delta H_m$ varies depending on the material considered. Specifically, a reduction is observed for the 100HV fibers, while a moderate increase is seen in the 30HV blend. Therefore, a composition-dependent response of the melting enthalpy from the elongational flow seem to emerge.
The corresponding crystallinity contents calculated in accordance with Eq. A.4 are reported in Table 13.

Beyond, in Figure 61B is presented the distribution of the α and γ crystalline phases for the fibers, in comparison to that of the corresponding extrudates. It is important to note that for materials in which only α was detected, no data are reported in the graph.
At 150 rpm, the 100LV fibers exhibit exclusively the α crystalline phase. In contrast, the 100HV matrix displays a near-equivalent content of α and γ. Also, for the 30HV blend the crystalline population consists solely of the α phase. At 300 rpm, a different situation is observed. In fact, the 100HV fibers contain only α, while both α and γ were present in the blend. Interesting insights arise from the comparison of the α/γ content of the fibers with the values calculated for the isotropic counterparts (Figure 61B). All isotropic materials processed at 150 rpm exhibit a coexistence of α and γ phases (see Section 4.3.2). However, after drawing the fibers of 100LV crystallize only in the α form. On the contrary, the γ is present in the drawn 100HV, and its relative content over α is even higher than the one of the corresponding isotropic counterpart. Lastly, the crystallinity of the fibers of 30HV was characterized by only α phase, similarly to what obtained for the ones of 100LV. Besides, also for the polymers compounded at 300 rpm with no elongational flow applied the simultaneous presence of α and γ was assessed. However, the latter was only present in the 30HV fibers and not in the 100HV ones.

The above analysis shows that elongational flow effectively tailors the stability of polymorphic phases regardless of the screw rotation speed considered. In particular, it appears to promote the formation of more stable α crystals, in accordance with the literature [555]. Furthermore, a secondary role of the MW seems to emerge, which can be related to the more intense memory effect expected in 100HV. In fact, the higher molecular weight results in greater entanglement density. Also, in the case of polyamides, it results in a larger quantity of intermolecular hydrogen bonding. These phenomena both hinder the chain mobility and increase macromolecular friction, thus inducing a greater memory effect. Consequently, an increased resistance to orienting the macromolecules in accordance with the uniaxial field is expected [464,478,530,548,549]. Furthermore, considering the evolution of the α/γ content in the fibers, the presence of γ in 100HV but not in 100LV, compounded at 150 rpm, can also be attributed to the memory effect hindering chain mobility. This is also in accordance with the formation of the solely α phase in the high MW fibers processed at 300 rpm. In fact, as discussed in Section 4.3.2, the isotropic 100HV compounded at the higher screw speed shows a more ordered chain conformation after compounding, as confirmed by the higher α/γ content compared to the material obtained at 150 rpm. Therefore, consistently with the experimental evidences, it is likely that elongational flow applied to this

higher-oriented crystalline population would align the macromolecules more effectively to form only the α phase. As a consequence, it was assessed that the simultaneous application of the uniaxial elongational and shear flows have a synergistic effect on the orientation of the macromolecules [548,552].

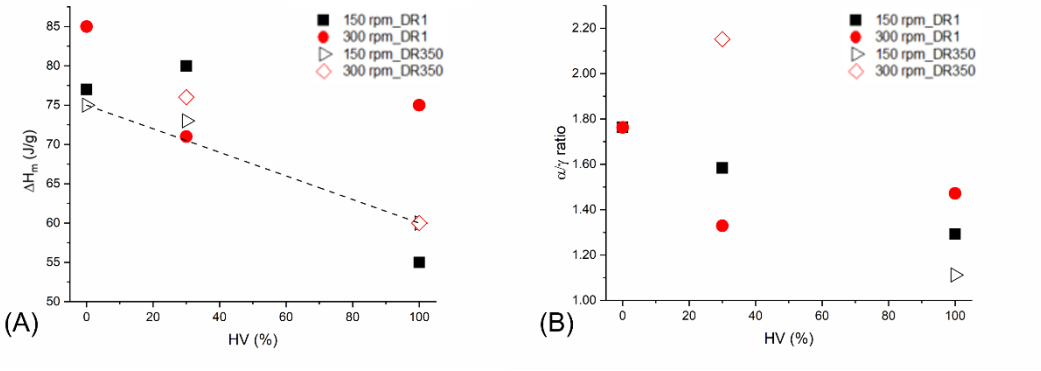


**Figure 61. Comparison of the (A) melting enthalpies and (B) α/γ content of the materials processed at 150 and 300 rpm in the case of presence or absence of the uniaxial elongational field. The data for the fibers characterized only by α phase are not shown. The dotted line represents the linear combination of the $\Delta H_m$ of the two matrices.**

**Table 13. Crystallinity content of the compounded non-stretched materials and the fibers having DR of 350, compounded at a screw speed of 150 or 300 rpm.**

| Material | Crystallinity content DR350 [%] | Crystallinity content DR1[%] |
|---|---|---|
| 100LV_150rpm | 33 | 33 |
| 30HV_150rpm | 32 | 35 |
| 100HV_150rpm | 26 | 24 |
| 30HV_300rpm | 33 | 31 |
| 100HV_300rpm | 26 | 33 |

It is important to note that the templating effect of elongational flow toward stabilization of the more stable crystalline phase is not in contradiction with the negligible impact on the resulting melting enthalpy, as highlighted in Figure 61A. In fact, the limited impact of the application of the elongational flow on the overall crystallinity content has been already reported in literature [245,255].

As explained in Section 2.4.1, relative to polymer structuring via drawing, the effect of the elongational flow on the final crystallinity content is determined by the crystallization kinetics of the polymer and the period during which the drawing is applied prior to complete solidification [251,556]. In this context, it is important to emphasize that elongational flow predominantly influences the nucleation stage rather than crystal growth. The flow-induced orientation and alignment of polymer chains in the molten state promotes the formation of a higher density of stable nuclei compared to quiescent conditions. As a general rule, an increase in the number of nucleation sites leads to an increase in crystallization kinetics. However, the influence of flow on the crystal growth rate was assessed to be less significant than its effect on nucleation [533,557–561]. Additionally, in the current system,

elongational flow is applied under non-isothermal conditions. Consequently, crystal growth is further constrained by the progressive decrease in temperature, which limits chain mobility and restricts the extent of crystal development. All the above explains the negligible variations observed in the final crystallinity content and, thus, in the melting enthalpy, despite the templating effect of elongational flow toward stabilization of the more stable crystalline phase [115,245,251,556,562–564].

In the following, the effect of the increasing intensity of the applied elongational flow on the microstructural changes obtained in a specific material is analyzed and discussed.

#### 5.2.2.1 100HV

In Figure 62A the melting enthalpies of the fibers of 100HV_150rpm and 100HV_300rpm are shown as function of the DR.
For a screw speed of 150 rpm, a positive impact of the increase of the elongational flow intensity emerges for DR in the range 50 to 200. However, the further enhancement of the draw ratio up to 350 appears to provide no additional benefits in terms of $\Delta H_m$. Conversely, increasing the intensity of the applied elongational flow emerged to have a negligible impact on the $\Delta H_m$ of fibers produced at 300 rpm across the entire DR range. Besides, from the comparison of the values calculated for the fibers having the same DR and produced at two different screw speeds, can be appreciated that the difference in the melting enthalpies decreases as the intensity of the applied elongational flow increased. And, in particular, the values are comparable starting from a DR of 100.

Furthermore, Figure 62B reports the α/γ contents as function of the DR for the fibers processed at 150 or 300 rpm. In the first case, both crystalline phases are present regardless the intensity of the elongational flow applied. Also, the clear predominance of α over γ is observed for a DR corresponding to 100 and 200, while a comparable content of the two was calculated for the fibers having draw ratio of 50 and 350. On the other hand, for those obtained at a screw speed of 300 rpm, only the α phase was detected across the entire DR range.

Taking into consideration the evolution of the melting enthalpy and the α/γ content as a function of the processing parameters (Figure 62A and B), the evolution of the microstructure can be explained by considering the effects of simultaneously applying shear and elongational flow from a macromolecular point of view. In the previous paragraph, the main impact was assessed to be the tailoring of the distribution of the crystalline phases. This suggests that the applied fields play a significant role in affecting the macromolecular orientation. In particular, a higher macromolecular disorder and entanglement density is expected for a screw speed of 150 rpm, due to the lower shear rate during the compounding step. This could lead to a greater impact of the applied elongational flow on the orientation of the macromolecules in the crystalline phases, even at low intensities of the uniaxial field. Besides, it is important to note that the application of the elongational flow also affects the order in the amorphous phase. In particular, in the case of PA6, the

macromolecular conformations of the chains in the oriented amorphous domains and the γ phase were found to be similar [463,565]. Therefore, it can be suggested that applying the elongational flow to the 100HV processed at 150 rpm promotes the transformation of the amorphous oriented phase into γ crystals due to the conformational adjustment of macromolecules and in presence of a good extent of contraints to the chains' mobility. Additionally, the decrease in relative α content as DR increases could be related to the material's high memory effect, which hinders further orientation of the chains in the more stable configuration. In fact, not only the slippage and orientation of the macromolecules subjected to uniaxial non-isothermal elongational flow is limited by the intermolecular H-bonding and entanglements that tie the polymer chains together [463,474], but also the presence of the crystalline-like domains alongside the macromolecules in the amorphous-like conformation influences the relaxation dynamics and, consequently, the mobility of the chains themselves [566]. On the other hand, this explanation could account for the presence of only the α phase in the fibers obtained at 300 rpm. In fact, the higher macromolecular orientation achieved after compounding may be sufficient to allow the transformation of the amorphous phase into γ crystals and furtherly into the more ordered α owing to the application of the elongational flow.

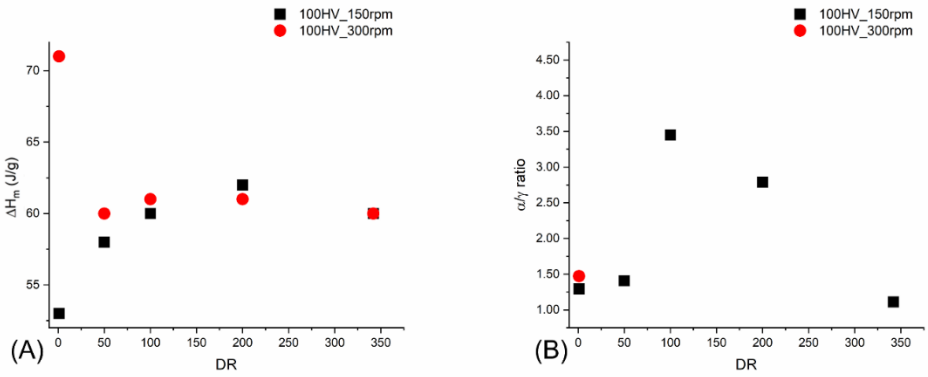


**Figure 62. Comparison of the (A) melting enthalpies and (B) α/γ ratio for the 100HV blend compounded at 150 or 300 rpm and drawn down to different DR. In (B) The data for the fibers characterized only by α phase are not shown.**

### 5.2.2.2 30HV

In the case of 30HV fibers, the evolution of the microstructure in terms of both melting enthalpy and mutual distribution of the α and γ phases in relation to the increase in the intensity of the applied elongational flow is shown in Figure 63A and B, respectively.

Firstly, considering fibers processed at 150 rpm, a decrease in the $\Delta H_m$ can be observed as the DR increases up to a draw ratio of 100 (Figure 63A). For higher elongational flow intensities applied, the melting enthalpy increases again. Additionally, a decrease in $\Delta H_m$ with increasing draw ratio is observed for the fibers processed at 300 rpm. In this case, however, the value decreases up to a DR of 200. Therefore, it is reasonable to conclude that the trend of melting enthalpy as a

function of elongational flow intensity appears to be nonlinear for fibers with bimodal MW distributions, regardless of the screw speed considered. On the other hand, an effect of the applied shear rate is suggested by a comparison of the $\Delta H_m$ of fibers with the same DR. In fact, the values clearly differ up to a DR of 100, with higher melting enthalpy associated to the blend processed at 300 rpm. However, at greater draw ratios the difference between the corresponding $\Delta H_m$ decreases considerably.

Turning to Figure 63B, it emerges that α is the predominant crystalline phase in the fibers obtained at 150 rpm. In particular, it is the only phase present when the DR is greater than or equal to 100. However, for blends processed at 300 rpm, solely α was detected at draw ratios of 50 and 100, while γ represents a significant portion of the crystals for the fibers having higher DR. Thus, although the elongational flow strongly promoted the formation of α in the fibers obtained at 150 rpm, the uneven α/γ content trend in the fibers obtained at 300 rpm does not allow to draw conclusions about the effect of the shear rate intensity on polymorphism when elongational flow is applied to the blend.

Therefore, in light of the interpretation provided for the behavior of the $\Delta H_m$ and polymorphism of 100HV fibers as function of the processing parameters (see Section 5.2.2.1), what discussed in the present section for the 30HV-based systems suggests that the bimodal MW distribution may play an important role in affecting the evolution of macromolecular dynamics. In particular, this could be sought within the different relaxation of the chains compared to monomodal matrices. In fact, it has been assessed that the relaxation time within systems with a multimodal MW is not only determined by the Rouse relaxation times of the family of chains having different MWs considered independently, but an interaction factor must also be considered [567]. Specifically, the latter is related to the delay in relaxation of a single chain due to surrounding unrelaxed macromolecules that represent a constrain to the local mobility of the neighboring [478,567–573]. Furthermore, the phenomenon was found to be fostered not only by the introduction of high MW chains, but also by low MW ones. In particular, although short macromolecules are characterized by a short relaxation time, they still impose constraints on their surroundings, thereby increasing the overall relaxation time of the system [568,574–576].

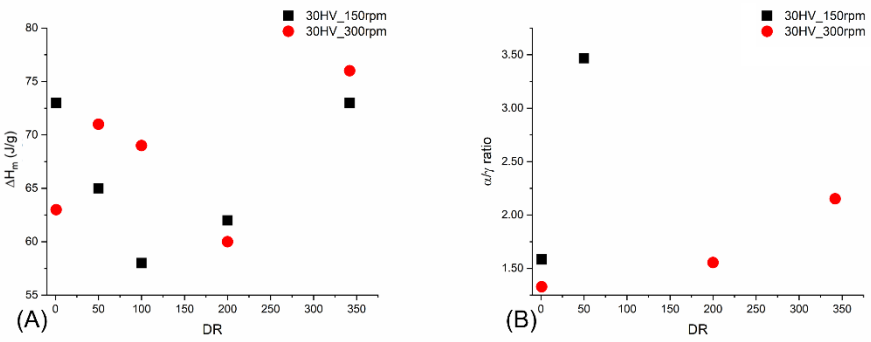


**Figure 63. Comparison of the (A) melting enthalpies and (B) α/γ ratio for the 30HV blend compounded at 150 or 300 rpm and drawn down to different DR. In (B) The data for the fibers characterized only by α phase are not shown.**

## 5.2.3 Mechanical properties

In Figure 64A and B, the strength at break and deformation at break of the isotropic materials processed at 150 or 300 rpm are reported. As expected, a minor impact of the increase of the screw speed on the resulting tensile properties is appreciated [577,578].

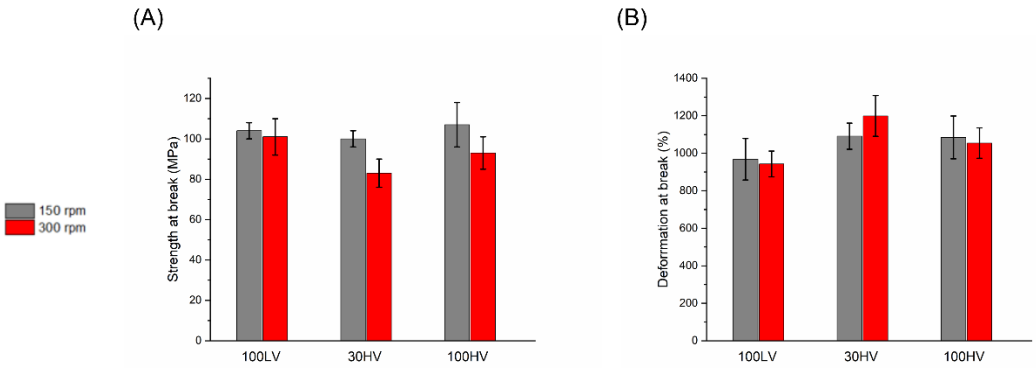


**Figure 64. (A) Strength at break and (B) deformation at break of the isotropic materials processed at 150 or 300 rpm.**

The fibers produced at different elongational flow intensities were tested for the tensile mechanical properties. The results were analyzed in order to assess the role of the processing parameters discussed so far. The stress-strain curves for 100HV and 30HV drawn at different DRs are shown in Figure 65**Error! Reference source not found.**A and B, which refer, respectively, to the materials processed at 150 and 300 rpm.

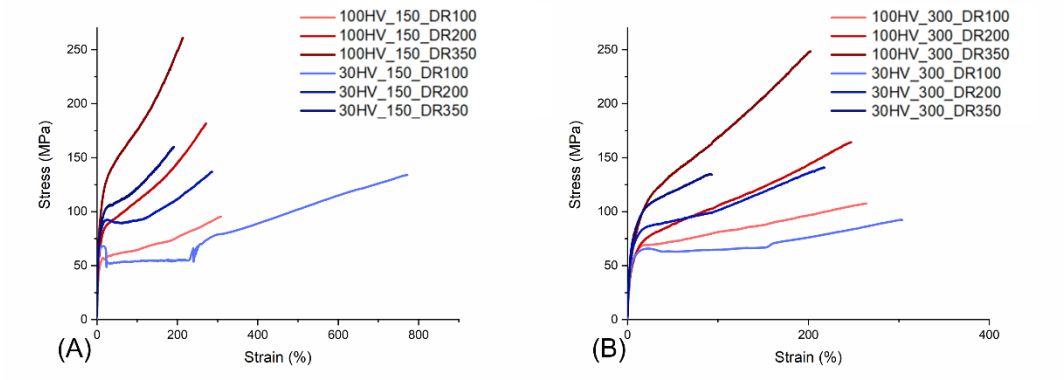


**Figure 65. Stress vs strain curves for the 100HV and 30HV fibers having different DR and processed at (A) 150 or (B) 300 rpm.**

Firstly, considering the mechanical behavior of the 100HV-based systems obtained at 150 rpm, the graphs show the typical initial linear elastic deformation, followed by a sudden change in the slope of the curve. The latter is indicative of the strain hardening occurring within the fibers [579,580]. Additionally, comparing the stress-strain curves of fibers drawn at increasing elongational flow intensities clearly emerges an increase in slope as a function of DR. Furthermore, considering that the slope is proportional to the strain hardening modulus, it can be concluded that increasing the intensity of the applied uniaxial field effectively promotes strain hardening [581–583]. From a microstructural point of view, this enhancement can be explained by considering that strain hardening is related to macromolecular orientation and entanglement density [579,584]. Thus, the enhancement of the strain hardening slope at higher DR is in accordance with the discussion provided in previous sections (see Sections 5.2.1 and 5.2.2), which evidenced an overall improvement in macromolecular orientation with increased applied elongational flow.

Accordingly, the 100HV fibers obtained at 300 rpm exhibit initial elastic deformation, followed by strain hardening and an increase in slope with DR (Figure 65B). Therefore, the above discussion can be applied to the present systems as well. Additionally, the predominant role of elongational flow over shear in determining the evolution of stress-strain curves at increasing DR can be suggested.

When analyzing the stress-strain curves of the 30HV fibers, a different mechanical behavior is observed compared to that of the 100HV fibers. Starting from the blend processed at 150 rpm (Figure 65A), 30HV_150rpm_DR100 is characterized by the initial linear elastic deformation, followed by the yield point and the strain softening prior to the stress plateau and the increase of the slope of the stress-strain curve. From a microstructural perspective, the stress plateau corresponds to the plastic deformation of the material, resulting from the stretching and orientation of the chains in the axial direction. This phenomenon is peculiar to macromolecules with a poorly oriented conformation, in which free volume plays a crucial role in facilitating molecular motion. Then, the increase in slope of the stress-strain curve reveals the occurrence of strain hardening and the orientation of macromolecules in the direction of tensile stress application [579,580,584,585].

Additionally, the noisy fluctuations at the end of the plastic deformation segment of the 30HV_150rpm_DR100 stress-strain curve can be attributed to abrupt local cracking during the plastic flow stage [586].
However, the mechanical behavior changes with an increase in DR (Figure 65A). In particular, for the fiber with DR 200, the strain softening and length of the plastic deformation segment decreased. Besides, the stress plateau is suppressed in the 30HV_150rpm_DR350 samples, and the strain hardening occurs directly after linear elastic deformation at low strain. These variations in mechanical behavior are likely to be determined by the different macromolecular conformations obtained in the fibers when higher intensities of elongational flow are applied. In fact, the lowering of the plastic deformation segment with the increase of the DR may be related to a more ordered and aligned chains' conformation achieved already during the non-isothermal drawing step.
The mechanical behavior and microstructural considerations of the 30HV_300 rpm fibers (Figure 65B) are comparable to those of the 30HV_150 rpm fibers discussed above. In this case, as well, an increase in DR resulted in a progressive decrease in the plastic deformation segment of the stress-strain curve due to the greater macromolecular order achieved during production. Therefore, as was assessed for the 100HV fibers, also in the case of the bimodal MW, the effect of elongational flow prevails over the one of the shear in determining the tensile behavior.

Furthermore, comparing the stress-strain curves of unimodal and bimodal MW fibers processed at the same screw speed (Figure 65A and B) reveals that the macromolecular characteristics also have a role in determining the mechanical behavior. In fact, when considering fibers having the same DR, the more pronounced strain hardening is always associated with 100HV. This can be attributed to the higher average MW of the matrix compared to the blend containing only 30 wt% of HV [587,588]. Additionally, the 30HV exhibits plastic deformation, whereas the 100HV does not, regardless of the DR considered. This behavior indicates that a different macromolecular conformation was obtained in the two cases when the same elongational flow was applied. In particular, the 100HV chains achieve good orientation already in the drawing step, even at low DR. Meanwhile, the blend retains a more disordered conformation. This can be related to the different relaxation time and memory effect intensity expected in the two cases, and affecting the conformational disorder [470,478,530,567,568,571].

To gain further insights into the effect of the intensity of the elongational flow on the strength and elongation at break of the fibers, the corresponding dimensionless values were examined as function of the DR (Figure 66). As reported in Section A.3.4, the data were obtained as the ratio between the experimental results of the fibers and that of the corresponding isotropic material. This approach highlights the contribution of improved macromolecular orientation to tensile mechanical properties [589].

First, considering the dimensionless strength of the materials processed at 150 rpm (Figure 66A), it can be appreciated that the values for the 100HV fibers increase as function of the DR. On the other hand, the 100LV and 30HV both show a quite consistent trend, and their values are comparable with those of the non-

stretched materials. These observations also apply to the dimensionless strength at break of the materials processed at 300 rpm (Figure 66B). In this case, too, only the high MW shows an actual increase in the values with increasing the intensity of the applied elongational flow.
Focusing on the dimensionless deformation at break, all materials processed at 150 rpm show a clear decrease in values compared to their isotropic counterparts (Figure 66C). However, the data obtained for the 100HV fibers remains nearly constant, regardless of the DR considered. Conversely, both the 100LV and the blend demonstrate a reduction in dimensionless deformation as the intensity of the applied elongational flow increased. Lastly, when the compounding screw speed of 300 rpm was exploited (Figure 66D), the obtained 100HV's values still retain a quite constant trend, independently from the DR considered. On the other hand, the 30HV shows an abrupt decrease in dimensionless deformation up to a DR of 100 and then remains constant, reaching a value comparable to that of the high-MW matrix.

The above observations raise some considerations. As emerged from Figure 65, the stress-strain curves of both the 100HV and 30HV fibers changed as a function of DR. Thus, the role of elongational flow in determining tensile behavior was assessed as function of the MW and MW distribution. However, the increase in dimensionless strength with increasing elongational flow intensity was only observed for the high MW-based fibers. Considering that the increase in strength is related to the enhanced orientation of the macromolecules due to the applied uniaxial field [589,590], it can be appreciated that only in the 100HV fibers the enhancement in macromolecular orientation was sufficient to actual increase the mechanical strength at break. Besides, it is known form the literature that the tensile properties are related to the average molecular weight of the polymer, while the MW distribution have an effect depending on the DR [590]. From the comparison of the dimensionless strength of the 100LV and 30HV a comparable trend in the data can be appreciated (Figure 66A). Thus, it can be suggested that in the present study, the average MW has a predominant role in determining the dimensionless strength in comparison to the MW distribution.
Furthermore, the data referred to the same material processed at 150 or 300 rpm are comparable (Figure 66A and B). As a result, it is likely to assume that the synergistic effect of the application of the shear and elongational flow on the orientation of the macromolecules is not significant enough to impact on the tensile strength [548,552].

Furthermore, in PA6 the different polymorphic species were found to play a role in determining its mechanical properties [503,591–593]. In fact, the different rotational conformations of the chains in the α and γ crystalline phases result in different H-bonding distances between the amide groups of adjacent macromolecules. As a consequence, the different macromolecular arrangements in α and γ result in a different shear deformation resistance of the crystals under tensile stress [464,492,493,495,556,591,594]. For these reasons, to gain further insight into the relationship between microstructure and mechanical properties, a comparison was made between the α/γ content and the resulting strength at break. Focusing on

the α/γ ratio of the fibers having DR of 350 (see Figure 61B), the 100HV was characterized by the exclusive presence of α for a compounding speed of 300 rpm, while both crystalline species were detected at 150 rpm. As a consequence, a higher strength at break and lower deformation at break would have been expected for 100HV_300rpm_DR350 compared to 100HV_150rpm_DR350. However, from the results reported in Figure 66, both the properties emerged to be comparable and independent from the screw speed used for the processing. Additionally, when the blend is considered, solely α phase was detected in the 30HV_150rpm_DR350, while γ was also present in the 30HV_300rpm_DR350. The latter would suggest a difference in the tensile behavior of the two fibers which, however, emerged to have comparable values of dimensionless strength and deformation at break (Figure 66). Therefore, it would appear that the materials do not exhibit the expected mechanical behavior, if the distribution of the crystalline phases present is taken into account.
This discrepancy is likely due to the fact that previous studies on this topic have typically evaluated optimized crystalline structures, in which a single phase is deliberately formed and tested. In contrast, the samples analyzed in the present study contain both α and γ phases simultaneously, making it difficult to isolate their individual contributions to the mechanical performances. Actually, this interpretation is consistent with earlier findings [489,556,565,594,595]. Specifically, it has been assessed that additional chain conformations emerge if the microstructure is not properly tailored. In particular, crystalline defects are introduced in the α and γ crystals, while the amorphous phase exhibit highly oriented non-crystalline regions whose structural chains' conformations resemble the γ phase rather than consisting solely of random coils. Consequently, the complex macromolecular architecture makes it difficult to identify the distinct roles played by α and γ crystals in determining the tensile behavior.

In conclusion, the present study assessed the effect of processing parameters on tensile strength and related it to the corresponding microstructure. In particular, the importance of macromolecular orientation on the tensile behavior was highlighted, while the effect of polymorphism was deemed negligible.

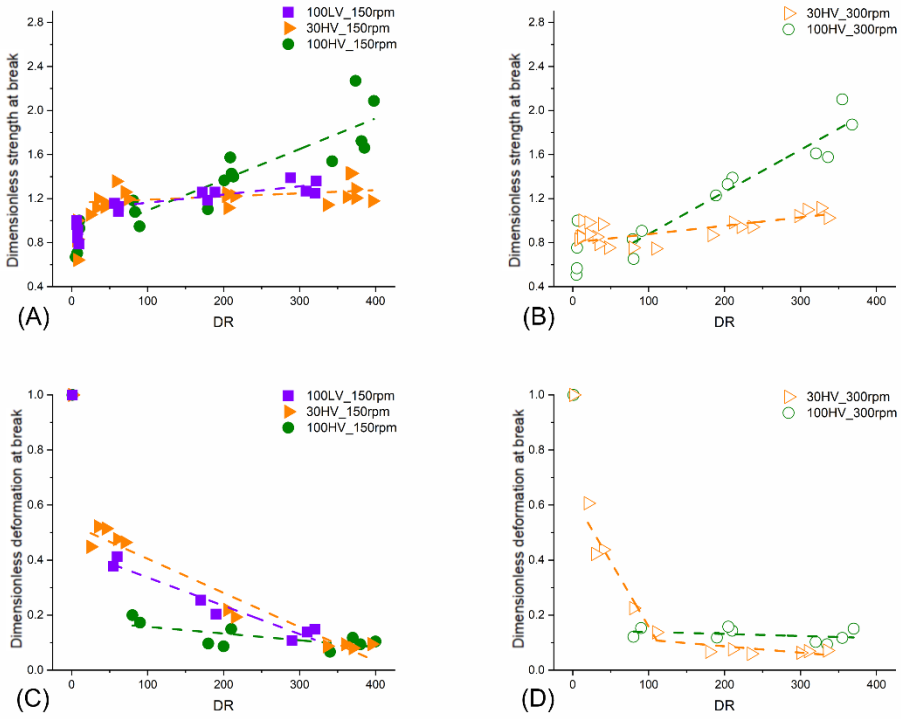


**Figure 66. Dimensionless (A, B) strength and (C, D) deformation at break of the fibers having different DR and obtained from the polymers processed at (A, C) 150 or (B, D) 300 rpm.**

## 5.3 Concluding remarks

This study investigated the processing parameters-microstructure-properties relationship in PA6, focusing on the role of compounding screw rotation speed, intensity of uniaxial elongational flow, average MW and MW distribution. Also, the mechanical behavior was investigated as final property. What emerged is the primary importance of the average molecular weight and elongational flow over the other parameters considered.

In fact, the first affects the entanglement density, that strongly influences the deformability of the material. The MW distribution emerged to play a secondary role when combined with high shear rates, by stabilizing the melt during drawing and enhancing the deformability.

Focusing on the elongational flow, it introduces significant changes in the microstructure. Although it reduces the overall crystallinity in some conditions as, in particular, in monomodal systems where it counteracts shear-induced crystallization, it consistently promotes chain orientation and the formation of the more stable α crystalline phase. This enhanced orientation contributes to improved mechanical properties, such as increased strength and strain hardening, especially in the high MW matrix. However, when considering the bimodal MW system, the effect of elongational flow on crystallinity is more complex. At low shear rates, it generally reduces crystallinity, while at high shear rates it can increase it. However,

the impact on the relative abundance of α and γ crystalline phases is less consistent, and no clear trend was established across all processing conditions.

Besides, the average MW and elongational flow showed a combined effect in determining the tensile properties, due to their role in tailoring the microstructure. In particular, the high MW matrix processed under strong elongational flow exhibited pronounced strain hardening and higher tensile strength but lower elongation at break, attributable to well-oriented macromolecular chains. In contrast, in presence of low MW chains and at lower DR, a more ductile behavior with less strength was observed.

Lastly, despite the variations in the content of the α and γ crystalline phases, a negligible effect of the polymorphism on the mechanical behavior was appreciated.

# Chapter 6

# Effect of elongational flow and LDH aspect ratio on PA6 homopolymer blends


## Abstract

This Chapter investigates the relationships between processing parameters, microstructure and properties in PA6-based nanocomposites containing double-layered hydroxide as a nanofiller. The study focused on the effects of compounding screw speed (150 or 300 rpm), non-isothermal uniaxial elongational flow intensity, average MW (high and low viscosity), MW distribution (mono- and bimodal), and aspect ratio of the LDHs (low and high). The nanofiller concentration was maintained constant at 10 wt%. The materials were characterized using scanning electron microscopy, thermal and mechanical analyses. Also, the drawability in the molten state was evaluated.

The positive impact of polymer viscosity, screw speed, and elongational flow on promoting tactoids' rupture and platelet dispersion emerged. Conversely, the effect of the aspect ratio was found to be related to the applied flow field due to the interplay between strong lamellar interactions and the tendency to align with uniaxial flow. Besides, the general nucleating effect of the LDHs on the polymer matrix was assessed, as well as the dependency of the melting enthalpy on the dispersion, intercalation, and orientation of the nanofiller platelets. Considering the polymorphism, the predominant role of the MW of the matrix over the filler's aspect ratio and the intensity of the applied elongational flow in determining the α-to-γ content emerged in the monomodal MW systems. Lastly, the presence of LDHs was found to have a positive effect on the nanocomposites' drawability, which also depended on the MW, MW distribution, and screw speed.

## 6.1 Introduction

In addition to the effect of the application of the elongational flow in the processing parameters-microstructure-properties relationship of matrices and polymer blends, as discussed in Chapters 5, its role is worth to be further investigated in the case of polymer-based nanocomposites. In fact, such materials represent a valuable alternative to traditional composites as they represent a solid compromise between low cost and weight, coupled with good mechanical properties [589,596–601]. In this field, LDHs are classified as two-dimensional layered filler, characterized by sub-micrometric dimensions and very high surface area, providing enhanced interactions with the polymer matrix when a good dispersion is reached [589,597,600,602,603]. The phenomenon occurs owing to the intercalation of the polymer chains in-between the nanofiller layers or the exfoliation of the filler [115,589,599,600,602,604]. The final morphology is strongly related to the interactions with the polymer matrix, which determine the resulting properties of the nanocomposite. In particular, when poor interactions occur, a phase-separated material is obtained and the performances are comparable with those of traditional composites However, increased interactions with the matrix lead to intercalation and property improvement, while the true potential of nanocomposites is realized when the nanofiller is fully exfoliated. In this case, the final properties greatly exceed those obtained with a traditional approach because the interaction surface area between the filler and the polymer matrix is maximized and microscopically homogeneous materials are obtained. In both cases, the composite can be referred as “nano-composite” [589,596,597,603,605,606].

Considering the importance of good interfaces in order to obtain materials with better performance, it is common practice to modify the surface of fillers to improve interaction with the matrix. In the specific case of layered fillers, ion exchange is one of the most effective methods and consists of inserting counterions between adjacent lamellae. In this way, they are less tightly packed. In addition, usually the counterions have higher chemical affinity with the host polymer matrix than unmodified LDHs. As a result, the insertion of polymer chains between the lamellae is promoted, ultimately resulting in enhanced intercalation and exfoliation [597,603,607].

Furthermore, the concentration of the filler is important in order to effectively obtain a nanocomposite. In fact, if the concentration is too high, aggregation occurs and, as a result, the advantages associated with the large surface area are lost. One of the main negative effects is observed for the mechanical properties. Specifically, the tensile strength generally increases with increasing nanoclay concentration up to a value beyond which the material shows performance comparable to those of the traditional composite. This has been associated with the aggregation of filler particles and the formation of agglomerates having micrometric dimensions [589,596,603,608–610].

Another strategy that can be used to promote the dispersion of nanofillers in the polymer matrix involves the production step of the nanocomposite itself. In particular, when considering melt blending, it was found that the application of a

non-isothermal uniaxial elongational flow on the material promotes the breakdown of aggregates that typically form during conventional melt compounding. As a result, an improved morphology characterized by a dispersion of nanometric-sized fillers is obtained [115,137,589,611–613]. Furthermore, it has been found that when the elongational flow is applied to a composite containing anisotropic nanofillers, such as nanoclays, the nanofillers orient in the direction of the applied flow. As a consequence, an overall anisotropic morphology is obtained in the nanocomposite, and the systems that are subjected to stretching exhibit enhanced properties compared to those having an isotropic microstructure [555,614,615]. More importantly, in the case of nanoclays and LDHs, it has been demonstrated that the application of non-isothermal elongational flow induces the occurrence of a sort of transition from intercalated to exfoliated morphology. In particular, an increase of the interlayer distance in the tactoids and intercalated structures present in the as-compounded nanocomposites was observed, resulting in the formation of exfoliated morphologies or intercalated structures characterized by a higher interlayer distance as compared to the isotropic materials [115,589].

In the present study, PA6-based nanocomposites were produced, and the relationships between processing parameters, microstructure and properties was investigated in presence of the non-isothermal uniaxial elongational flow. In particular, the three polymeric system studied in Chapter 5 were used. Namely, the 100HV and 100LV matrices, and the 30HV blend. Then, two LDHs differing solely by the surface area were selected (identified alternatively as D17 – high surface area – and D25 – low surface area, as detailed in Appendix A.1.2). In all cases, the nanofiller concentration was maintained constant at 10 wt%. Besides, on a processing point of view, the compounding screw speed was set at 150 or 300 rpm alternatively, while increasing intensities of elongational flows were used and quantified with the DR of the resulting fiber (see Eq. A.3).

An overview of the variables and constant factors used is reported in Table 14.

In the present Chapter, the material identification will include information regarding the amount of HV in the polymer, the type of hydrotalcite, the extruder screw rotation speed, and the application of uniaxial elongational flow. For instance, "30HV_150rpm_D17_DR1" indicates a composite with a matrix consisting of 30 wt% HV and 70 wt% LV. The material was compounded at 150 rpm and contains hydrotalcite D17. Lastly, no uniaxial flow was applied to the material at the die exit.

Besides, in the case of morphological characterization, the images of the fibers will be labeled as "fiber" because for all the materials the smallest diameter available was selected and analyzed. Also, “nofiller” refers to the unfilled polymeric materials.

It is important to emphasize that, in the present Chapter, the results are discussed also in light of the findings reported in Chapters 4 and 5, which addressed the relationship between processing parameters, microstructure, and final properties in PA6-based homopolymer blends subjected either exclusively to shear flow or to combined shear and elongational flow. In particular, the data from those earlier chapters are labeled as “nofiller,” to distinguish them from the formulations

introduced here and containing LDHs. Additionally, the data marked as "DR1" correspond specifically to the dataset discussed in Chapter 4, in which no elongational flow was applied.

**Table 14. Variables and constant factors used for the production of the PA6-based nanocomposite fibers.**

| | Factor | Levels | | |
|---|---|---|---|---|
| Variables | Screw speed [rpm] | 150 | | 300 |
| | MW distribution | Monomodal | | Bimodal |
| | HV:LV content [wt% of HV] | 0 | 30 | 100 |
| | Stretching speed [rpm] | From 0 to 1000 or to filament breakage - Acceleration mode | | |
| | Filler aspect ratio | D25 (low) | | D17 (high) |
| Constants | Filler content [wt%] | 10 | | |
| | Feed rate [g/h] | 290 | | |
| | Temperature [°C] - from hopper to die | 220\220\225\230\230\230\230\230 | | |

# 6.2 Characterization

## 6.2.1 Drawability

In Figure 67A and B are presented the BSR (see Eq. A.2) of the composites containing D25 and D17, respectively. Additionally, the data concerning the unfilled materials and discussed in Section 5.2.1 are recalled in Figure 67C.

Firstly, focusing on the composites containing the low aspect ratio LDHs (Figure 67A), it can be appreciated that the two monomodal MW polymer-based materials were not affected by breakage when the compounding speed of 150 rpm was used for the production. Also, this great drawability was observed in the high MW-based material processed at 300 rpm, while an abrupt reduction affected the low MW polymer-based one obtained in the same conditions.
Besides, a different behavior characterized the composite based on the 30HV blend. In fact, the composite was affected by breakage despite the screw rotation speed used in the production step. Additionally, the enhancement of the applied shear rate resulted in the decrease of the drawability.

Considering the materials filled with high aspect ratio LDHs (Figure 67B), it emerges that the low MW polymer-based composite has a lower drawability than the high MW polymer-based one when the two are compounded at 150 rpm. In fact, only the former was affected by breakage. However, when the higher processing speed was used, none of the unimodal MW distribution polymer-based materials break during the drawing step. On the contrary, the 30HV-based composite showed a great drawability when compounded at 150 rpm, while a detrimental decrease of the BSR affected the material obtained with a screw speed of 300 rpm.

Furthermore, from the comparison of the drawability of the composites containing D25 or D17 alternatively, further considerations emerged. In fact, the 100HV-based composites exhibit remarkable drawability. Notably, this appears to be unaffected by variations in screw rotation speed or by the aspect ratio of the nanofiller itself. In addition, when comparing the BSR calculated for the nanocomposites with those of the unfilled matrices (Figure 67C), the data suggest that the presence of LDHs contributes positively to the structural integrity and deformation capacity of the material during the application of uniaxial elongational flow, because the suppression of breakage during the drawing step is achieved.

On the other hand, the drawability of the 100LV-based nanocomposites seems to support an interplay between the aspect ratio of the nanofiller and the screw rotation speed during processing. Specifically, the results indicate that when a low aspect ratio filler (D25) is employed, the drawability of the material reaches its maximum if subjected to a low shear rate. In contrast, when a high aspect ratio filler is used (D17), the optimal drawability is observed at the highest screw rotation speed, suggesting that increased shear promotes better dispersion or alignment of the high aspect ratio particles, thereby enhancing the material's deformation capability. Besides, regardless of the specific combination of processing parameters and filler geometry, it is evident that the inclusion of LDHs consistently improves the drawability of the composite compared to the neat polymer matrix. This improvement is particularly notable given that fiber production was not achievable in the case of the pure 100LV polymer processed at 300 rpm, as shown in Figure 67C.

Lastly, considering the 30HV-based nanocomposite, regardless from the aspect ratio of the LDH, the drawability is poorly affected by the increase of the rotation screw speed during compounding. On the other hand, taking into account the behavior of the unfilled blends (Figure 67C), the introduction of the nanofiller promoted the inversion of the dependence of drawability on the shear rate applied.

Summarizing, when considering monomodal polymer matrices, the introduction of LDHs generally has a positive impact on the material's deformability. Interestingly, the influence of shear rate and nanofiller aspect ratio on these composites appears to depend primarily on the MW of the polymer. Specifically, in high MW systems, the effect of these processing parameters becomes secondary or even negligible, as drawability is consistently maximized regardless of the conditions applied. Conversely, in low MW systems, it is the combined effect of shear rate and aspect ratio that ultimately governs the final drawability of the composite.

A different behavior emerges when a bimodal MW polymer is considered. In this case, the drawability trend observed in the composite diverges significantly from that of both high and low MW monomodal matrices. Also, the behavior differs from that of the unfilled bimodal polymer. Notably, for the LDH-filled bimodal system, drawability is consistently maximized at low screw rotation speeds, independent of the aspect ratio of the nanofiller used. This suggests a distinct and possibly synergistic interaction between the bimodal polymer architecture and the filler under low-shear processing conditions.

Therefore, from the above discussion it can be appreciated that the role of the MW and MW distribution is predominant in determining the effect of the screw rotation speed and aspect ratio on the drawability of the composites.

To gain further insight on the effect of the processing parameters in determining the drawability of the composites, some rheological aspects have to be considered. In Section 5.2.1, the role of the entanglement density in determining material stretchability was discussed, with particular emphasis on how MW, MW distribution, and screw rotation speed affect macromolecular orientation [198,478,545,548,550,551,554]. Besides, the introduction of LDHs into the polymeric systems, can lead to various phenomena, either enhancing or reducing the drawability of the composites. An improvement in drawability is typically observed when the nanofillers are well-aligned with the flow direction and free of agglomerates [616,617]. Also, in PA6\LDHs systems the local slippage of macromolecules at the nanofiller interface has been reported to facilitate macromolecular mobility [616]. On the other hand, reduced drawability in layered nanocomposites can result from several factors. For instance, if intercalation occurs the macromolecules may be partially immobilized on the LDHs surface, hindering their ability to orient along the elongational flow direction [589,616]. Additionally, limited drawability may be attributed to filler morphology. In particular, insufficient disaggregation or poor alignment of the filler particles can obstruct the movement of macromolecules, and further hinder their response to elongational flow [616,617].

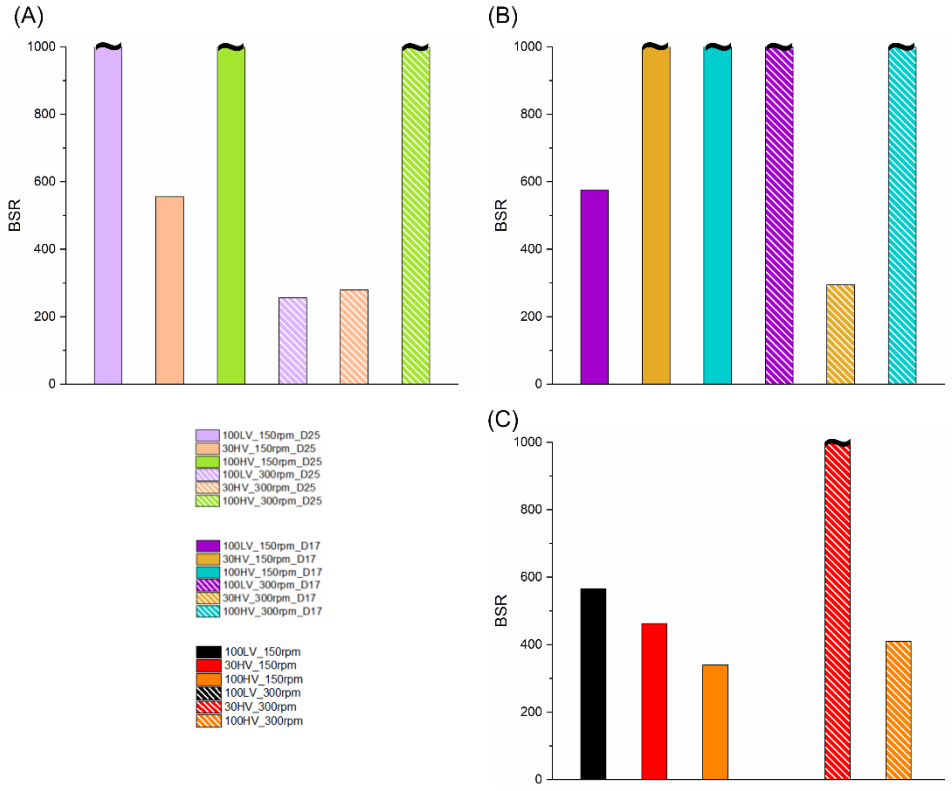


**Figure 67. BSR of the materials compounded at 150 or 300 rpm containing (A) D25 or (B) D17. In (C) the data relative to the unfilled materials are reported. The "~" indicates the materials in which no breakage was observed with the experimental conditions used. Besides, it was not possible to obtain the fibers for the 100LV_300rpm, thus no data are reported.**

## 6.2.2 Morphology

The morphology of the nanocomposites containing D25 or D17 was examined. In particular, the characterization focused on comparing the unstretched material with the drawn fibers to assess how processing conditions affect the distribution and alignment of LDHs particles. Also, elemental mapping and spectra via EDX were employed to evaluate the dispersion of magnesium (Mg) and aluminum (Al), thus providing insight into the presence of aggregates and the distribution of the nanofiller. Lastly, it is important to note that all morphological observations were carried out on the cross-sections of the samples, corresponding to the direction perpendicular to both the material flow direction and the axis of uniaxial elongation.

### 6.2.2.1 D25

Firstly, the morphology of the nanocomposites containing the lowest aspect ratio LDHs will be presented and discussed.

In Figure 68A, the cross-section of the 100LV_150rpm_D25_DR1 is shown. As confirmed by the EDX analyses reported in Figure 68B and C for areas 1 and 2 respectively, agglomerates are clearly distinguished in the isotropic material. Indeed, the poor deagglomeration was confirmed by the spectra reported in Figure 68D referred to area 3, highlighting the absence of both Al and Mg, which would

have been indicative of the presence of dispersed LDHs.
On the contrary, an improvement in the dispersion of the nanofiller was achieved in the same material processed at higher screw speed, in accordance with the literature [618–621]. In fact, as can be appreciated from the cross-section of the 100LV_300rpm_D25_DR1 reported in Figure 69A, an important reduction of the dimensions of the clusters of LDHs is obtained (see the EDX spectra of area 1 in Figure 69B) if compared with the morphology described above (Figure 68A). Besides, the enhanced dispersion of the nanofiller is confirmed from the spectra of area 2 reported in Figure 69C. Therefore, owing to the application of the higher shear rate, the intercalation of the polymer chains in-between the LDHs' layers was promoted in the isotropic nanocomposite processed at 300 rpm.

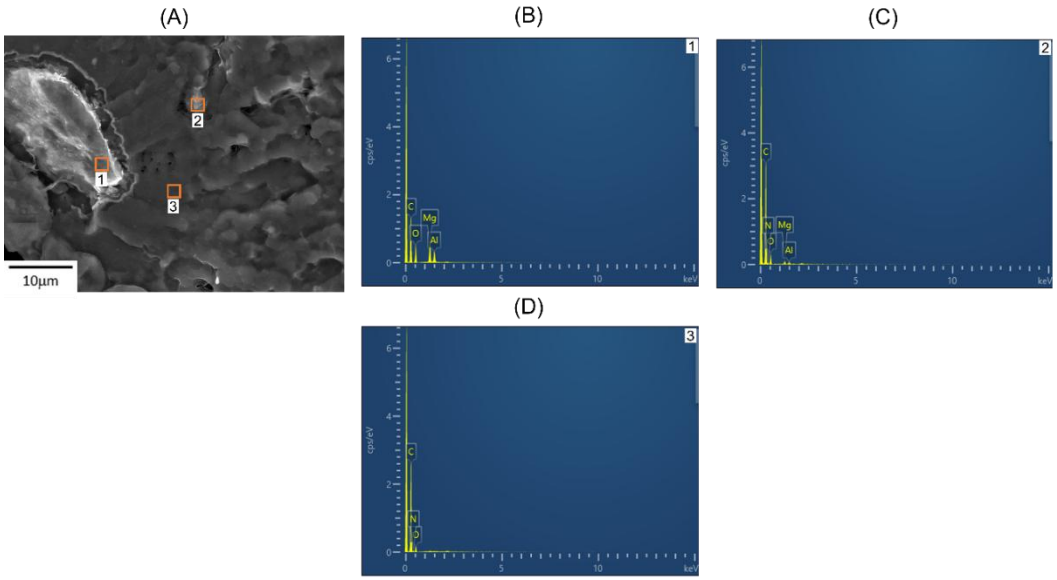


**Figure 68. (A) Morphological analysis of the 100LV_150rpm_D25_DR1 and corresponding EDX spectra of the spots labelled as (B) 1, (C) 2 and (D) 3.**

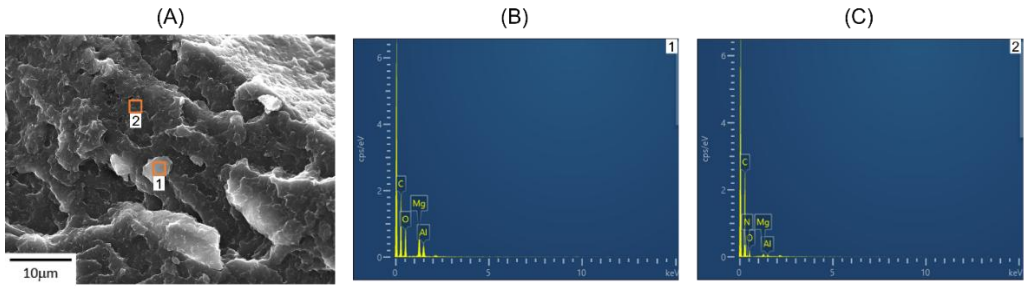


**Figure 69. (A) Morphological analysis of the 100LV_300rpm_D25_DR1 and corresponding EDX spectra of the spots labelled as (B) 1 and (C) 2.**

Furthermore, the morphology of the 100LV-based systems greatly improved after the application of the elongational flow. In fact, in the material compounded at 150 rpm the breakage of the agglomerates was effectively achieved in the fibers, if compared to those present in the isotropic counterpart (see Figure 70A and Figure

68A, respectively). Specifically, a homogeneous dispersion of tactoids in the matrix was obtained (see the EDX spectra for areas 1 and 2 in Figure 70B and C). Also, successfully intercalation of the nanofiller lamellae was confirmed by the EDX spectra of area 3 (Figure 70D), in which the presence of Al and Mg was assessed. Besides, a further improvement of the morphology can be appreciated when considering the cross-section of 100LV_300rpm_D25_fiber reported in Figure 71A. In fact, in this case nor tactoids or stacked lamellae were detected from the EDX maps of Al and Mg (see Figure 71B and C, respectively). On the other hand, the homogeneous dispersion and distribution was revealed from the elemental analyses, thus indicating that a good intercalation or even exfoliation of the LDHs was achieved.

These improvements in microstructure are owed to the applied elongational flow having an active role in both the breakup of the agglomerates and the preferential orientation of the nanofiller in accordance with the direction of the uniaxial field [115,137,589,622–624]. In addition, considering the BSR of the just discussed fibers further considerations of the role of the shear and elongational flow emerge. In fact, 100LV_150rpm_D25_fiber did not break during the drawing step, while 100LV_300rpm_D25_fiber broke at a BSR of about 300 (see Figure 67A). In other words, the morphologies of the former samples (Figure 70) result from applying a much more intense elongational flow that that applied to the former set of fibers (Figure 71). However, the better dispersion of LDHs in the polymer is observed for those obtained at higher rotation speeds. This can be explained by considering the morphology of the isotropic nanocomposites in the two cases. Micrometric agglomerates were found in 100LV_150rpm_D25_DR1 (Figure 68) but not in 100LV_300rpm_D25_DR1 (Figure 69) because the higher shear rate applied in the latter case promoted the distribution of the nanofiller in the matrix already during the compounding step. Therefore, this analysis highlighted the decisive role of elongational flow in dispersing the nanofiller and intercalating it with macromolecules, but also assesses the positive effect of increasing the shear rate in fostering the homogeneous distribution of intercalated LHDs layers in the resulting fibers [115].

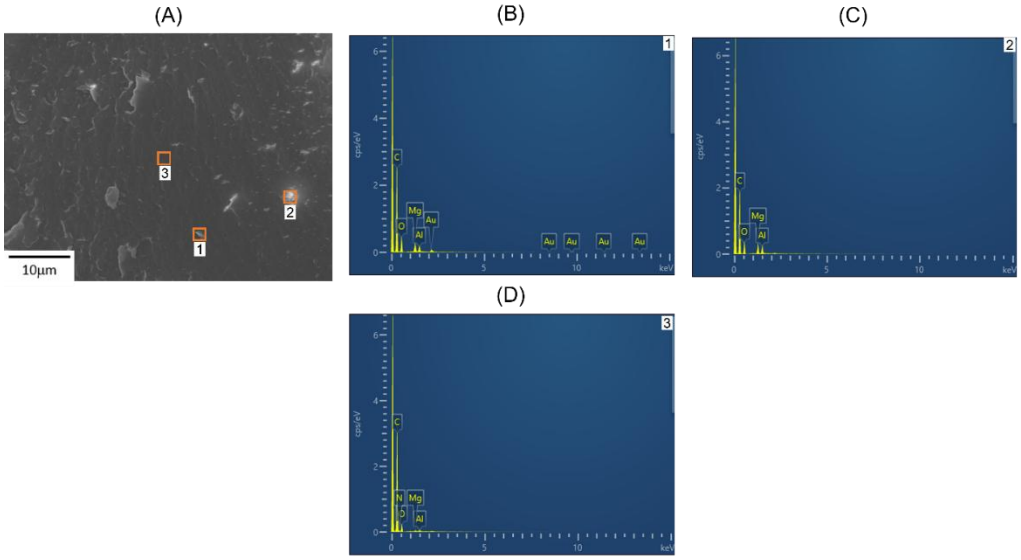


**Figure 70. (A) Morphological analysis of the 100LV_150rpm_D25_fiber and corresponding EDX spectra of the spots labelled as (B) 1, (C) 2 and (D) 3.**

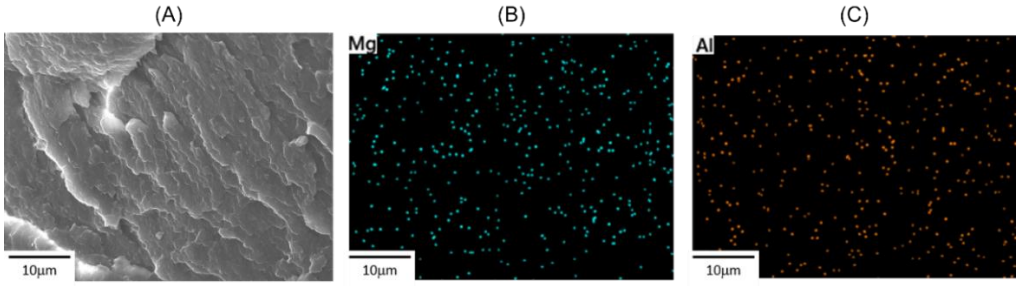


**Figure 71. (A) Morphological analysis of the 100LV_300rpm_D25_fiber and corresponding EDX maps of the (B) Mg and (C) Al.**

In Figure 72 and Figure 73 the morphological analyses of the isotropic nanocomposites based on 100HV and processed at 150 or 300 rpm, respectively, are reported. In the first case, the homogeneous distribution of nanometric tactoids clearly emerges, highlighting a good microstructure achieved in the 100HV_150rpm_D25_DR1. Besides, when the isotropic nanocomposite compounded at 300 rpm is considered, the EDX maps (see Figure 73B and C for Mg and Al, respectively) confirms the further improvement of the dispersion of the nanofiller owing to the grater shear rate applied [618–621]. In particular, in this case the intimate contact with the macromolecules was achieved thanks to the intercalation of the LDHs' layers.

Furthermore, additional considerations emerge from the comparison of the morphological analyses of the isotropic 100LV- (Figure 68 and Figure 69) and 100HV-based (Figure 72 and Figure 73) nanocomposites processed at 150 or 300 rpm. Specifically, considering the nanocomposites processed at the same screw speed, a systematic improvement of the microstructure is appreciated for those having the high MW matrix. At 150 rpm, aggregates are observed in 100LV_150rpm_D25_DR1 (Figure 68A) but are not present in the

100HV_150rpm_D25_DR1 (Figure 72A), where a uniform distribution of nanometric stacks of lamellae was achieved instead. Additionally, at 300 rpm only in the 100LV_300rpm_D25_DR1 tactoids were present (Figure 69A), while a homogeneous distribution of intercalated nanofiller was obtained in the 100HV_300rpm_D25_DR1 (Figure 73A). The improved morphology obtained for composites with a higher MW matrix compared to those with a lower MW one, with the other process parameters kept unchanged, can be attributed to the different viscosities of the two polymers [521,625–628]. In fact, as discussed in Chapter 4 referring to Figure 54, the 100HV is characterized by a higher viscosity if compared to 100LV, regardless the rotation speed used for compounding. Therefore, since a matrix with higher viscosity is more effective at transmitting shear forces to the nanofiller, 100HV is expected to foster the breakage and dispersion of the nanofiller more effectively than 100LV. Thus, it is consistent with the more homogeneous microstructures obtained in nanocomposites processed at the same screw speed with a 100HV matrix. Furthermore, it is important to note that the positive impact of increasing the screw rotation speed in promoting the achievement of a well-dispersed morphology is effective, independently from the MW considered.

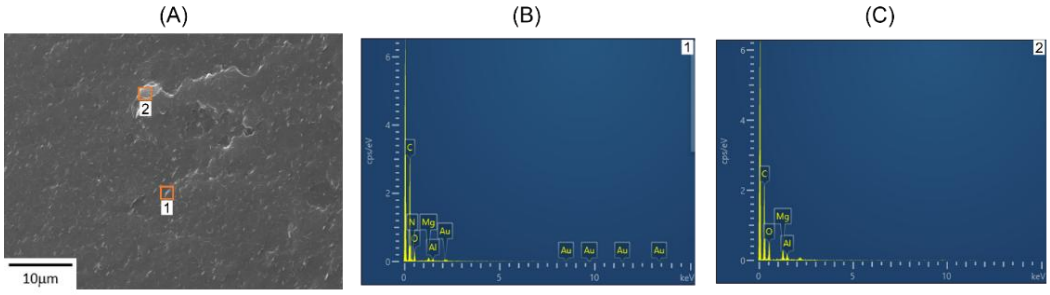


**Figure 72. (A) Morphological analysis of the 100HV_150rpm_D25_DR1 and corresponding EDX spectra of the spots labelled as (B) 1 and (C) 2.**

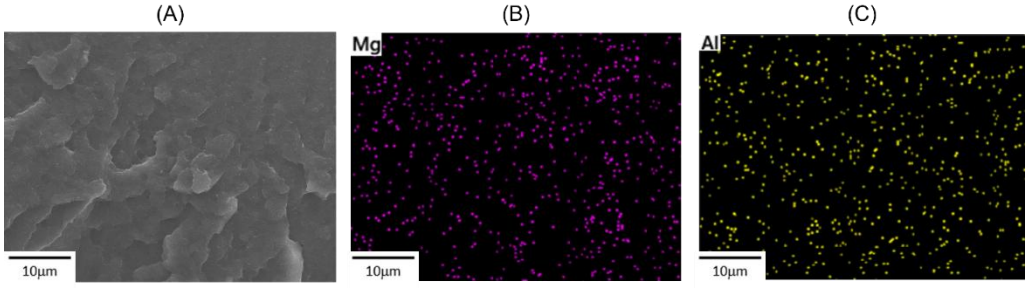


**Figure 73. (A) Morphological analysis of the 100HV_300rpm_D25_DR1 and corresponding EDX maps of the (B) Mg and (C) Al.**

The morphologies of the cross-sections of the fibers of 100HV_150rpm_D25 and 100HV_300rpm_D25 are reported in Figure 74A and Figure 75A, respectively. In the material compounded at the lower screw speed, a homogeneous dispersion of nanometric tactoids is appreciated, and confirmed by the EDX spectra in Figure 74B. Additionally, a similar conformation of the nanofiller was obtained for the fibers processed at 300 rpm.

From the comparison of the morphologies of the fibers based of 100HV with the corresponding isotropic materials (see Figure 72 and Figure 73 for 100HV_150rpm_D25_DR1 and 100HV_300rpm_D25_DR1, respectively), an apparent agglomeration of the nanofiller seem to have occurred during the drawing step. This behavior has been already reported in the literature and concerns the application of the elongational flow to nanocomposites characterized by a homogeneous distribution of intercalated or exfoliated nanolayers after the melt compounding step [115,629–632]. More specifically, the nanofiller reaggregation has been associated with two synergistic phenomena. On one hand, the layers dispersed after the compounding step are characterized by a higher mobility compared to tactoids. Additionally, electrostatic interactions occur between neighboring platelets of nanofillers due to the superficial charges. Consequently, when elongational flow is applied to a well-dispersed nanocomposite, the separated layers of nanofillers first align according to the direction of the uniaxial field. Then, when the platelets are close enough for electrostatic interaction to occur, they stick together, forming house of cards structures and agglomerates [115,632].

Furthermore, considering the BSR of the two systems, it emerges that the fibers of 100HV_150rpm_D25 and 100HV_300rpm_D25 were stretched with the same intensity of elongational flow (see Figure 67A). In the above discussion relative to the 100LV-based systems, the morphology of the corresponding isotropic material, and thus of the shear rate applied during the compounding step, emerged to have a role in promoting the effectiveness of the elongational flow in improving the breakup of the nanofiller and the dispersion of the LDHs' platelet in the polymeric matrix [115]. On the contrary, the fibers having 100HV as a matrix show a comparable morphology regardless of the screw speed used in the compounding step (see Figure 74 and Figure 75). This behavior can be explained considering that the isotropic 100HV-based nanocomposites were characterized by well-dispersed morphologies. As a consequence, a comparable impact of the elongational flow on the LDHs' dispersion and orientation can be suggested. In fact, it is likely that after the primary breakup of the tactoids and increasing of the interlayer distance between the platelet, the two systems had a similar morphological evolution owing to the application of the uniaxial field to well-intercalated microstructures. Therefore, leading to similar re-agglomeration phenomena [115]. As a consequence, it can be appreciated that the effect of the elongational flow on the evolution of nanofiller organization is unaffected by the shear rate applied during compounding, if a well-dispersed morphology was already obtained prior to drawing.

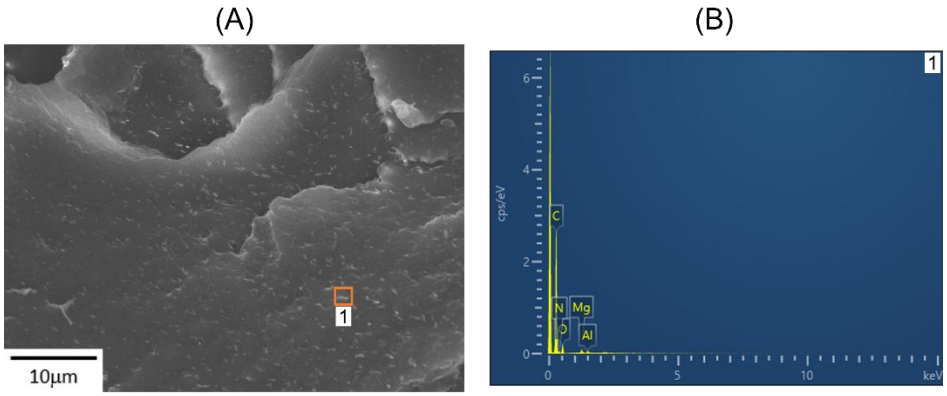


**Figure 74. (A) Morphological analysis of the 100HV_150rpm_D25_fiber and corresponding EDX spectrum of the spots labelled as (B) 1.**

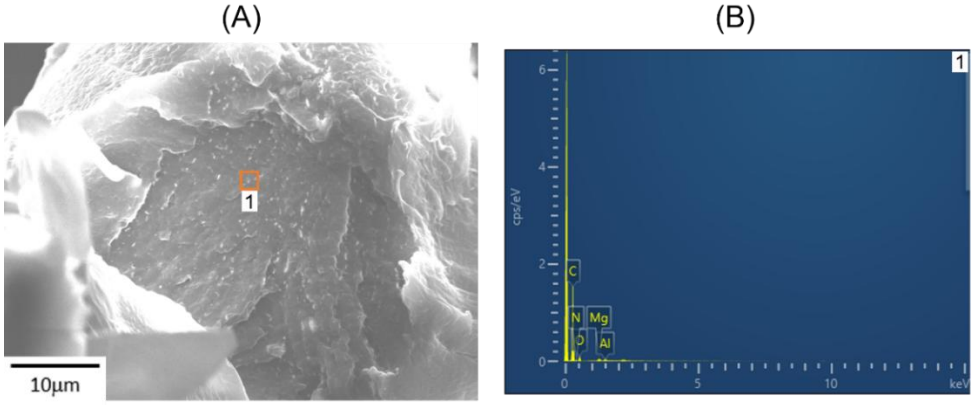


**Figure 75. (A) Morphological analysis of the 100HV_300rpm_D25_fiber and corresponding EDX spectrum of the spots labelled as (B) 1**

Moving forward to the bimodal MW blend, Figure 76A shows the morphology of the isotropic nanocomposite processed at 150 rpm. As confirmed by the EDX spectra in Figure 76 B and C (for area 1 and 2, respectively), a homogeneous distribution of nanometric stacks of lamellae emerges within the surface. Furthermore, the nanocomposite based on 30HV and processed at 300 rpm (Figure 77A) shows a significant reduction in tactoids' size and quantity compared to the same material compounded at 150 rpm (Figure 76A). Besides, a superior dispersion of the LDHs' layers was achieved up to intercalation with the polymer matrix and eventually exfoliation, as confirmed by the EDX spectrum in Figure 77B. This improvement in the dispersion of the nanofiller within the nanocomposite, which occurred with an increase in screw speed during the compounding step, is consistent with observations in the case of monomodal MW-based materials (see Figure 68, 68, 71 and 72). As in those cases, the improved morphology is attributed to the positive impact of the higher shear rate on breaking the stacks of lamellae and dispersing them in the polymeric matrix [618–621].

Additionally, comparing the mophologies of the isotropic nanocomposites processed at the same screw speed provides insight into the role of the viscosity of

the polymeric matrix in the nanofiller dispersion during compounding. In fact, when the materials processed at 150 rpm are considered, the dimension and distribution of the tactoids in 30HV_150rpm_D25_DR1 (Figure 76) is in-between those of the 100LV_150rpm_D25_DR1 (Figure 68) and 100HV_150rpm_D25_DR1 (Figure 72). Also, a similar trend is appreciated for the nanocomposites compounded at 300 rpm (see Figure 69, 72 and 76 for 100LV_300rpm_D25_DR1, 100HV_300rpm_D25_DR1 and 30HV_300rpm_D25_DR1, respectively). These evidences can be explained considering that the viscosity of the 30HV blend emerged to be in-between those of the two unimodal MW matrices, independently from the screw speed considered (see Figure 54 in Chapter 4). Since the shear stress transmitted to the nanofiller during compounding that promotes the tactoids' breakup is dependent on the viscosity of the polymeric matrix, and since the latter is between those of the two monomodal MW matrices in the case of the blend, the final morphology obtained is in accordance with the expected results based on the effect of viscosity on LDHs dispersion [521,625–628].

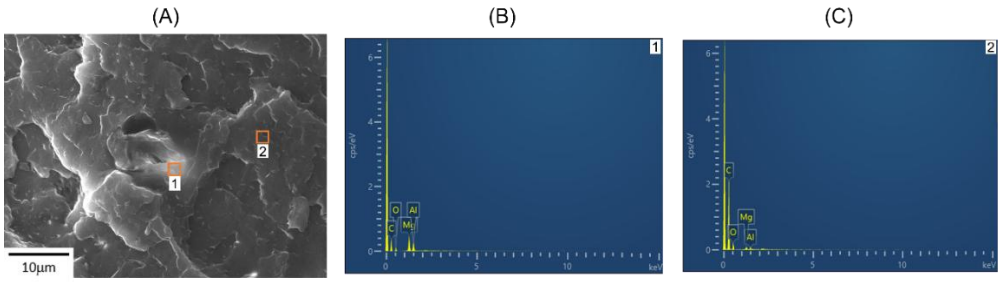


**Figure 76. (A) Morphological analysis of the 30HV_150rpm_D25_DR1 and corresponding EDX spectra of the spots labelled as (B) 1 and (C) 2.**

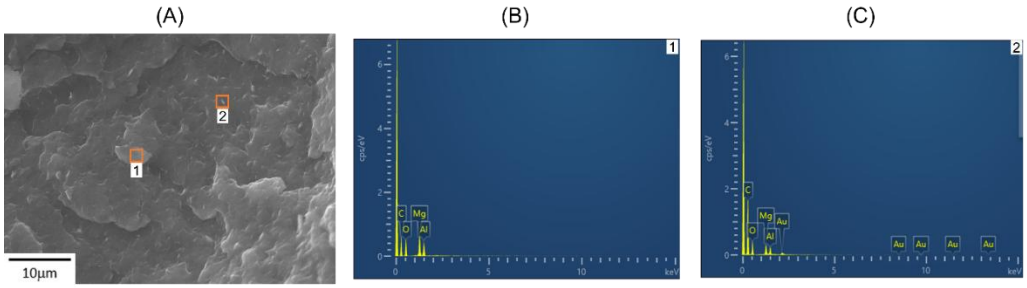


**Figure 77. (A) Morphological analysis of the 30HV_300rpm_D25_DR1 and corresponding EDX spectra of the spots labelled as (B) 1 and (C) 2.**

The morphology obtained in the 30HV_150rpm_D25_fiber is reported in Figure 78A. The EDX spectra show the simultaneous presence of stacked lamellae (see Figure 78B and C) and intercalated LDHs platelets well-dispersed in the polymeric matrix (see Figure 78D). Furthermore, when the fibers processed at 300 rpm are considered, a further improvement in layers dispersion was assessed (Figure 79A). In fact, few nanometric tactoids are present (see Figure 79B for area 1), while most of the section is characterized by a homogeneous morphology, in

which the intercalated lamellae are uniformly dispersed in the polymer matrix, as evidenced by the EDX spectrum of area 2 reported in Figure 79C.

From the comparison of the cross-sections of the 30HV-based fibers (Figure 78 and Figure 79) with the morphologies of the corresponding isotropic nanocomposites (Figure 76 and Figure 77, respectively), it can be clearly appreciated the role of the applied elongational flow in promoting the overall breakup of the nanofillers' tactoids towards a dispersion of LDHs' platelets in the polymeric matrix [115,137,589,622–624].

On the other hand, considering the BSR (see Figure 67A) it emerges that 30HV_150rpm_D25_fiber was exposed to a more intense elongational flow than 30HV_300rpm_D25_fiber. Also, a more homogeneous dispersion and distribution of the nanofiller was assessed in the isotropic material corresponding to the latter system (see Figure 76 and Figure 77 for 30HV_150rpm_D25_DR1 and 30HV_300rpm_D25_DR1, respectively). According to the discussion on 100LV-based nanocomposites, the more homogeneous morphology obtained in the isotropic 30HV containing D25 and compounded at 300 rpm likely promoted the dispersion of the LDH layers within the matrix through the applied elongational flow, resulting in better dispersion in the fibers processed at 300 rpm [115].

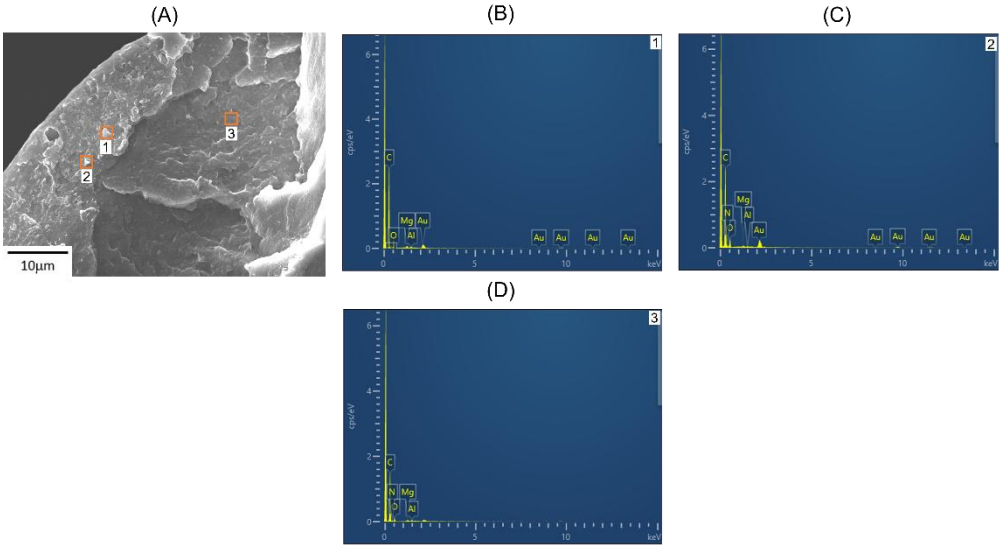


**Figure 78. (A) Morphological analysis of the 30HV_150rpm_D25_fiber and corresponding EDX spectra of the spots labelled as (B) 1, (C) 2 and (D) 3.**

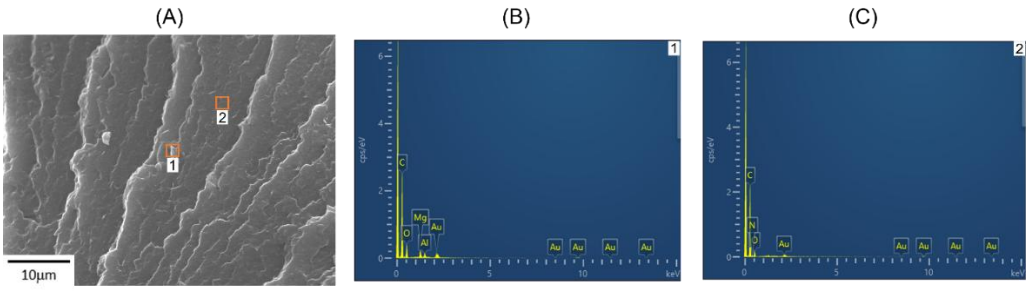


**Figure 79. (A) Morphological analysis of the 30HV_300rpm_D25_fiber and corresponding EDX spectra of the spots labelled as (B) 1 and (C) 2.**

### 6.2.2.2 D17

Considering the filler having the larger surface area, the morphologies of the composites based on the 100LV matrix and processed without applying the elongational flow, at a screw speed of 150 or 300 rpm alternatively, are reported in Figure 80 and Figure 81, respectively. The compounding performed at the lowest shear rates (Figure 80A) resulted in a poor dispersion of the filler. In fact, the presence of large agglomerates clearly emerges from the EDX maps showing the Mg and Al distribution across the surface (see Figure 80B and C, respectively). However, as highlighted by the elemental maps shown in Figure 81B and C (corresponding to Mg and Al, respectively), even when processing the material at the highest screw rotation speed a quite inhomogeneous morphology was obtained.

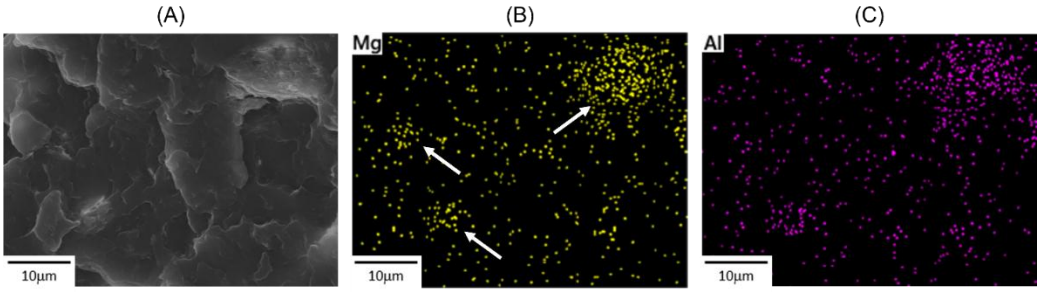


**Figure 80. (A) Morphological analysis of the 100LV_150rpm_D17_DR1 and corresponding EDX maps of the (B) Mg and (C) Al. The white arrow indicates the aggregate of LDH.**

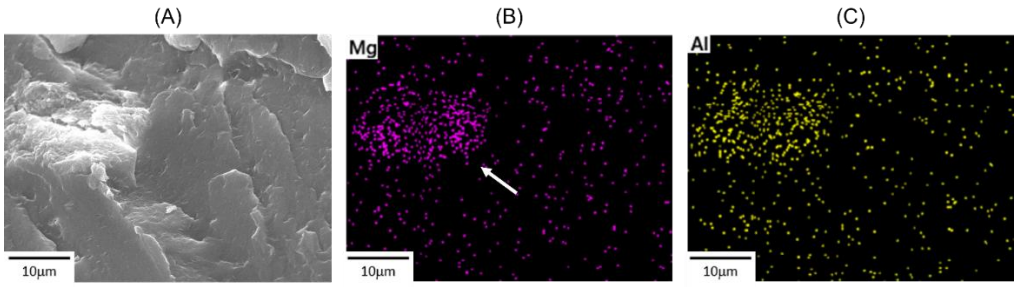


**Figure 81. (A) Morphological analysis of the 100LV_300rpm_D17_DR1 and corresponding EDX maps of the (B) Mg and (C) Al. The white arrow indicates the aggregate of LDH.**

On the other hand, when the uniaxial elongational flow was applied, an excellent dispersion of D17 in the 100LV matrix was reached at both the screw speeds. This can be clearly appreciated in Figure 82A for 100LV_150rpm_D17_fiber and in Figure 83A for 100LV_300rpm_D17_fiber. Besides, in the two cases the good distribution was confirmed with the EDX mapping of the corresponding cross-sections (see Figure 82B and C for the Mg and Al distribution in 100LV_150rpm_D17_fiber, and Figure 83B and C for the Mg and Al distribution in 100LV_300rpm_D17_fiber).

As discussed in Section 6.2.2.1, the good dispersion and distribution of the LDHs' platelets, up until they intercalate with polymer macromolecules, is due to the action of elongational flow. In fact, owing to the uniaxial flow applied, the nanofillers first reorient according to the axial direction. Then, the layers progressively exfoliate [115,137,589,622–624].

Additionally, it is interesting to note that the two fibers were obtained at different BSR (see Figure 67B) and, in particular, 100LV_300rpm_D17_fiber was not affected by rupture during the drawing step. Nonetheless, comparable morphologies emerged from the analyses of the cross sections (Figure 82 and Figure 83 for 100LV_150rpm_D17_fiber and 100LV_300rpm_D17_fiber, respectively). Considering the presence of agglomerates in the corresponding isotropic systems and the homogeneous distribution of dispersed intercalated nanofiller platelets in the fibers, it can be appreciated that in the 100LV-based nanocomposites containing D17 the beneficial effects of the elongational flow on achieving a good nanofiller distribution prevails over any impact related to the initial inhomogeneous morphology, even at low intensities of the applied uniaxial field.

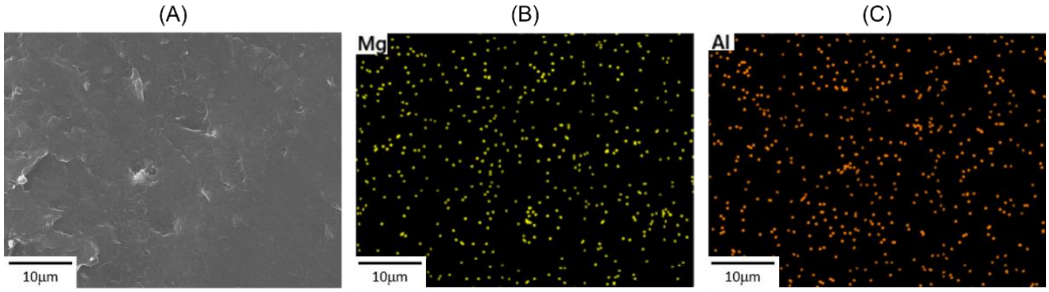


**Figure 82. (A) Morphological analysis of the 100LV_150rpm_D17_fiber and corresponding EDX maps of the (B) Mg and (C) Al.**

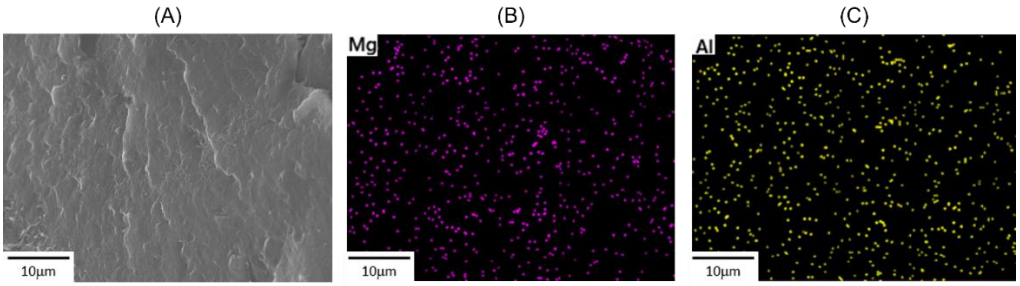


**Figure 83. (A) Morphological analysis of the 100LV_300 rpm _D17_fiber and corresponding EDX maps of the (B) Mg and (C) Al.**

Focusing on the isotropic 100HV-based nanocomposites, a homogeneous distribution of nanometric LDHs' tactoids characterizes the morphology of the material compounded at 150 rpm (Figure 84A), as confirmed by the EDX spectra of area 1 and 2 reported in Figure 84B and C, respectively. A further improvement of the microstructure is appreciated in the material processed at 300 rpm. In fact, the cross-section shown in Figure 85A clearly shows the absence of stacks of lamellae. Additionally, EDX maps reveal a uniform distribution of intercalated or exfoliated layers of LDHs within the polymeric matrix (Figure 85B and C for Mg and Al, respectively).

The improvement in the morphology of the nanocomposite, as assessed by comparing the 100HV_300rpm_D17_DR1 and the 100HV_150rpm_D17_DR1, was attributed to the increased shear rate applied to the former, which promoted the dispersion and distribution of the nanofiller in the matrix [618–621].

Besides, comparing the morphologies of isotropic nanocomposites containing D17 and based on 100HV or 100LV yields similar considerations with respect to viscosity as those found in the presence of D25 (see Section 6.2.2.1). In particular, the most homogeneous dispersion of LDHs down to nanometric dimensions, or even intercalation of the layers, was achieved in the high-MW matrix-based nanocomposites when the same screw rotation speed was used during compounding (see Figure 80 and Figure 84 for 100LV_150rpm_D17_DR1 and 100HV_150rpm_D17_DR1; Figure 81 and Figure 85 for 100LV_300rpm_D17_DR1 and 100HV_300rpm_D17_DR1). This evidence can be attributed to the higher viscosity of the high MW matrix (see Figure 54 in Chapter

4) allowing a more effectively transmission of the forces to the nanofiller, thus promoting its breakup and dispersion in the polymer matrix [521,625–628].

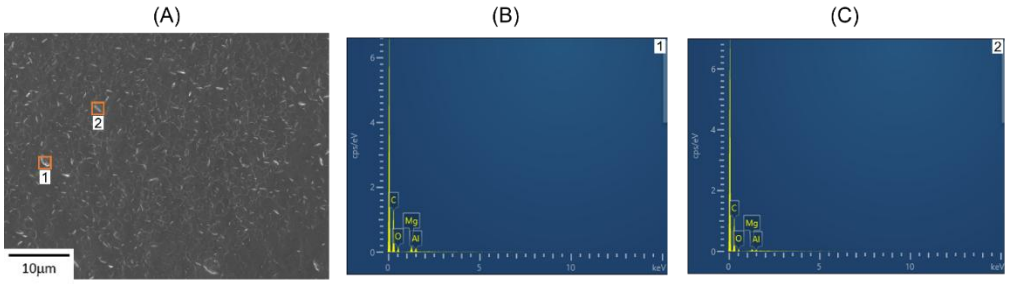


**Figure 84. (A) Morphological analysis of the 100HV_150rpm _D17_DR1 and corresponding EDX spectra of the spots labelled as (B) 1 and (C) 2.**

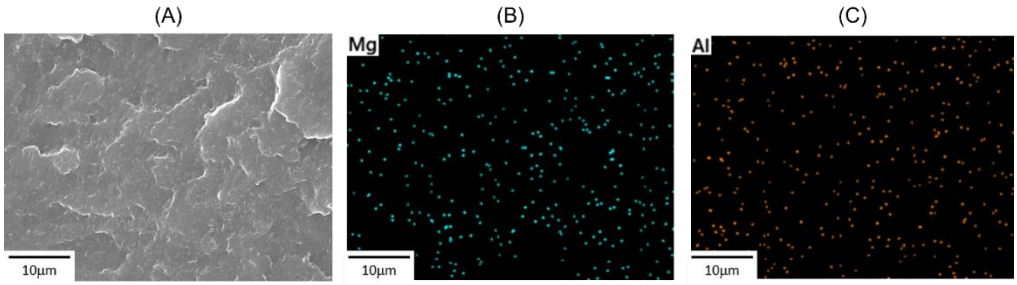


**Figure 85. (A) Morphological analysis of the 100HV_300rpm_D17_DR1 and corresponding EDX maps of the (B) Mg and (C) Al.**

Following the application of the elongational flow on the 100HV-based composite processed at 150 rpm, stacks of lamellae are detected across the surface of the fibers (Figure 86A), as confirmed by the corresponding elemental analyses of area 1 and 2 (Figure 86B and C, respectively). This morphology can be explained by the aforementioned re-agglomeration phenomena occurring when the elongational flow is applied to a nanocomposite in which good dispersion of the filler was achieved during the compounding step. In fact, as previousely explained (see Section 6.2.2.1), firstly the elongational flow fosters the separation of the platelets of the nanofillers. Then, if the layers are close enough for the superficial charges to interact electrostatically, reagglomeration occurs [115,629–632].
Conversely, no such structures emerge from morphological analyses of 100HV_300rpm_D17_fiber (Figure 87A). In fact, as assessed by the EDX maps (see Figure 87B and C for Mg and Al, respectively), a good intercalation and distribution of the LDHs' platelets was maintained in the fibers of the nanocomposite processed at 300 rpm.

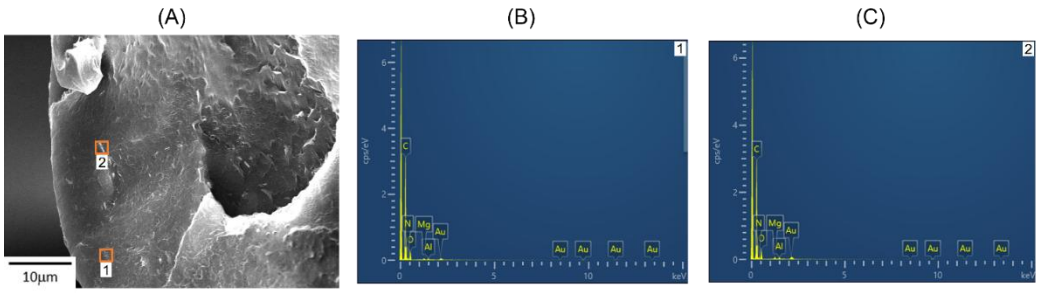


**Figure 86. (A) Morphological analysis of the 100HV_150rpm_D17_fiber and corresponding EDX spectra of the spots labelled as (B) 1 and (C) 2.**

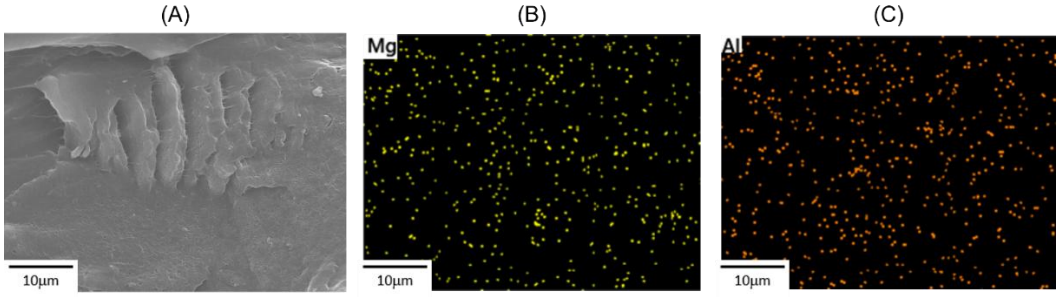


**Figure 87. (A) Morphological analysis of the 100HV_300rpm_D17_fiber and corresponding EDX maps of the (B) Mg and (C) Al.**

Lastly, when the 30HV-based nanocomposite was investigated, the presence of micrometric agglomerates embedded in the matrix of the isotropic materials was observed, regardless the screw rotation speed exploited. Specifically, Figure 88A refers to 30HV_150rpm_D17_DR1, while Figure 89A shows the morphology of 30HV_300rpm_D17_DR1. Further confirmation can be found in the corresponding elemental maps (Figure 88A and B for the Mg and Al in 30HV_150rpm_D17_DR1; Figure 89A and B for the Mg and Al in 30HV_300rpm_D17_DR1), which also highlight the minor role of the enhanced shear rate applied at higher screw speed in promoting the dispersion of the nanofiller. In fact, a modest reduction in agglomerate size is observed and a slight improvement in LDHs' distribution within the polymer matrix are achieved when comparing the morphological results of 30HV_300rpm_D17_DR1 with those of 30HV_150rpm_D17_DR1.

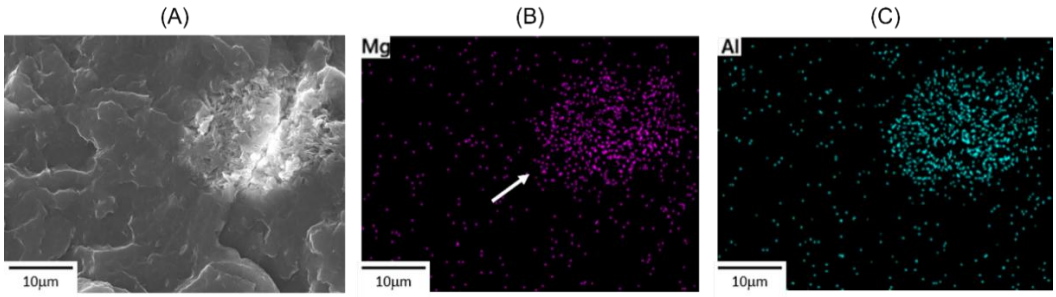


**Figure 88. (A) Morphological analysis of the 30HV_150rpm_D17_DR1 and corresponding EDX maps of the (B) Mg and (C) Al. The white arrow indicates the aggregate of LDH.**

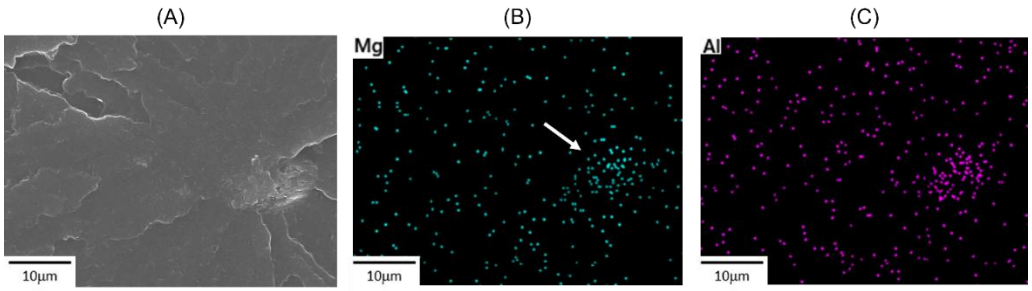


**Figure 89. (A) Morphological analysis of the 30HV_300rpm_D17_DR1 and corresponding EDX maps of the (B) Mg and (C) Al. The white arrow indicates the aggregate of LDH.**

Although agglomerates were observed in the isotropic nanocomposites based on 30HV, the morphology of the corresponding fibers was found to be characterized by a homogeneous distribution of intercalated or even exfoliated LHDs dispersed throughout the polymer matrix. In fact, the uniform microstructure was confirmed for both 30HV_150rpm_D17_fiber and 30HV_300rpm_D17_fiber from the corresponding EDX maps (see Figure 90 and Figure 91, respectively). These findings demonstrate that the application of elongational flow is particularly effective in promoting the breakdown of nanofillers into platelets and facilitate their uniform distribution, independently from the screw rotation speed used during processing [115,137,589,622–624]. Besides, it has to be taken into consideration that the fibers in the two cases are characterized by different BSR. As can be appreciated in Figure 67B, those compounded at 150 rpm were not affected by rupture during the drawing step, while a BSR of about 300 was calculated for the 30HV_300rpm_D17_fiber. A similar behavior in morphology evolution due to elongational flow has been already observed in the case of 100LV-based nanocomposites containing D17 (see Figure 82 and Figure 83 for the fibers obtained at 150 or 300 rpm). As discussed above, the initial presence of micrometric agglomerates in isotropic materials indicates that the beneficial effect of the uniaxial field in determining the final microstructure prevails over the possible role played by the initial morphology. This is evident from the good intercalation of dispersed LDH platelets following elongational flow, regardless of its intensity.

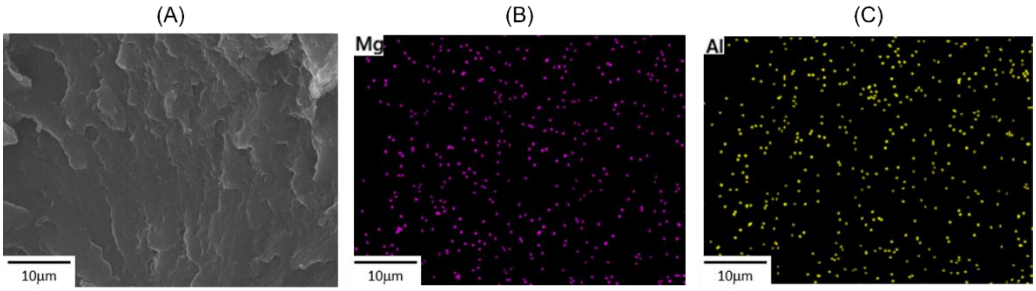


**Figure 90. (A) Morphological analysis of the 30HV_150rpm_D17_fiber and corresponding EDX maps of the (B) Mg and (C) Al.**

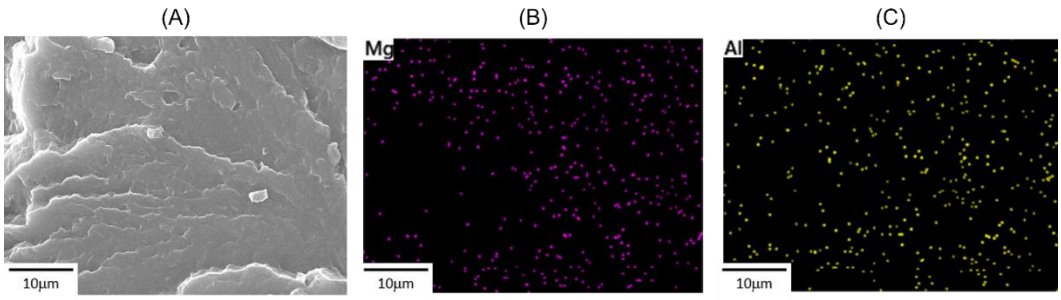


**Figure 91. (A) Morphological analysis of the 30HV_300rpm_D17_fiber and corresponding EDX maps of the (B) Mg and (C) Al.**

### 6.2.2.3 The effect of the aspect ratio

Furthermore, the role of the LDH aspect ratio on the morphology can be investigated. Considering the isotropic materials, some differences in the morphology were obtained depending on the polymeric matrix considered. In the case of 100LV, agglomerates were obtained at 150 rpm in presence of both D25 and D17 (Figure 68 and Figure 80, respectively). However, a difference was appreciated for the compounding screw speed of 300 rpm. In this second case, tactoids and dispersed intercalated lamellae were detected for the nanocomposite containing D25 (see Figure 69), while micrometric agglomerates of D17 were still present dispite the higher screw rotation speed (see Figure 81).
Conversly, comparable morphologies emerged from the comparison of the 100HV-based isotropic nanocomposites containing D25 or D17 and compounded at the same screw speed. In fact, at 150 rpm the uniform distribution of nanometric stacks of lamellae was assessed in both cases (see, Figure 72 for D25 and Figure 84 for D17), while a homogeneous distribution of intercalated LDHs emerges at 300 rpm (see, Figure 73 and Figure 85 for D25 and D17, respectively).
Lastly, for the blend processed at 150 rpm, in presence of D25 a homogeneous dispersion of tactoids along with a good dipersion of intercalated lamellae was obtaiend (Figure 76). On the other hand, in the nancomposite containing D17 processed in the same conditions micrometric agglomerates were detected (Figure 88). A different final morphology depending on the aspect ratio of the nanofiller considered was obtained also in the isotropic materials compounded at 300 rpm. In fact, a good dispersion of distribution of intercalated LDHs' lamellae was achieved for D25, with some nanometric tactoids still present (see Figure 77), while micrometric agglomerates of nanofiller were obtained when the material containing D17 was considered (Figure 89).

From the above analisys, it has been clearly highlighted the role of the aspect ratio of LDHs in determining the final morphology of the isotropic nanocomposites. In fact, to a greater aspect ratio corresponds a larger superficial area exposed for a single platelet resulting in a greater number of available interactions. This is one of the strengths of using nanometric fillers, which allow greater interaction with the polymer matrix, modifying the final properties of the material. However, the greater

number of exposed available interactions also represents an obstacle to the dispersion of these fillers at the single layer level, because the filler-filler affinity is greater than the filler-polymer affinity. For this reason, as the aspect ratio increases the greater number of attrative interactions between the layers, preferentially fosters the adhesion between the platelets and hinders the dispersion in the polymeric matrix. Besides, this phenomenon is particulary strong in the case of the LDHs, which are characterized by a larger surface charge density if compared with conventional cationic nanclays [589,633–636]. The above is in accordance with the observations emerged from the morphological analyses and showing that agglomerates were more likely to form in the case of D17 than in the case of D25. In addition, from these observations, further considerations on the role of the polymer viscosity and applied shear rate as function of the aspect ratio can be suggested. In fact, when focusing on a single matrix, it was found that isotropic nanocomposites containing D25 and obtained at 300 rpm have a more homogeneous distribution of intercalated platelets and nanometric tactoids than the corresponding materials compounded at 150 rpm. However, the same improvement associated with an increase in the applied shear rate was not clearly observed in nanocomposites containing D17. Specifically, negligible variations were observed for both nanocomposites with a 100LV matrix and those with a 30HV matrix. These findings can be explained by considering that the shear stress transmitted to the nanofiller depends not only on the applied shear rate but also on the matrix's viscosity [521,625–628]. Thus, as discussed above, and considering the viscosities of 100HV, 30HV, and 100LV (see Figure 67), the former is expected to be more efficient at transmitting shear stress to the dispersed LDHs. Therefore, considering the larger number of interactions between the layers in D17, it is reasonable to suggest that the shear forces transmitted by 100LV and 30HV are insufficient to overcome the interaction between particles, thereby promoting agglomerate breakup even at the highest screw speed used in the present study.

In addition, the effect of the aspect ratio can also be evaluated in presence of the uniaxial elongational flow. In this case, it is important to compare fibers obtained at similar BSR, in order to evaluate the same intensity of applied field. According to the literature, a filler with a higher aspect ratio is expected to align more effectively with the direction of the applied flow [637]. This would expose the lamellar domains to interlamellar sliding due to elongational flow-induced deformation of the tactoids [115,615]. Consequently, the dispersion and distribution of D17 LDHs would be expected to be more effective than that of D25. For instance, this can be observed from the comparison of the morphologies of the nanocomposites based on 30HV. In fact, for both the materials containing D25 or D17, a well-dispersed distribution of intercalated layers was detected after the application of the elongational flow (see Figure 79 and Figure 91, respectively). However, taking into consideration the corresponding microstructure of the isotropic materials in the two cases, a greater impact of the application of the uniaxial field emerged to be obtained in the case of D17. In particular, a well-dispersed microstructure with only few stacks of lamellae were observed in 30HV_300rpm_D25_DR1 (Figure 77), while agglomerates were present in the case

of 30HV_300rpm_D17_DR1 (Figure 89). Therefore, a greater impact would be suggested for the application of the elongational flow to the nanocomposite containing the higher aspect ratio nanofiller. On the other hand, when considering the fibers obtained from the 100HV-based nancomposites, a similar evolution of the mophology is appreciated in the case of those compounded at 150 rpm. In particular, independently from the nanofiller considered, the cross-section of the isotropic materials was characterized by a homogeneous distribution of nanometric stacks of lamellae (see Figure 72 and Figure 84 in presence of D25 and D17, respectively). Also, the fibers in the two cases presented domains of stacked lamellae of LDHs for both D25 and D17 (see Figure 74 and Figure 86, respectively). Furthermore, considering materials based on 100HV and processed at 300 rpm, the isotropic materials exhibited a morphology in which the good dispersion of intercalated lamellae was appreciated (Figure 73 and Figure 85 for 100HV_300rpm_D25_DR1 and 100HV_300rpm_D17_DR1, respectively). However, the fiber cross-sections showed that intercalation was maintained only in the presence of D17 (Figure 87), while for D25, re-aggregation occurred (Figure 75).

These evidence of re-agglomeration emerging within materials having 100HV as a matrix could be attributed to macromolecular orientation according to the direction of elongational flow application and hindered mobility within the system due to increased viscosity during non-isothermal drawing. Indeed, both macromolecules and nanofillers align with the direction of the applied elongational flow [115,548,549,615,637]. However, since the stretching process takes place under non-isothermal conditions, there is a progressive change in the relaxation dynamics of the system over time. Specifically, the increase in viscosity with decreasing temperature reduces the mobility of the macromolecules and consequently that of the nanofiller, which limits its dispersion promoted by the elongational flow [115,463,474]. Therefore, the system is less likely to oppose platelet reaggregation when the nanofiller gets stuck.

Taking into consideration what discussed for the 30HV- and 100HV-based drawn nanocomposites, it seems that increasing the aspect ratio of the nanofiller positively impacts its dispersion in the matrix when elongational flow is applied. However, the results also suggest that viscosity plays a role in reagglomeration due to superficial interactions between platelets.

### 6.2.3 DSC

In Figure 92, the cooling ramps of the composites containing D25, D17 and the corresponding polymer matrices compounded at 150 or 300 rpm alternatively, are shown.

In the case of the 100HV-based materials, higher crystallization temperatures characterize the composites processed at both 150 (Figure 92A) and 300 rpm (Figure 92B), if compared with the corresponding polymeric matrices. In fact, regardless of the screw speed considered, the values obtained in presence of D25 and D17 are quite comparable, with the first one being slightly higher. In addition, similar considerations can be referred to the composites based on 30HV. Independently of whether the materials were processed at 150 or 300 rpm (Figure 92C and D, respectively), the peak crystallization temperatures recorded for the composites containing D25 and D17 are comparable. Furthermore, they are only slightly higher than the value of the corresponding unfilled polymer matrix. Lastly, when the materials based on the 100LV are considered, a slight increase in the crystallization temperature is appreciated in the case of the composites, being the ones containing D25 associated to the higher values, at both 150 and 300 rpm (Figure 92E and F, respectively).

The increase of the crystallization temperature along with the earlier crystallization observed for the composites in comparison with the corresponding matrices may be associated with to heterogeneous nucleating role played by the LDHs [589,595,638,639].

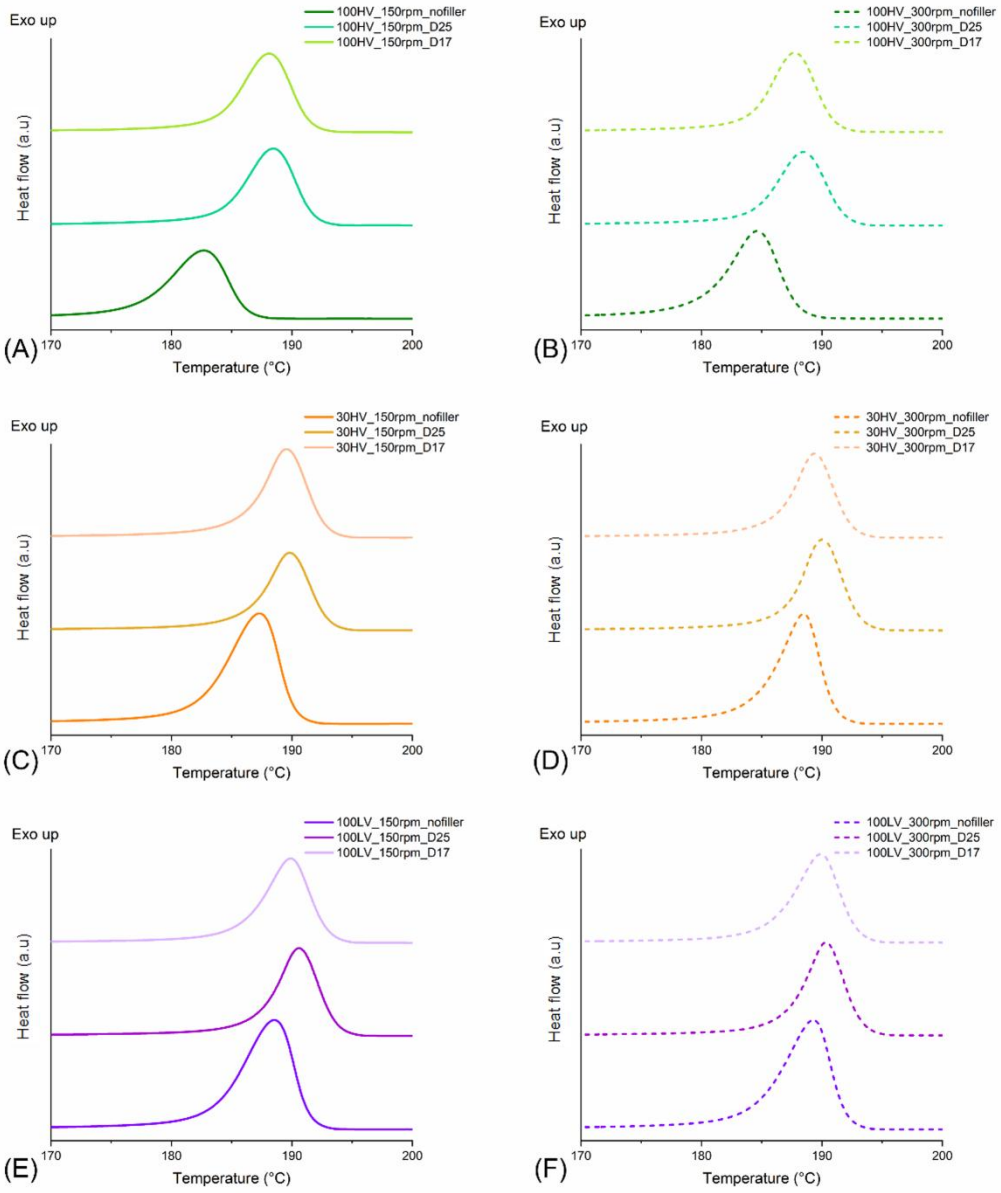


**Figure 92. DSC thermograms of the materials recorded during the cooling ramp. In each graph is reported the comparison of a specific polymer matrix processed at a constant screw speed with the corresponding composites. The constant variable are (A) 100HV_150rpm, (B) 100HV_300rpm, (C) 30HV_150rpm, (D) 30HV_300rpm, (E) 100LV_150rpm and (F) 100LV_300rpm.**

The melting enthalpies of the nanocomposites were calculated from the second heating ramp in the case of the isotropic systems and from the first heating cycle when the fibers were considered. The values for the nanocomposites are shown, as function of the HV content in the matrix, in Figure 93A and B for the materials processed at screw rotation speeds of 150 and 300 rpm, respectively. In particular, the $\Delta H_m$ obtained for the isotropic materials is compared with that of the fibers having DR of 350. Also, the values of the unfilled matrices obtained in the same conditions are reported.

Firstly, considering the systems compounded at 150 rpm (Figure 93A), the melting enthalpies of the 100LV-based materials in absence of elongational flow seem to suggest that the introduction of the nanofillers causes a decrease of the $\Delta H_m$,; in

particular, the lower values are obtained in correspondence of the higher surface area LDHs. Besides, also in the case of the 30HV-based materials, a decrease of the melting enthalpy can be appreciated from the comparison of the values of the matrix and as-compounded nanocomposites. However, in the present case, the $\Delta H_m$ obtained in presence of D25 and D17 are comparable. Lastly, a different behavior is appreciated when considering 100HV as a matrix. In particular, the introduction of the LDHs seems to slightly promote the increase of the melting enthalpy, and comparable values are obtained for the two nanofillers considered.

The melting enthalpies of the materials processed at 300 rpm are reported in Figure 93B. The lowering of the $\Delta H_m$ is appreciated for the 100LV-based after the introduction of the nanofiller, with the higher melting enthalpy associated to 100LV_300rpm_D25 if compared to 100LV_300rpm_D17. Also, a similar behavior is appreciated in the case of the materials based on 100HV. In fact, the $\Delta H_m$ of 100HV_300rpm_D25_DR1 is greater than the one of 100HV_300rpm_D17_DR1, and both are lower than that of the unfilled matrix. Lastly, in the case of the materials having 30HV as a matrix, the introduction of D25 resulted in a negligible variation of the $\Delta H_m$, while a significative decrease was obtained in presence of D17, when the values were compared to the one of 30HV_300rpm_nofiller_DR1.

Additional consideration emerged from the comparison of the melting enthalpies calculated for the materials processed at 150 or 300 rpm (see Figure 93A and B), alternatively, also taking into consideration the variation of the HV content in the matrix. In the case of D25, the $\Delta H_m$ of the 100LV- and 100HV-based composites processed at 150 rpm slightly decreased with the increasing of the MW. Accordingly, the same trend is appreciated in the materials compounded at 300 rpm. Besides, it is worth to mention that the values obtained at the higher screw rotation speed are greater than the ones calculated for the corresponding materials processed at 150 rpm, regardless the MW considered. The increase of the $\Delta H_m$ with the enhancement of the shear rate applied is appreciated also from the comparison between the 30HV_150rpm_D25_DR1 with the 30HV_300rpm_D25_DR1. However, a different behavior emerges when the melting enthalpy of the 30HV-based composite is compared with those of the corresponding 100LV- and 100HV-based, obtained at the same screw speed. In fact, if a lower $\Delta H_m$ is obtained at 150 rpm taking into consideration the value expected form the linear combination of the melting enthalpies of the two monomodal-based composites, at 300 rpm the melting enthalpy is greater than the one expected.

In presence of D17, the $\Delta H_m$ of the two monomodal MW-based composites processed at 150 rpm increased with MW, while the opposite trend was observed for the materials obtained at 300 rpm. In addition, the increase of the screw rotation speed had a slightly positive impact on the melting enthalpy of the composite based on 100LV, while negatively affecting the one of the 100HV-based material. Lastly, the behavior of the 30HV to which D25 was added, highlighted a melting enthalpy value in accordance with the one expected following the linear combination of the one of the 100LV_150rpm_D25_DR1 and 100HV_150rpm_D25_DR1, when processed at 150 rpm, while a lower $\Delta H_m$ than the expected was calculated for the

30HV_300rpm_D25_DR1. Also, the melting enthalpy of 30HV_150rpm_D25_DR1 emerged to be lower than the one of 30HV_300rpm_D25_DR1, similarly to what reported for the 100HV-based composites.

From the above discussion has emerged that, in general, the introduction of LDHs into PA6 reduces the melting enthalpy compared to the unfilled polymer processed under the same conditions. However, the increase of the $\Delta H_m$ with the introduction of a nanofiller is often reported in literature, owing to its contribution as heterogenous nucleating agent [589,640]. As known, this is strongly related to the degree of exfoliation and distribution of the filler in the polymeric matrix [597,603,605,606]. In fact, that is in accordance with the considerations emerged from the morphological investigation discussed in Section 6.2.2, where the presence of aggregates was assessed in most of the composites after the compounding step (see Figure 68, 68, 71, 75, 76, 79, 80, 83, 87, 88). However, that is not the case of the 100HV-based materials processed at 300 rpm and containing D25 or D17 (see Figure 73 and 84, respectively). Specifically, even if both the composites showed a homogeneous morphology after the compounding step, the melting enthalpies in the two cases was still lower than that of 100HV_300rpm_nofiller_DR1 (Figure 93B). A possible explanation for this behavior may be related to the intercalation extent of LDHs, which has been reported to play a negative a role in determining the melting enthalpy when resulting in the limited mobility of the intercalated macromolecules [582,617,620]. Besides, the different interaction of the macromolecules with the intercalated LDHs may likely affect the evolution of the melting enthalpy as function of the screw speed and MW, therefore determining a different behavior of the composites containing D25 or D17, alternatively.

Having investigated the impact of the MW and rotation speed on the melting enthalpy, let's now consider the role of the elongational flow. In Figure 93A, the data referred to the materials compounded at 150 rpm are reported. First, consider the difference in $\Delta H_m$ between the isotropic materials and the fibers. Starting from the D25, negligible variations were appreciated with the introduction of the filler in 100LV- or 30HV-based materials. On the contrary, a negative impact of the application of the elongational flow on the 100HV_150rpm_D25 emerged. Besides, for the composites containing D17, a positive effect of the application of the elongational flow was appreciated for the 100LV-based material, while a negligible impact was appreciated on the melting enthalpy of the 100HV-based one. Also, the decrease of the $\Delta H_m$ was obtained with the application of the elongational flow on the 30HV_150rpm_D17. Lastly, different behaviors can be observed when comparing the melting enthalpies of two composites having the same matrix. In fact, while in the case of 100LV the two values are almost comparable, for the matrix with the higher MW, the composite containing D17 shows the highest $\Delta H_m$. Conversely, between the blend-based, the value calculated for 30HV_150rpm_D25_DR350 prevails.

From the above, it can be seen that no clear trend emerges in the variation of the melting enthalpy in the presence of elongational flow, either with changes in high MW content or with variations in the type of filler. However, by comparing the

values obtained for composite fibers with those for the corresponding polymer, it is clear that the higher $\Delta H_m$ is obtained in the latter case, regardless of the filler and matrix considered.

In Figure 93B are reported the melting enthalpies of the materials drawn after compounding at 300 rpm. First, in the case of the 100LV matrix, the variation is negligible when considering those containing D25 compared to the value calculated in the absence of stretching. However, introducing D25 seems to negatively impact $\Delta H_m$ for both 100HV and 30HV. Furthermore, when considering the effect of elongational flow on composites containing D17, a clear increase in melting enthalpy is observed compared to non-drawn material, regardless of the HV content in the matrix. On top of that it is interesting to note that, for the composites produced at 300 rpm, the $\Delta H_m$ calculated for a certain polymeric matrix after the application of the elongational flow is quite comparable, regardless the presence of D25 or D17. Also, at least for the 100HV- and 30HV-based materials for which the melting enthalpy of the pristine fiber is available, the introduction of the filler emerged to be detrimental on the $\Delta H_m$.

Based on the discussion of how the melting enthalpy varies with processing parameters after elongational flow is applied to composites, it appears that the rotational speed of the screws plays a role. In fact, the addition of filler negatively affected the $\Delta H_m$ of all the drawn materials, if compared to the ones of the corresponding pristine fibers. However, a consistent trend seems to emerge for those processed at 300 rpm. Specifically, for the composites containing D17 the enhancement of the melting enthalpy regardless the polymeric matrix, may be related to the effective orientation of the nanofiller in accordance with the uniaxial elongational flow [555,614,615]. Specifically, this is also confirmed by the homogeneous microstructure observed in the morphological analyses.
Furthermore, since the melting enthalpy obtained for composites containing D25 or D17 is comparable for materials processed at 300 rpm, it could also be suggested that the effect of elongational flow under these processing conditions prevails over the potential role of the different surface area on the melting enthalpy.

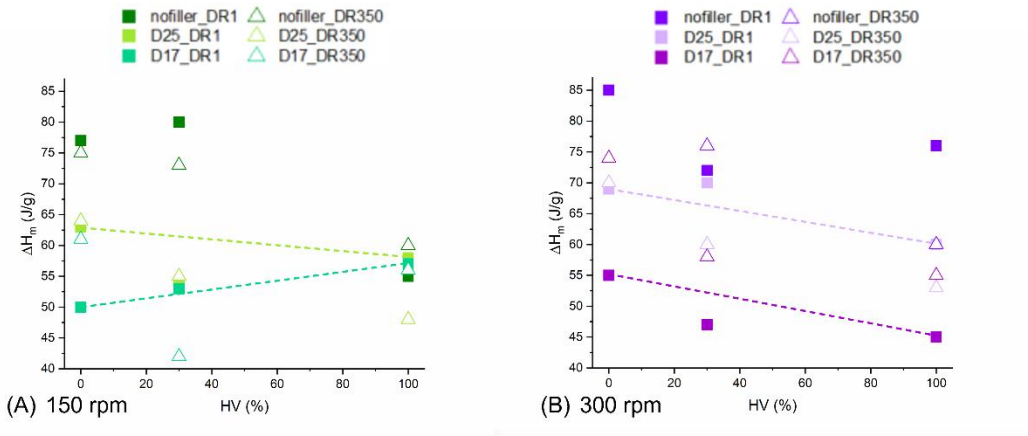


**Figure 93. Melting enthapies of the polymers and corresponding composites processed at (A) 150 or (B) 300 rpm, in absence of elongational flow and for the fibers having a DR of 350. The dashed line refer to the linear combinations of the values referred ot the 100LV- and 100HV- based composites containing the same LDH and in absence of elongational flow.**

Lastly, the relative content of the α over γ crystalline phases in the composites produced in presence or absence of applied elongational flow has been investigated. In Figure 94A, are reported the results for the materials compounded at 150 rpm. Focusing on those to which no elongational flow was applied, the α/γ content of the 100LV polymer in presence of D25 emerged to be comparable with the of the pristine matrix. On the contrary, a noticeable increase of the γ content was appreciated when the composite containing D17 was considered. Additionally, form the comparison of the α/γ ratio in the 100HV-based materials emerged the lowering of the relative content of the two phases in presence of both D25 or D17. However, when considering the α/γ content in the corresponding composites having a low and a high MW matrix, it seems that in first case, the stability of the two crystalline phases is affected by the change in the molecular weight of the matrix and, in particular, its increase appears to promote the stability of the γ phase. On the other hand, the composites containing D17 show quite comparable values of α/γ content, independently from the MW of the matrix considered. In the case of the 30HV-based materials, the introduction of the D25 lowers the α/γ ratio if compared to the one of the pristine blend, meaning a higher relative content of γ phase in the first case. Conversely, the values calculated for 30HV_150rpm_D17_DR1 and 30HV_150rpm_nofiller_DR1 are comparable. Further observations emerge when comparing the α/γ content of the 30HV-based composites with the ones of the corresponding matrices-based. In fact, a deviation from the expectations according to the linear combinations of the values of the matrices-based ones is observed regardless considering D25 or D17. However, in the first case the α/γ content decreased, while in the second case, it increases.

Following with the discussion, the results relative to the materials compounded at 300 rpm in absence of elongational flow are reported in Figure 94B. A significative decrease of the α/γ ratio is appreciated in the 100LV-based composites if compared with the corresponding pristine matrix. Also, the value obtained for the

100LV_300rpm_D17_DR1 is greater than the one of 100LV_300rpm_D25_DR1. Furthermore, the decrease of the α/γ content in the composites if compared to that of the pristine matrix is appreciated in the 100HV-based materials. In addition, the values obtained in presence of D25 and D17 are comparable. Focusing on the 30HV-based composites, a α/γ ratio slightly higher than the one of the 30HV_300rpm_nofiller_DR1 was obtained for 30HV_300rpm_D25_DR1, and the value further increased in the case of 30HV_300rpm_D17_DR1. Lastly, taking into consideration the α/γ content expected for the blend-based composites according to the linear combination of the values relative to the corresponding matrices-based, higher experimental values were obtained regardless considering D25 or D17.

On top of that, some considerations emerge from the comparison of the α/γ content of a specific composite processed at 150 or 300 rpm, alternatively. Focusing on the composites containing D25, the value greatly decreased at higher screw speed for the 100LV-based material, while a negligible effect seems to affect those containing the 100HV matrix. On the contrary, the α/γ ratio was positively affected by the increase of the screw speed in compounding those based on 30HV. Furthermore, in presence of D17, a significative variation of the reciprocal content of the α to γ phases was observed only for the composites having 100LV as polymeric matrix.

From the above discussion, some considerations relatively to the role of the processing parameters in determining the polymorphism emerged. For instance, in presence of a high MW matrix it appears that the ratio between the α and γ phases in the composite is independent of the rotation speed of the screws in the compounding step and the type of filler. Also, the values are lower than the one of the corresponding pristine matrix processed in the same conditions. Furthermore, a combined effect of the high screw rotation speed and bimodal MW may be suggested to promote the α/γ content obtained for the composites if compared with the one expected according to the linear combination of the corresponding matrices-based materials. In addition, the α/γ of the 30HV_300rpm_D25_DR1 and 30HV_300rpm_D17_DR1 is comparable or larger than the one of the 30HV-blend. Taking into account the literature on the subject, there are few studies investigating the relationship between the presence of nanofillers and the stability of polymorphic crystalline phases in PA6 [595,596,601,640]. Furthermore, although there is agreement on the central role of the degree of filler exfoliation, studies disagree on which phase, α or γ, is stabilized by the increase of the parameter [595,640].

The α/γ content calculated for composites obtained in the presence of the elongational flow and compounded at 150 or 300 rpm is discussed below (Figure 94A and B, respectively). It is important to note that, in the cases in which the α phase is the only one present, the data are not reported in the graphs.

In accordance with the data shown in Figure 94A, α is the only phase present in the fibers of the 100LV-based materials processed at 150 rpm, regardless considering D25 or D17 as a filler. This is consistent with what was already observed for 100LV_150rpm_nofiller_DR350. Furthermore, the composites having a high MW matrix showed a comparable α/γ content, and the value was independent from the filler considered. Besides, those values of α/γ are comparable with the one of

100HV_150rpm_nofiller_DR350. On the contrary, focusing on the data relative to 30HV_150rpm_D25_DR350 and 30HV_150rpm_D17_DR350, a different crystalline phase distribution emerges. In fact, the first composite only contains α phase, as in the case of 30HV_150rpm_nofiller_DR350, while the second also presents γ.

Considering the α/γ ratio of materials processed without elongation flow (Figure 94A) and the above discussion of the values calculated for the corresponding fibers, it may reasonably be considered a combined effect of elongational flow and MW in the case of monomodal-MW distribution. In fact, the application of the elongational flow to the low MW materials results in the suppression of the γ phase, regardless the presence or type of LDH present; while when the high MW matrix is considered, a comparable content of α and γ is obtained, independently from the other parameters considered.

In Figure 94B the α/γ content of the fibers obtained from the materials processed at 300 rpm are reported. Both the composites having 100LV as a matrix are characterized by only α phase. On the other hand, also γ is present in those based on 100HV. In addition, a greater α/γ value is associated to 100HV_300rpm_D25_DR350 if compared to 100HV_300rpm_D17_DR350, while 100HV_300rpm_nofiller_DR350 presented only α. Lastly, when the 30HV-based composites are considered, comparable values of α/γ are obtained regardless the presence of D25 or D17. Also, the values are lower than the one of 30HV_300rpm_nofiller_DR350, thus indicating a higher relative content of γ when the filler is present.

Furthermore, focusing on the crystalline population of the materials with a monomodal MW, evidences emerge that are consistent with what has already been highlighted for those processed at 150 rpm. In particular, at 300 rpm, the 100LV-based fibers only present α phase, while the simultaneous presence of α and γ is observed in the 100HV-based composites. Thus, also at the higher screw speed it can be considered a combined effect of the MW and elongational flow in determining the crystalline phase distribution of the monomodal MW-based materials.

In conclusion, the analysis of the distribution of alpha and gamma phases in materials subjected to elongational flow suggests that the presence of filler has a secondary effect. Specifically, when a monomodal MW distribution is considered, the formation of alpha or gamma phases in the fibers seems to be primarily determined by the MW of the polymer matrix in the presence of elongational flow. Therefore, the templating effect of elongational flow seems to prevail over the presence of filler, which could affect chain mobility [245,251,556,596,640,641].

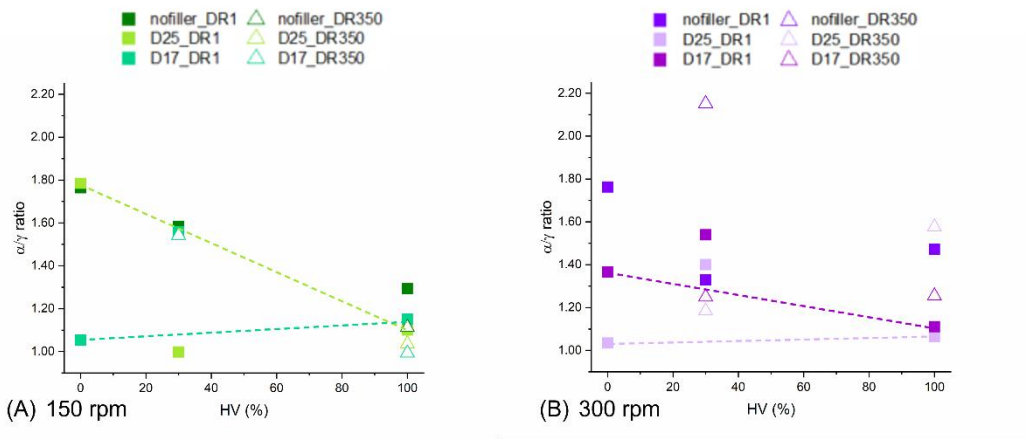


**Figure 94. α/γ content of the polymers and corresponding composites processed at (A) 150 or (B) 300 rpm, in absence of elongational flow and for the fibers having DR of 350. The dashed line refer to the linear combinations of the values referred ot the 100LV- and 100HV- based composites containing the same LDH and in absence of elongational flow.**

## 6.2.4 Mechanical properties

The Young modulus, strength at break and deformation at break of the isotropic nanocomposites were compared to those of the unfilled polymers and are reported in Figure 95A, B and C, respectively. As expected, the tensile properties of the nanocomposites are affected by the dispersion and distribution of the nanofiller in the polymeric matrix [589]. In particular, the Young modulus and strength at break are positively affected or comparable to the unfilled samples for those in which a homogeneous morphology was achieved, while their decrease is appreciated in presence of LDHs agglomerates as, for instance, in the case of 100LV. The opposite trend is associated to the deformation at break.

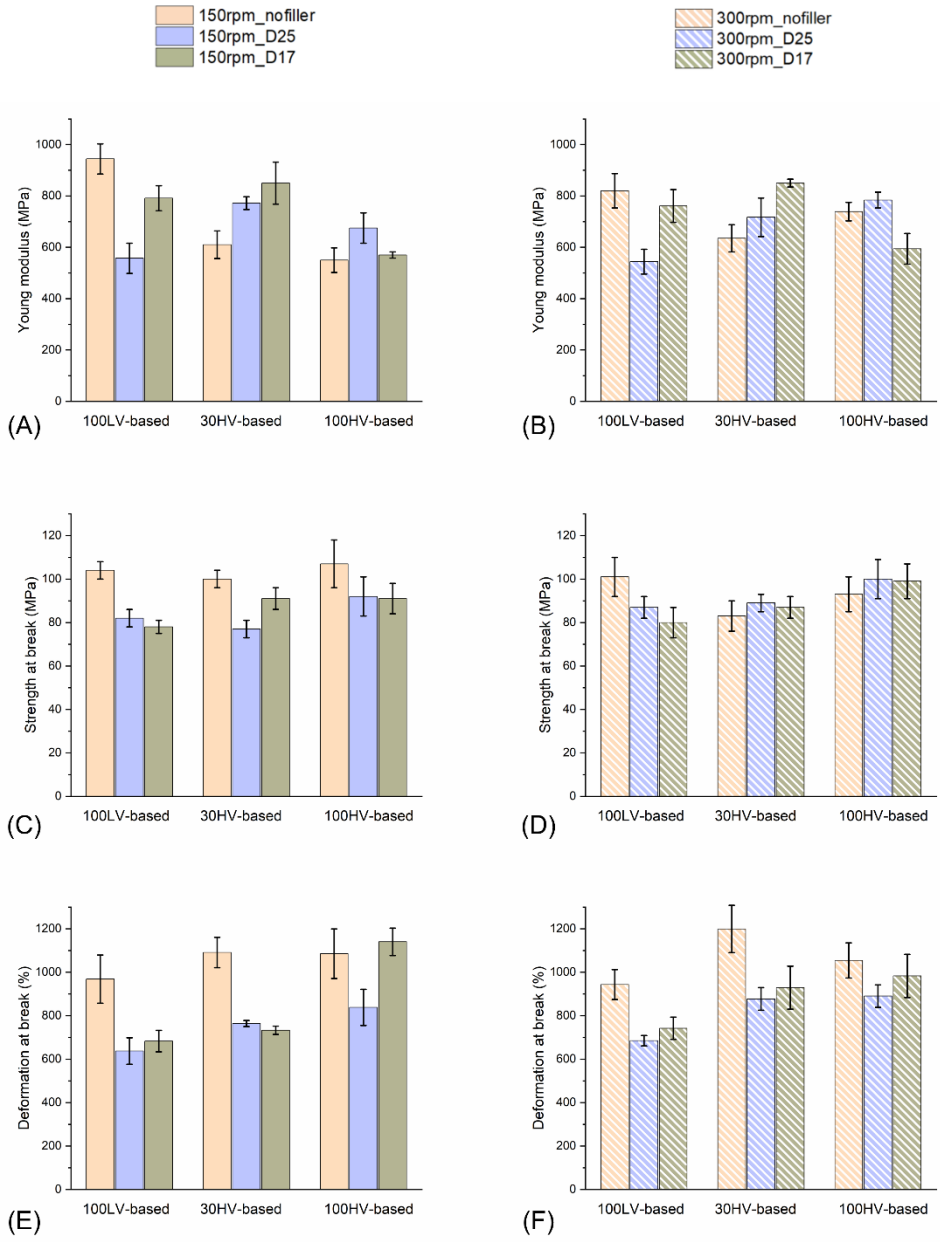


**Figure 95. Young modulus, strength at break and deformation at break of the isotropic materials processed at (A), (C), (E) 150 or (B), (D), (F) 300 rpm, respectively.**

Furthermore, the tensile stength of the nanocomposites fibers was evaluated considering the variation of the dimensionless strength at break as function of the DR (Figure 96). As reported in Section A.3.4., the values were calculated as the ratio between the experimental values of the fibers and the corresponding strength at break of the isotropic material. This approach allows to highlight the contribution provided by the orientation phenomena to the tensile strength [123,589,642].

In the case of the 100HV-based materials (Figure 96A and B), an almost linear increase of the dimensionless strength as a function of the DR is observed for all the systems, regardless of the presence of LDHs and of the screw speed. This behavior indicates the effectiveness of the applied elongational flow in promoting

macromolecular orientation, without promoting any evolution of the LDHs dispersion/distribution [123,642].

Differently, for 30HV-based materials processed at 150 rpm (Figure 96C), the tensile strength is not affected by the application of the elongational flow for both the unfilled blend and the system containing D17, while a different trend is observed for 30HV_150_D25. More specifically, in this case, a progressive increase of the tensile strength as a function of DR is appreciated. This feature suggests that, upon the application of the elongational flow, the morphology of the nanocomposite is able to modify. Concerning the behavior of the materials processed at 300 rpm (Figure 96D), a non-monotonic trend can be noticed, indicating the occurrence of different phenomena affecting in different ways the tensile behavior of the fibers. However, no significant differences were observed between the unfilled blend and the nanocomposites.

Lastly, as clearly observable in Figure 96E, the introduction of D25 in 100LV matrix dramatically change the tensile behavior of the material as a function of the applied elongational flow. In fact, as already noticed for the system 30HV_150_D25, a remarkable increase of the tensile strength as compared to the unfilled matrix is noticed. Also in this case, this result can be ascribed to some evolution of the nanocomposite morphology resulting from the elongation.

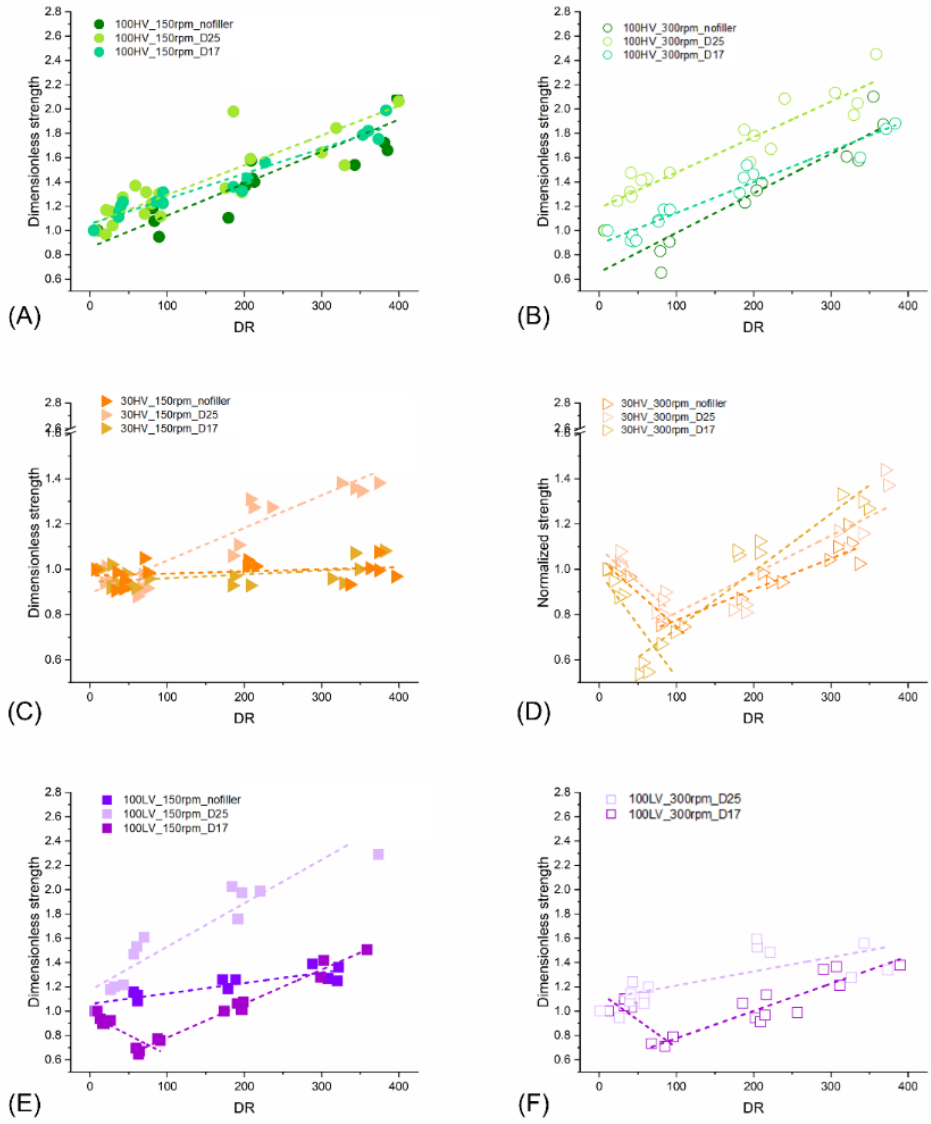


**Figure 96. Dimensionless strength of the materials as function of the DR. In each graph is reported the comparison of a specific polymer matrix processed at a constant screw speed with the corresponding composites. The constant variable are (A) 100HV_150rpm, (B) 100HV_300rpm, (C) 30HV_150rpm, (D) 30HV_300rpm, (E) 100LV_150rpm and (F) 100LV_300rpm. In all cases, the dashed lines represent the trend of the data having the same color.**

In order to gain some additional insight about the behavior of 30HV- and 100LV-based materials, the normalized strength at break was calculated. This parameter corresponds to the ratio between the dimensionless tensile strength of the nanocomposite fiber and the corresponding value of the unfilled polymeric matrix having comparable DR. This approach allows eliminating the reinforcing effect associated with the orientation phenomena of the macromolecules, thus emphasizing the role of the elongational flow-induced evolution of the nanocomposites' morphology on their tensile behavior [123,589,642]. Specifically, a flat trend in the graph reveals that the increase of the strength at break as function fo the DR is only related to the enhanced orientation of the macromolecules along

the direction of the elongational flow, thile a positive slope can be related to a progressively improved dispersion of the nanofiller [589].

As can be appreciated in Figure 97A and B, for both nanocomposites a significant increase of the tensile strength, indicating that the material's morphology can evolve when stretched in non-isothermal conditions. In particular, as anticipated before and as assessed through morphological analyses, this evolution involves a progressive disruption of the nanofiller agglomerates formed during the melt compounding stage. Furthermore, it can be inferred that, similarly to what noticed in nanocomposites s incorporating anionic nanoclays, the elongational flow also promotes an increase of the interlayer spacing within tactoids or intercalated hybrids already present in the melt-compounded materials, resulting in an amplification of intercalation or, possibly, in the formation of exfoliated hybrids. Finally, a preferential alignment of the nanofillers along the flow direction, potentially contributing to the improved tensile strength of the fibers, cannot be excluded.

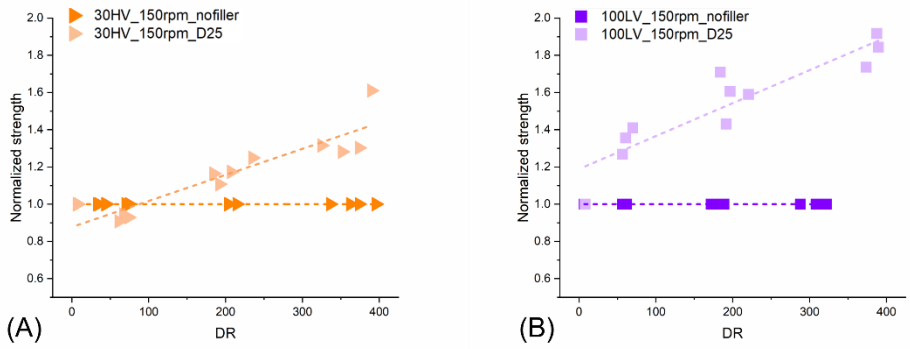


**Figure 97. Comparison of the normalized strength at break of the unfilled and D25-containing nanocomposite processed at 150 rpm for (A) 30HV-based and (B) 100LV-based materials. In all cases, the dashed lines represent the trend of the data.**

## 6.3 Concluding remarks

In the present Chapter it has been investigated the processing parameter-microstructure-properties relationship in PA6-based composites containing LDH. In particular, the role of the uniaxial elongational flow, aspect ratio of the filler, screw rotation speed and high-to-low MW content was deepened.

The study revealed that the presence of LDHs generally improves the drawability of composites compared to unfilled polymers, independently from the aspect ratio considered. However, the extent of improvement depends on the MW, the MW distribution, as well as the screw speed. In particular, for monomodal systems, high MW always corresponds to good drawability, while in low MW nanocomposites it depends on both the screw rotation speed and the aspect ratio of the nanofiller. On the other hand, greater deformability is achieved at low speeds for bimodal MW-based materials, regardless of the filler aspect ratio.

Furthermore, focusing on the morphology of isotropic materials revealed additional considerations regarding the role of the parameters examined. Specifically, the polymer's higher viscosity proved favorable in promoting tactoids' rupture and platelet dispersion owing to its greater effectiveness in transmitting shear stress to the embedded nanofiller. Additionally, increasing the screw rotation speed from 150 to 300 rpm showed a general improvement in LDH dispersion and promoted intercalation. Besides, applying elongational flow has consistently improved the dispersion of nanofillers, especially when initial agglomerates were present. The increasing viscosity related to the MW of the matrix and the decrease in temperature during the drawing step were suggested to have an impact on the formation of such structures.

Lastly, the crucial role of the aspect ratio of the nanofiller in relation to the nature of the applied field was revealed. Specifically, higher aspect ratio LDHs were more difficult to disperse in the presence of shear flow due to strong interactions between the lamellae. However, when subjected to elongational flow, they showed a greater tendency to align and disperse in the direction of the uniaxial field. This effect was particularly evident in 30HV and 100LV materials.

Additionally, it was noted that the addition of LDHs generally had a nucleating effect on the matrix, as evidenced by the comparison of the crystallization temperatures of isotropic materials. However, the effect on the melting enthalpy varies. In particular, the decrease was attributed to non-optimal dispersion of the nanofiller, as revealed by morphological analysis of the isotropes. Furthermore, applying elongational flow produced ambiguous results. Generally, the $\Delta H_m$ decreased. However, fibers containing D17 and obtained at 300 rpm show a positive variation compared to the value calculated for the corresponding isotropes. This variation is probably related to the better intercalation and orientation of the platelets obtained under these conditions, as revealed by the morphological analysis.

Finally, the ratio between the α and γ crystalline phases in isotropic materials was shown to depend more on the MW of the matrix than on the aspect ratio of the filler. Additionally, when elongational flow is applied to monomodal matrices, the α phase predominates in low-MW materials, while also γ was found in the high MW-based nanocomposites, regardless of the presence of D17 or D25. Thus, it has been found that the effect of the filler is secondary to that of the MW and elongational flow in determining the resulting α over γ content.

Lastly, in terms of mechanical properties, the increase in the strength at break as a function of DR highlighted the effectiveness of elongational flow in orienting polymer chains. Additionally, the improved distribution and orientation of LDHs was demonstrated for 30HV- and 100LV-based composites.

# Chapter 7

# Conclusions and perspectives

The increasing demand for high-performance polymer-based materials has highlighted the crucial importance of understanding the relationship between processing parameters, microstructure, and the resulting properties. In particular, the development of microstructured polymer systems through solvent-free approaches represents a highly attractive route from both scientific and industrial perspectives. Nevertheless, this field of research is still in its early stages, and few studies on this subject are available in the literature.

Within this context, the aim of the present PhD work was to investigate how variations in processing conditions could be used to control the microstructure, thereby tuning the final properties of twin-screw extruded homopolymer-based materials. On the formulation point of view, two distinct polymer systems were considered: an apolar HDPE-based and a polar PA6-based one, including different combinations of high and low molecular weight matrices. Particular attention was also given to the introduction of layered double hydroxides as nanofillers in polar systems to further tailor morphology and performance. Additionally, the screw rotation speed and barrel temperature profile were considered as variables in the compounding process. Finally, the effect of a non-isothermal uniaxial elongational flow applied on the material right after the die was analyzed in the case of polar systems.

First, an extensive analysis of the current state of knowledge was conducted, which led to the development of a comprehensive overview on solvent-free approaches for producing structured polymer systems. Given their relevance as the most industrially exploited methods for the melt processing of thermoplastic materials, the focus was particularly on extrusion- and injection molding-based technologies. Within this framework, the relationships between processing parameters and the resulting microstructure were critically examined. It is worth noting that the particular attention paid to the tailoring role played by the flow fields generated during processing onto the resulting microstructure represents a distinctive novelty of this work.

Focusing on the experimental results, in the case of the HDPE blends the study was conducted according to a Design of Experiment strategy, considering variations in the blend composition, screw rotation speed, and processing temperature. Also, the thermal and rheological analyses were interpreted using a multilinear regression model and Principal Component Analysis, respectively. These approaches allow the extraction of quantitative relationships between processing variables and the resulting microstructure, and represent a novelty in this fields. In fact, in accordance with the literature no such strategies were previously adopted for the statistical analysis of the characterization results of thermoplastic systems. Overall, this work demonstrated the potential of applying multivariate analytical strategies to polymer melt compounding, providing a structured and quantitative framework for evaluating the effects of processing variables on microstructure. Besides, the insights gained open promising perspectives for extending this methodology to more complex systems, where the interplay of multiple parameters becomes even more critical.

Referring to the PA6-based systems, the first experimental campaign investigated the processing–structure relationships in the presence of shear flow alone. In particular, the blend composition and the screw rotation speed were considered as variable parameters. A distinctive methodological advancement of this study was the use of Ludovic® simulations, which enabled to model the quantitative information on the actual thermo-mechanical field experienced by the material along the screw profile. Specifically, the knowledge of the actual shear rate, temperature profile and residence time, allowed a more accurate interpretation of the microstructural outcomes, establishing a clear relation with the operating conditions.

Besides, the study assessed that the final morphology of PA6 blends is dictated by the competition between the flow-induced crystallization and the memory effect. In particular, the intensity of the two phenomena is strongly related to chain entanglements and hydrogen bonding density which, in turn, affect the macromolecular constraints and, thus, the final microstructure. As a consequence, these findings demonstrate that under sufficiently intense thermo-mechanical fields FIC can dominate over the memory effect in controlling polymorphism. This result is notable, as the tailoring of polymorphism via compounding has not yet been systematically addressed and the present study offers promising perspectives for the targeted tuning of polymorphism.

Subsequently, the effect of the superposition of a non-isothermal uniaxial elongational flow in PA6-based systems was investigated, considering its role in determining the mechanical properties, and drawability in the molten state. In particular, the study highlighted the primary importance of the average molecular weight and applied elongational flow. The former was found to strongly influence entanglement density, which plays a central role in governing deformability and strain hardening. The latter consistently promoted chain orientation, particularly in monomodal systems, favoring the formation of the more stable α crystalline phase. Besides, the molecular weight distribution was assessed playing a secondary yet significant role, particularly under high shear conditions.

Notably, from the experimental trial emerged that despite the observed changes in the relative α/γ content, the polymorphic composition had a negligible impact on the mechanical properties. Additionally, it emphasized the need to consider the synergistic interplay between average MW, MW distribution, and deformation field when tailoring structured PA6-based materials with twin-screw extrusion.

Lastly, the analysis of the relationship between parameters, microstructure and properties was extended to PA6-based nanocomposites containing layered double hydroxides, evaluating how processing conditions and filler geometry influence microstructure and properties. The study analyzed the effects of screw speed, elongational flow intensity, polymer molecular weight and its distribution, and the aspect ratio of the LDH platelets, while maintaining a constant nanofiller concentration of 10 wt%. Also, the materials were characterized through SEM, thermal and mechanical analyses, and molten-state drawability tests.

What emerged, is the role of the LDHs aspect ratio as a key factor primarily in relation to the type of flow field applied during processing. Under shear-dominated conditions, high-aspect-ratio fillers exhibited limited tactoids' rupture and poorer dispersion due to strong lamellar interactions, whereas low-aspect-ratio LDHs dispersed more effectively. Conversely, when elongational flow was applied, high-aspect-ratio fillers showed a markedly improved tendency to align and disperse along the drawing direction, demonstrating that uniaxial flow can overcome the limitations observed under shear. In contrast, the aspect ratio played only a secondary role in determining the thermal properties of the nanocomposites. In particular, the nucleating effect of the nanofiller was observed regardless its geometry, and variations in melting enthalpy were mainly associated with the degree of dispersion rather than the aspect ratio itself. Similarly, the α/γ crystalline phase content depended predominantly on the matrix molecular weight and on the elongational flow, while the impact of the filler geometry remained marginal.

As emerged, the experimental work carried out in this dissertation provided new and valuable insights into the processing–microstructure–properties relationships of homopolymer blends processed via twin-screw extrusion. At the same time, the results have clearly highlighted several research directions that will require further development to fully exploit the structure-oriented processing strategies explored in this work at the industrial scale. In particular, the most critical aspect concerns the modeling of non-equilibrium phase transitions during flow. Current predictive models remain limited in their ability to describe complex crystallization pathways, transient morphologies, and the interplay between flow fields and molecular dynamics. Future efforts should therefore focus on implementing and refining constitutive and crystallization models capable of capturing not only model systems, but also real case scenarios.

Finally, although twin-screw extrusion is one of the most important processing technologies, injection molding is another fundamental technique for the industrial production of thermoplastic components. Based on the insights gained from this study, a significant future research direction will be to extend the processing–structure–properties methodology to injection molding. For instance, this would consist in investigating how pressure, cooling rate, and complex filling dynamics

influence crystallinity, morphology development and final properties. In summary, the outcomes of this research provide a solid foundation for the future development of predictive, processing-driven strategies for the design of high-performance polymer-based materials.

# Appendix A

## A.1 Materials

### A.1.1 Polymers

HDPE Lupolen 5021 DX (HMW) was manufactured by LyondellBasell (Houston, TX, USA). It was characterized by a melt flow rate (190 °C/2.16 kg) of 0.25 g/10 min and a density of 0.950 g/cm$^3$).

HDPE Eraclene MP90U (LMW) was supplied by Versalis (San Donato Milanese, Italy). It had a melt flow rate (190 °C/2.16 kg) of 7 g/10 min and a density of 0.960 g/cm$^3$.

PA6 Radipol S24 (LV), having a relative viscosity (MAR01 method) of 2.4 dL/g, was manufactured by RADICI Group (Gandino, Italy).

PA6 Radipol S40P (HV) was characterized by a relative viscosity (MAR01 method) of 4.0 dL/g and was supplied by RADICI Group (Gandino, Italy).

### A.1.2 Fillers

Magnesium/Aluminum hydrotalcites (LDH) manufactured by Prolabin&Tefarm s.r.l. (Ponte Felcino, Italy). Both of them were substituted with oleate ion and the ratio between the magnesium and aluminum cations was 2:1. The chemical formula is reported in Eq. A.1.

$$[Mg_{0.66}Al_{0.34}(OH)_2]\,(C_{18}H_{33}O_2)_{0.34}\,x\,0.9\,H_2O \qquad \text{Eq. A.1}$$

24DL17 (D17) was characterized by a surface area of 8.1 m$^2$/g and the 50$^{th}$ and 90$^{th}$ percentile of the size distribution were 8.39 and 20.74 μm, respectively. In the case of 24DL25 (D25), the surface area was 2.6 m$^2$/g, while the 50$^{th}$ percentile was 18.67 μm and the 90$^{th}$ 48.91 μm.

Therefore, in the dissertation, it will be referred to as D17 as the LDH having the highest aspect ratio, while D25 will be referred to as the filler having a lower aspect ratio.

# A.2 Processing

## A.2.1 Melt compounding

Compounding was performed with a ThermoFisher Process 11 (Waltham, MA, USA) co-rotating twin-screw extruder (diameter = 11 mm, L/D = 40, barrel length = 440 mm, die diameter = 2.5 mm) equipped with eight independent heating zones, seven internal and one external corresponding to the die. The same screw profile was used for both the polyethylene and polyamide-based formulations. As shown in Figure 98, it consisted of three kneading blocks and four conveyor sections. In particular, the kneading blocks had different stagger angles. The first one was designed to plasticize the material and consisted of three sets of elements at 30°, 60° and 90°. Then, the second zone was characterized by a constant angle of 60°, while in the third kneading section there were stagger angles of 60° and 90°. The corresponding codes and characteristics of each screw segment are reported in Table 15. Specifically, the letter "C" identifies the conveying elements and the number corresponds to the sequential position starting from the hopper. For example, "C1" is the first conveying zone. On the other hand, the letter "K" was used for the kneading sections and the numbers refer to the stagger angle between the disks. For instance, "K30-60-90" identifies the kneading zone in which three stagger angles have been used. Namely, 30° in the first part, then 60° and 90° in the following one.
Additionally, A and B represent the position of the hopper and side feeder, respectively. In particular, the latter was exploited solely for the production of the nanocomposites discussed in Chapter 6.

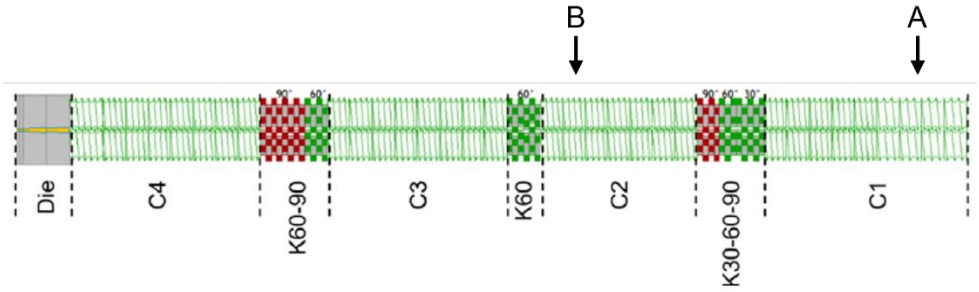


**Figure 98. Schematic representation of the screw profile adopted. The sections are distinguished with dashed lines and the corresponding code was reported. A and B represent the position of the hopper and side feeder, respectively [163]. Adapted under CC BY 4.0 license.**

**Table 15. Codes and corresponding characteristics of the different sections of the screw profile exploited [163].**

| Code | Screw element | Length [mm] |
|---|---|---|
| C1 | Conveying – pitch 7.5 mm | 44.00 |
| | Conveying – pitch 5.5 mm | 55.00 |
| K30-60-90 | Kneading – angle 30° | 13.75 |
| | Kneading – angle 60° | 8.25 |
| | Kneading – angle 90° | 11.00 |
| C2 | Conveying – pitch 5.5 mm | 77.00 |
| K60 | Kneading – angle 60° | 16.50 |
| C3 | Conveying – pitch 5.5 mm | 88.00 |
| K60-90 | Kneading – angle 60° | 11.00 |
| | Kneading – angle 90° | 22.00 |
| C4 | Conveying – pitch 5.5 mm | 77.00 |
| | Conveying – pitch 6 mm | 16.50 |

Focusing on the temperature profile and screw rotation speed, the values were optimized depending on the polymer. Both were also considered as factors in the design of experiments (DoE). For these reasons, the values used are given in the corresponding sections (Chapters 3 to 6).
Finally, a feed rate of 270 g/h was used for the polyethylene-based materials (Chapter 3), while 290 g/h was exploited for the polyamide ones (Chapters 4 to 6).

## A.2.2 Spinning

The non-isothermal uniaxial elongational flow was applied to the molten material at the exit of the die using an IdeaInstr (Italy) RheoSpin apparatus equipped with a series of pulleys that catch the hot filament and transfer it to a final pulley rotating in acceleration. As a result, fibers with different draw ratios were collected. It is worth to note that the uniaxial stretching occurs at room temperature, thereby causing the filament to gradually cool down during the process of elongation, until ultimately solidification is attained.

The stretching was performed in non-isothermal conditions (laboratory environment at room temperature), with the pulling caster accelerating from 0 to 1000 rpm. The drawing stopped at a rotation speed lower than the maximum one in case the filament broke prematurely, while the wheel has decelerated after reaching 1000 rpm if the material has withstood this drawing intensity. The latter case will be clearly highlighted where present. The Breaking Stretching Ratio (BSR) is

defined as the ratio of the drawing speed applied by the RheoSpin that causes fiber rupture of the fiber, and the extrusion speed [115]. The speed at break corresponds to the linear velocity of the drawing pulley. The extrusion speed, on the other hand, can be expressed as the volumetric flow rate of the extruded material passing through the die. Therefore, the BSR was calculated according to Eq. A.2.

$$BSR = \frac{\pi * D * N}{\frac{Q_v}{A}} \quad \text{Eq. A.2}$$

In this equation, π denotes the mathematical constant approximately equal to 3.14, D represents the diameter of the drawing pulley, N is the drawing speed at break of the pulley, $Q_v$ indicates the volumetric flow rate, and A corresponds to the section of the die. It is worth noting that the BSR corresponding to the maximum drawing speed of 1000 rpm is 1132.
The stretching extent of the obtained fibers was evaluated with the draw ratio, calculated in accordance to Eq. A.3 [254]:

$$DR = \frac{{D_{Die}}^2}{{D_{Fiber}}^2} \quad \text{Eq. A.3}$$

Where DR is the draw ratio, $D_{Die}$ is the diameter of the extrudate in correspondance of the die that in the study was maintained constant at 2.5 mm, $D_{Fiber}$ is the diameter of the fiber after the stretching step.

### A.2.3 Compression molding

A Collin P200 T (Maitenbeth, Germany) was used for the hot compression molding of the samples for rheological characterization. Polyethylene-based materials were held at 190 °C and 100 bar for 3 min. The same holding time was maintained for the polyamides, while the temperature and pressure were set at 230 °C and 50 bar, respectively.

## A.3 Characterization techniques

### A.3.1 Differential Scanning Calorimetry (DSC)

Thermal characterization was performed with Q20 (TA Instrument—New Castle, DE, USA). For all the systems analyzed the sample mass was 7 ± 1 mg, the chamber was purged with a nitrogen flow of 50 mL/min, and two heating scans were applied. The parameter values of the thermal ramps are reported for the PE- and PA-based systems in Table 16. Three specimens were tested for each material, with the reported values corresponding to the average of these measurements, while the presented thermograms were selected as representative of the overall trends observed across the tested samples.
The melting temperature ($T_m$) was determined by identifying the maximum of the

endothermic peak, while the crystallization temperature was evaluated based on the maximum of the exothermic peak. Additionally, the melting enthalpy was calculated as the integral of the area under the endothermic peak. Besides, the crystallinity content was estimated in accordance with Eq. A.4

$$Crystallinity\ [\%] = \frac{\Delta H_m}{\Delta H^0} * 100 \qquad \text{Eq. A.4}$$

Where $\Delta H_m$ is the melting enthalpy corresponding to the the integral of the melting peak, $\Delta H^0$ is the melting enthalpy of the 100 % crystalline polymer (see Table 16).

It is important to note that, in the specific case of the polyethylene homopolymer blends discussed in Chapter 3, the analysis of the variation of the $\Delta H_m$ was performed through the evaluation of the difference between the experimental and the theoretical data. Then, the results were investigated with the multilinear regression method. Thus, considering the approach being exploited specifically in the case of HDPE homopolymer blends in absence of uniaxal elongational flow, the equation exploited are introduced and detailed punctually in Section 3.2.1 in Chapter 3.

The deconvolution of the peaks was performed where needed, using the Peak Deconvolution tool in Origin 2020. The Gaussian distribution was selected as the fitting function [500,643].

**Table 16. Heating and cooling ramps used for the systems based on PE and PA, and corresponding melting enthalpy of the 100 % crystalline polymer used for the evaluation of the crystallinity.**

| System | Heating and cooling ramps [°C; °C/min] | Melting enthalpy of the 100 % crystalline polymer [J/g] |
|---|---|---|
| Polyethylene-based | 0 to 200; 10<br>200 to 0; 10<br>0 to 200; 10 | 290 [415] |
| Polyamide-based | 0 to 250; 10<br>250 to 0; 10<br>0 to 250; 10 | 230 [489] |

## A.3.2 Rheometry

The rheological analyses were performed using an ARES parallel plate—plate geometry rheometer (TA Instruments—New Castle, DE, USA). The diameter of the plates was 25 mm, and a gap of 1 mm was maintained. The frequency sweep test was conducted in a nitrogen atmosphere, with the frequency ranging from 100 to 0.1 rad/s. The strain amplitude was constant, with a value that was determined by preliminary strain sweep tests to be within the linear viscoelastic region. At least two specimens were tested for each material and those reported were selected as

representative of the trend of the tested samples.
The analysis temperatures selected for the different systems are reported in Table 17. Two distinct analysis temperatures were used for polyethylene-based systems. Further information on this topic can be found in Chapter 3 (see Section 3.1) on the study of HDPE homopolymer blends.

**Table 17. Analysis temperatures used for the rheological characterizations.**

| System | Analysis temperature [°C] |
|---|---|
| Polyethylene-based | 175<br>190 |
| Polyamide-based | 250 |

## A.3.3 Morphological analysis

For the morphological characterization was used an EVO 15 (Zeiss — Oberkochen, Germany) Scanning Electron Microscope (SEM). The beam voltage and working distance were maintained at 20 kV and 8.5 mm, respectively. The elemental analyses were performed owing to EDX (Energy Dispersive X-ray spectroscopy) using an X-ray probe model 40 (Oxford Ultim Max — High Wycombe, UK).

The fracture surfaces were obtained from cryogenic fracture in liquid nitrogen. In the case of the fibers, the section perpendicular to the uniaxial elongational flow applied was observed. The morphological analyses presented were selected after observing at least three different fracture surfaces for each material.

## A.3.4 Mechanical properties

The tensile tests were performed with an Instron 5966 dynamometer (Instron — Norwood, MA, USA) at room temperature. The instrument was equipped with a 2 kN load cell and the initial crosshead distance of 3 mm was used. For both the PE-based and the PA-based samples, the crosshead speed was maintained constant at 50 mm/min. At least five specimens were tested for each kind of sample, and the results averaged for the evaluation of the Young modulus, strength at break and deformation at break. In addition, the stress–strain curves reported in Figure 65 refer to the tests performed on individual specimens and were selected for each material as representative of the overall trend observed across the tested samples.

Besides, the dimensionless strengths was calculated for each material as the ratio between the strength at break of the fiber and the corresponding value of the material to which no elongational flow was applied. The same method was used to calculate the dimensionless deformation. In addition, the normalized strength

values were calculated as the dimnsionless strength normalized with respect to the dimensionless values of the unfilled polymeric matrix [589].

# References


1. Mishra, R.K.; Maria, H.J.; Joseph, K.; Thomas, S. Basic Structural and Properties Relationship of Recyclable Microfibrillar Composite Materials from Immiscible Plastics Blends: An Introduction. In *Micro and Nano Fibrillar Composites (MFCs and NFCs) from Polymer Blends*; Elsevier Inc.: Amsterdam, The Netherlands, 2017; pp. 1–25 ISBN 978-0-08-101992-4.
2. Zhong, G.J.; Yang, S.G.; Lei, J.; Li, Z.M. Flow-Induced Polymer Crystallization under Pressure and Its Engineering Application in "Structuring" Polymer Processing. *Macromolecules* **2024**, *57*, 789–809, doi:10.1021/acs.macromol.3c01846.
3. Chen, Y.; Ma, Y.; Yin, Q.; Pan, F.; Cui, C.; Zhang, Z.; Liu, B. Advances in Mechanics of Hierarchical Composite Materials. *Compos. Sci. Technol.* **2021**, *214*, 108970, doi:10.1016/j.compscitech.2021.108970.
4. Mishnaevsky, L.; Tsapatsis, M. Hierarchical Materials: Background and Perspectives. *MRS Bull.* **2016**, *41*, 661–664, doi:10.1557/mrs.2016.189.
5. Wu, T.; Wang, K.; Chen, X.; Yang, X.; Xiang, M.; Fu, Q. Practicing the Concept of "Structuring" Processing in the Manufacture of Polymer Films. *Sci. China Chem.* **2023**, *66*, 993–1010, doi:10.1007/s11426-022-1520-9.
6. Wan, C.; Bowen, C.R. Multiscale-Structuring of Polyvinylidene Fluoride for Energy Harvesting: The Impact of Molecular-, Micro- and Macro-Structure. *J. Mater. Chem. A.* **2017**, *5*, 3091–3128, doi:10.1039/c6ta09590a.
7. Serpe, G.; Jarrin, J.; Dawans, F. Morphology-Processing Relationships in Polyethylene-Polyamide Blends. *Polym. Eng. Sci.* **1990**, *30*, 553–565, doi:10.1002/pen.760300908.
8. Kalay, G.; Kalay, C.R. Structure and Physical Property Relationships in Processed Polybutene-1. *J. Appl. Polym. Sci.* **2003**, *88*, 814–824, doi:10.1002/app.11639.
9. Jancar, J.; Douglas, J.F.; Starr, F.W.; Kumar, S.K.; Cassagnau, P.; Lesser, A.J.; Sternstein, S.S.; Buehler, M.J. Current Issues in Research on Structure-Property Relationships in Polymer Nanocomposites. *Polymer* **2010**, *51*, 3321–3343, doi:10.1016/j.polymer.2010.04.074.
10. Resch, K.; Wallner, G.M.; Teichert, C.; Gahleitner, M. Highly Transparent Polypropylene Cast Films: Relationships between Optical Properties, Additives, and Surface Structure. *Polym. Eng. Sci.* **2007**, *47*, 1021–1032, doi:10.1002/pen.20781.
11. Di Sacco, F.; Gahleitner, M.; Wang, J.; Portale, G. Systematic Investigation on the Structure-Property Relationship in Isotactic Polypropylene Films Processed via Cast Film Extrusion. *Polymers* **2020**, *12*, 1636, doi:10.3390/polym12081636.
12. Fakirov, S. Nano-/Microfibrillar Polymer-Polymer and Single Polymer Composites: The Converting Instead of Adding Concept. *Compos. Sci. Technol.* **2013**, *89*, 211–225, doi:10.1016/j.compscitech.2013.10.007.
13. Wang, K.; Chen, F.; Li, Z.; Fu, Q. Control of the Hierarchical Structure of Polymer Articles via "Structuring" Processing. *Prog. Polym. Sci.* **2014**, *39*, 891–920, doi:10.1016/j.progpolymsci.2013.05.012.

14. An, F.Z.; Wang, Z.W.; Hu, J.; Gao, X.Q.; Shen, K.Z.; Deng, C. Morphology Control Technologies of Polymeric Materials during Processing. *Macromol. Mater. Eng.* **2014**, *299*, 400–423, doi:10.1002/mame.201300216.
15. Laird, E.D.; Li, C.Y. Structure and Morphology Control in Crystalline Polymer-Carbon Nanotube Nanocomposites. *Macromolecules* **2013**, *46*, 2877–2891, doi:10.1021/ma400035j.
16. Pesneau, I.; At Kadi, A.; Bousmina, M.; Cassagnau, P.; Michel, A. From Polymer Blends to in Situ Polymer/Polymer Composites: Morphology Control and Mechanical Properties. *Polym. Eng. Sci.* **2002**, *42*, 1990–2004, doi:10.1002/pen.11091.
17. Banerjee, R.; Ray, S.S. Role of Rheology in Morphology Development and Advanced Processing of Thermoplastic Polymer Materials: A Review. *ACS Omega* **2023**, *8*, 27969–28001, doi:10.1021/acsomega.3c03310.
18. Tabatabaei, S.H.; Carreau, P.J.; Ajji, A. Effect of Processing on the Crystalline Orientation, Morphology, and Mechanical Properties of Polypropylene Cast Films and Microporous Membrane Formation. *Polymer* **2009**, *50*, 4228–4240, doi:10.1016/j.polymer.2009.06.071.
19. Chandran, S.; Baschnagel, J.; Cangialosi, D.; Fukao, K.; Glynos, E.; Janssen, L.M.C.; Müller, M.; Muthukumar, M.; Steiner, U.; Xu, J.; et al. Processing Pathways Decide Polymer Properties at the Molecular Level. *Macromolecules* **2019**, *52*, 7146–7156, doi:10.1021/acs.macromol.9b01195.
20. Kuzmanović, M.; Delva, L.; Cardon, L.; Ragaert, K. Relationship between the Processing, Structure, and Properties of Microfibrillar Composites. *Adv. Mater.* **2020**, *32*, 2003938, doi:10.1002/adma.202003938.
21. Li, Y.; Yi, X.; Yu, T.; Xian, G. An Overview of Structural-Functional-Integrated Composites Based on the Hierarchical Microstructures of Plant Fibers. *Adv. Compos. Hybrid Mater.* **2018**, *1*, 231–246, doi:10.1007/s42114-017-0020-3.
22. Karger-Kocsis, J.; Bárány, T. Single-Polymer Composites (SPCs): Status and Future Trends. *Compos. Sci. Technol.* **2014**, *92*, 77–94, doi:10.1016/j.compscitech.2013.12.006.
23. Biswas, S.K.; Sano, H.; Shams, M.I.; Yano, H. Three-Dimensional-Moldable Nanofiber-Reinforced Transparent Composites with a Hierarchically Self-Assembled “Reverse” Nacre-like Architecture. *ACS Appl. Mater. Interfaces* **2017**, *9*, 30177–30184, doi:10.1021/acsami.7b09390.
24. Baer, E.; Hiltner, A.; Keith, H.D.; Hilmer, A. Hierarchical Structure in Polymeric Materials. *Science* **1987**, *235*, 1015–1022, doi:10.1126/science.3823866.
25. Gorbatikh, L.; Liu, Q.; Romanov, V.; Mehdikhani, M.; Matveeva, A.; Shishkina, O.; Aravand, A.; Wardle, B.; Verpoest, I.; Lomov, S.V. Hierarchical Design of Structural Composite Materials down to the Nanoscale via Experimentation and Modelling. *IOP Conf. Ser.: Mater. Sci. Eng.* **2018**, *406*, 012002, doi:10.1088/1757-899X/406/1/012002.
26. Wang, L.; Lin, J.; Zhang, X. Hierarchical Microstructures Self-Assembled from Polymer Systems. *Polymer* **2013**, *54*, 3427–3442, doi:10.1016/j.polymer.2013.03.054.
27. Lakes, R. Materials with Structural Hierarchy. *Nature* **1993**, *361*, 511–515, doi:10.1038/361511a0.
28. Sang, Z.H.; Xie, X.L.; Zhou, S.Y.; Li, Y.; Yan, Z.; Xu, L.; Zhong, G.J.; Li, Z.M. Gradient Structure of Crystalline Morphology in Injection-Molded Polylactide Parts Tuned by Oscillation Shear Flow and Its Influence on

Thermomechanical Performance. *Ind. Eng. Chem. Res.* **2017**, *56*, 6295–6306, doi:10.1021/acs.iecr.7b00930.
29. Guan, Q.; Lai, F.S.; Mccarthy, S.P.; Chiu, D.; Zhu, X.; Shen, K. Morphology and Properties of Self-Reinforced High Density Polyethylene in Oscillating Stress Field. *Polymer* **1997**, *38*, 5251–5253, doi:10.1016/S0032-3861(97)00182-1.
30. Lei, J.; Jiang, C.; Shen, K. Biaxially Self-Reinforced High-Density Polyethylene Prepared by Dynamic Packing Injection Molding. II. Microstructure Investigation. *J. Appl. Polym. Sci.* **2004**, *93*, 1591–1596, doi:10.1002/app.20639.
31. Lei, J.; Jiang, C.; Shen, K. Biaxially Self-Reinforced High-Density Polyethylene Prepared by Dynamic Packing Injection Molding. I. Processing Parameters and Mechanical Properties. *J. Appl. Polym. Sci.* **2004**, *93*, 1584–1590, doi:10.1002/app.20640.
32. Mi, D.; Xia, C.; Jin, M.; Wang, F.; Shen, K.; Zhang, J. Quantification of the Effect of Shish-Kebab Structure on the Mechanical Properties of Polypropylene Samples by Controlling Shear Layer Thickness. *Macromolecules* **2016**, *49*, 4571–4578, doi:10.1021/acs.macromol.6b00822.
33. Zhong, Y.; Chen, L.; Gao, J.; Guo, J.; Xing, C.; Li, Y.; Wang, Z. Structural Evolution of High-Entanglement Ultrahigh Molecular Weight Polyethylene Films with Reserved Shish Crystals during the Hot Stretching Process. *Macromolecules* **2024**, *57*, 2176–2190, doi:10.1021/acs.macromol.3c01991.
34. Yang, S.G.; Li, Y.; Lei, J.; Zhong, G.J.; Li, Z.M. Oriented Polar Crystals in Poly(Vinylidene Fluoride) Produced by Simultaneously Applying Pressure and Flow. *Macromol. Chem. Phys.* **2018**, *219*, doi:10.1002/macp.201800299.
35. Zhou, Q.; Liu, F.; Guo, C.; Fu, Q.; Shen, K.; Zhang, J. Shish-Kebab-like Cylindrulite Structures Resulted from Periodical Shear-Induced Crystallization of Isotactic Polypropylene. *Polymer* **2011**, *52*, 2970–2978, doi:10.1016/j.polymer.2011.05.002.
36. Chen, Y.; Fang, D.; Hsiao, B.S.; Li, Z. Insight into Unique Deformation Behavior of Oriented Isotactic Polypropylene with Branched Shish-Kebabs. *Polymer* **2015**, *60*, 274–283, doi:10.1016/j.polymer.2015.01.058.
37. Liu, Z.; Liu, X.; Zheng, G.; Dai, K.; Liu, C.; Shen, C. New Insight into Lamellar Branching of β-Nucleated Isotactic Polypropylene upon Melt-Stretching: WAXD and SAXS Study. *J. Mater. Sci.* **2014**, *50*, 599–604, doi:10.1007/s10853-014-8618-0.
38. Xie, X.L.; Li, Y.; Xu, J.Z.; Yan, Z.; Zhong, G.J.; Li, Z.M. Largely Enhanced Mechanical Performance of Poly(Butylene Succinate) Multiple System via Shear Stress-Induced Orientation of the Hierarchical Structure. *J. Mater. Chem. A.* **2018**, *6*, 13373–13385, doi:10.1039/c8ta03778g.
39. Fakirov, S. Nano- and Microfibrillar Single-Polymer Composites: A Review. *Macromol. Mater. Eng.* **2013**, *298*, 9–32, doi:10.1002/mame.201200226.
40. Liu, D.; Tian, N.; Cui, K.; Zhou, W.; Li, X.; Li, L. Correlation between Flow-Induced Nucleation Morphologies and Strain in Polyethylene: From Uncorrelated Oriented Point-Nuclei, Scaffold-Network, and Microshish to Shish. *Macromolecules* **2013**, *46*, 3435–3443, doi:10.1021/ma400024m.
41. Pan, Y.; Li, N.; Wang, J.; Wang, D.; Pan, X.; Liu, C.; Jian, X. The Role of Expansion Angle and Speed on Shish-Kebab Formation in Expansion Pipe Extruder Head Explored by High Temperature Rapid Stretch. *Polym. Test.* **2021**, *104*, 107387, doi:10.1016/j.polymertesting.2021.107387.

42. Xu, H.; Zhong, G.J.; Fu, Q.; Lei, J.; Jiang, W.; Hsiao, B.S.; Li, Z.M. Formation of Shish-Kebabs in Injection-Molded Poly(L-Lactic Acid) by Application of an Intense Flow Field. *ACS Appl. Mater. Interfaces* **2012**, *4*, 6774–6784, doi:10.1021/am3019756.
43. Zhang, Z.C.; Deng, L.; Lei, J.; Li, Z.M. Isotactic Polypropylene Reinforced Atactic Polypropylene by Formation of Shish-Kebab Superstructure. *Polymer* **2015**, *78*, 120–133, doi:10.1016/j.polymer.2015.09.070.
44. Wang, Y.; Na, B.; Fu, Q.; Men, Y. Shear Induced Shish-Kebab Structure in PP and Its Blends with LLDPE. *Polymer* **2004**, *45*, 207–215, doi:10.1016/j.polymer.2003.10.020.
45. Nie, M.; Han, R.; Wang, Q. Formation and Alignment of Hybrid Shish-Kebab Morphology with Rich Beta Crystals in an Isotactic Polypropylene Pipe. *Ind. Eng. Chem. Res.* **2014**, *53*, 4142–4146, doi:10.1021/ie403944k.
46. Liang, S.; Wang, K.; Tang, C.; Zhang, Q.; Du, R.; Fu, Q. Unexpected Molecular Weight Dependence of Shish-Kebab Structure in the Oriented Linear Low Density Polyethylene/High Density Polyethylene Blends. *J. Chem. Phys.* **2008**, *128*, 174902, doi:10.1063/1.2904561.
47. Wang, K.; Chen, F.; Zhang, Q.; Fu, Q. Shish-Kebab of Polyolefin by "Melt Manipulation" Strategy in Injection-Molding: A Convenience Pathway from Fundament to Application. *Polymer* **2008**, *49*, 4745–4755, doi:10.1016/j.polymer.2008.08.020.
48. Liu, T.; Ju, J.; Chen, F.; Wu, B.; Yang, J.; Zhong, M.; Peng, X.; Kuang, T. Superior Mechanical Performance of In-Situ Nanofibrillar HDPE/PTFE Composites with Highly Oriented and Compacted Nanohybrid Shish-Kebab Structure. *Compos. Sci. Technol.* **2021**, *207*, 108715, doi:10.1016/j.compscitech.2021.108715.
49. Zhou, S.Y.; Niu, B.; Xie, X.L.; Ji, X.; Zhong, G.J.; Hsiao, B.S.; Li, Z.M. Interfacial Shish-Kebabs Lengthened by Coupling Effect of In Situ Flexible Nanofibrils and Intense Shear Flow: Achieving Hierarchy To Conquer the Conflicts between Strength and Toughness of Polylactide. *ACS Appl. Mater. Interfaces* **2017**, *9*, 10148–10159, doi:10.1021/acsami.7b00479.
50. Shahnooshi, M.; Javadi, A.; Nazockdast, H.; Ottermann, K.; Altstädt, V. Rheological Rationalization of in Situ Nanofibrillar Structure Development: Tailoring of Nanohybrid Shish-Kebab Superstructures of Poly (Lactic Acid) Crystalline Phase. *Polymer* **2020**, *211*, 123040, doi:10.1016/j.polymer.2020.123040.
51. Han, R.; Nie, M.; Wang, Q. Control over β-Form Hybrid Shish-Kebab Crystals in Polypropylene Pipe via Coupled Effect of Self-Assembly β Nucleating Agent and Rotation Extrusion. *J. Taiwan Inst. Chem. Eng.* **2015**, *52*, 158–164, doi:10.1016/j.jtice.2015.02.002.
52. Na, B.; Wang, Y.; Zhang, Q.; Fu, Q. Shish and Its Relaxation Dependence of Re-Crystallization of Isotactic Polypropylene from an Oriented Melt in the Blends with High-Density Polyethylene. *Polymer* **2004**, *45*, 6245–6260, doi:10.1016/j.polymer.2004.07.016.
53. Kmetty, Á.; Bárány, T.; Karger-Kocsis, J. Self-Reinforced Polymeric Materials: A Review. *Prog. Polym. Sci.* **2010**, *35*, 1288–1310, doi:10.1016/j.progpolymsci.2010.07.002.
54. Fakirov, S. A New Approach to Plastic Recycling via the Concept of Microfibrillar Composites. *Adv. Ind. Eng. Polym. Res.* **2021**, *4*, 187–198, doi:10.1016/j.aiepr.2021.02.001.

55. Liu, W.; Nie, M.; Wang, Q. In-Situ Microfibrillation of Polystyrene(PS)/Polybutene-1 (PB-1) Composites Prepared via Melt Drawing:Morphological Evolution and Properties. *J. Polym. Res.* **2014**, *21*, 1–8, doi:10.1007/s10965-014-0489-1.
56. Friedrich, K.; Evstatiev, M.; Fakirov, S.; Evstatiev, O.; Ishii, M.; Harrass, M. Microfibrillar Reinforced Composites from PET/PP Blends: Processing, Morphology and Mechanical Properties. *Compos. Sci. Technol.* **2005**, *65*, 107–116, doi:10.1016/j.compscitech.2004.06.008.
57. Lin, X.D.; Cheung, W.L. Study of Poly(Ethylene Terephthalate)/Polypropylene Microfibrillar Composites. I. Morphological Development in Melt Extrusion. *J. Appl. Polym. Sci.* **2003**, *89*, 1743–1752, doi:10.1002/app.12190.
58. Li, X.; Xin, C.; Huang, Y.; Kang, K.; He, Y. Effect of Dispersed Phase on the Morphology of in Situ Microfibrils and the Viscoelastic Properties of Its Composite via Direct Extrusion. *J. Appl. Polym. Sci.* **2018**, *135*, 46286, doi:10.1002/app.46286.
59. Jiang, Y.; Mi, D.; Wang, Y.; Wang, T.; Shen, K.; Zhang, J. Composite Contains Large Content of In Situ Microfibril, Prepared Directly by Injection Molding: Morphology and Property. *Macromol. Mater. Eng.* **2018**, *303*, 1800270, doi:10.1002/mame.201800270.
60. Xia, X.C.; Yang, W.; Zhang, Q.P.; Wang, L.; He, S.; Yang, M.B. Large Scale Formation of Various Highly Oriented Structures in Polyethylene/Polycarbonate Microfibril Blends Subjected to Secondary Melt Flow. *Polymer* **2014**, *55*, 6399–6408, doi:10.1016/j.polymer.2014.10.013.
61. Zhao, Z.; Yang, Q.; Xiang, Z.; Kong, M.; Tang, D.; Huang, Y.; Liao, X.; Niu, Y. Effect of in Situ Poly(Ethylene Terephthalate) (PET) Microfibrils on the Morphological Structure and Crystallization Behavior of Isotactic Polypropylene (iPP) under an Intensive Shear Rate. *Polym. Adv. Technol.* **2015**, *26*, 1275–1284, doi:10.1002/pat.3565.
62. Jiang, C.H.; Zhong, G.J.; Li, Z.M. Recyclability of in Situ Microfibrillar Poly(Ethylene Terephthalate)/High- Density Polyethylene Blends. *Macromol. Mater. Eng.* **2007**, *292*, 362–372, doi:10.1002/mame.200600356.
63. Xu, L.; Zhong, G.J.; Ji, X.; Li, Z.M. Crystallization Behavior and Morphology of One-Step Reaction Compatibilized Microfibrillar Reinforced Isotactic Polypropylene/Poly(Ethylene Terephthalate) (iPP/PET) Blends. *Chin. J. Polym. Sci. (Engl. Ed.)* **2011**, *29*, 540–551, doi:10.1007/s10118-011-1066-2.
64. Xia, X.C.; Yang, W.; He, S.; Xie, D.D.; Zhang, R.Y.; Tian, F.; Yang, M.B. Formation of Various Crystalline Structures in a Polypropylene/Polycarbonate: In Situ Microfibrillar Blend during the Melt Second Flow. *Phys. Chem. Chem. Phys.* **2016**, *18*, 14030–14039, doi:10.1039/c6cp01426g.
65. Kuzmanović, M.; Delva, L.; Cardon, L.; Ragaert, K. The Effect of Injection Molding Temperature on the Morphology and Mechanical Properties of PP/PET Blends and Microfibrillar Composites. *Polymers* **2016**, *8*, 355, doi:10.3390/polym8100355.
66. Cheng, L.; Wang, J. Crystallization and Morphological and Crystal Structures of PP in an in Situ Microfibrillar Composite of Modified PA66 with PP. *Compos. Sci. Technol.* **2018**, *155*, 205–212, doi:10.1016/j.compscitech.2017.11.027.

67. Shi, M.; Wang, L.; Sun, J.; Yang, W.; Zhang, H. Morphology and Properties of Polyolefin Elastomer/Polyamide 6/Poly(Lactic Acid) In Situ Special-Shaped Microfibrillar Composites: Influence of Viscosity Ratio. *Polymers* **2022**, *14*, 4556, doi:10.3390/polym14214556.
68. Li, Z.M.; Li, L.B.; Shen, K.Z.; Yang, W.; Huang, R.; Yang, M.B. Transcrystalline Morphology of an in Situ Microfibrillar Poly(Ethylene Terephthalate)/Poly(Propylene) Blend Fabricated through a Slit Extrusion Hot Stretching-Quenching Process. *Macromol. Rapid Commun.* **2004**, *25*, 553–558, doi:10.1002/marc.200300086.
69. Li, Z.M.; Li, L.B.; Shen, K.Z.; Yang, M.B.O.; Huang, R. In-Situ Microfibrillar PET/iPP Blend via Slit Die Extrusion, Hot Stretching, and Quenching: Influence of Hot Stretch Ratio on Morphology, Crystallization, and Crystal Structure of iPP at a Fixed PET Concentration. *J. Polym. Sci., Part B: Polym. Phys.* **2004**, *42*, 4095–4106, doi:10.1002/polb.20262.
70. Jurczuk, K.; Galeski, A.; Piorkowska, E. All-Polymer Nanocomposites with Nanofibrillar Inclusions Generated in Situ during Compounding. *Polymer* **2013**, *54*, 4617–4628, doi:10.1016/j.polymer.2013.06.039.
71. Wong, W.S.Y.; Stachurski, Z.H.; Nisbet, D.R.; Tricoli, A. Ultra-Durable and Transparent Self-Cleaning Surfaces by Large-Scale Self-Assembly of Hierarchical Interpenetrated Polymer Networks. *ACS Appl. Mater. Interfaces* **2016**, *8*, 13615–13623, doi:10.1021/acsami.6b03414.
72. Brodoceanu, D.; Bauer, C.T.; Kroner, E.; Arzt, E.; Kraus, T. Hierarchical Bioinspired Adhesive Surfaces-A Review. *Bioinspir. Biomim.* **2016**, *11*, 1001, doi:10.1088/1748-3190/11/5/051001.
73. Tritschler, U.; Cölfen, H. Self-Assembled Hierarchically Structured Organic-Inorganic Composite Systems. *Bioinspir. Biomim.* **2016**, *11*, 5002, doi:10.1088/1748-3190/11/3/035002.
74. Liu, S.; Wang, S.; Sang, M.; Zhou, J.; Zhang, J.; Xuan, S.; Gong, X. Nacre-Mimetic Hierarchical Architecture in Polyborosiloxane Composites for Synergistically Enhanced Impact Resistance and Ultra-Efficient Electromagnetic Interference Shielding. *ACS Nano* **2022**, *16*, 19067–19086, doi:10.1021/acsnano.2c08104.
75. Lei, C.; Xie, Z.; Wu, K.; Fu, Q. Controlled Vertically Aligned Structures in Polymer Composites: Natural Inspiration, Structural Processing, and Functional Application. *Adv. Mater.* **2021**, *33*, 2103495, doi:10.1002/adma.202103495.
76. Kastelic, J.; Galeski, A.; Baer, E. The Multicomposite Structure of Tendon. *Connect. Tissue Res.* **1978**, *6*, 11–23, doi:10.3109/03008207809152283.
77. He, G.; Li, X.; Dai, Y.; Yang, Z.; Zeng, C.; Lin, C.; He, S. Constructing Bioinspired Hierarchical Structure in Polymer Based Energetic Composites with Superior Thermal Conductivity. *Compos. B: Eng.* **2019**, *162*, 678–684, doi:10.1016/j.compositesb.2019.01.046.
78. Mu, X.; Fitzpatrick, V.; Kaplan, D.L. From Silk Spinning to 3D Printing: Polymer Manufacturing Using Directed Hierarchical Molecular Assembly. *Adv. Healthc. Mater.* **2020**, *9*, 1901552, doi:10.1002/adhm.201901552.
79. Liu, J.; Huang, W.; Pang, Y.; Zhu, X.; Zhou, Y.; Yan, D. The in Vitro Biocompatibility of Self-Assembled Hyperbranched Copolyphosphate Nanocarriers. *Biomaterials* **2010**, *31*, 5643–5651, doi:10.1016/j.biomaterials.2010.03.068.

80. Van Dongen, S.F.M.; De Hoog, H.P.M.; Peters, R.J.R.W.; Nallani, M.; Nolte, R.J.M.; Van Hest, J.C.M. Biohybrid Polymer Capsules. *Chem. Rev.* **2009**, *109*, 6212–6274, doi:10.1021/cr900072y.
81. Materials with Structural Hierarchy.
82. Nofar, M.; Yenigul, B.S.; Ozdemir, B.; Kovanci, C.Y.; Ghanbari, A.; Jalali, A. Mechanical and Viscoelastic Properties of Polyethylene-Based Microfibrillated Composites from 100% Recycled Resources. *J. Appl. Polym. Sci.* **2021**, *138*, 50793, doi:10.1002/app.50793.
83. Gao, C.; Yu, L.; Liu, H.; Chen, L. Development of Self-Reinforced Polymer Composites. *Prog. Polym. Sci.* **2012**, *37*, 767–780, doi:10.1016/j.progpolymsci.2011.09.005.
84. Hees, T.; Zhong, F.; Stürzel, M.; Mülhaupt, R. Tailoring Hydrocarbon Polymers and All-Hydrocarbon Composites for Circular Economy. *Macromol. Rapid Commun.* **2019**, *40*, 1800608, doi:10.1002/marc.201800608.
85. Doncom, K.E.B.; Blackman, L.D.; Wright, D.B.; Gibson, M.I.; O'Reilly, R.K. Dispersity Effects in Polymer Self-Assemblies: A Matter of Hierarchical Control. *Chem. Soc. Rev.* **2017**, *46*, 4119–4134, doi:10.1039/c6cs00818f.
86. Frank, A.; Hils, C.; Weber, M.; Kreger, K.; Schmalz, H.; Schmidt, H.W. Hierarchical Superstructures by Combining Crystallization-Driven and Molecular Self-Assembly. *Angew. Chem. Int. Ed.* **2021**, *60*, 21767–21771, doi:10.1002/anie.202105787.
87. Lu, Y.; Lin, J.; Wang, L.; Zhang, L.; Cai, C. Self-Assembly of Copolymer Micelles: Higher-Level Assembly for Constructing Hierarchical Structure. *Chem. Rev.* **2020**, *120*, 4111–4140, doi:10.1021/acs.chemrev.9b00774.
88. Liang, R.; Xue, Y.; Fu, X.; Le, A.N.; Song, Q.; Qiang, Y.; Xie, Q.; Dong, R.; Sun, Z.; Osuji, C.O.; et al. Hierarchically Engineered Nanostructures from Compositionally Anisotropic Molecular Building Blocks. *Nat. Mater.* **2022**, *21*, 1434–1440, doi:10.1038/s41563-022-01393-0.
89. Sun, Z.; Liu, R.; Su, T.; Huang, H.; Kawamoto, K.; Liang, R.; Liu, B.; Zhong, M.; Alexander-Katz, A.; Ross, C.A.; et al. Emergence of Layered Nanoscale Mesh Networks through Intrinsic Molecular Confinement Self-Assembly. *Nat. Nanotechnol.* **2023**, *18*, 273–280, doi:10.1038/s41565-022-01293-z.
90. Zhao, C.; Mark, L.H.; Kim, S.; Chang, E.; Park, C.B.; Lee, P.C. Recent Progress in Micro-/Nano-Fibrillar Reinforced Polymeric Composite Foams. *Polym. Eng. Sci.* **2021**, *61*, 926–941, doi:10.1002/pen.25643.
91. Dziadowiec, D.; Matykiewicz, D.; Szostak, M.; Andrzejewski, J. Overview of the Cast Polyolefin Film Extrusion Technology for Multi-Layer Packaging Applications. *Materials* **2023**, *16*, 1071, doi:10.3390/ma16031071.
92. Naeimirad, M.; Krins, B.; Gruter, G.J.M. A Review on Melt-Spun Biodegradable Fibers. *Sustainability* **2023**, *15*, 14474, doi:10.3390/su151914474.
93. Hofman, A.H.; ten Brinke, G.; Loos, K. Hierarchical Structure Formation in Supramolecular Comb-Shaped Block Copolymers. *Polymer* **2016**, *107*, 343–356, doi:10.1016/j.polymer.2016.08.021.
94. Matsushita, Y.; Takano, A.; Hayashida, K.; Asari, T.; Noro, A. Hierarchical Nanophase-Separated Structures Created by Precisely-Designed Polymers with Complexity. *Polymer* **2009**, *50*, 2191–2203, doi:10.1016/j.polymer.2009.02.047.

95. Ma, L.; Huang, H.; Vargo, E.; Huang, J.; Anderson, C.L.; Chen, T.; Kuzmenko, I.; Ilavsky, J.; Wang, C.; Liu, Y.; et al. Diversifying Composition Leads to Hierarchical Composites with Design Flexibility and Structural Fidelity. *ACS Nano* **2021**, *15*, 14095–14104, doi:10.1021/acsnano.1c04606.
96. Datta, S.; Saha, M.L.; Stang, P.J. Hierarchical Assemblies of Supramolecular Coordination Complexes. *Acc. Chem. Res.* **2018**, *51*, 2047–2063, doi:10.1021/acs.accounts.8b00233.
97. Li, Y.; Jiang, T.; Lin, S.; Lin, J.; Cai, C.; Zhu, X. Hierarchical Nanostructures Self-Assembled from a Mixture System Containing Rod-Coil Block Copolymers and Rigid Homopolymers. *Sci. Rep.* **2015**, *5*, 10137, doi:10.1038/srep10137.
98. Li, Z.; Hillmyer, M.A.; Lodge, T.P. Morphologies of Multicompartment Micelles Formed by ABC Miktoarm Star Terpolymers. *Langmuir* **2006**, *22*, 9409–9417, doi:10.1021/la0620051.
99. Zhuang, Y.; Wang, L.; Lin, J. Hierarchical Nanostructures Self-Assembled from Diblock Copolymer/Homopolymer Blends with Supramolecular Interactions. *J. Phys. Chem. B.* **2011**, *115*, 7550–7560, doi:10.1021/jp2021853.
100. Tyler, C.A.; Qin, J.; Bates, F.S.; Morse, D.C. SCFT Study of Nonfrustrated ABC Triblock Copolymer Melts. *Macromolecules* **2007**, *40*, 4654–4668, doi:10.1021/ma062778w.
101. Qian, H.J.; Lu, Z.Y.; Chen, L.J.; Li, Z.S.; Sun, C.C. Computer Simulation of Cyclic Block Copolymer Microphase Separation. *Macromolecules* **2005**, *38*, 1395–1401, doi:10.1021/ma0478658.
102. Lin, S.; Numasawa, N.; Nose, T.; Lin, J. Brownian Molecular Dynamics Simulation on Self-Assembly Behavior of Rod-Coil Diblock Copolymers. *Macromolecules* **2007**, *40*, 1684–1692, doi:10.1021/ma062064l.
103. Qi, S.; Behringer, H.; Schmid, F. Using Field Theory to Construct Hybrid Particle-Continuum Simulation Schemes with Adaptive Resolution for Soft Matter Systems. *New J. Phys.* **2013**, *15*, 125009, doi:10.1088/1367-2630/15/12/125009.
104. Sides, S.W.; Kim, B.J.; Kramer, E.J.; Fredrickson, G.H. Hybrid Particle-Field Simulations of Polymer Nanocomposites. *Phys. Rev. Lett.* **2006**, *96*, 250601, doi:10.1103/PhysRevLett.96.250601.
105. Maurits, N.M.; Fraaije, J.G.E.M. Mesoscopic Dynamics of Copolymer Melts: From Density Dynamics to External Potential Dynamics Using Nonlocal Kinetic Coupling. *J. Chem. Phys.* **1997**, *107*, 5879–5889, doi:10.1063/1.474313.
106. Sevink, G.J.A.; Schmid, F.; Kawakatsu, T.; Milano, G. Combining Cell-Based Hydrodynamics with Hybrid Particle-Field Simulations: Efficient and Realistic Simulation of Structuring Dynamics. *Soft Matter* **2017**, *13*, 1594–1623, doi:10.1039/c6sm02252a.
107. Kolli, H.B.; De Nicola, A.; Bore, S.L.; Schäfer, K.; Diezemann, G.; Gauss, J.; Kawakatsu, T.; Lu, Z.Y.; Zhu, Y.L.; Milano, G.; et al. Hybrid Particle-Field Molecular Dynamics Simulations of Charged Amphiphiles in an Aqueous Environment. *J. Chem. Theory Comput.* **2018**, *14*, 4928–4937, doi:10.1021/acs.jctc.8b00466.
108. Bore, S.L.; Milano, G.; Cascella, M. Hybrid Particle-Field Model for Conformational Dynamics of Peptide Chains. *J. Chem. Theory Comput.* **2018**, *14*, 1120–1130, doi:10.1021/acs.jctc.7b01160.

109. Bore, S.L.; Kolli, H.B.; De Nicola, A.; Byshkin, M.; Kawakatsu, T.; Milano, G.; Cascella, M. Hybrid Particle-Field Molecular Dynamics under Constant Pressure. *J. Chem. Phys.* **2020**, *152*, 184908, doi:10.1063/5.0007445.
110. Wang, Z.; Ma, Z.; Li, L. Flow-Induced Crystallization of Polymers: Molecular and Thermodynamic Considerations. *Macromolecules* **2016**, *49*, 1505–1517, doi:10.1021/acs.macromol.5b02688.
111. Hu, W.B. Polymer Features in Crystallization. *Chin. J. Polym. Sci. (Engl. Ed.)* **2022**, *40*, 545–555, doi:10.1007/s10118-022-2710-8.
112. Hikosaka, M. Unified Theory of Nucleation of Folded-Chain Crystals (FCCs) and Extended-Chain Crystals (ECCs) of Linear-Chain Polymers: 2. Origin of FCC and ECC*. *Polymer* **1990**, *31*, 458–468, doi:10.1016/0032-3861(90)90385-C.
113. Hikosaka, M. Unified Theory of Nucleation of Folded-Chain Crystals and Extended-Chain Crystals of Linear-Chain Polymers. *Polymer* **1987**, *28*, 1257–1264, doi:10.1016/0032-3861(87)90434-4.
114. Yamazaki, S.; Hikosaka, M.; Toda, A.; Wataoka, I.; Gu, F. Role of Entanglement in Nucleation and "melt Relaxation" of Polyethylene. *Polymer* **2002**, *43*, 6585–6593, doi:10.1016/S0032-3861(02)00592-X.
115. Arrigo, R.; Malucelli, G.; Mantia, F.P.L. Effect of the Elongational Flow on the Morphology and Properties of Polymer Systems: A Brief Review. *Polymers* **2021**, *13*, 3529, doi:10.3390/polym13203529.
116. Liu, D.; Tian, N.; Huang, N.; Cui, K.; Wang, Z.; Hu, T.; Yang, H.; Li, X.; Li, L. Extension-Induced Nucleation under near-Equilibrium Conditions: The Mechanism on the Transition from Point Nucleus to Shish. *Macromolecules* **2014**, *47*, 6813–6823, doi:10.1021/ma501482w.
117. Han, C.C.; Yao, Y.; Zhang, R.; Hobbie, E.K. Effect of Shear Flow on Multi-Component Polymer Mixtures. *Polymer* **2006**, *47*, 3271–3286, doi:10.1016/j.polymer.2006.03.024.
118. Okamoto, M.; Kubo, H.; Kotaka, T. Elongational Flow-Induced Crystallization and Structure Development in Supercooled Poly(Ethylene Naphthalate). *Macromolecules* **1998**, *31*, 4223–4231, doi:10.1021/ma971713d.
119. Watanabe, K.; Suzuki, T.; Masubuchi, Y.; Taniguchi, T.; Takimoto, J.I.; Koyama, K. Crystallization Kinetics of Polypropylene under High Pressure and Steady Shear Flow. *Polymer* **2003**, *44*, 5843–5849, doi:10.1016/S0032-3861(03)00604-9.
120. Chen, L.B.; Huang, Y.H.; Zhao, X.; Liu, L.; Gu, J.D.; Liu, Z.Y.; Yang, W.; Fu, X.R.; Yang, M.B. Simulation and Experimental Studies on the Formation and Evolution of Hierarchical Crystalline Structures at the Multi-Melt Flow Interface. *Compos. - A: Appl. Sci. Manuf.* **2021**, *144*, 106269, doi:10.1016/j.compositesa.2020.106269.
121. Nie, C.; Peng, F.; Cao, R.; Cui, K.; Sheng, J.; Chen, W.; Li, L. Recent Progress in Flow-induced Polymer Crystallization. *J. Polym. Sci.* **2022**, *60*, 3149–3175, doi:10.1002/pol.20220330.
122. Yang, S.; Luo, C.; Lin, H.; Xu, P.P.; Xu, L.; Lei, J.; Zhong, G.J.; Li, Z.M. Robust Propylene-Ethylene Copolymer/Polypropylene Films: Extensional Stress-Induced Orientation Realized at Low Temperature Processing. *Polymer* **2020**, *206*, 122848, doi:10.1016/j.polymer.2020.122848.
123. Yaoita, T.; Isaki, T.; Masubuchi, Y.; Watanabe, H.; Ianniruberto, G.; Marrucci, G. Primitive Chain Network Simulation of Elongational Flows of Entangled Linear Chains: Stretch/Orientation-Induced Reduction of

Monomeric Friction. *Macromolecules* **2012**, *45*, 2773–2782, doi:10.1021/ma202525v.
124. White, J.L.; Spruiell, J.E. The Specification of Orientation and Its Development in Polymer Processing. *Polym. Eng. Sci.* **1983**, *23*, 247–256, doi:10.1002/pen.760230503.
125. Lacroix, C.; Grmela, M.; Carreau, P.J. Morphological Evolution of Immiscible Polymer Blends in Simple Shear and Elongational Flows. *J. Non-Newton. Fluid Mech.* **1999**, *86*, 37–59, doi:10.1016/S0377-0257(98)00201-8.
126. Van Drongelen, M.; Van Erp, T.B.; Peters, G.W.M. Quantification of Non-Isothermal, Multi-Phase Crystallization of Isotactic Polypropylene: The Influence of Cooling Rate and Pressure. *Polymer* **2012**, *53*, 4758–4769, doi:10.1016/j.polymer.2012.08.003.
127. Schuller, T.; Fanzio, P.; Galindo-Rosales, F.J. Analysis of the Importance of Shear-Induced Elastic Stresses in Material Extrusion. *Addit. Manuf.* **2022**, *57*, 102952, doi:10.1016/j.addma.2022.102952.
128. Tadmor, Z. Molecular Orientation in Injection Molding. *J. Appl. Polym. Sci.* **1974**, *18*, 1753–1772, doi:10.1002/app.1974.070180614.
129. Hosseini, H.; Seyev, V.A.; Erdyshev, B.V.B.; Orisov, A.A.B. Rheological Modeling of Polymeric Melts in Extruders upon Two-Dimensional Shear Flow. *Int. Polym. Process.* **2016**, *31*, 51–56, doi:10.3139/217.3131.
130. Ballenger TF; Chen IJ; Crowder JW; Hagler GE; Bogue DC; WHITE JL Polymer Melt Flow Instabilities in Extrusion. Investigation of the Mechanism and Material and Geometric Variables. *Trans. Soc. Rheol.* **1971**, *15*, 195–215, doi:10.1122/1.549207.
131. Liang, J.-Z. Characteristics of Melt Shear Viscosity during Extrusion of Polymers. *Polym. Test.* **2002**, *21*, 307–311, doi:10.1016/S0142-9418(01)00088-5.
132. Pandey, V.; Chen, H.; Ma, J.; Maia, J.M. Extension-Dominated Improved Dispersive Mixing in Single-Screw Extrusion. Part 2: Comparative Analysis with Twin-Screw Extruder. *J. Appl. Polym. Sci.* **2021**, *138*, 49765, doi:10.1002/app.49765.
133. Gupta, V.B.; Bhuvanesh, Y.C. *Manufactured Fibre Technology - Basic Principles of Flow during Fibre Spinning*; Gupta, V.B., Kothari, V.K., Eds.; Chapman & Hall: London, UK, 1997;
134. Collier, J.; Petrovan, S.; Patil, P.; Collier, B. Elongational Rheology of Fiber Forming Polymers. *J. Mater. Sci.* **2005**, *40*, 5133–5137, doi:10.1007/s10853-005-4402-5.
135. Münstedt, H.; Kurzbeck, S.; Stange, J. Importance of Elongational Properties of Polymer Melts for Film Blowing and Thermoforming. *Polym. Eng. Sci.* **2006**, *46*, 1190–1195, doi:10.1002/pen.20588.
136. Revenu, P.; Guillet, J.; Carrot, C. Elongational Flow of Polyethylenes in Isothermal Melt Spinning. *J. Rheol.* **1993**, *37*, 1041–1056, doi:10.1122/1.550408.
137. Yuan, Z.; Chen, X.; Yu, D.; Fernandes, P.; Faroughi, A.; Ferrás, L.L.; Afonso, A.M. Recent Advances in Elongational Flow Dominated Polymer Processing Technologies. *Polymers* **2021**, *13*, 1792, doi:10.3390/polym13111792.
138. Haworth, B.; Jumpa, S. Extensional Flow Characterisation and Extrusion Blow Moulding of High Density Polyethylene Modified by Calcium

Carbonate. *Plast. Rubber Compos.* **1999**, *28*, 363–378, doi:10.1179/146580199101540529.
139. La Mantia, F.P.; Scaffaro, R.; Carianni, G.; Mariani, P. Rheological Properties of Different Film Blowing Polyethylene Samples under Shear and Elongational Flow. *Macromol. Mater. Eng.* **2005**, *290*, 159–164, doi:10.1002/mame.200400237.
140. Münstedt, H.; Steffl, T.; Malmberg, A. Correlation between Rheological Behaviour in Uniaxial Elongation and Film Blowing Properties of Various Polyethylenes. *Rheol. Acta* **2005**, *45*, 14–22, doi:10.1007/s00397-005-0435-6.
141. Gupta, R.K.; Meizner, A.B.; Wissbrun, K.F. Modeling of Polymeric Film-Blowing Processes. *Polym. Eng. Sci.* **1982**, *22*, 172–181, doi:10.1002/pen.760220307.
142. Münstedt, H. Extensional Rheology and Processing of Polymeric Materials. *Int. Polym. Process.* **2018**, *33*, 594–618, doi:10.3139/217.3532.
143. Qin, S.; Jin, T.; Zhang, H.; Zhou, H.; Liu, J.; Xu, X. Optimization of Hot Drawing Process of Ultra-High Molecular Weight Polyethylene Monofilament Prepared by Melt Spinning. *J. Appl. Polym. Sci.* **2022**, *139*, 53075, doi:10.1002/app.53075.
144. Hufenus, R.; Yan, Y.; Dauner, M.; Kikutani, T. Melt-Spun Fibers for Textile Applications. *Materials* **2020**, *13*, 1–32, doi:10.3390/ma13194298.
145. Yu, W.; Wang, L.; Shi, J. Influence of Drawing and Annealing on the Crystallization, Viscoelasticity, and Mechanical Properties for Middle-Molecular-Weight Polyethylene Fishing Monofilaments. *Fibers Polym.* **2018**, *19*, 1050–1056, doi:10.1007/s12221-018-7610-8.
146. Baimark, Y.; Molloy, R.; Molloy, N.; Siripitayananon, J.; Punyodom, W.; Sriyai, M. Synthesis, Characterization and Melt Spinning of a Block Copolymer of L-Lactide and ε-Caprolactone for Potential Use as an Absorbable Monofilament Surgical Suture. *J. Mater. Sci.: Mater. Med.* **2005**, *16*, 699–707, doi:10.1007/s10856-005-2605-6.
147. Charuchinda, A.; Molloy, R.; Siripitayananon, J.; Molloy, N.; Sriyai, M. Factors Influencing the Small-Scale Melt Spinning of Poly(ε-Caprolactone) Monofilament Fibres. *Polym. Int.* **2003**, *52*, 1175–1181, doi:10.1002/pi.1234.
148. Siripitayananon, J.; Molloy, R.; Bunkird, S.; Kleawkla, A.; Panjakha, R.; Chooprayoon, P. Effects of Hot-Drawing and Annealing on the Morphology and Mechanical Properties of Biodegradable Polyester Monofilament Fibers. *Int. Polym. Process.* **2008**, *23*, 161–167, doi:10.3139/217.2025.
149. Nazmul Islam, G.M.; Collie, S.; Qasim, M.; Azam Ali, M. Highly Stretchable and Flexible Melt Spun Thermoplastic Conductive Yarns for Smart Textiles. *Nanomaterials* **2020**, *10*, 1–23, doi:10.3390/nano10122324.
150. Oh, M.O.; Kim, S.H. Conformational Development of Polylactide Films Induced by Uniaxial Drawing. *Polym. Int.* **2014**, *63*, 1247–1253, doi:10.1002/pi.4630.
151. Wang, X.; Zheng, H.; Sun, Y. Study on Structures and Properties of Ultra-Hot Drawing UHMWPE Fibers Fabricated via Dry Spinning Method. *J. Polym. Eng.* **2018**, *38*, 863–870, doi:10.1515/polyeng-2017-0400.
152. Taheri, H.; Nóbrega, J.M.; Samyn, P.; Covas, J.A. The Effect of Temperature and Drawing Ratio on the Mechanical Properties of Polypropylene Monofilaments. *AIP Conf. Proc.* **2014**, *1593*, 80–85, doi:10.1063/1.4873739.

153. Deroiné, M.; Pillin, I.; Le Maguer, G.; Chauvel, M.; Grohens, Y. Development of New Generation Fishing Gear: A Resistant and Biodegradable Monofilament. *Polym. Test.* **2019**, *74*, 163–169, doi:10.1016/j.polymertesting.2018.11.039.
154. Spruiell, J.E. *Structure Formation in Polymeric Fibers - Structure Formation During Melt Spinning*; Salem, D.R., Ed.; Hanser: Munich, Germany, 2001;
155. Furuhashi, Y.; Kimura, Y.; Yoshie, N.; Yamane, H. Higher-Order Structures and Mechanical Properties of Stereocomplex-Type Poly(Lactic Acid) Melt Spun Fibers. *Polymer* **2006**, *47*, 5965–5972, doi:10.1016/j.polymer.2006.06.001.
156. Schimanski, T.; Peijs, T.; Lemstra, P.J.; Loos, J. Influence of Postdrawing Temperature on Mechanical Properties of Melt-Spun Isotactic Polypropylene. *Macromolecules* **2004**, *37*, 1810–1815, doi:10.1021/ma034949s.
157. Pötschke, P.; Paul, D.R. Formation of Co-Continuous Structures in Melt-Mixed Immiscible Polymer Blends. *J. Macromol. Sci., Polym. Rev.* **2003**, *43*, 87–141, doi:10.1081/MC-120018022.
158. Utracki, L.A. On the Viscosity-Concentration Dependence of Immiscible Polymer Blends. *J. Rheol.* **1991**, *35*, 1615–1637, doi:10.1122/1.550248.
159. Pan, D.; Chen, L.; He, H.; Deng, K.; Qin, Z. Deformation of Dispersed Polystyrene Droplets in Immiscible Polypropylene/Polystyrene Blend Fibers under Uniaxial Elongational Flow. *Fibers Polym.* **2016**, *17*, 1343–1351, doi:10.1007/s12221-016-6233-1.
160. Delaby, I.; Ernst, B.; Germain, Y.; Muller, R. Droplet Deformation in Polymer Blends during Uniaxial Elongational Flow: Influence of Viscosity Ratio for Large Capillary Numbers. *J. Rheol.* **1994**, *38*, 1705–1720, doi:10.1122/1.550568.
161. García-Masabet, V.; Pérez, O.S.; Cailloux, J.; Abt, T.; Sánchez-Soto, M.; Carrasco, F.; Maspoch, M.L. PLA/PA Bio-Blends: Induced Morphology by Extrusion. *Polymers* **2020**, *12*, doi:10.3390/polym12010010.
162. Grace, H.P. Dispersion Phenomena in High Viscosity Immiscible Fluid Systems and Application of Static Mixers as Dispersion Devices in Such Systems. *Chem. Eng. Commun.* **1982**, *14*, 225–277, doi:10.1080/00986448208911047.
163. Cravero, F.; Arrigo, R.; Frache, A. Processing/Microstructure Relationships in Melt Compounded Polyamide 6 with Different Molecular Weights: Effect of Screw Speed and Viscosity Ratio. *Polym. Eng. Sci.* **2025**, *65*, 2525–2538, doi:10.1002/pen.27165.
164. Ma, G.Q.; Sun, Z.B.; Ren, J.Y.; Zeng, Y.; Jia, D.Z.; Li, Y.; Guan, B.; Zhong, G.J.; Li, Z.M. Reorganization of Hydrogen Bonding in Biobased Polyamide 5,13 under the Thermo-Mechanical Field: Hierarchical Microstructure Evolution and Achieving Excellent Mechanical Performance. *Biomacromolecules* **2022**, *23*, 3990–4003, doi:10.1021/acs.biomac.2c00826.
165. Wang, L.; Dong, X.; Huang, M.; Wang, D. Transient Microstructure in Long Alkane Segment Polyamide: Deformation Mechanism and Its Temperature Dependence. *Polymer* **2016**, *97*, 217–225, doi:10.1016/j.polymer.2016.05.038.
166. Cai, Z.; Liu, X.; Zhou, Q.; Wang, Y.; Zhu, C.; Xiao, X.; Fang, D.; Bao, H. The Structure Evolution of Polyamide 1212 after Stretched at Different Temperatures and Its Correlation with Mechanical Properties. *Polymer* **2017**, *117*, 249–258, doi:10.1016/j.polymer.2017.04.037.

167. Thyashan, N.; Perera, Y.S.; Xiao, R.; Abeykoon, C. Investigation of the Effect of Materials and Processing Conditions in Twin-Screw Extrusion. *Int. J. Lightweight Mater. Manuf.* **2024**, *7*, 353–361, doi:10.1016/j.ijlmm.2023.09.003.
168. Bernagozzi, G.; Arrigo, R.; Frache, A. Evolution of the Microstructure of PP-LDHs Nanocomposites during Melt Compounding: A Simulation Approach. *Polymers* **2024**, *16*, 70, doi:10.3390/polym16010070.
169. Cravero, F.; Arrigo, R.; Frache, A. Processing-Driven Structuring of Polymer-Based Materials: A Brief Overview. *Polymers* **2025**, *17*, 76, doi:10.3390/polym17182483.
170. Teyssandier, F.; Cassagnau, P.; Gérard, J.F.; Mignard, N.; Mélis, F. Morphology and Mechanical Properties of PA12/Plasticized Starch Blends Prepared by High-Shear Extrusion. *Mater. Chem. Phys.* **2012**, *133*, 913–923, doi:10.1016/j.matchemphys.2012.01.117.
171. Louizi, M.; Massardier, V.; Cassagnau, P. Contribution of High-Shear Processing to the Compatibilization of (PP/EPR)/PE Ternary Blends. *Macromol. Mater. Eng.* **2014**, *299*, 674–688, doi:10.1002/mame.201300268.
172. Raj, A.; Samuel, C.; Malladi, N.; Prashantha, K. Enhanced (Thermo)Mechanical Properties in Biobased Poly(l-Lactide)/Poly(Amide-12) Blends Using High Shear Extrusion Processing without Compatibilizers. *Polym. Eng. Sci.* **2020**, *60*, 1902–1916, doi:10.1002/pen.25426.
173. Zhang, L.; Lu, C.; Dong, P.; Wang, K.; Zhang, Q. Realizing Mechanically Reinforced All-Polyethylene Material by Dispersing UHMWPE via High-Speed Shear Extrusion. *Polymer* **2019**, *180*, 121711, doi:10.1016/j.polymer.2019.121711.
174. Zhang, L.; Lu, C.; Dong, P.; Wang, K. Realizing Self-Reinforcement of Polyethylene via High-Speed Shear Processing. *J. Polym. Res.* **2019**, *26*, 236, doi:10.1007/s10965-019-1899-x.
175. Yu, W. jin; Xu, S. man; Zhang, L.; Fu, Q. Morphology and Mechanical Properties of Immiscible Polyethylene/Polyamide12 Blends Prepared by High Shear Processing. *Chin. J. Polym. Sci. (Engl. Ed.)* **2017**, *35*, 1132–1142, doi:10.1007/s10118-017-1954-1.
176. Sui, G.; Jing, M.; Zhao, J.; Wang, K.; Zhang, Q.; Fu, Q. A Comparison Study of High Shear Force and Compatibilizer on the Phase Morphologies and Properties of Polypropylene/Polylactide (PP/PLA) Blends. *Polymer* **2018**, *154*, 119–127, doi:10.1016/j.polymer.2018.09.005.
177. Shimizu, H.; Li, Y.; Kaito, A.; Sano, H. Formation of Nanostructured PVDF/PA11 Blends Using High-Shear Processing. *Macromolecules* **2005**, *38*, 7880–7883, doi:10.1021/ma051395f.
178. Farahanchi, A.; Boehm, E.; Orbey, N.; Malloy, R. The Effect of Ultra-High Speed Twin Screw Extrusion on ABS/Organoclay Nanocomposite Blend Properties. *Polym. Eng. Sci.* **2017**, *57*, 60–68, doi:10.1002/pen.24385.
179. Farahanchi, A.; Malloy, R.A.; Sobkowicz, M.J. Extreme Shear Processing for Exfoliating Organoclay in Nanocomposites with Incompatible Polymers. *Polymer* **2018**, *145*, 117–126, doi:10.1016/j.polymer.2018.04.056.
180. Li, Y.; Shimizu, H. Fabrication of Nanostructured Polycarbonate/Poly(Methyl Methacrylate) Blends with Improved Optical and Mechanical Properties by High-Shear Processing. *Polym. Eng. Sci.* **2011**, *51*, 1437–1445, doi:10.1002/pen.21879.
181. Pi, L.; Nie, M.; Wang, Q. Crystalline Composition and Morphology in Isotactic Polypropylene Pipe under Combining Effects of Rotation Extrusion

and Fibril β-Nucleating Agent. *J. Vinyl Addit. Technol.* **2019**, *25*, 195–202, doi:10.1002/vnl.21686.
182. Nie, M.; Bai, S.B.; Wang, Q. High-Density Polyethylene Pipe with High Resistance to Slow Crack Growth Prepared via Rotation Extrusion. *Polym. Bull.* **2010**, *65*, 609–621, doi:10.1007/s00289-010-0270-5.
183. Liu, W.; Wang, Q.; Nie, M. Structure and Performance of Polybutene-1 Pipes Produced via Mandrel Rotation Extrusion. *J. Polym. Eng.* **2014**, *34*, 15–22, doi:10.1515/polyeng-2013-0245.
184. Chen, B.; Yang, H.; Shen, K.; Fu, Q.; Gao, X. The Effect of High-Temperature Annealing on Thermal Properties and Morphology of Polyethylene Pipes Prepared by Rotational Shear. *Polymer* **2020**, *204*, 122770, doi:10.1016/j.polymer.2020.122770.
185. Han, R.; Nie, M.; Bai, S.; Wang, Q. Control over Crystalline Form in Polypropylene Pipe via Mandrel Rotation Extrusion. *Polym. Bull.* **2013**, *70*, 2083–2096, doi:10.1007/s00289-013-0963-7.
186. Yang, H.; Luo, X.; Shen, K.; Yuan, Y.; Fu, Q.; Gao, X.; Jiang, L. The Role of Mandrel Rotation Speed on Morphology and Mechanical Properties of Polyethylene Pipes Produced by Rotational Shear. *Polymer* **2019**, *184*, 121915, doi:10.1016/j.polymer.2019.121915.
187. Intawong, N.-T.; Arajang, A.D.; Domsom, S.U.; Oochooshai, T.Y.; Antala, C.K. An Annular Rotating-Die Technique in Extrusion Process: Effect of Mandrel Rotating Speed on Extrudate Swell Behavior of HDPE Parison. *Int. Polym. Process.* **2014**, *5*, 607–615, doi:10.3139/217.2930.
188. Lu, X.; Qian, R.; Brown, N.; Buczala, C. The Effect of Pressure and Contaminants on Slow Crack Growth in a Butt Fusion in a Polyethylene Gas Pipe. *J. Appl. Polym. Sci.* **1992**, *46*, 1417–1427, doi:10.1002/app.1992.070460812.
189. Guo, Y.; Wang, Q.; Bai, S. The Effect of Rotational Extrusion on the Structure and Properties of HDPE Pipes. *Polym. Plast. Technol. Mater.* **2010**, *49*, 908–915, doi:10.1080/03602551003773098.
190. Lu, X.; Zhou, Z.; Brown, N. The Anisotropy of Slow Crack Growth in Polyethylene Pipes. *Polym. Eng. Sci.* **1994**, *34*, 109–115, doi:10.1002/pen.760340206.
191. Nie, M.; Wang, Q.; Bai, S.B.; Li, Z.; Huang, A. The Formation and Evolution of the Hierarchical Structure of Polyethylene Pipe during Extrusion Processing. *J. Macromol. Sci., Part B: Phys.* **2014**, *53*, 205–216, doi:10.1080/00222348.2013.810092.
192. Nie, M.; Li, X.; Hu, X.; Wang, Q. Effect of Die Temperature on Morphology and Performance of Polyethylene Pipe Prepared via Mandrel Rotation Extrusion. *J. Macromol. Sci., Part B: Phys.* **2014**, *53*, 1442–1452, doi:10.1080/00222348.2014.928161.
193. Pi, L.; Hu, X.; Nie, M.; Wang, Q. Role of Ultrahigh Molecular Weight Polyethylene during Rotation Extrusion of Polyethylene Pipe. *Ind. Eng. Chem. Res.* **2014**, *53*, 13828–13832, doi:10.1021/ie502452u.
194. Li, Y.; Nie, M.; Wang, Q. Synergistic Effect of Self-Assembling Nucleating Agent and Crystallization Promoter on Polypropylene Random Copolymer Pipes via Rotation Extrusion. *Polym. Eng. Sci.* **2016**, *56*, 866–873, doi:10.1002/pen.24315.
195. Tang, H.I.; Hiltner, A.; Baer, E. Biaxial Orientation of Polypropylene by Hydrostatic Solid State Extrusion Part III: Mechanical Properties and

Deformation Mechanisms. *Polym. Eng. Sci.* **1987**, *27*, 876–886, doi:10.1002/pen.760271203.
196. Han, R.; Nie, M.; Bai, S.-B.; Wang, Q. Effect of the Mandrel Rotation Speed and Inner Wall Cooling Rate on the Performance and Structure of Polypropylene Block-Copolymer Pipe. *Int. Polym. Process.* **2013**, *5*, 496–505, doi:10.3139/217.2761.
197. Shao, H.; Yao', W.; Huang, B.; Zhao, Y. Effect of Crystallinity and Spherulite Structure on the Mechanical Properties of Poly(I-Butene). *J. Polym. Eng.* **2009**, *29*, 341–353, doi:10.1515/POLYENG.2009.29.6.341.
198. Kong, D.C.; Yang, M.H.; Zhang, X.S.; Du, Z.C.; Fu, Q.; Gao, X.Q.; Gong, J.W. Control of Polymer Properties by Entanglement: A Review. *Macromol. Mater. Eng.* **2021**, *306*, 2100536, doi:10.1002/mame.202100536.
199. Qingfeng, W.; Nanqiao, Z.; Bing, L.; Ping, Z. Study on the Effect of Axial Vibration of Screw in Plasticating Process (Extrusion Part). *Polym. Plast. Technol. Mater.* **2008**, *47*, 318–324, doi:10.1080/03602550701870065.
200. An, F.Z.; Gao, X.Q.; Lei, J.; Deng, C.; Li, Z.M.; Shen, K.Z. Vibration Assisted Extrusion of Polypropylene. *Chin. J. Polym. Sci.* **2015**, *33*, 688–696, doi:10.1007/s10118-015-1617-z.
201. Ibar, J.P. Processing Polymer Melts under Rheo-Fluidification Flow Conditions, Part 1: Boosting Shear-Thinning by Adding Low Frequency Nonlinear Vibration to Induce Strain Softening. *J. Macromol. Sci., Part B: Phys.* **2013**, *52*, 407–441, doi:10.1080/00222348.2012.711999.
202. Zsayev, A.Z.; Wong, C.M.; Zeng, X. Effect of Oscillations During Extrusion on Rheology and Mechanical Properties of Polymers. *Adv. Polym. Tech.* **1990**, *10*, 31–45, doi:10.1002/adv.1990.060100104.
203. Casulli, J.; Clermont, J.R.; Ziegler, A.V.; Mena, B. The Oscillating Die: A Useful Concept in Polymer Extrusion. *Polym. Eng. Sci.* **1990**, *30*, 1551–1556, doi:10.1002/pen.760302310.
204. Fridman, M.L.; Peshkovsky, S.L.; Vinogradov, G.V. The Rheology of Thermoplastics Under Conditions of Spiral Flow and Vibrations on Extrusion. *Polym. Eng. Sci.* **1981**, *21*, 755–767, doi:10.1002/pen.760211204.
205. Chen, J.; Chen, Y.; Li, H.; Lai, S.Y.; Jow, J. Physical and Chemical Effects of Ultrasound Vibration on Polymer Melt in Extrusion. *Ultrason. Sonochemistry* **2010**, *17*, 66–71, doi:10.1016/j.ultsonch.2009.05.005.
206. Guo, S.; Li, Y.; Chen, G.; Li, H. Ultrasonic Improvement of Rheological and Processing Behaviour of LLDPE during Extrusion. *Polym. Int.* **2003**, *52*, 68–73, doi:10.1002/pi.1005.
207. Chen, Y.; Li, H. Mechanism for Effect of Ultrasound on Polymer Melt in Extrusion. *J. Polym. Sci., Part B: Polym. Phys.* **2007**, *45*, 1226–1233, doi:10.1002/polb.21132.
208. Liu, G.; Li, H. Extrusion of Ultrahigh Molecular Weight Polyethylene under Ultrasonic Vibration Field. *J. Appl. Polym. Sci.* **2003**, *89*, 2628–2632, doi:10.1002/app.12163.
209. Ibar, J.P. Control of Polymer Properties by Melt Vibration Technology: A Review. *Polym. Eng. Sci.* **1998**, *38*, 1–20, doi:10.1002/pen.10161.
210. Cao, Y.; Li, H. Influence of Ultrasound on the Processing and Structure of Polypropylene during Extrusion. *Polym. Eng. Sci.* **2002**, *42*, 1534–1540, doi:10.1002/pen.11049.
211. Kaiyuan, C.; Nanqiao, Z.; Bin, L.; Shengping, W. Effect of Vibration Extrusion on the Structure and Properties of High-Density Polyethylene Pipes. *Polym. Int.* **2009**, *58*, 117–123, doi:10.1002/pi.2500.

212. Qu, J.; Zeng, G.; Feng, Y.; Jin, G.; He, H.; Cao, X. Effect of Screw Axial Vibration on Polymer Melting Process in Single-Screw Extruders. *J. Appl. Polym. Sci.* **2006**, *100*, 3860–3876, doi:10.1002/app.22293.
213. Gao, X.; Zhang, J.; Chen, C.; Shen, K. Effect of Vibration Extrusion on High-Density Polyethylene. *J. Appl. Polym. Sci.* **2007**, *106*, 552–557, doi:10.1002/app.26551.
214. Chen, K.Y.; Zhou, N.Q.; Liu, B.; Jin, G. Improved Mechanical Properties and Structure of Polypropylene Pipe Prepared under Vibration Force Field. *J. Appl. Polym. Sci.* **2009**, *114*, 3612–3620, doi:10.1002/app.30997.
215. Peng, B.; Wu, H.; Bao, W.; Guo, S.; Chen, Y.; Huang, H.; Chen, H.; Lai, S.Y.; Jow, J. Effects of Ultrasound on the Morphology and Properties of Propylene-Based Plastomer/Nanosilica Composites. *Polym. Int.* **2011**, *43*, 91–96, doi:10.1038/pj.2010.95.
216. Chen, G.; Guo, S.; Li, Y. Dynamic Rheological Properties of High-Density Polyethylene/Polystyrene Blends Extruded in the Presence of Ultrasonic Oscillations. *J. Appl. Polym. Sci.* **2004**, *92*, 3153–3158, doi:10.1002/app.20282.
217. Isayev, A.I.; Hong, C.K.; Kim, K.J. Continuous Mixing and Compounding of Polymer/Filler and Polymer/Polymer Mixtures with the Aid of Ultrasound. *Rubber Chem. Technol.* **2003**, *76*, 923–947, doi:10.5254/1.3547782.
218. Oh, J.S.; Isayev, A.I.; Rogunova, M.A. Continuous Ultrasonic Process for in Situ Compatibilization of Polypropylene/Natural Rubber Blends. *Polymer* **2003**, *44*, 2337–2349, doi:10.1016/S0032-3861(03)00080-6.
219. Bing, L.; Qiao, Z.N.; Hong, Z.Z.; Hua, L.W. Study on Mechanical Properties and Molecular Aggregate of the Dynamic Extrusion Polymer Filling System. *Polym. Plast. Technol. Eng.* **2007**, *46*, 293–298, doi:10.1080/03602550601155724.
220. Qu, J.; Qin, X.; Cao, X.; Jin, G. Effect of Vibrating Extrusion on the Structure and Mechanical Properties of Isotactic Polypropylene. *Polym. Plast. Technol. Eng.* **2006**, *45*, 1065–1071, doi:10.1080/03602550600728836.
221. Isayev, A.I.; Wong, C.M.; Zeng, X. Flow of Thermoplastics in an Annular Die under Orthogonal Oscillations. *J. Non-Newton. Fluid Mech.* **1990**, *34*, 375–397, doi:10.1016/0377-0257(90)80030-4.
222. Li, Y.; Chen, G.; Guo, S.; Li, H. Effect of Ultrasonic Oscillations on the Rheological Behavior and Morphology of Illite-Filled High-Density Polyethylene Composites. *J. Appl. Polym. Sci.* **2005**, *96*, 379–384, doi:10.1002/app.21440.
223. Wang, Z.W.; Hu, J.; An, F.Z.; Gong, J.W.; Gao, X.Q.; Deng, C.; Shen, K.Z. Vibration-Dependent Morphology and Crystal Structure of Isotactic Polypropylene. *J. Mater. Sci.* **2013**, *48*, 6986–6993, doi:10.1007/s10853-013-7507-2.
224. Palierne, J.F. Linear Rheology of Viscoelastic Emulsions with Interfacial Tension. *Rheol Acta* **1990**, *29*, 204–214, doi:10.1007/BF01331356.
225. Dreval, V.E.; Vinogradov, G.V.; Plotnikova, E.P.; Zabugina, M.P.; Krasnikova, N.P.; Kotova, E.V.; Pelzbauer, Z. Deformation of Melts of Mixtures of Incompatible Polymers in a Uniform Shear Field and the Process of Their Fibrillation. *Rheol Acta* **1983**, *22*, 102–107, doi:10.1007/BF01679834.
226. Wang, Y.; Zhao, W.; Wang, X.; Wu, D. Preparation, Mechanical Properties and Microstructure of Polyoxymethylene Fiber through Melt Spinning and

Hot Drawing by Using Injection-Molding Grade Resins. *Fibers Polym.* **2016**, *17*, 1464–1474, doi:10.1007/s12221-016-6586-5.
227. Bashirgonbadi, A.; Delva, L.; Caron, E.; Marchesini, F.H.; Van Geem, K.M.; Ragaert, K. The Interplay between Macromolecular Structure, Rheology, Processing Condition, and Morphology for (Linear) Low Density Polyethylenes in Film Blowing. *Polymer* **2024**, *290*, 126566, doi:10.1016/j.polymer.2023.126566.
228. Boone, J.; Loxt, F.; Pottie, S. Deficiencies of Polypropylene in i t s Use as a Food-Packaging Material-a Review. *Packag. Technol. Sci.* **1993**, *6*, 277–281, doi:10.1002/pts.2770060508.
229. Wu, F.; Misra, M.; Mohanty, A.K. Challenges and New Opportunities on Barrier Performance of Biodegradable Polymers for Sustainable Packaging. *Prog. Polym. Sci.* **2021**, *117*, 101395, doi:10.1016/j.progpolymsci.2021.101395.
230. Chellamani, K.P.; Veerasubramanian, D.; Vignesh Balaji, R.S. Surgical Sutures: An Overview. *J. Acad. Indus. Res.* **2013**, *1*, 778–782.
231. Byrne, M.; Aly, A. The Surgical Suture. *Aesthet. Surg. J.* **2019**, *39*, S67–S72, doi:10.1093/asj/sjz036.
232. Chikhalikar, K.; Banik, S.; Azad, L.B.; Jadhav, K.; Mahajan, S.; Ahmad, Z.; Kulkarni, S.; Gupta, S.; Doshi, P.; Pol, H.; et al. Extrusion Film Casting of Long Chain Branched Polypropylene. *Polym. Eng. Sci.* **2015**, *55*, 1977–1987, doi:10.1002/pen.24039.
233. Saffar, A.; Ajji, A.; Carreau, P.J.; Kamal, M.R. The Impact of New Crystalline Lamellae Formation during Annealing on the Properties of Polypropylene Based Films and Membranes. *Polymer* **2014**, *55*, 3156–3167, doi:10.1016/j.polymer.2014.05.017.
234. Ding, L.; Zhang, D.; Yan, N.; Zhang, S.; Wu, T.; Yang, F.; Lan, F.; Cao, Y.; Xiang, M. The Structure Changes of Polypropylene Precursor Film with Different Die Draw Ratio during Annealing. *Polymer* **2020**, *208*, 122958, doi:10.1016/j.polymer.2020.122958.
235. Hu, B.; Cai, Q.; Xu, R.; Mo, H.; Chen, C.; Zhang, F.; Lei, C. Influence of Uniaxial Cold Stretching Followed by Uniaxial Hot Stretching Conditions on Crystal Transformation and Microstructure in Extrusion Cast and Annealed Polyvinylidene Fluoride Porous Membranes. *J. Plast. Film and Sheeting* **2015**, *31*, 269–285, doi:10.1177/8756087914564394.
236. Lin, Y.; Tu, W.; Verpaalen, R.C.P.; Zhang, H.; Bastiaansen, C.W.M.; Peijs, T. Transparent, Lightweight, and High Strength Polyethylene Films by a Scalable Continuous Extrusion and Solid-State Drawing Process. *Macrom. Mater. Eng.* **2019**, *304*, 1900138, doi:10.1002/mame.201900138.
237. Rauwendaal, C. *Understanding Extrusion*; Hanser Publications: Munich, Germany, 2018;
238. Zhu, M.F.; Yang, H.H. *Handbook of Fiber Chemistry - Polypropylene Fibers*; Menachem, L., Ed.; CRC Press: Boca Raton, FL, USA, 2007;
239. Peacock, A.J.; Calhoun, A. *Polymer Chemistry: Properties and Applications*; Hanser: Munich, Germany, 2006;
240. Wang, F.; Liu, L.; Xue, P.; Jia, M.; Wang, S.; Cai, J. The Influence of Formation Temperatures on the Crystal Structure and Mechanical Properties of Ultrahigh-Molecular-Weight Polyethylene/High-Density Polyethylene-Blend Fibers Prepared by Melt Spinning. *J. Ind. Text.* **2020**, *49*, 1011–1035, doi:10.1177/1528083719827371.

241. Bayramol, D.V. Investigation on the Effect of Draw Ratio on Voltage Outputs of Polarised Isotactic Polypropylene Monofilaments. *Tekst. ve Muhendis* **2016**, *23*, 166–171, doi:10.7216/1300759920162310301.
242. Rudolf, A.; Smole, M.S. Structure-Properties Relations of the Drawn Poly(Ethylene Terephthalate) Filament Sewing Thread. *J. Appl. Polym. Sci.* **2008**, *110*, 2641–2648, doi:10.1002/app.25008.
243. Zhang, J.M.; Hua, Q.; Reynolds, C.T.; Zhao, Y.; Dai, Z.; Bilotti, E.; Tang, J.; Peijs, T. Preparation of High Modulus Poly(Ethylene Terephthalate): Influence of Molecular Weight, Extrusion, and Drawing Parameters. *Int. J. Polym. Sci.* **2017**, *2017*, doi:10.1155/2017/2781425.
244. Sabard, M.; Gouanvé, F.; Espuche, E.; Fulchiron, R.; Seytre, G.; Fillot, L.A.; Trouillet-Fonti, L. Influence of Film Processing Conditions on the Morphology of Polyamide 6: Consequences on Water and Ethanol Sorption Properties. *J. Membr. Sci.* **2012**, *415–416*, 670–680, doi:10.1016/j.memsci.2012.05.048.
245. Xie, J.; Yin, L.; Wu, Y.; Xu, R.; Lei, C. The Effect of the Melt-Drawing Ratio on the Microstructure and Mechanical Properties of Poly(Butylene Succinate) Cast Films with Row-Nucleated Lamellar Structure. *Polym. Test.* **2021**, *104*, 107394, doi:10.1016/j.polymertesting.2021.107394.
246. Zhou, Y.G.; Turng, L.S.; Shen, C.Y. Morphological Evolution and Orientation Development of Stretched iPP Films: Influence of Draw Ratio. *J. Polym. Sci., Part B: Polym. Phys.* **2010**, *48*, 1223–1234, doi:10.1002/polb.22013.
247. Zhou, Y.G.; Wu, W.B.; Zou, J.; Turng, L.S. Dual-Scale Modeling and Simulation of Film Casting of Isotactic Polypropylene. *J. Plast. Film Sheeting* **2016**, *32*, 239–271, doi:10.1177/8756087915595853.
248. Liu, J.; Xu, M.; Zhang, S.; Liang, J.; Quan, H.; Liu, J.; Shi, H.; Gao, D. Influences of Processing on the Phase Transition and Crystallization of Polypropylene Cast Films. *J. Appl. Polym. Sci.* **2014**, *131*, 41100, doi:10.1002/app.41100.
249. Mai, F.; Tu, W.; Bilotti, E.; Peijs, T. The Influence of Solid-State Drawing on Mechanical Properties and Hydrolytic Degradation of Melt-Spun Poly(Lactic Acid) (PLA) Tapes. *Fibers* **2015**, *3*, 523–538, doi:10.3390/fib3040523.
250. Xu, R.; Zeng, S.; Wang, J.; Kang, J.; Xiang, M.; Yang, F. Impact of Different Die Draw Ratio on Crystalline and Oriented Properties of Polypropylene Cast Films and Annealed Films. *J. Polym. Res.* **2018**, *25*, 142, doi:10.1007/s10965-018-1534-2.
251. Xu, R.; Xie, J.; Lei, C. Influence of Melt-Draw Ratio on the Crystalline Behaviour of a Polylactic Acid Cast Film with a Chi Structure. *RSC Adv.* **2017**, *7*, 39914–39921, doi:10.1039/c7ra05422j.
252. Sadeghi, F.; Ajji, A.; Carreau, P.J. Study of Polypropylene Morphology Obtained from Blown and Cast Film Processes: Initial Morphology Requirements for Making Porous Membrane by Stretching. *J. Plast. Film Sheeting* **2005**, *21*, 199–216, doi:10.1177/8756087905057085.
253. Agassant, J.F.; Demay, Y.; Sollogoub, C.; Silagy, D. Cast Film Extrusion: An Overview of Experimental and Theoretical Approaches. *Int. Polym. Process.* **2005**, *20*, 136–148, doi:10.3139/217.1874.
254. Gnoffo, C.; Arrigo, R.; Frache, A. An Upcycling Strategy for Polyethylene Terephthalate Fibers: All-Polymer Composites with Enhanced Mechanical Properties. *J. Compos. Sci.* **2024**, *8*, 527, doi:10.3390/jcs8120527.

255. Xu, R.; Chen, X.; Xie, J.; Cai, Q.; Lei, C. Influence of Melt-Draw Ratio on the Crystalline Structure and Properties of Polypropylene Cast Film and Stretched Microporous Membrane. *Ind. Eng. Chem. Res.* **2015**, *54*, 2991–2999, doi:10.1021/acs.iecr.5b00215.
256. Sadeghi, F.; Ajji, A.; Carreau, P.J. Analysis of Row Nucleated Lamellar Morphology of Polypropylene Obtained from the Cast Film Process: Effect of Melt Rheology and Process Conditions. *Polym. Eng. Sci.* **2007**, *47*, 1170–1178, doi:10.1002/pen.20837.
257. Hu, B.; Lei, C.; Xu, R.; Shi, W.; Cai, Q.; Mo, H.; Chen, C. Influence of Melt-Draw Ratio on the Structure and Properties of Poly(Vinylidiene Fluoride) Cast Film. *J. Plast. Film Sheeting* **2014**, *30*, 300–313, doi:10.1177/8756087913508122.
258. Yang, D.C.; Thomas, E.L. An Electron Microscopy and X-Ray Diffraction Study of the Microstructures of Melt-Drawn Polyethylene Films. *J. Mater. Sci.* **1984**, *19*, 2098–2110, doi:10.1007/BF01058086.
259. Shanak, H.; Naumann, A.; Lion, J.; Götz, W.; Pelster, R. Orientation of Nano-Crystallites and Anisotropy of Uniaxially Drawn α-Polyamide 6 Films: XRD, FTIR, and Microwave Measurements. *J. Mater. Sci.* **2014**, *49*, 8074–8083, doi:10.1007/s10853-014-8515-6.
260. Zhang, J.; Li, Y.; Ma, G.; Ren, J.; Wang, G.; Zhang, S.; Zhang, M.; Luan, J. Study of the Microstructure Formation Mechanisms of Poly(Ether-Ether-Ketone) Monofilaments via Melt Spinning. *J. Appl. Polym. Sci.* **2023**, *140*, 53365, doi:10.1002/app.53365.
261. Houichi, H.; Maazouz, A.; Elleuch, B. Crystallization Behavior and Spherulitic Morphology of Poly(Lactic Acid) Films Induced by Casting Process. *Polym. Eng. Sci.* **2015**, *55*, 1881–1888, doi:10.1002/pen.24028.
262. Zeng, B.; Ai, J.; Xia, M.; Pang, Y.; Zheng, Y.; Shen, J.; Guo, S. Deep Insight into the Effect of Microstructure Evolution on Film-Forming Properties of Polylactide during Uniaxial Hot-Stretching Process. *Macromolecules* **2024**, *57*, 4937–4946, doi:10.1021/acs.macromol.4c00249.
263. Ma, A.; Xu, L.; Yin, B.; Yang, M.; Xie, B. Influences of Melt-Draw Ratio and Annealing on the Crystalline Structure and Orientation of Poly(4-Methyl-1-Pentene) Casting Films. *RSC Adv.* **2016**, *6*, 62038–62044, doi:10.1039/C6RA08156H.
264. Tabatabaei, S.H.; Carreau, P.J.; Ajji, A. Structure and Properties of MDO Stretched Polypropylene. *Polymer* **2009**, *50*, 3981–3989, doi:10.1016/j.polymer.2009.06.059.
265. Cui, K.; Ma, Z.; Tian, N.; Su, F.; Liu, D.; Li, L. Multiscale and Multistep Ordering of Flow-Induced Nucleation of Polymers. *Chem. Rev.* **2018**, *118*, 1840–1886, doi:10.1021/acs.chemrev.7b00500.
266. Wei, Q.-Y.; Huang, J.-Z.; Jia, D.-Z.; Lei, J.; Huang, H.-D.; Lin, H.; Xu, J.-Z.; Zhong, G.-J.; Li, Z.-M. Integration of Stiffness, Ductility, Heat Resistance, and Transparency for Polylactide Films by Manipulation of Amorphous Chain Networks and Oriented Nanocrystals. *Macromolecules* **2024**, *57*, 3706–3718, doi:10.1021/acs.macromol.4c00215.
267. Lin, Y.J.; Dias, P.; Chen, H.Y.; Chum, S.; Hiltner, A.; Baer, E. Oxygen Permeability of Biaxially Oriented Polypropylene Films. *Polym. Eng. Sci.* **2008**, *48*, 642–648, doi:10.1002/pen.20988.
268. Wang, F.; Liu, L.; Xue, P.; Jia, M.; Sun, H. A Study of the Mechanical Behavior and Crystal Structure of UHMWPE/HDPE Blend Fibers Prepared

by Melt Spinning. *J. Eng. Fibers Fabr.* **2018**, *13*, 23–36, doi:10.1177/155892501801300304.
269. Youn, C.; Gwak, H.J.; Bae, Y.; Kim, D.; Yeang, B.J.; Doh, S.J.; Yeo, S.Y. Improving Mechanical Properties of Melt-Spun Polyetherimide Monofilaments by Thermal Drawing. *J. Appl. Polym. Sci.* **2022**, *139*, 53155, doi:10.1002/app.53155.
270. Bai, H.; Wang, Y.; Zhang, Z.; Han, L.; Li, Y.; Liu, L.; Zhou, Z.; Men, Y. Influence of Annealing on Microstructure and Mechanical Properties of Isotactic Polypropylene with β-Phase Nucleating Agent. *Macromolecules* **2009**, *42*, 6647–6655, doi:10.1021/ma9001269.
271. Zia, Q.; Mileva, D.; Androsch, R. Rigid Amorphous Fraction in Isotactic Polypropylene. *Macromolecules* **2008**, *41*, 8095–8102, doi:10.1021/ma801455m.
272. Hedesiu, C.; Demco, D.E.; Kleppinger, R.; Vanden Poel, G.; Gijsbers, W.; Blümich, B.; Remerie, K.; Litvinov, V.M. Effect of Temperature and Annealing on the Phase Composition, Molecular Mobility, and the Thickness of Domains in Isotactic Polypropylene Studied by Proton Solid-State NMR, SAXS, and DSC. *Macromolecules* **2007**, *40*, 3977–3989, doi:10.1021/ma070014q.
273. Jiang, Z.; Tang, Y.; Rieger, J.; Enderle, H.F.; Lilge, D.; Roth, S.V.; Gehrke, R.; Wu, Z.; Li, Z.; Li, X.; et al. Structural Evolution of Melt-Drawn Transparent High-Density Polyethylene during Heating and Annealing: Synchrotron Small-Angle X-Ray Scattering Study. *Eur. Polym. J.* **2010**, *46*, 1866–1877, doi:10.1016/j.eurpolymj.2010.06.004.
274. Xu, R.J.; Lei, C.; Cai, Q.; Hu, B.; Shi, W.; Mo, H.; Chen, C. Micropore Formation Process during Stretching of Polypropylene Casting Precursor Film. *Plast. Rubber Compos.* **2014**, *43*, 257–263, doi:10.1179/1743289814Y.0000000100.
275. Fakirov, S.; Bhattacharyya, D.; Lin, R.J.T.; Fuchs, C.; Friedrich, K. Contribution of Coalescence to Microfibril Formation in Polymer Blends during Cold Drawing. *J. Macromol. Sci., Part B: Phys.* **2007**, *46 B*, 183–194, doi:10.1080/00222340601044375.
276. Yan, X.; Gao, Z.; Zhu, C.; Song, L.; Qi, D.; Mao, N. Microfibrillation and Properties of Poly (Styrene Acrylate) Microspheres Reinforced Polymethyl Methacrylate Composite Fibers. *Mater. Lett.* **2023**, *330*, 133319, doi:10.1016/j.matlet.2022.133319.
277. Song, L.; Wang, J.; Yan, X.; Cui, Z.; Li, J.; Qi, D. Microfibrillation Structure Evolution and Mechanical Properties of MS@PMHNTs Reinforced Polymethyl Methacrylate Composite Fiber. *Compos. Commun.* **2022**, *31*, 101108, doi:10.1016/j.coco.2022.101108.
278. Kuzmanović, M.; Delva, L.; Mi, D.; Martins, C.I.; Cardon, L.; Ragaert, K. Development of Crystalline Morphology and Its Relationship with Mechanical Properties of PP/PET Microfibrillar Composites Containing POE and POE-g-MA. *Polymers* **2018**, *10*, 291, doi:10.3390/polym10030291.
279. Rosales, C.; Aranburu, N.; Otaegi, I.; Pettarin, V.; Bernal, C.; Müller, A.J.; Guerrica-Echevarriá, G. Improving the Mechanical Performance of LDPE/PP Blends through Microfibrillation. *ACS Appl. Polym. Mater.* **2022**, *4*, 3369–3379, doi:10.1021/acsapm.1c01932.
280. Jayanarayanan, K.; Ravichandran, A.; Rajendran, D.; Sivathanupillai, M.; Venkatesan, A.; Thomas, S.; Joseph, K. Morphology and Mechanical

Properties of Normal Blends and In-Situ Microfibrillar Composites from Low-Density Polyethylene and Poly(Ethylene Terephthalate). *Polym. Plast. Technol. Eng.* **2010**, *49*, 442–448, doi:10.1080/03602550903414043.
281. Kuzmanović, M.; Delva, L.; Martins, C.I.; Cardon, L.; Ragaert, K. MFC Concept as a Possible Solution for Closed-Loop Recycling of Food Packaging Trays. *AIP Conf. Proc.* **2020**, *2205*, 020071, doi:10.1063/1.5142986.
282. Fakirov, S. Polymer Nanocomposites: Why Their Mechanical Performance Does Not Justify the Expectation and a Possible Solution to the Problem? *Express Polym. Lett.* **2020**, *14*, 436–466, doi:10.3144/expresspolymlett.2020.36.
283. Zhang, A.; Chai, J.; Yang, C.; Zhao, J.; Zhao, G.; Wang, G. Fibrosis Mechanism, Crystallization Behavior and Mechanical Properties of in-Situ Fibrillary PTFE Reinforced PP Composites. *Mater. Des.* **2021**, *211*, 110157, doi:10.1016/j.matdes.2021.110157.
284. Jurczuk, K.; Galeski, A. Thermoplastic Elastomers Reinforced with Poly(Tetrafluoroethylene) Nanofibers. *Eur. Polym. J.* **2016**, *80*, 58–69, doi:10.1016/j.eurpolymj.2016.04.031.
285. Evstatiev, M.; Fakirov, S. Microfibrillar Reinforcement of Polymer Blends. *Polymer* **1992**, *33*, 877–880, doi:10.1016/0032-3861(92)90354-Y.
286. Fakirov, S.; Bhattacharyya, D.; Shields, R.J. Nanofibril Reinforced Composites from Polymer Blends. *Colloids Surf. A: Physicochem. Eng. Asp.* **2008**, *313–314*, 2–8, doi:10.1016/j.colsurfa.2007.05.038.
287. Anstey, A.; Chang, E.; Kim, E.S.; Rizvi, A.; Kakroodi, A.R.; Park, C.B.; Lee, P.C. Nanofibrillated Polymer Systems: Design, Application, and Current State of the Art. *Prog. Polym. Sci.* **2021**, *113*, 101346, doi:10.1016/j.progpolymsci.2020.101346.
288. Wang, Y.; Sun, W.; Liu, S.; Ji, H.; Chen, X.; Zhu, H.; Zhao, H.; Ma, Y.; Xie, L. The Formation of a Highly Oriented Structure and Improvement of Properties in PP/PA6 Polymer Blends during Extrusion-Stretching. *Polymers* **2020**, *12*, 878, doi:10.3390/POLYM12040878.
289. Jayanarayanan, K.; Thomas, S.; Joseph, K. In Situ Microfibrillar Blends and Composites of Polypropylene and Poly (Ethylene Terephthalate): Morphology and Thermal Properties. *J. Polym. Res.* **2011**, *18*, 1–11, doi:10.1007/s10965-009-9384-6.
290. Evstatiev, M.; Fakirov, S.; Krasteva, B.; Friedrich, K.; Covas, J.A.; Cunha, &a M. RecycIing of PoIy(ethyIene terephthaIate) as PoIymer-PoIymer Composites. *Polym. Eng. Sci.* **2002**, *42*, 826–835, doi:10.1002/pen.10994.
291. Hosseinnezhad, R.; Vozniak, I.; Romano, D.; Rastogi, S.; Regnier, G.; Piorkowska, E.; Galeski, A. Formation of UHMWPE Nanofibers during Solid-State Deformation. *Nanomaterials* **2022**, *12*, 3825, doi:10.3390/nano12213825.
292. Vozniak, I.; Hosseinnezhad, R.; Morawiec, J.; Galeski, A. Nanofibrillar Green Composites of Polylactide/Polyhydroxyalkanoate Produced in Situ Due to Shear Induced Crystallization. *Polymers* **2019**, *11*, 1811, doi:10.3390/polym11111811.
293. Voznyak, Y.; Morawiec, J.; Galeski, A. Ductility of Polylactide Composites Reinforced with Poly(Butylene Succinate) Nanofibers. *Compos. - A: Appl. Sci. Manuf.* **2016**, *90*, 218–224, doi:10.1016/j.compositesa.2016.07.011.
294. Hosseinnezhad, R.; Vozniak, I.; Morawiec, J.; Galeski, A.; Dutkiewicz, S. In Situ Generation of Sustainable PLA-Based Nanocomposites by Shear

Induced Crystallization of Nanofibrillar Inclusions. *RSC Adv.* **2019**, *9*, 30370–30380, doi:10.1039/c9ra05919a.
295. Hosseinnezhad, R.; Vozniak, I.; Morawiec, J.; Galeski, A. Nanofibrillar Green Composites of Polylactide/Polyamide Produced in Situ Due to Shear Induced Crystallization. *Compos. Commun.* **2020**, *22*, 100512, doi:10.1016/j.coco.2020.100512.
296. Hosseinnezhad, R.; Vozniak, I.; Morawiec, J.; Galeski, A. Evolution of Green In-Situ Generated Polyamide Nanofibers Controlled by Viscoelasticity. *Express Polym. Lett.* **2021**, *15*, 250–261, doi:10.3144/expresspolymlett.2021.22.
297. Vozniak, I.; Hosseinnezhad, R.; Morawiec, J.; Galeski, A. Microstructural Evolution of Poly(ε-Caprolactone), Its Immiscible Blend, and in Situ Generated Nanocomposites. *Polymers* **2020**, *12*, 1–14, doi:10.3390/polym12112587.
298. Hosseinnezhad, R. Shear-Induced and Nanofiber-Nucleated Crystallization of Novel Aliphatic-Aromatic Copolyesters Delineated for in Situ Generation of Biodegradable Nanocomposites. *Polymers* **2021**, *13*, 2315, doi:10.3390/polym13142315.
299. Jurczuk, K.; Galeski, A.; Galeski, A. All-Polymer Fibrillar Nanocomposites and Method for Manufacture Thereof 2011.
300. Bernland, K.; Smith, P. Nucleating Polymer Crystallization with Poly(Tetrafluoroethylene) Nanofibrils. *J. Appl. Polym. Sci.* **2009**, *114*, 281–287, doi:10.1002/app.30425.
301. Krajenta, J.; Pawlak, A.; Galeski, A. Deformation of Disentangled Polypropylene Crystalline Grains into Nanofibers. *J Polym Sci B Polym Phys* **2016**, *54*, 1983–1994, doi:10.1002/polb.24105.
302. Jurczuk, K.; Galeski, A.; Morawiec, J. Effect of Poly(Tetrafluoroethylene) Nanofibers on Foaming Behavior of Linear and Branched Polypropylenes. *Eur. Polym. J.* **2017**, *88*, 171–182, doi:10.1016/j.eurpolymj.2017.01.024.
303. Jurczuk, K.; Galeski, A.; Piorkowska, E. Strain Hardening of Molten Thermoplastic Polymers Reinforced with Poly(Tetrafluoroethylene) Nanofibers. *J. Rheol.* **2014**, *58*, 589–605, doi:10.1122/1.4867389.
304. Huang, A.; Kharbas, H.; Ellingham, T.; Mi, H.; Turng, L.S.; Peng, X. Mechanical Properties, Crystallization Characteristics, and Foaming Behavior of Polytetrafluoroethylene-Reinforced Poly(Lactic Acid) Composites. *Polym. Eng. Sci.* **2017**, *57*, 570–580, doi:10.1002/pen.24454.
305. Huang, A.; Peng, X.; Turng, L.S. In-Situ Fibrillated Polytetrafluoroethylene (PTFE) in Thermoplastic Polyurethane (TPU) via Melt Blending: Effect on Rheological Behavior, Mechanical Properties, and Microcellular Foamability. *Polymer* **2018**, *134*, 263–274, doi:10.1016/j.polymer.2017.11.053.
306. Wang, K.; Wu, F.; Zhai, W.; Zheng, W. Effect of Polytetrafluoroethylene on the Foaming Behaviors of Linear Polypropylene in Continuous Extrusion. *J. Appl. Polym. Sci.* **2013**, *129*, 2253–2260, doi:10.1002/app.38959.
307. Galeski, S.; Piorkowska, E.; Rozanski, A.; Regnier, G.; Galeski, A.; Jurczuk, K. Crystallization Kinetics of Polymer Fibrous Nanocomposites. *European Polymer Journal* **2016**, *83*, 181–201, doi:10.1016/j.eurpolymj.2016.08.002.
308. Evstatiev, M.; Fakirov, S.; Bechtold, G.; Friedrich, K. Structure-Property Relationships of Injection- and Compression-Molded Microfibrillar-Reinforced PET/PA-6 Composites. *Adv. Polym. Technol.* **2000**, *19*, 249–259, doi:10.1002/1098-2329(200024)19:4<249::aid-adv2>3.0.co;2-r.

309. Fakirov, S.; Evstatiev, M.; Schultz, J.M. Microfibrillar Reinforced Composite from Drawn Poly(Ethylene Terephthalate) / Nylon-6 Blend. *Polymer* **1993**, *34*, doi:10.1016/0032-3861(93)90700-K.
310. Evstatiev, M.; Fakirov, S.; Schultz, J.M.; Friedrich, K. In Situ Fibrillar Reinforced PET/PA-6/PA-66 Blend. *Polym. Eng. Sci.* **2001**, *41*, 192–204, doi:10.1002/pen.10721.
311. Wang, Y.; Li, G.; Wan, Z.; Zhu, H.; Ma, Y.; Xie, L. Establishment of Dynamic Prediction Model on Morphology Development of Polypropylene/Polyamide 6 Blends under in-Situ Fibrillation Flow. *Polymer* **2024**, *294*, 126722, doi:10.1016/j.polymer.2024.126722.
312. Huang, W.-Y.; Shen, J.-W.; Chen, X.-M. Effect of Composition on Phase Morphology and Mechanical Properties of PP/PA66 in Situ Composites via Extrusion-Drawing-Injection Method. *J. Mater. Sci.* **2003**, *38*, 541–547, doi:10.1023/A:1021837607104.
313. Kharghanian, M.; Perchicot, R.; Irusta, S.; Argon, C.Y.; Leonardi, F.; Dagreou, S. Manufacture and Rheological Behavior of All Recycled PET/PP Microfibrillar Blends. *Polym. Eng. Sci.* **2023**, *63*, 1702–1715, doi:10.1002/pen.26317.
314. Gonzalez-Nunez, R.; Arellano, M.; Moscoso, F.J.; Gonzalez-Romero, V.M.; Favis, B.D. Polymer Communication Determination of a Limiting Dispersed Phase Concentration for Coalescence in PA6/HDPE Blends under Extensional Flow. *Polymer* **2001**, *42*, 5485–5489, doi:10.1016/S0032-3861(00)00918-6.
315. Li, Z.-M.; Yang, M.-B.; Feng, J.-M.; Yang, W.; Huang, R. Morphology of in Situ Poly(Ethylene Terephthalate)/ Polyethylene Microfiber Reinforced Composite Formed via Slit-Die Extrusion and Hot-Stretching. *Mater. Res. Bull.* **2002**, *37*, 2185–2197, doi:10.1016/S0025-5408(02)00894-2.
316. Li, Z.-M.; Yang, M.-B.; Lu, A.; Feng, J.-M.; Huang, R. Tensile Properties of Poly(Ethylene Terephthalate) and Polyethylene in-Situ Microfiber Reinforced Composite Formed via Slit Die Extrusion and Hot-Stretching. *Mater. Lett.* **2002**, *56*, 756–762, doi:10.1016/S0167-577X(02)00609-2.
317. Qiao, Y.; Li, Q.; Jalali, A.; Yang, J.; Wang, X.; Zhao, N.; Jiang, Y.; Wang, S.; Hou, J.; Jiang, J. In-Situ Microfibrillated Poly(ε-Caprolactone)/ Poly(Lactic Acid) Composites with Enhanced Rheological Properties, Crystallization Kinetics and Foaming Ability. *Compos. B Eng.* **2021**, *208*, 108594, doi:10.1016/j.compositesb.2020.108594.
318. Xie, L.; Xu, H.; Niu, B.; Ji, X.; Chen, J.; Li, Z.M.; Hsiao, B.S.; Zhong, G.J. Unprecedented Access to Strong and Ductile Poly(Lactic Acid) by Introducing in Situ Nanofibrillar Poly(Butylene Succinate) for Green Packaging. *Biomacromolecules* **2014**, *15*, 4054–4064, doi:10.1021/bm5010993.
319. Mi, D.; Wang, Y.; Kuzmanovic, M.; Delva, L.; Jiang, Y.; Cardon, L.; Zhang, J.; Ragaert, K. Effects of Phase Morphology on Mechanical Properties: Oriented/Unoriented PP Crystal Combination with Spherical/Microfibrillar PET Phase. *Polymers* **2019**, *11*, 248, doi:10.3390/polym11020248.
320. Shahnooshi, M.; Javadi, A.; Nazockdast, H.; Altstädt, V. Development of in Situ Nanofibrillar Poly (Lactic Acid)/Poly (Butylene Terephthalate) Composites: Non-Isothermal Crystallization and Crystal Morphology. *Eur. Polym. J.* **2020**, *125*, 109489, doi:10.1016/j.eurpolymj.2020.109489.
321. Gokgoz Erkoc, I.; Guven, T.; Yildirim, F.; Sözer, M.; Güner, F. Effect of Screw Speed, Drawing Ratio and PET Concentration on the Properties of

PET/PP Blends. *Acta Phys. Pol. A* **2018**, *134*, 442–446, doi:10.12693/APhysPolA.134.442.
322. Gonzalez-Nunez, R.; Favis, B.D.; Cafweau, P.J.; Lavallee, C. Factors Influencing the Formation of Elongated Morphologies in Immiscible Polymer Blends During Melt Processing. *Polym. Eng. Sci.* **1993**, *33*, 851–859, doi:10.1002/pen.760331310.
323. Chapleau, N.; Favis, B.D. Droplet/Fibre Transitions in Immiscible Polymer Blends Generated during Melt Processing. *J. Mater. Sci.* **1995**, *30*, 142–150, doi:10.1007/BF00352143.
324. Perilla, J.E.; Jana, S.C. A Time-scale Approach for Analysis of Coalescence in Processing Flows. *Polym. Eng. Sci.* **2004**, *44*, 2254–2265, doi:10.1002/pen.20253.
325. Favis, B.D.; Willis, J.M. Phase Size/Composition Dependence in Immiscible Blends: Experimental and Theoretical Considerations. *J. Polym. Sci., Part B: Polym. Phys.* **1990**, *28*, 2259–2269, doi:10.1002/polb.1990.090281208.
326. Zanjanijam, A.R.; Hakim, S.; Azizi, H. Morphological, Dynamic Mechanical, Rheological and Impact Strength Properties of the PP/PVB Blends: The Effect of Waste PVB as a Toughener. *RSC Adv.* **2016**, *6*, 44673–44686, doi:10.1039/c6ra04143d.
327. Fuchs, C.; Bhattacharyya, D.; Friedrich, K.; Fakirov, S. Application of Halpin-Tsai Equation to Microfibril Reinforced Polypropylene/Poly(Ethylene Terephthalate) Composites. *Compos. Interfaces* **2006**, *13*, 331–344, doi:10.1163/156855406777408485.
328. Rybnikar, F.; Kaszonyiova, M. Epitaxial Crystallization of Linear Polyethylene in Blends with Isotactic Polypropylene. *J. Macromol. Sci., Part B: Phys.* **2014**, *53*, 217–232, doi:10.1080/00222348.2013.808522.
329. Taepaiboon, P.; Junkasem, J.; Dangtungee, R.; Amornsakchai, T.; Supaphol, P. *In Situ* Microfibrillar-reinforced Composites of Isotactic Polypropylene/Recycled Poly(Ethylene Terephthalate) System and Effect of Compatibilizer. *J of Applied Polymer Sci* **2006**, *102*, 1173–1181, doi:10.1002/app.24402.
330. Utracki, L.A.; Shi, H. Development of Polymer Blend Morphology During Compounding in a Twin-Screw Extruder. Part I: Droplet Dispersion and Coalescence-A Review. *Polym. Eng. Sci.* **1992**, *32*, 1824–1833, doi:10.1002/pen.760322405.
331. Yousfi, M.; Soulestin, J.; Marcille, S.; Lacrampe, M.F. In-Situ Nano-Fibrillation of Poly(Butylene Succinate-Co-Adipate) in Isosorbide-Based Polycarbonate Matrix. Relationship between Rheological Parameters and Induced Morphological and Mechanical Properties. *Polymer* **2021**, *217*, 123445, doi:10.1016/j.polymer.2021.123445.
332. Yi, X.; Xu, L.; Wang, Y.L.; Zhong, G.J.; Ji, X.; Li, Z.M. Morphology and Properties of Isotactic Polypropylene/Poly(Ethylene Terephthalate) in Situ Microfibrillar Reinforced Blends: Influence of Viscosity Ratio. *Eur. Polym. J.* **2010**, *46*, 719–730, doi:10.1016/j.eurpolymj.2009.12.027.
333. Min, K.; White, J.L.; Fellers, J.F. Development of Phase Morphology in Incompatible Polymer Blends during Mixing and Its Variation in Extrusion*. *Polym. Eng. Sci.* **1984**, *24*, 1327–1336, doi:10.1002/pen.760241710.
334. Zhao, C.; Mark, L.H.; Alshrah, M.; Soltani, I.; Lee, P.C.; Park, C.B. Challenge in Manufacturing Nanofibril Composites with Low Matrix Viscosity: Effects of Matrix Viscosity and Fibril Content. *Eur. Polym. J.* **2019**, *121*, 109310, doi:10.1016/j.eurpolymj.2019.109310.

335. Favis, B.D.; Chalifoux, J.P. Influence of Composition on the Morphology of Polypropylene/Polycarbonate Blends. *Polymer* **1988**, *29*, 1761–1767, doi:10.1016/0032-3861(88)90388-6.
336. Zhong, G.J.; Li, Z.M.; Li, L.B.; Mendes, E. Crystalline Morphology of Isotactic Polypropylene (iPP) in Injection Molded Poly(Ethylene Terephthalate) (PET)/iPP Microfibrillar Blends. *Polymer* **2007**, *48*, 1729–1740, doi:10.1016/j.polymer.2007.01.056.
337. Jayanarayanan, K.; Jose, T.; Thomas, S.; Joseph, K. Effect of Draw Ratio on the Microstructure, Thermal, Tensile and Dynamic Rheological Properties of Insitu Microfibrillar Composites. *Eur. Polym. J.* **2009**, *45*, 1738–1747, doi:10.1016/j.eurpolymj.2009.02.024.
338. Jayanarayanan, K.; Thomas, S.; Joseph, K. Morphology, Static and Dynamic Mechanical Properties of in Situ Microfibrillar Composites Based on Polypropylene/Poly (Ethylene Terephthalate) Blends. *Compos. - A: Appl. Sci. Manuf.* **2008**, *39*, 164–175, doi:10.1016/j.compositesa.2007.11.008.
339. He, H.; Chen, L.; Zhang, Y.; Hong, S.; Zhou, Y.; Zhu, M. Studies on Melt Spinning of Sea-Island Fibers. I. Morphology Evolution of Polypropylene/Polystyrene Blend Fibers. *Fibers Polym.* **2014**, *15*, 1941–1949, doi:10.1007/s12221-014-1941-x.
340. Li, Z.M.; Yang, M.B.; Xie, B.H.; Feng, J.M.; Huang, R. In-Situ Microfiber Reinforced Composite Based on PET and PE via Slit Die Extrusion and Hot Stretching: Influences of Hot Stretching Ratio on Morphology and Tensile Properties at a Fixed Composition. *Polym. Eng. Sci.* **2003**, *43*, 615–628, doi:10.1002/pen.10050.
341. Li, Z.M.; Yang, W.; Li, L.B.; Xie, B.H.; Huang, R.; Yang, M.B. Morphology and Nonisothermal Crystallization of in Situ Microfibrillar Poly(Ethylene Terephthalate)/Polypropylene Blend Fabricated through Slit-Extrusion, Hot-Stretch Quenching. *J. Polym. Sci., Part B: Polym. Phys.* **2004**, *42*, 374–385, doi:10.1002/polb.10660.
342. Li, Z.M.; Li, L.; Shen, K.Z.; Yang, M.B.; Huang, R. In Situ Poly(Ethylene Terephthalate) Microfibers- and Shear-Induced Non-Isothermal Crystallization of Isotactic Polypropylene by on-Line Small Angle X-Ray Scattering. *Polymer* **2005**, *46*, 5358–5367, doi:10.1016/j.polymer.2005.04.016.
343. Sun, J.; Li, J.; Huang, A.; Shi, M.; Luo, S.; Li, J.; Luo, Z.; Qin, S. Constructing In Situ Microfibrillar PA6/PLA Composites with High Strength and High Toughness by a Strong Shear Flow Field. *Polymer* **2024**, *311*, 127544, doi:10.1016/j.polymer.2024.127544.
344. Friedrich, K.; Ueda, E.; Kamo, H.; Evstatiev, M.; Krasteva, B.; Fakirov, S. Direct Electron Microscopic Observation of Transcrystalline Layers in Microfibrillar Reinforced Polymer-Polymer Composites. *J. Mater. Sci.* **2002**, *37*, 4299–4305, doi:10.1023/A:1020692200486.
345. Kakroodi, A.R.; Kazemi, Y.; Nofar, M.; Park, C.B. Tailoring Poly(Lactic Acid) for Packaging Applications via the Production of Fully Bio-Based in Situ Microfibrillar Composite Films. *Chem. Eng. J.* **2017**, *308*, 772–782, doi:10.1016/j.cej.2016.09.130.
346. Kakroodi, A.R.; Kazemi, Y.; Rodrigue, D.; Park, C.B. Facile Production of Biodegradable PCL/PLA in Situ Nanofibrillar Composites with Unprecedented Compatibility between the Blend Components. *Chem. Eng. J.* **2018**, *351*, 976–984, doi:10.1016/j.cej.2018.06.152.

347. Quan, H.; Li, Z.M.; Yang, M.B.; Huang, R. On Transcrystallinity in Semi-Crystalline Polymer Composites. *Compos. Sci. Technol.* **2005**, *65*, 999–1021, doi:10.1016/j.compscitech.2004.11.015.
348. Abreu, A.A.; Talabi, S.I.; De Almeida Lucas, A. Influence of Nucleating Agents on Morphology and Properties of Injection-molded Polypropylene. *Polym. Adv. Technol.* **2021**, *32*, 2197–2206, doi:10.1002/pat.5252.
349. Zhu, P.; Edward, G. Distribution of Shish-Kebab Structure of Isotactic Polypropylene under Shear in the Presence of Nucleating Agent. *Macromolecules* **2004**, *37*, 2658–2660, doi:10.1021/ma0358374.
350. Chen, J.; Schneider, K.; Heinrich, G. In-Situ Synchrotron X-Ray Study on the Structure Variation of Morphology-Identified Injection-Molded β-Nucleated iPP under Tensile Deformation. *Polymers* **2021**, *13*, 3730, doi:10.3390/polym13213730.
351. Allan, P.S.; Bevis, M.J.; Gibson, J.R.; May, C.J.; Pinwill, I.E. Shear Controlled Orientation Technology for the Management of Reinforcing Fibres in Moulded and Extruded Composite Materials. *J. Mater. Process. Technol.* **1996**, *56*, 272–281, doi:10.1016/0924-0136(96)85104-1.
352. Kalay, G.; Sousa, R.A.; Reis, R.L.; Cunha, A.M.; Bevis, M.J. Enhancement of the Mechanical Properties of a High-Density Polyethylene. *J. Appl. Polym. Sci.* **1999**, *73*, 2473–2483, doi:10.1002/(SICI)1097-4628(19990919)73:12<2473::AID-APP16>3.0.CO;2-O.
353. Kalay, G.; Zhong, Z.; Allan, P.; Bevis, M.J. The Occurrence of the 7-Phase in Injection Moulded Polypropylene in Relation to the Processing Conditions. *Polymer* **1996**, *37*, 2077–2085, doi:10.1016/0032-3861(96)85852-6.
354. Ogbonna, C.I.; Kalay, G.; Allan, P.S.; Bevis, M.J. The Self-reinforcement of Polyolefins Produced by Shear Controlled Orientation in Injection Molding. *J. Appl. Polym. Sci.* **1995**, *58*, 2131–2135, doi:10.1002/app.1995.070581126.
355. Zhang, A.Y.; Jisheng, E.; Allan, P.S.; Bevis, M.J. Enhancement in Micro-Fatigue Resistance of UHMWPE and HDPE Processed by SCORIM. *J. Mater. Sci.* **2002**, *37*, 3189–3198, doi:10.1023/A:1016114513003.
356. Kalay, G.; Bevis, M.J. Processing and Physical Property Relationships in Injection-Molded Isotactic Polypropylene. 2. Morphology and Crystallinity. *J. Polym. Sci., Part B: Polym. Phys.* **1997**, *35*, 265–291, doi:10.1002/(SICI)1099-0488(19970130)35:2<265::AID-POLB6>3.0.CO;2-R.
357. Kalay, G.; Bevis, M.J. Processing and Physical Property Relationships in Injection-Molded Isotactic Polypropylene. 1. Mechanical Properties. *J. Polym. Sci., Part B: Polym. Phys.* **1997**, *35*, 241–263, doi:10.1002/(SICI)1099-0488(19970130)35:2<241::AID-POLB5>3.0.CO;2-V.
358. Kalay, G.; Bevis, M.J. The Effect of Shear Controlled Orientation in Injection Moulding on the Mechanical Properties of an Aliphatic Polyketone. *J. Polym. Sci., Part B: Polym. Phys.* **1997**, *35*, 415–430, doi:10.1002/(SICI)1099-0488(199702)35:3<415::AID-POLB2>3.0.CO;2-R.
359. Kalay, G.; Kalay, C.R. Interlocking Shish-Kebab Morphology in Polybutene-1. *J. Polym. Sci., Part B: Polym. Phys.* **2002**, *40*, 1828–1834, doi:10.1002/polb.10246.

360. Kalay, G.; Kalay, C.R. Compounding and Injection Molding of Polybutene-1/Polypropylene Blends. *J. Appl. Polym. Sci.* **2003**, *88*, 806–813, doi:10.1002/app.11617.
361. Ghosh, S.; Viana, J.C.; Reis, R.L.; Mano, J.F. Oriented Morphology and Enhanced Mechanical Properties of Poly(l-Lactic Acid) from Shear Controlled Orientation in Injection Molding. *Mater. Sci. Eng. A* **2008**, *490*, 81–89, doi:10.1016/j.msea.2008.01.003.
362. Mano, J.F.; Sousa, R.A.; Reis, R.L.; Cunha, A.M.; Bevis, M.J. Viscoelastic Behaviour and Time-Temperature Correspondence of HDPE with Varying Levels of Process-Induced Orientation. *Polymer* **2001**, *42*, 6187–6198, doi:10.1016/S0032-3861(01)00090-8.
363. Zheng, S.; Wang, Y.; Zhu, Y.; Zheng, C. Recent Advances in Structural Design of Conductive Polymer Composites for Electromagnetic Interference Shielding. *Polym. Compos.* **2024**, *45*, 43–76, doi:10.1002/pc.27773.
364. Chen, Y.H.; Zhong, G.J.; Wang, Y.; Li, Z.M.; Li, L. Unusual Tuning of Mechanical Properties of Isotactic Polypropylene Using Counteraction of Shear Flow and β-Nucleating Agent on β-Form Nucleation. *Macromolecules* **2009**, *42*, 4343–4348, doi:10.1021/ma900411f.
365. Guan, Q.; Shen, K.; Ji, J.; Zhu, J. Structure and Properties of Self-Reinforced Polyethylene Prepared by Oscillating Packing Injection Molding Under Low Pressure. *J. Appl. Polym. Sci.* **1995**, *55*, 1797–1804, doi:10.1002/app.1995.070551310.
366. Guan, Q.; Zhu, X.; Chiu, D.; Shen, K.; Lai, F.S.; Mccarthy, S.P. Self-Reinforcement of Polypropylene by Oscillating Packing Injection Molding Under Low Pressure. *J. Appl. Polym. Sci.* **1996**, *62*, 755–762, doi:10.1002/(SICI)1097-4628(19961031)62:5%3C755::AID-APP6%3E3.0.CO;2-V.
367. Chen, L.M.; Shen, K. Biaxial Self-Reinforcement of Isotactic Polypropylene Prepared in Uniaxial Oscillating Stress Field by Injection Molding. II. Morphology. *J. Appl. Polym. Sci.* **2000**, *78*, 1911–1917, doi:10.1002/1097-4628(20001209)78:11%3C1911::AID-APP90%3E3.0.CO;2-M.
368. Zhang, G.; Jiang, L.; Shen, K.; Guan, Q. Self-Reinforcement of High-Density Polyethylene/Low-Density Polyethylene Prepared by Oscillating Packing Injection Molding under Low Pressure. *J. Appl. Polym. Sci.* **1999**, *71*, 799–804, doi:10.1002/(SICI)1097-4628(19990131)71:5%3C799::AID-APP13%3E3.0.CO;2-2.
369. Wang, Y.; Zou, H.; Fu, Q.; Zhang, G.; Shen, K. Super Polyolefin Blends Achieved via Dynamic Packing Injection Molding: Tensile Strength. *J. Appl. Polym. Sci.* **2002**, *85*, 236–243, doi:10.1002/app.10909.
370. Na, B.; Wang, K.; Zhang, Q.; Du, R.; Fu, Q. Tensile Properties in the Oriented Blends of High-Density Polyethylene and Isotactic Polypropylene Obtained by Dynamic Packing Injection Molding. *Polymer* **2005**, *46*, 3190–3198, doi:10.1016/j.polymer.2005.01.094.
371. Na, B.; Zhang, Q.; Wang, K.; Li, L.; Fu, Q. Origin of Various Lamellar Orientations in High-Density Polyethylene/Isotactic Polypropylene Blends Achieved via Dynamic Packing Injection Molding: Bulk Crystallization vs. Epitaxy. *Polymer* **2005**, *46*, 819–825, doi:10.1016/j.polymer.2004.11.110.
372. Na, B.; Zhang, Q.; Wang, Y.; Du, R.; Fu, Q. Three-Dimensional Phase Morphologies in HDPE/EVA Blends Obtained via Dynamic Injection Packing Molding. *Polymer* **2003**, *44*, 5737–5747, doi:10.1016/S0032-3861(03)00524-X.

373. Na, B.; Zhang, Q.; Fu, Q.; Zhang, G.; Shen, K. Super Polyolefin Blends Achieved via Dynamic Packing Injection Molding: The Morphology and Mechanical Properties of HDPE/EVA Blends. *Polymer* **2002**, *43*, 7367–7376, doi:10.1016/S0032-3861(02)00637-7.
374. Wang, Y.; Xiao, Y.; Zhang, Q.; Gao, X.L.; Fu, Q. The Morphology and Mechanical Properties of Dynamic Packing Injection Molded PP/PS Blends. *Polymer* **2003**, *44*, 1469–1480, doi:10.1016/S0032-3861(03)00011-9.
375. Wang, Y.; Zhang, Q.; Na, B.; Du, R.; Fu, Q.; Shen, K. Dependence of Impact Strength on the Fracture Propagation Direction in Dynamic Packing Injection Molded PP/EPDM Blends. *Polymer* **2003**, *44*, 4261–4271, doi:10.1016/S0032-3861(03)00366-5.
376. Zhang, G.; Fu, Q.; Shen, K.; Jian, L.; Wang, Y. Studies on Blends of High-Density Polyethylene and Polypropylene Produced by Oscillating Shear Stress Field. *J. Appl. Polym. Sci.* **2002**, *86*, 58–63, doi:10.1002/app.10910.
377. Cao, W.; Wang, K.; Zhang, Q.; Du, R.; Fu, Q. The Hierarchy Structure and Orientation of High Density Polyethylene Obtained via Dynamic Packing Injection Molding. *Polymer* **2006**, *47*, 6857–6867, doi:10.1016/j.polymer.2006.07.037.
378. Su, R.; Su, J.; Wang, K.; Yang, C.; Zhang, Q.; Fu, Q. Shear-Induced Change of Phase Morphology and Tensile Property in Injection-Molded Bars of High-Density Polyethylene/Polyoxymethylene Blends. *Eur. Polym. J.* **2009**, *45*, 747–756, doi:10.1016/j.eurpolymj.2008.12.009.
379. Huang, Y.F.; Xu, J.Z.; Li, J.S.; He, B.X.; Xu, L.; Li, Z.M. Mechanical Properties and Biocompatibility of Melt Processed, Self-Reinforced Ultrahigh Molecular Weight Polyethylene. *Biomaterials* **2014**, *35*, 6687–6697, doi:10.1016/j.biomaterials.2014.04.077.
380. Hu, T.; Hua, W.Q.; Zhong, G.J.; Wang, Y.D.; Gao, Y.T.; Hong, C.X.; Li, Z.M.; Bian, F.G.; Xiao, T.Q. Nondestructive and Quantitative Characterization of Bulk Injection-Molded Polylactide Using SAXS Microtomography. *Macromolecules* **2020**, *53*, 6498–6509, doi:10.1021/acs.macromol.0c01177.
381. Hou, F.Y.; Mi, D.S.; Zhou, M.; Zhang, J. The Influences of a Novel Shear Layer-Spherulites Layer Alternated Structure on the Mechanical Properties of Injection-Molded Isotactic Polypropylene. *Polymer* **2017**, *122*, 12–21, doi:10.1016/j.polymer.2017.06.035.
382. Liang, S.; Yang, H.; Wang, K.; Zhang, Q.; Du, R.; Fu, Q. Unique Crystal Morphology and Tensile Properties of Injection-Molded Bar of LLDPE by Adding HDPE with Different Molecular Weights. *Acta Mater.* **2008**, *56*, 50–59, doi:10.1016/j.actamat.2007.09.008.
383. Su, R.; Wang, K.; Zhao, P.; Zhang, Q.; Du, R.; Fu, Q.; Li, L.; Li, L. Shear-Induced Epitaxial Crystallization in Injection-Molded Bars of High-Density Polyethylene/Isotactic Polypropylene Blends. *Polymer* **2007**, *48*, 4529–4536, doi:10.1016/j.polymer.2007.06.001.
384. Gu, X.; Hong, R.; Leng, J.; Hu, M.; Fu, Q.; Zhang, J. Evolution of iPP/HDPE Morphology under Different Mold Temperatures via Multiflow Vibration Injection Molding: Thermal Field Simulation and Oriented Structures. *Ind. Eng. Chem. Res.* **2020**, *59*, 6741–6750, doi:10.1021/acs.iecr.0c00097.
385. Kikuchi, A.; Coulter, J.P.; Gomatam, R.R. Assessing the Effect of Processing Variables on the Mechanical Response of Polysytrene Molded Using Vibration-Assisted Injection Molding Process. *J. Appl. Polym. Sci.* **2006**, *99*, 2603–2613, doi:10.1002/app.22396.

386. Li, Y.; Shen, K. Improving the Mechanical Properties of Polypropylene via Melt Vibration. *J. Appl. Polym. Sci.* **2008**, *109*, 90–96, doi:10.1002/app.27412.
387. Li, Y.; Shen, K. Self-Reinforced High-Density Polyethylene Prepared by Low-Frequency, Vibration-Assisted Injection Molding. 1. Processing Conditions and Physical Properties. *J. Macromol. Sci., Part B: Phys.* **2009**, *48*, 736–744, doi:10.1080/00222340902958406.
388. Li, Y.; Shen, K. Effect of Low-Frequency Melt Vibration on HDPE Morphology. *Polym. Int.* **2009**, *58*, 484–488, doi:10.1002/pi.2553.
389. Zhang, J.; Shen, K.; Gao, Y.; Yuan, Y. Mechanical Properties and Structure of High-Density Polyethylene Samples Prepared by Injection Molding with Low-Frequency Vibration. *J. Appl. Polym. Sci.* **2005**, *96*, 818–823, doi:10.1002/app.21034.
390. Lei, Y.; Wu, Q.; Zhang, Q. Morphology and Properties of Microfibrillar Composites Based on Recycled Poly (Ethylene Terephthalate) and High Density Polyethylene. *Compos. A: Appl. Sci. Manuf.* **2009**, *40*, 904–912, doi:10.1016/j.compositesa.2009.04.017.
391. Zhang, Y.; Zhang, J.; Qian, X.; Deng, P.; Shen, K. Morphology Evolution Including Formation of Cylindrulite in Isotactic Polypropylene Derived from Periodical Shear Field. *Polymer* **2012**, *53*, 4318–4327, doi:10.1016/j.polymer.2012.07.013.
392. Jin, M.; Liu, K.; Liu, H.; Zhang, Y.; Du, H.; Li, X.; Zhang, J. Effects of Polyolefin Elastomer and β-Nucleating Agent on Morphological Evolution of Isotactic Polypropylene under an Intensive Shear Rate. *Polym. Test.* **2014**, *39*, 1–11, doi:10.1016/j.polymertesting.2014.07.008.
393. Youbing, L.; Yongheng, L.; Xueqin, G.; Yuan, Y.; Wenti, K.; Kaizhi, S. Structure and Properties of Polyethylene Prepared via Low-Frequency Vibration-Assisted Injection Molding. *J. Polym. Sci., Part B: Polym. Phys.* **2005**, *43*, 13–21, doi:10.1002/polb.20122.
394. Fu, Q.; Wang, Y.; Li, Q.; Zhang, G. Adding EPDM Rubber Makes Poly(Propylene) Brittle. *Macrom. Mater. Eng.* **2002**, *287*, 391–394, doi:10.1002/1439-2054(20020601)287:6<391::AID-MAME391>3.0.CO;2-7.
395. Wang, Y.; Fu, Q.; Li, Q.; Zhang, G.; Shen, K.; Wang, Y.Z. Ductile-Brittle-Transition Phenomenon in Polypropylene/Ethylene-Propylene-Diene Rubber Blends Obtained by Dynamic Packing Injection Molding: A New Understanding of the Rubber-Toughening Mechanism. *J. Polym. Sci., Part B: Polym. Phys.* **2002**, *40*, 2086–2097, doi:10.1002/polb.10260.
396. Wang, Y.; Zou, H.; Fu, Q.; Zhang, G.; Shen, K.; Thomann, R. Shear-Induced Morphological Change in PP/LLDPE Blend. *Macromol. Rapid Commun.* **2002**, *23*, 749–752, doi:10.1002/1521-3927(20020901)23:13<749::AID-MARC749>3.0.CO;2-X.
397. Su, R.; Zhang, Z.; Gao, X.; Ge, Y.; Wang, K.; Fu, Q. Polypropylene Injection Molded Part with Novel Macroscopic Bamboo-like Bionic Structure. *J. Phys. Chem. B.* **2010**, *114*, 9994–10001, doi:10.1021/jp1020802.
398. Jiang, Z.; Tang, Y.; Rieger, J.; Enderle, H.F.; Lilge, D.; Roth, S.V.; Gehrke, R.; Heckmann, W.; Men, Y. Two Lamellar to Fibrillar Transitions in the Tensile Deformation of High-Density Polyethylene. *Macromolecules* **2010**, *43*, 4727–4732, doi:10.1021/ma100303d.
399. Jiang, Z.; Wang, Y.; Fu, L.; Whiteside, B.; Wyborn, J.; Norris, K.; Wu, Z.; Coates, P.; Men, Y. Tensile Deformation of Oriented Poly(ε-Caprolactone)

and Its Miscible Blends with Poly(Vinyl Methyl Ether). *Macromolecules* **2013**, *46*, 6981–6990, doi:10.1021/ma401052x.
400. Jiang, Z.; Tang, Y.; Rieger, J.; Enderle, H.F.; Lilge, D.; Roth, S.V.; Gehrke, R.; Wu, Z.; Li, Z.; Men, Y. Structural Evolution of Tensile Deformed High-Density Polyethylene at Elevated Temperatures: Scanning Synchrotron Small- and Wide-Angle X-Ray Scattering Studies. *Polymer* **2009**, *50*, 4101–4111, doi:10.1016/j.polymer.2009.06.063.
401. Chen, Y.; Zhong, G.; Hsiao, B.S.; Li, Z. Structure Evolution upon Uniaxial Drawing Skin- and Core-Layers of Injection-Molded Isotactic Polypropylene by in Situ Synchrotron X-Ray Scattering. *J. Polym. Sci., Part B: Polym. Phys.* **2013**, *51*, 1618–1631, doi:10.1002/polb.23376.
402. Jiang, Z.; Tang, Y.; Men, Y.; Enderle, H.F.; Lilge, D.; Roth, S.V.; Gehrke, R.; Rieger, J. Structural Evolution of Tensile-Deformed High-Density Polyethylene during Annealing: Scanning Synchrotron Small-Angle X-Ray Scattering Study. *Macromolecules* **2007**, *40*, 7263–7269, doi:10.1021/ma0627572.
403. Flory, P.J.; Yoon, D.Y. Molecular Morphology in Semicrystalline Polymers. *Nature* **1978**, *272*, 226–229, doi:10.1038/272226a0.
404. Zhang, J.; Lei, Y.; Yang, L.; Zhou, Q.; Wen, Y.; Shen, K.; Fu, Q. Mechanical Property and Crystal Structure of Nylon6 Samples Prepared by Vibration Injection Molding. *Polym. Plast. Technol. Mater.* **2009**, *48*, 251–256, doi:10.1080/03602550802674606.
405. Yang, J.; Zhang, Y.; Zhang, Y. Brittle-Ductile Transition of PP/POE Blends in Both Impact and High Speed Tensile Tests. *Polymer* **2003**, *44*, 5047–5052, doi:10.1016/S0032-3861(03)00438-5.
406. Cravero, F.; Cavallini, N.; Arrigo, R.; Savorani, F.; Frache, A. The Effect of Processing Conditions on the Microstructure of Homopolymer High-Density Polyethylene Blends: A Multivariate Approach. *Polymers* **2024**, *16*, doi:10.3390/polym16070870.
407. Kissin, Y.V *Polyethylene—End-Use Properties and Their Physical Meaning*; 2nd ed.; Hanser Publishers: Cincinnati, OH, USA, 2000;
408. Mufarrij, F.; Ashrafi, O.; Navarri, P.; Khojasteh, Y. Development and Lifecycle Assessment of Various Low- and High-Density Polyethylene Production Processes Based on CO2 Capture and Utilization. *J. Clean. Prod.* **2023**, *414*, 137624, doi:10.1016/j.jclepro.2023.137624.
409. Fitri, M.; Mahzan, S.; Anggara, F. The Mechanical Properties Requirement for Polymer Composite Automotive Parts - A Review. *IJATEC* **2021**, *1*, 125–133, doi:10.37869/ijatec.v1i3.38.
410. Karaki, A.; Hammoud, A.; Masad, E.; Khraisheh, M.; Abdala, A.; Ouederni, M. A Review on Material Extrusion (MEX) of Polyethylene - Challenges, Opportunities, and Future Prospects. *Polymer* **2024**, *307*, 127333, doi:10.1016/j.polymer.2024.127333.
411. Du, Z.-C.; Yang, H.; Luo, X.-H.; Xie, Z.-X.; Fu, Q.; Gao, X.-Q. The Role of Mold Temperature on Morphology and Mechanical Properties of PE Pipe Produced by Rotational Shear. *Chin J Polym Sci* **2020**, *38*, 653–664, doi:10.1007/s10118-020-2363-4.
412. Ma, Y.; Zhang, X.; Lu, Y.; Lv, J.; Zhu, N.; Hu, L. Effect of Transverse Flow on Flame Spread and Extinction over Polyethylene-Insulated Wires. *Proc. Combust. Inst.* **2021**, *38*, 4727–4735, doi:10.1016/j.proci.2020.06.228.

413. Muralisrinivasan, N.S. *Polymer Blends and Composites: Chemistry and Technology*; Wiley ; Scrivener Publishing: Hoboken, New Jersey : Beverly, Massachusetts, 2017; ISBN 978-1-118-11889-4.
414. Zhao, L.; Choi, P. A Review of the Miscibility of Polyethylene Blends. *Mater. Manuf. Process.* **2006**, *21*, 135–142, doi:10.1081/AMP-200068644.
415. Bai, L.; Li, Y.M.; Yang, W.; Yang, M.B. Rheological Behavior and Mechanical Properties of High-Density Polyethylene Blends with Different Molecular Weights. *J. Appl. Polym. Sci.* **2010**, *118*, 1356–1363, doi:10.1002/app.32329.
416. Oliveira, A.D.B.; Freitas, D.M.G.; Araújo, J.P.; Cavalcanti, S.N.; Câmara, D.S.; Agrawal, P.; Mélo, T.J.A. HDPE/LLDPE Blends: Rheological, Thermal, and Mechanical Properties. *Mater. Res. Innov.* **2020**, *24*, 289–294, doi:10.1080/14328917.2019.1655623.
417. Cecon, V.S.; Da Silva, P.F.; Vorst, K.L.; Curtzwiler, G.W. The Effect of Post-Consumer Recycled Polyethylene (PCRPE) on the Properties of Polyethylene Blends of Different Densities. *Polym. Degrad. Stabil.* **2021**, *190*, 109627, doi:10.1016/j.polymdegradstab.2021.109627.
418. Agrawal, P.; Silva, M.H.A.; Cavalcanti, S.N.; Freitas, D.M.G.; Araújo, J.P.; Oliveira, A.D.B.; Mélo, T.J.A. Rheological Properties of High-Density Polyethylene/Linear Low-Density Polyethylene and High-Density Polyethylene/Low-Density Polyethylene Blends. *Polym. Bull.* **2022**, *79*, 2321–2343, doi:10.1007/s00289-021-03635-8.
419. Salakhov, I.I.; Shaidullin, N.M.; Chalykh, A.E.; Matsko, M.A.; Shapagin, A.V.; Batyrshin, A.Z.; Shandryuk, G.A.; Nifant'ev, I.E. Low-Temperature Mechanical Properties of High-Density and Low-Density Polyethylene and Their Blends. *Polymers* **2021**, *13*, 1821, doi:10.3390/polym13111821.
420. Sarkhel, G.; Banerjee, A.; Bhattacharya, P. Rheological and Mechanical Properties of LDPE/HDPE Blends. *Polym. Plast. Technol. Eng.* **2006**, *45*, 713–718, doi:10.1080/03602550600609663.
421. Juan, R.; Domínguez, C.; Robledo, N.; Paredes, B.; García-Muñoz, R.A. Incorporation of Recycled High-Density Polyethylene to Polyethylene Pipe Grade Resins to Increase Close-Loop Recycling and Underpin the Circular Economy. *J. Clean. Prod.* **2020**, *276*, 124081, doi:10.1016/j.jclepro.2020.124081.
422. Nagy, D.; Weltsch, Z. Crystallinity and Oscillatory Shear Rheology of Polyethylene Blends. *Materials* **2023**, *16*, 6402, doi:10.3390/ma16196402.
423. Kobayashi, K.; Atarashi, H.; Yamazaki, S.; Kimura, K. Effect of the Blend Ratio of Cyclic and Linear Polyethylene Blends on Isothermal Crystallization in the Quiescent State. *Polym J* **2023**, *55*, 1393–1398, doi:10.1038/s41428-023-00833-1.
424. Muthuraj, R.; Misra, M.; Mohanty, A.K. Biodegradable Compatibilized Polymer Blends for Packaging Applications: A Literature Review. *J. Appl. Polym. Sci.* **2018**, *135*, 45726, doi:10.1002/app.45726.
425. Liao, H.; Qi, L.; Tao, G.; Liu, C. Dynamic Rheological Behavior of Two LDPE/HDPE Binary Blending Melts. *Polym. Bull.* **2015**, *72*, 1197–1205, doi:10.1007/s00289-015-1332-5.
426. Kwag, H.; Rana, D.; Cho, K.; Rhee, J.; Woo, T.; Lee, B.H.; Choe, S. Binary Blends of Metallocene Polyethylene with Conventional Polyolefins: Rheological and Morphological Properties. *Polym. Eng. Sci.* **2000**, *40*, 1672–1681, doi:10.1002/pen.11299.

427. Yamaguchi, M.; Abe, S. LLDPE/LDPE Blends. I. Rheological, Thermal, and Mechanical Properties. *J. Appl. Polym. Sci.* **1999**, *74*, 3153–3159, doi:10.1002/(sici)1097-4628(19991220)74:13<3153::aid-app18>3.0.co;2-t.
428. Vicente-Alique, E.; Vega, J.F.; Robledo, N.; Nieto, J.; Martínez-Salazar, J. Study of the Effect of the Molecular Architecture of the Components on the Melt Rheological Properties of Polyethylene Blends. *J. Polym. Res.* **2015**, *22*, doi:10.1007/s10965-015-0705-7.
429. Lee, H.S.; Denn, M.M. Blends of Linear and Branched Polyethylenes. *Polym. Eng. Sci.* **2000**, *40*, 1132–1142, doi:10.1002/pen.11241.
430. *Handbook of Polymer Science and Technology*; Cheremisinoff, N.P., Ed.; M. Dekker: New York, 1989; Vol. 4; ISBN 978-0-8247-8174-3.
431. Hill, M.J.; Barham, P.J.; Keller, A.; Rosney, C.C.A. Phase Segregation in Melts of Blends of Linear and Branched Polyethylene. *Polymer* **1991**, *32*, 1384–1393, doi:10.1016/0032-3861(91)90418-i.
432. Alamo, R.G.; Graessley, W.W.; Krishnamoorti, R.; Lohse, D.J.; Londono, J.D.; Mandelkern, L.; Stehling, F.C.; Wignall, G.D. Small Angle Neutron Scattering Investigations of Melt Miscibility and Phase Segregation in Blends of Linear and Branched Polyethylenes as a Function of the Branch Content. *Macromolecules* **1997**, *30*, 561–566, doi:10.1021/ma961196j.
433. Hameed, T.; Hussein, I.A. Rheological Study of the Influence of Mw and Comonomer Type on the Miscibility of M-LLDPE and LDPE Blends. *Polymer* **2002**, *43*, 6911–6929, doi:10.1016/s0032-3861(02)00627-4.
434. Muñoz-Escalona, A.; Lafuente, P.; Vega, J.F.; Muñoz, M.E.; Santamaría, A. Rheological Behaviour of Metallocene Catalysed High Density Polytheylene Blends. *Polymer* **1997**, *38*, 589–594, doi:10.1016/S0032-3861(96)00551-4.
435. Hay, J.N.; Zhou, X.-Q. The Effect of Mixing on the Properties of Polyethylene Blends. *Polymer* **1993**, *34*, 2282–2288, doi:10.1016/0032-3861(93)90809-O.
436. Vadhar, P.; Kyu, T. Effects of Mixing on Morphology, Rheology, and Mechanical Properties of Blends of Ultra-high Molecular Weight Polyethylene with Linear Low-density Polyethylene. *Polym. Eng. Sci.* **1987**, *27*, 202–210, doi:10.1002/pen.760270305.
437. Zhang, J.; Hirschberg, V.; Rodrigue, D. Blending Recycled High-Density Polyethylene HDPE (rHDPE) with Virgin (vHDPE) as an Effective Approach to Improve the Mechanical Properties. *Recycling* **2022**, *8*, 2, doi:10.3390/recycling8010002.
438. Krishnaswamy, R.K.; Yang, Q. Influence of Phase Segregation on the Mechanical Properties of Binary Blends of Polyethylenes That Differ Considerably in Molecular Weight. *Polymer* **2007**, *48*, 5348–5354, doi:10.1016/j.polymer.2007.07.018.
439. Tinçer, T.; Coşkun, M. Melt Blending of Ultra High Molecular Weight and High Density Polyethylene: The Effect of Mixing Rate on Thermal, Mechanical, and Morphological Properties. *Polym. Eng. Sci.* **1993**, *33*, 1243–1250, doi:10.1002/pen.760331904.
440. Zhong, F.; Schwabe, J.; Hofmann, D.; Meier, J.; Thomann, R.; Enders, M.; Mülhaupt, R. All-Polyethylene Composites Reinforced via Extended-Chain UHMWPE Nanostructure Formation during Melt Processing. *Polymer* **2018**, *140*, 107–116, doi:10.1016/j.polymer.2018.02.027.
441. Pan, X.; Huang, Y.; Zhang, Y.; Liu, B.; He, X. Improved Performance and Crystallization Behaviors of Bimodal HDPE/UHMWPE Blends Assisted by

Ultrasonic Oscillations. *Mater. Res. Express* **2018**, *6*, 035306, doi:10.1088/2053-1591/aaf36f.
442. De Santis, F.; Boragno, L.; Jeremic, D.; Albunia, A.R. Trimodal Polyethylene Polymer Design for More Sustainable Packaging Applications. *Polymer* **2024**, *295*, 126740, doi:10.1016/j.polymer.2024.126740.
443. Liu, Y.; Gao, S.; Hsiao, B.S.; Norman, A.; Tsou, A.H.; Throckmorton, J.; Doufas, A.; Zhang, Y. Shear Induced Crystallization of Bimodal and Unimodal High Density Polyethylene. *Polymer* **2018**, *153*, 223–231, doi:10.1016/j.polymer.2018.08.020.
444. Leardi, R. Experimental Design in Chemistry: A Tutorial. *Anal. Chim. Acta* **2009**, *652*, 161–172, doi:10.1016/j.aca.2009.06.015.
445. Ballabio, D. A MATLAB Toolbox for Principal Component Analysis and Unsupervised Exploration of Data Structure. *Chemometr. Intell. Lab. Syst.* **2015**, *149*, 1–9, doi:10.1016/j.chemolab.2015.10.003.
446. Sergent, M.; Mathieu, Didier; Phan-Tan-Luu, Roger; Drava, Giuliana Correct and Incorrect Use of Multilinear Regression. *Chemometr. Intell. Lab. Syst.* **1995**, *27*, 153–162, doi:10.1016/0169-7439(95)80020-A.
447. Leardi, R.; Melzi, C.; Polotti, G. CAT (Chemometric Agile Tool) Available online: https://gruppochemiometria.it/index.php/software (accessed on 14 July 2025).
448. Chen, D.-H.; Hong, L.; Nie, X.-W.; Wang, X.-L.; Tang, X.-Z. Study on Rheological Properties and Relaxational Behavior of Poly(Dianilinephosphazene)/Low-Density Polyethylene Blends. *Eur. Polym. J.* **2003**, *39*, 871–876, doi:10.1016/S0014-3057(02)00348-8.
449. Shi, D.; Hu, G.-H.; Ke, Z.; Li, R.K.Y.; Yin, J. Relaxation Behavior of Polymer Blends with Complex Morphologies: Palierne Emulsion Model for Uncompatibilized and Compatibilized PP/PA6 Blends. *Polymer* **2006**, *47*, 4659–4666, doi:10.1016/j.polymer.2006.04.058.
450. Bro, R.; Smilde, A.K. Principal Component Analysis. *Anal. Methods* **2014**, *6*, 2812–2831, doi:10.1039/C3AY41907J.
451. Yan, C.; Huang, W.; Lin, P.; Zhang, Y.; Lv, Q. Chemical and Rheological Evaluation of Aging Properties of High Content SBS Polymer Modified Asphalt. *Fuel* **2019**, *252*, 417–426, doi:10.1016/j.fuel.2019.04.022.
452. Tian, Y.; Li, H.; Sun, L.; Zhang, H.; Harvey, J.; Yang, J.; Yang, B.; Zuo, X. Laboratory Investigation on Rheological, Chemical and Morphological Evolution of High Content Polymer Modified Bitumen under Long-Term Thermal Oxidative Aging. *Constr. Build. Mater.* **2021**, *303*, 124565, doi:10.1016/j.conbuildmat.2021.124565.
453. Tafuro, G.; Costantini, A.; Baratto, G.; Busata, L.; Semenzato, A. Rheological and Textural Characterization of Acrylic Polymer Water Dispersions for Cosmetic Use. *Ind. Eng. Chem. Res.* **2019**, *58*, 23549–23558, doi:10.1021/acs.iecr.9b05319.
454. Liu, Y.; Leng, Y.; Xiao, S.; Zhang, Y.; Ding, W.; Ding, B.; Wu, Y.; Wang, X.; Fu, Y. Effect of Inulin with Different Degrees of Polymerization on Dough Rheology, Gelatinization, Texture and Protein Composition Properties of Extruded Flour Products. *LWT* **2022**, *159*, 113225, doi:10.1016/j.lwt.2022.113225.
455. Suprabha Raj, A.; Boyacioglu, M.H.; Dogan, H.; Siliveru, K. Investigating the Contribution of Blending on the Dough Rheology of Roller-Milled Hard Red Wheat. *Foods* **2023**, *12*, 2078, doi:10.3390/foods12102078.

456. Bartkowiak, A.; Lewandowicz, J.; Rojewska, M.; Krüger, K.; Lulek, J.; Prochaska, K. Study of Viscoelastic, Sorption and Mucoadhesive Properties of Selected Polymer Blends for Biomedical Applications. *J. Mol. Liq.* **2022**, *361*, 119623, doi:10.1016/j.molliq.2022.119623.
457. Milano Chemometrics and QSAR Research Group PCA Toolbox for MATLAB Available online: https://michem.unimib.it/ download/matlab-toolboxes/pca-toolbox-for-matlab/ (accessed on 26 September 2023).
458. Wood-Adams, P.M.; Dealy, J.M.; deGroot, A.W.; Redwine, O.D. Effect of Molecular Structure on the Linear Viscoelastic Behavior of Polyethylene. *Macromolecules* **2000**, *33*, 7489–7499, doi:10.1021/ma991533z.
459. Xu, L.; Huang, H. Relaxation Behavior of Poly(Lactic Acid)/Poly(Butylene Succinate) Blend and a New Method for Calculating Its Interfacial Tension. *J. Appl. Polym. Sci.* **2012**, *125*, doi:10.1002/app.36910.
460. Agrawal, P.; Araújo, A.P.M.; Lima, J.C.C.; Cavalcanti, S.N.; Freitas, D.M.G.; Farias, G.M.G.; Ueki, M.M.; Mélo, T.J.A. Rheology, Mechanical Properties and Morphology of Poly(Lactic Acid)/Ethylene Vinyl Acetate Blends. *J. Polym. Environ.* **2019**, *27*, 1439–1448, doi:10.1007/s10924-019-01445-8.
461. Jozaghkar, M.R.; Jahani, Y.; Arabi, H.; Ziaee, F. Preparation and Assessment of Phase Morphology, Rheological Properties, and Thermal Behavior of Low-Density Polyethylene/Polyhexene-1 Blends. *Polym. Plast. Technol. Eng.* **2018**, *57*, 757–765, doi:10.1080/03602559.2017.1344858.
462. Hameed, T.; Hussein, I.A. Melt Miscibility and Mechanical Properties of Metallocene LLDPE Blends with HDPE: Influence of Mw of LLDPE. *Polym. J.* **2006**, *38*, 1114–1126, doi:10.1295/polymj.PJ2005254.
463. Murthy, N.S. Hydrogen Bonding, Mobility, and Structural Transitions in Aliphatic Polyamides. *J. Polym. Sci., Part B: Polym. Phys.* **2006**, *44*, 1763–1782, doi:10.1002/polb.20833.
464. Seguela, R. Overview and Critical Survey of Polyamide 6 Structural Habits: Misconceptions and Controversies. *J. Polym. Sci.* **2020**, *58*, 2971–3003, doi:10.1002/pol.20200454.
465. Lee, J.K.; Lim, H.S. Movement, Wear Comfort, and Compression Evaluation of Nylon and Polyurethane Blend Stretch Knit Material and 3D Virtual Fitting Stress Strain Comparison. *Fibers Polym.* **2023**, *24*, 2541–2555, doi:10.1007/s12221-023-00246-0.
466. Rodríguez, M. del P.; Vázquez-Vélez, E.; Martinez, H.; Torres-Islas, A. Life Cycle Analysis of a Novel Process from the Automotive Industry in Mexico for Recycling Nylon 6,6 into Polymeric Coatings. *Sustainability* **2023**, *15*, doi:10.3390/su15129810.
467. Guo, A.; Liu, C.; Li, S.; Zhou, X.; Wang, J.; Wang, S.; Qu, P.; Hu, Y. Water Absorption Rates and Mechanical Properties of Material Extrusion-Printed Continuous Carbon Fiber-Reinforced Nylon Composites. *J. Mater. Sci. Res. Technol.* **2022**, *21*, 3098–3112, doi:10.1016/j.jmrt.2022.10.134.
468. Shakiba, M.; Rezvani Ghomi, E.; Khosravi, F.; Jouybar, S.; Bigham, A.; Zare, M.; Abdouss, M.; Moaref, R.; Ramakrishna, S. Nylon—A Material Introduction and Overview for Biomedical Applications. *Polym. Adv. Technol.* **2021**, *32*, 3368–3383, doi:10.1002/pat.5372.
469. Khanna, Y.P.; Kumar, R.; Reimschuessel, A.C. Memory Effects in Polymers. III. Processing History vs. Crystallization Rate of Nylon 6—Comments on the Origin of Memory Effect. *Polym. Eng. Sci.* **1988**, *28*, 1607–1611, doi:10.1002/pen.760282406.

470. Liu, X.; Wang, Y.; Wang, Z.; Cavallo, D.; Müller, A.J.; Zhu, P.; Zhao, Y.; Dong, X.; Wang, D. The Origin of Memory Effects in the Crystallization of Polyamides: Role of Hydrogen Bonding. *Polymer* **2020**, *188*, doi:10.1016/j.polymer.2019.122117.
471. Fornes, T.D.; Paul, D.R. Crystallization Behavior of Nylon 6 Nanocomposites. *Polymer* **2003**, *44*, 3945–3961, doi:10.1016/S0032-3861(03)00344-6.
472. Garcia, D.; Starkweather, H.W. Hydrogen Bonding in Nylon 66 and Model Compounds. *J. Polym. Sci.* **1985**, *23*, 537–555, doi:10.1002/pol.1985.180230310.
473. Wang, Z.; Lin, N.; Kang, H.; Hao, X.; Liu, R. Isodimorphism in Polyamide 56/Polyamide 66 Blends with Controllable Thermal and Mechanical Properties. *ACS Appl. Polym. Mater.* **2022**, *4*, 9407–9416, doi:10.1021/acsapm.2c01683.
474. Avramova, N.; Fakirov, S. Cumulative Erasing Effect in the Melt Memory of Nylon 6. *J. Polym. Sci., Part B: Polym. Phys.* **1986**, *24*, 761–768, doi:10.1002/polb.1986.090240403.
475. Murthy, N.S.; Stamm, M.; Sibilia, J.P.; Krimm, S. Structural Changes Accompanying Hydration in Nylon 6. *Macromolecules* **1989**, *22*, 1261–1267, doi:10.1021/ma00193a043.
476. Schroeder, L.R.; Cooper, S.L. Hydrogen Bonding in Polyamides. *J. Appl. Phys.* **1976**, *47*, 4310–4317, doi:10.1063/1.322432.
477. Skrovanek, D.J.; Painter, P.C.; Coleman, M.M. Hydrogen Bonding in Polymers. 2. Infrared Temperature Studies of Nylon 11. *Macromolecules* **1986**, *19*, 1002, doi:10.1021/ma00157a037.
478. Sangroniz, L.; Müller, A.J.; Cavallo, D. Origin of Melt Memory Effects in Poly(Ethylene Oxide): The Crucial Role of Entanglements. *Macromol. Rapid Commun.* **2024**, *45*, 2400011, doi:10.1002/marc.202400011.
479. Jariyavidyanont, K.; Mallardo, S.; Cerruti, P.; Di Lorenzo, M.L.; Boldt, R.; Rhoades, A.M.; Androsch, R. Shear-Induced Crystallization of Polyamide 11. *Rheol. Acta* **2021**, *60*, 231–240, doi:10.1007/s00397-021-01264-6.
480. Zhou, W.; Cui, K.; Tian, N.; Liu, D.; Liu, Y.; Meng, L.; Li, X.; He, J.; Li, L.; Li, X.; et al. Disentanglement Decelerating Flow-Induced Nucleation. *Polymer* **2013**, *54*, 942–947, doi:10.1016/j.polymer.2012.11.074.
481. Zhu, S.; Wang, Z.; Su, F.; Zhou, W.; Tian, N.; Li, X.; Li, L. The Influence of Inertia and Elastic Retraction on Flow-Induced Crystallization of Isotactic Polypropylene. *J. Rheol.* **2013**, *57*, 1281–1296, doi:10.1122/1.4812671.
482. Courty, S.; Gornall, J.L.; Terentjev, E.M. Induced Helicity in Biopolymer Networks under Stress. *PNAS* **2005**, *102*, 13457–13460, doi:10.1073/pnas.0506864102.
483. Olmsted, P.D.; Poon, W.C.K.; Mcleish, T.C.B.; Terrill, N.J.; Ryan, A.J. Spinodal-Assisted Crystallization in Polymer Melts. *Phys. Rev. Lett.* **1998**, *81*, 373–376, doi:10.1103/PhysRevLett.81.373.
484. Shimada, T.; Doi, M.; Okano, K. Concentration Fluctuation of Stiff Polymers. III. Spinodal Decomposition. *J. Chem. Phys.* **1988**, *88*, 7181–7186, doi:10.1063/1.454370.
485. Doi, M.; Shimada, T.; Okano, K. Concentration Fluctuation of Stiff Polymers. II. Dynamical Structure Factor of Rod-like Polymers in the Isotropic Phase. *J. Chem. Phys.* **1988**, *88*, 4070–4075, doi:10.1063/1.453861.

486. Ziabicki, A.; Alfonso, G.C. A Simple Model of Flow-Induced Crystallization Memory. *Macromol. Symp.* **2002**, *185*, 211–231, doi:10.1002/1521-3900(200208)185:1%3C211::AID-MASY211%3E3.0.CO;2-B.
487. Roozemond, P.C.; Peters, G.W.M. Flow-Enhanced Nucleation of Poly(1-Butene): Model Application to Short-Term and Continuous Shear and Extensional Flow. *J. Rheol.* **2013**, *57*, 1633–1653, doi:10.1122/1.4821609.
488. Roozemond, P.C.; Steenbakkers, R.J.A.; Peters, G.W.M. A Model for Flow-Enhanced Nucleation Based on Fibrillar Dormant Precursors. *Macromol. Theor. Simul.* **2011**, *20*, 93–109, doi:10.1002/mats.201000059.
489. Vanden Poel, G.; Mathot, V.B.F. High Performance Differential Scanning Calorimetry (HPer DSC): A Powerful Analytical Tool for the Study of the Metastability of Polymers. *Thermochim. Acta* **2007**, *461*, 107–121, doi:10.1016/j.tca.2007.04.009.
490. Khanna, Y.P.; Reimschuessel, A.C. Memory Effects in Polymers. I. Orientational Memory in the Molten State; Its Relationship to Polymer Structure and Influence on Recrystallization Rate and Morphology. *J. Appl. Polym. Sci.* **1988**, *35*, 2259–2268, doi:10.1002/app.1988.070350824.
491. Lotz, B. Original Crystal Structures of Even-Even Polyamides Made of Pleated and Rippled Sheets. *Macromolecules* **2021**, *54*, 551–564, doi:10.1021/acs.macromol.0c02404.
492. Cavallo, D.; Gardella, L.; Alfonso, G.C.; Portale, G.; Balzano, L.; Androsch, R. Effect of Cooling Rate on the Crystal/Mesophase Polymorphism of Polyamide 6. *Colloid Polym. Sci.* **2011**, *289*, 1073–1079, doi:10.1007/s00396-011-2428-6.
493. Kyotani, M.; Mitsuhashi, S. Studies on Crystalline Forms of Nylon 6. 11. Crystallization from the Melt. *J. Polym. Sci.* **1972**, *2*, 1497–1508, doi:10.1002/pol.1972.160100807.
494. Mileva, D.; Kolesov, I.; Androsch, R. Morphology of Cold-Crystallized Polyamide 6. *Colloid Polym. Sci.* **2012**, *290*, 971–978, doi:10.1007/s00396-012-2657-3.
495. Penel-Pierron, L.; Depecker, C.; Sé, R.; La, G.; Lefebvre, J.-M. Structural and Mechanical Behavior of Nylon 6 Films Part I. Identification and Stability of the Crystalline Phases. *J. Polym. Sci., Part B: Polym. Phys.* **2001**, *39*, 484–495.
496. Mayoral, B.; Harkin-Jones, E.; Khanam, P.N.; Almaadeed, M.A.; Ouederni, M.; Hamilton, A.R.; Sun, D. Melt Processing and Characterisation of Polyamide 6/Graphene Nanoplatelet Composites. *RSC Adv.* **2015**, *5*, 52395–52409, doi:10.1039/c5ra08509h.
497. Furushima, Y.; Nakada, M.; Ishikiriyama, K.; Toda, A.; Androsch, R.; Zhuravlev, E.; Schick, C. Two Crystal Populations with Different Melting/Reorganization Kinetics of Isothermally Crystallized Polyamide 6. *J. Polym. Sci., Part B: Polym. Phys.* **2016**, *54*, 2126–2138, doi:10.1002/polb.24123.
498. Massaro, R.; Roozemond, P.; Van Puyvelde, P. Flow-Induced Crystallization of Polyamide-6. *Int. Polym. Process.* **2018**, *3*.
499. Skorupska, M.; Kulczyk, M.; Przybysz, S.; Skiba, J.; Mizeracki, J.; Ryszkowska, J. Mechanical Reinforcement of Polyamide 6 by Cold Hydrostatic Extrusion. *Materials* **2021**, *14*, doi:10.3390/ma14206045.
500. Skorupska, M.; Kulczyk, M.; Denis, P.; Grzęda, D.; Czajka, A.; Ryszkowska, J. Structural Hierarchy of PA6 Macromolecules after Hydrostatic Extrusion. *Materials* **2023**, *16*, doi:10.3390/ma16093435.

501. Parodi, E.; Peters, G.W.M.; Govaert, L.E. Structure-Properties Relations for Polyamide 6, Part 2: Influence of Processing Conditions during Injection Moulding on Deformation and Failure Kinetics. *Polymers* **2018**, *10*, doi:10.3390/polym10070779.
502. Dencheva, N.; Denchev, Z.; Oliveira, M.J.; Funari, S.S. Relationship between Crystalline Structure and Mechanical Behavior in Isotropic and Oriented Polyamide 6. *J of Applied Polymer Sci* **2007**, *103*, 2242–2252, doi:10.1002/app.25250.
503. Yan, X.; Imai, Y.; Shimamoto, D.; Hotta, Y. Relationship Study between Crystal Structure and Thermal/Mechanical Properties of Polyamide 6 Reinforced and Unreinforced by Carbon Fiber from Macro and Local View. *Polymer* **2014**, *55*, 6186–6194, doi:10.1016/j.polymer.2014.09.052.
504. Li, C.; Shan, P.; Soares, J.B.P.; Penlidis, A. HDPE/LLDPE Reactor Blends with Bimodal Microstructures-Part I: Mechanical Properties. *Polymer* **2002**, *43*, 7345–7365, doi:doi.org/10.1016/S0032-3861(02)00703-6.
505. Long, C.; Dong, Z.; Wang, K.; Yu, F.; He, C.; Chen, Z.R. Molecular Weight Distribution Shape Approach for Simultaneously Enhancing the Stiffness, Ductility and Strength of Isotropic Semicrystalline Polymers Based on Linear Unimodal and Bimodal Polyethylenes. *Polymer* **2023**, *275*, doi:10.1016/j.polymer.2023.125936.
506. Kim, J.H.; Min, B.R.; Kang, Y.S. Thermodynamic Model of the Glass Transition Behavior for Miscible Polymer Blends. *Macromolecules* **2006**, *39*, 1297–1299, doi:10.1021/ma052436a.
507. Wróblewska, A.A.; Leoné, N.; De Wildeman, S.M.A.; Bernaerts, K.V. Towards High-Performance Materials Based on Carbohydrate-Derived Polyamide Blends. *Polymers* **2019**, *11*, doi:10.3390/polym11030413.
508. Wang, L.; Dong, X.; Huang, M.; Müller, A.J.; Wang, D. The Effect of Microstructural Evolution during Deformation on the Post-Yielding Behavior of Self-Associated Polyamide Blends. *Polymer* **2017**, *117*, 231–242, doi:10.1016/j.polymer.2017.04.038.
509. Cagiao, M.E.; Ania, F.; Baltá Calleja, F.J.; Hirami, M.; Shimomura, T. Structure-Microhardness Correlation in Blends of Nylon 6/Nylon 66 Monofilaments. *J. Appl. Polym. Sci.* **2000**, *77*, 636–643, doi:10.1002/(SICI)1097-4628(20000718)77:3<636::AID-APP19>3.0.CO;2-R.
510. Sciences Computers Consultants Ludovic® Software Available online: https://www.scconsultants.com/en/ludovic-twin-screw-simulation-software.html (accessed on 1 February 2024).
511. Castéran, F.; Ibanez, R.; Argerich, C.; Delage, K.; Chinesta, F.; Cassagnau, P. Application of Machine Learning Tools for the Improvement of Reactive Extrusion Simulation. *Macrom. Mater. Eng.* **2020**, *305*, doi:10.1002/mame.202000375.
512. Bochmann, E.S.; Gryczke, A.; Wagner, K.G. Validation of Model-Based Melt Viscosity in Hot-Melt Extrusion Numerical Simulation. *Pharmaceutics* **2018**, *10*, doi:10.3390/pharmaceutics10030132.
513. Dubey, S.P.; Abhyankar, H.A.; Marchante, V.; Brighton, J.L.; Blackburn, K.; Temple, C.; Bergmann, B.; Trinh, G.; David, C. Modelling and Validation of Synthesis of Poly Lactic Acid Using an Alternative Energy Source through a Continuous Reactive Extrusion Process. *Polymers* **2016**, *8*, doi:10.3390/polym8040164.

514. Durin, A.; eM icheli, P.D.; -C Nguyen, H.; avid, C.D.; alette, R.V.; ergnes, B.V. Comparison between 1D and 3D Approaches for Twin-Screw Extrusion Simulation. *Int. Polym. Process.* **2014**, *5*, 641–648, doi:10.3139/217.2951.
515. Slapnik, J.; Liu, Y.; Kupfer, R.; Lucyshyn, T.; Nardin, B.; Pinter, G. Low-Temperature Fibre Direct Compounding of Cellulose Fibres into PA6. *Materials* **2022**, *15*, 6600, doi:10.3390/ma15196600.
516. Elsabbagh, A.; Steuernagel, L.; Ring, J. Natural Fibre/PA6 Composites with Flame Retardance Properties: Extrusion and Characterisation. *Compos. B: Eng.* **2017**, *108*, 325–333, doi:10.1016/j.compositesb.2016.10.012.
517. Kim, Y.S.; Kim., J.K.; Jeon., E.S. Effect of the Compounding Conditions of Polyamide 6, Carbon Fiber, and Al2O3 on the Mechanical and Thermal Properties of the Composite Polymer. *Materials* **2019**, *12*, 3047, doi:10.3390/ma12183047.
518. Vannini, M.; Marchese, P.; Celli, A.; Marega, C.; Lorenzetti, C. Strategy to Improve PA6 Performances by Melt Compounding. *Polym. Test.* **2018**, *67*, 84–91, doi:10.1016/j.polymertesting.2018.02.021.
519. Porter, R.S.; Johnson, J.F. The Effect of Molecular Weight and Distribution on Polymer Rheology near the Entanglement Region. *Trans. Soc. Rheol.* **1963**, *7*, 241–252, doi:10.1122/1.548955.
520. Pearson, G.H.; Garfield, L.J. The Effect of Molecular Weight and Weight Distribution Upon Polymer Melt Rheology. *Polym. Eng. Sci.* **1978**, *18*, 583–589.
521. Fornes, T.D.; Yoon, P.J.; Keskkula, H.; Paul, D.R. Nylon 6 Nanocomposites: The Effect of Matrix Molecular Weight. *Polymer* **2001**, *42*, 9929–9940, doi:10.1016/S0032-3861(01)00552-3.
522. Kiziltas, A.; Nazari, B.; Gardner, D.J.; Bousfield, D.W. Polyamide 6-Cellulose Composites: Effect of Cellulose Composition on Melt Rheology and Crystallization Behavior. *Polym. Eng. Sci.* **2014**, *54*, 739–746, doi:10.1002/pen.23603.
523. Tang, J.; Xu, B.; Xi, Z.; Pan, X.; Zhao, L. Controllable Crystallization Behavior of Nylon-6/66 Copolymers Based on Regulating Sequence Distribution. *Ind. Eng. Chem. Res.* **2018**, *57*, 15008–15019, doi:10.1021/acs.iecr.8b02671.
524. Koyama, K.; Suryadevara, J.; Spuriell, J.E. Effect of Molecular Weight on High-speed Melt Spinning of Nylon 6. *J. Appl. Polym. Sci.* **1986**, *31*, 2203–2229, doi:10.1002/app.1986.070310723.
525. Chivers, R.A.; Moore, D.R. The Effect of Molecular Weight and Crystallinity on the Mechanical Properties of Injection Moulded Poly(Aryl-Ether-Ether-Ketone) Resin. *Polymer* **1994**, *35*, 110–116, doi:10.1016/0032-3861(94)90057-4.
526. Naudy, S.; David, L.; Rochas, C.; Fulchiron, R. Shear Induced Crystallization of Poly(m-Xylylene Adipamide) with and without Nucleating Additives. *Polymer* **2007**, *48*, 3273–3285, doi:10.1016/j.polymer.2007.03.076.
527. Housmans, J.W.; Peters, G.W.M.; Meijer, H.E.H. Flow-Induced Crystallization of Propylene/Ethylene Random Copolymers. *J. Therm. Anal. Calorim.* **2009**, *98*, 693–705, doi:10.1007/s10973-009-0532-3.
528. Rhoades, A.M.; Gohn, A.M.; Seo, J.; Androsch, R.; Colby, R.H. Sensitivity of Polymer Crystallization to Shear at Low and High Supercooling of the Melt. *Macromolecules* **2018**, *51*, 2785–2795, doi:10.1021/acs.macromol.8b00195.

529. van Meerveld, J.; Peters, G.W.M.; Hütter, M. Towards a Rheological Classification of Flow Induced Crystallization Experiments of Polymer Melts. *Rheol. Acta* **2004**, *44*, 119–134, doi:10.1007/s00397-004-0382-7.
530. Sangroniz, L.; Meabe, L.; Basterretxea, A.; Sardon, H.; Müller, A.J.; Cavallo, D. Chemical Structure Drives Memory Effects in the Crystallization of Homopolymers. *Macromolecules* **2020**, *53*, 4874–4881, doi:10.1021/acs.macromol.0c00751.
531. Khanna, Y.P.; Reimschuessel, A.C.; Banerjie, A.; Altman, C. Memory Effects in Polymers. II. Processing History vs. Crystallization Rate of Nylon 6—Observation of Phenomenon and Product Behavior. *Polym. Eng. Sci.* **1988**, *28*, 1600–1606, doi:10.1002/pen.760282405.
532. Doufas, A.K. A Microstructural Flow-Induced Crystallization Model for Film Blowing: Validation with Experimental Data. *Rheol Acta* **2014**, *53*, 269–293, doi:10.1007/s00397-013-0749-8.
533. Hadinata, C.; Boos, D.; Gabriel, C.; Wassner, E.; Rüllmann, M.; Kao, N.; Laun, M. Elongation-Induced Crystallization of a High Molecular Weight Isotactic Polybutene-1 Melt Compared to Shear-Induced Crystallization. *J. Rheol.* **2007**, *51*, 195–215, doi:10.1122/1.2426977.
534. Nitta, K.H. On the Orientation-Induced Crystallization of Polymers. *Polymers* **2016**, *8*, doi:10.3390/polym8060229.
535. Perkins, T.T.; Smith, D.E.; Chu, S. Single Polymer Dynamics in an Elongational Flow. *Science* **1997**, *276*, 2016–2021, doi:10.1126/science.276.5321.2016.
536. Alcock, B.; Cabrera, N.O.; Barkoula, N.M.; Peijs, T. The Effect of Processing Conditions on the Mechanical Properties and Thermal Stability of Highly Oriented PP Tapes. *Eur. Polym. J.* **2009**, *45*, 2878–2894, doi:10.1016/j.eurpolymj.2009.06.025.
537. Foster, R.J.; Hine, P.J.; Ward, I.M. The Effect of Draw Ratio on the Mechanical Properties and Crystalline Structure of Single Polymer Polypropylene Composites. *Polymer* **2016**, *91*, 156–161, doi:10.1016/j.polymer.2016.03.042.
538. He, Y.; Xu, W.-H.; Zhang, H.; Qu, J.-P. Constructing Bone-Mimicking High-Performance Structured Poly(Lactic Acid) by an Elongational Flow Field and Facile Annealing Process. *ACS Appl. Mater. Interfaces* **2020**, *12*, 13411–13420, doi:10.1021/acsami.0c01528.
539. Irvine, P.A.; Smith, P. Development of the Axial Young's Modulus with Draw Ratio of Flexible-Chain Polymers. *Macromolecules* **1986**, *19*, 240–242, doi:10.1021/ma00155a038.
540. Mourad, A.-H.I.; Bekheet, N.; El-Butch, A.; Abdel-Latif, L.; Nafee, D.; Barton, D.C. The Effects of Process Parameters on the Mechanical Properties of Die Drawn Polypropylene. *Polymer Testing* **2005**, *24*, 169–180, doi:10.1016/j.polymertesting.2004.09.006.
541. Münstedt, H. Various Features of Melt Strain Hardening of Polymeric Materials in Uniaxial Extension and Their Relation to Molecular Structure: Review of Experimental Results and Their Interpretation. *Rheol. Acta* **2023**, *62*, 333–363, doi:10.1007/s00397-023-01400-4.
542. Nadella, H.P.; Spruiell, J.E.; White, J.L. Drawing and Annealing of Polypropylene Fibers: Structural Changes and Mechanical Properties. *J. Appl. Polym. Sci.* **1978**, *22*, 3121–3133, doi:10.1002/app.1978.070221108.
543. Peterlin, A. Drawing and Extrusion of Semi-Crystalline Polymers. *Colloid Polym. Sci.* **1987**, *265*, 357–382, doi:10.1007/BF01412215.

544. Kavassalis, T.A.; Noolandi, J. A New Theory of Entanglements and Dynamics in Dense Polymer Systems. **1988**, *21*.
545. Ansari, M.; Hatzikiriakos, S.G.; Sukhadia, A.M.; Rohlfing, D.C. Melt Fracture of Two Broad Molecular Weight Distribution High-density Polyethylenes. *Polym. Eng. Sci.* **2012**, *52*, 795–804, doi:10.1002/pen.22144.
546. Shenoy, A.V.; Saini, D.R. An Approach to the Estimation of Polymer Melt Elasticity. *Rheol. Acta* **1984**, *23*, 608–616, doi:10.1007/bf01438801.
547. Shenoy, A.V.; Saini, D.R. Estimation of Melt Elasticity of Degraded Polymer from Melt Flow Indext. *Polym. Degrad. Stabil.* **1985**, *11*, 297–307, doi:10.1016/0141-3910(85)90034-5.
548. La Mantia, F.P.; Acierno, D. Influence of the Molecular Structure on the Melt Strength and Extensibility of Polyethylenes. *Polym. Eng. Sci.* **1985**, *25*, 279–283, doi:10.1002/pen.760250505.
549. Muke, S.; Ivanov, I.; Kao, N.; Bhattacharya, S.N. The Melt Extensibility of Polypropylene. *Polym. Int.* **2001**, *50*, 515–523, doi:10.1002/pi.654.
550. Fu, J.; Wang, Y.; Shen, K.; Fu, Q.; Zhang, J. Insight into Shear-Induced Modification for Improving Processability of Polymers: Effect of Shear Rate on the Evolution of Entanglement State. *J. Polym. Sci., Part B: Polym. Phys.* **2019**, *57*, 598–606, doi:10.1002/polb.24816.
551. Laun, H.M.; Schuch, H. Transient Elongational Viscosities and Drawability of Polymer Melts. *J. Rheol.* **1989**, *33*, 119–175, doi:10.1122/1.550058.
552. Muke, S.; Ivanov, I.; Kao, N.; Bhattacharya, S.N. Extensional Rheology of Polypropylene Melts from the Rheotens Test. *J. Non-Newton. Fluid Mech.* **2001**, *101*, 77–93, doi:10.1016/S0377-0257(01)00142-2.
553. Kazatchkov, I.B.; Hatzikiriakos, S.G.; Bohnet, N.; Goyal, S.K. Influence of Molecular Structure on the Rheological and Processing Behavior of Polyethylene Resins. *Polym. Eng. Sci.* **1999**, *39*, 804–815, doi:10.1002/pen.11468.
554. Shivokhin, M.E.; Urbanczyk, L.; Michel, J.; Bailly, C. The Influence of Molecular Weight Distribution of Industrial Polystyrene on Its Melt Extensional and Ultimate Properties. *Polym. Eng. Sci.* **2016**, *56*, 1012–1020, doi:10.1002/pen.24331.
555. Garofalo, E.; Russo, G.M.; Di Maio, L.; Incarnato, L. Study on the Effect of Uniaxial Elongational Flow on Polyamide Based Nanocomposites. *Macromol. Symp.* **2007**, *247*, 110–119, doi:10.1002/masy.200750113.
556. Ito, M.; Takahashi, A.; Araki, N.; Kanamoto, T. Effects of Molecular Weight on the Drawing and the Draw Efficiency of Nylon-6. *Polymer* **2001**, *42*, 241–248, doi:10.1016/s0032-3861(00)00278-0.
557. Wang, X.; Ouyang, J.; Liu, Y. Prediction of Flow Effect on Crystal Growth of Semi-Crystalline Polymers Using a Multi-Scale Phase-Field Approach. *Polymers* **2017**, *9*, 634, doi:10.3390/polym9120634.
558. De Gennes, P.G. Coil-Stretch Transition of Dilute Flexible Polymers under Ultrahigh Velocity Gradients. *J. Chem. Phys.* **1974**, *60*, 5030–5042, doi:10.1063/1.1681018.
559. Spina, R.; Spekowius, M.; Hopmann, C. Multiphysics Simulation of Thermoplastic Polymer Crystallization. *Materials & Design* **2016**, *95*, 455–469, doi:10.1016/j.matdes.2016.01.123.
560. Wang, X.; Ouyang, J.; Zhou, W.; Liu, Z. A Phase Field Technique for Modeling and Predicting Flow Induced Crystallization Morphology of Semi-Crystalline Polymers. *Polymers* **2016**, *8*, 230, doi:10.3390/polym8060230.

561. Janeschitz-Kriegl, H.; Ratajski, E. Some Fundamental Aspects of the Kinetics of Flow-Induced Crystallization of Polymers. *Colloid Polym. Sci.* **2010**, *288*, 1525–1537, doi:10.1007/s00396-010-2266-y.
562. Samon, J.M.; Schultz, J.M.; Hsiao, B.S.; Seifert, S.; Stribeck, N.; Gurke, I.; Collins, G.; Saw, C. Structure Development during the Melt Spinning of Polyethylene and Poly(Vinylidene Fluoride) Fibers by in Situ Synchrotron Small- and Wide-Angle X-Ray Scattering Techniques. *Macromolecules* **1999**, *32*, 8121–8132, doi:10.1021/ma9906332.
563. Doufas, A.K.; Dairanieh, I.S.; Mchugh, A.J. A Continuum Model for Flow-Induced Crystallization of Polymer Melts. *J. Rheol.* **1999**, 85-, doi:10.1122/1.550978.
564. Nakamura, K.; Watanabe, T.; Amano, T.; Katayama, K. Some Aspects of Nonisothermal Crystallization of Polymers. 111. Crystallization During Melt Spinning. *J. Appl. Polym. Sci.* **1974**, *18*, 615–623, doi:10.1002/app.1974.070180223.
565. Murthy, N.S.; Bray, R.G.; Correale, S.T.; Moore, R.A.F. Drawing and Annealing of Nylon-6 Fibres: Studies of Crystal Growth, Orientation of Amorphous and Crystalline Domains and Their Influence on Properties. *Polymer* **1995**, *36*, 3863–3873, doi:10.1016/0032-3861(95)99780-x.
566. Kwak, S.; Kim, J.H.; Lee, J. Correlation between Local Mobility and Mechanical Properties of High-speed Melt-spun Nylon-6 Fibers. *J. Polym. Sci., Part B: Polym. Phys.* **2001**, *39*, 993–1000, doi:10.1002/polb.1076.
567. Szántó, L.; Feng, Y.; Zhong, F.; Hees, T.; Van Ruymbeke, E.; Mülhaupt, R.; Friedrich, C. Ultra-Broad Molecular Weight Distribution Effects on Viscoelastic Properties of Linear Multimodal PE. *J. Rheol.* **2019**, *63*, 773–784, doi:10.1122/1.5109481.
568. Auhl, D.; Chambon, P.; McLeish, T.C.B.; Read, D.J. Elongational Flow of Blends of Long and Short Polymers: Effective Stretch Relaxation Time. *Phys. Rev. Lett.* **2009**, *103*, 136001, doi:10.1103/PhysRevLett.103.136001.
569. Cloizeaux, J.D. Double Reptation vs. Simple Reptation in Polymer Melts. *Europhys. Lett.* **1988**, *5*, 437–442, doi:10.1209/0295-5075/5/5/010.
570. Morshedian, J.; Karbalaei-Bagher, M.; Bayazian, H.; Jamshidi, A.; Razavi-Nouri, M. Unraveling the Bimodality of Polypropylene Film Grades Using Rheological Shear and Elongational Measurements: Inconsistent Results of Gel Permeation Chromatography. *Polym. Sci. Ser. A* **2018**, *60*, 523–529, doi:10.1134/s0965545x18040065.
571. Tsenoglou, C. Molecular Weight Polydispersity Effects on the Viscoelasticity of Entangled Linear Polymers. *Macromolecules* **1991**, *24*, 1762–1767, doi:10.1021/ma00008a012.
572. Van Ruymbeke, E.; Kaivez, A.; Hagenaars, A.; Daoust, D.; Godard, P.; Keunings, R.; Bailly, C. Characterization of Sparsely Long Chain Branched Polycarbonate by a Combination of Solution, Rheology and Simulation Methods. *J. Rheol.* **2006**, *50*, 949–973, doi:10.1122/1.2357188.
573. van Ruymbeke, E.; Liu, C.-Y.; Bailly, C. *Quantitative Tube Model Predictions for the Linear Viscoelasticity of Linear Polymers*; Rheology Reviews; The British Society of Rheology, 2007;
574. Micic, P.; Bhattacharya, S.N.; Field, G. Melt Strength and Elastic Behaviour of LLDPE/LDPE Blends. *Int. Polym. Process.* **1996**, *11*, 14–20, doi:10.3139/217.960014.

575. Park, S.J.; Larson, R.G. Tube Dilation and Reptation in Binary Blends of Monodisperse Linear Polymers. *Macromolecules* **2004**, *37*, 597–604, doi:10.1021/ma0343683.
576. Viovy, J.L.; Rubinstein, M.; Colby, R.H. Constraint Release in Polymer Melts: Tube Reorganization versus Tube Dilation. *Macromolecules* **1991**, *24*, 3587–3596, doi:10.1021/ma00012a020.
577. Beaugrand, J.; Berzin, F. Lignocellulosic Fiber Reinforced Composites: Influence of Compounding Conditions on Defibrization and Mechanical Properties. *J. Appl. Polym. Sci.* **2013**, *128*, 1227–1238, doi:10.1002/app.38468.
578. Puch, F.; Hopmann, C. Experimental Investigation of the Influence of the Compounding Process and the Composite Composition on the Mechanical Properties of a Short Flax Fiber–Reinforced Polypropylene Composite. *Polym. Compos.* **2015**, *36*, 2282–2290, doi:10.1002/pc.23141.
579. Alasfar, R.H.; Ahzi, S.; Barth, N.; Kochkodan, V.; Khraisheh, M.; Koç, M. A Review on the Modeling of the Elastic Modulus and Yield Stress of Polymers and Polymer Nanocomposites: Effect of Temperature, Loading Rate and Porosity. *Polymers* **2022**, *14*, 360, doi:10.3390/polym14030360.
580. Chen, K.; Schweizer, K.S. Theory of Yielding, Strain Softening, and Steady Plastic Flow in Polymer Glasses under Constant Strain Rate Deformation. *Macromolecules* **2011**, *44*, 3988–4000, doi:10.1021/ma200436w.
581. Kurelec, L.; Teeuwen, M.; Schoffeleers, H.; Deblieck, R. Strain Hardening Modulus as a Measure of Environmental Stress Crack Resistance of High Density Polyethylene. *Polymer* **2005**, *46*, 6369–6379, doi:10.1016/j.polymer.2005.05.061.
582. Merlette, T.C.; Hem, J.; Crauste-Thibierge, C.; Ciliberto, S.; Clément, F.; Sotta, P.; Long, D.R. Theory of Plasticity and Strain Hardening of Glassy Polymers. *Macromolecules* **2023**, *56*, 6510–6526, doi:10.1021/acs.macromol.3c00526.
583. Van Melick, H.G.H.; Govaert, L.E.; Meijer, H.E.H. On the Origin of Strain Hardening in Glassy Polymers. *Polymer* **2003**, *44*, 2493–2502, doi:10.1016/S0032-3861(03)00112-5.
584. Meijer, H.E.H.; Govaert, L.E. Mechanical Performance of Polymer Systems: The Relation between Structure and Properties. *Prog. Polym. Sci.* **2005**, *30*, 915–938, doi:10.1016/j.progpolymsci.2005.06.009.
585. Aleksy, N.; Kermouche, G.; Bergheau, J.M.; Loubet, J.L.; Pavan, S. Mechanical Investigation of the Healing Phenomenon of the PMMA. *Int. J. Mater. Form.* **2010**, *3*, 575–578, doi:10.1007/s12289-010-0835-8.
586. Liu, H.; Wu, F.-Y.; Zhong, G.-J.; Li, Z.-M. Predicting the Complex Stress-Strain Curves of Polymeric Solids by Classification-Embedded Dual Neural Network. *Mater. Des.* **2023**, *227*, 111773, doi:10.1016/j.matdes.2023.111773.
587. Nunes, R.W.; Martin, J.R.; Johnson, J.F. Influence of Molecular Weight and Molecular Weight Distribution on Mechanical Properties of Polymers. *Polym. Eng. Sci.* **1982**, *22*, 205–228, doi:10.1002/pen.760220402.
588. Schollenberger, C.S.; Dinbergs, K. Thermoplastic Polyurethane Elastomer Molecular Weight-Property Relations. Further Studies. *J. Elastomers Plast.* **1979**, *11*, 58–91, doi:10.1177/009524437901100104.
589. Gnoffo, C.; Arrigo, R.; Sisani, M.; Frache, A. Elongational Flow-Induced Microstructure Evolutions in Polypropylene/Layered Double Hydroxides

Nanocomposites. *Polym. Compos.* **2024**, *45*, 6606–6617, doi:10.1002/pc.28221.
590. Andreassen, E.; Myhre, O.J.; Hinrichsen, E.L.; Grøstad, K. Effects of Processing Parameters and Molecular Weight Distribution on the Tensile Properties of Polypropylene Fibers. *J. Appl. Polym. Sci.* **1994**, *52*, 1505–1517, doi:10.1002/app.1994.070521015.
591. De Rosa, C.; Scoti, M.; Di Girolamo, R.; Ballesteros, O.R.; Auriemma, F.; Malafronte, A. Polymorphism in Polymers: A Tool to Tailor Material's Properties. *Polym. Cryst.* **2020**, *3*, doi:10.1002/pcr2.10101.
592. Sattar, S.; Bhagatji, J.D.; Nazmus Saquib, M.; Pedrazzoli, D.; Zhang, M.; Kravchenko, S.G.; Kravchenko, O.G. Influence of Flow-Induced Polymorphism and Fiber Morphology on Mechanical Behavior in Long Discontinuous Glass Fiber Polyamide Composites. *Compos. A: Appl. Sci. Manuf.* **2024**, *185*, 108353, doi:10.1016/j.compositesa.2024.108353.
593. D'Aniello, C.; Rizzo, P.; Guerra, G. Polymorphism and Mechanical Properties of Syndiotactic Polystyrene Films. *Polymer* **2005**, *46*, 11435–11441, doi:10.1016/j.polymer.2005.09.052.
594. Uematsu, H.; Kawasaki, T.; Koizumi, K.; Yamaguchi, A.; Sugihara, S.; Yamane, M.; Kawabe, K.; Ozaki, Y.; Tanoue, S. Relationship between Crystalline Structure of Polyamide 6 within Carbon Fibers and Their Mechanical Properties Studied Using Micro-Raman Spectroscopy. *Polymer* **2021**, *223*, 123711, doi:10.1016/j.polymer.2021.123711.
595. Zwane, R.; Sadiku, E.; Ray, S.; Luruli, N. Thermal and Rheological Properties of Polyamide 6/Layered Double Hydroxide Clay Composites. *Polym. Compos.* **2019**, *27*, 567–581, doi:10.1177/0967391119853969.
596. Ghanta, T.S.; Aparna, S.; Verma, N.; Purnima, D. Review on Nano-and Microfiller-based Polyamide 6 Hybrid Composite: Effect on Mechanical Properties and Morphology. *Polym. Eng. Sci.* **2020**, *60*, 1717–1759, doi:10.1002/pen.25447.
597. Fu, S.; Sun, Z.; Huang, P.; Li, Y.; Hu, N. Some Basic Aspects of Polymer Nanocomposites: A Critical Review. *Nano Mater. Sci.* **2019**, *1*, 2–30, doi:10.1016/j.nanoms.2019.02.006.
598. Jordan, J.; Jacob, K.I.; Tannenbaum, R.; Sharaf, M.A.; Jasiuk, I. Experimental Trends in Polymer Nanocomposites—a Review. *Mater. Sci. Eng. A* **2005**, *393*, 1–11, doi:10.1016/j.msea.2004.09.044.
599. Liu, J.; Hui, D.; Lau, D. Two-Dimensional Nanomaterial-Based Polymer Composites: Fundamentals and Applications. *Nanotechnol. Rev.* **2022**, *11*, 770–792, doi:10.1515/ntrev-2022-0041.
600. Qadir, A.; Le, T.K.; Malik, M.; Amedome Min-Dianey, K.A.; Saeed, I.; Yu, Y.; Choi, J.R.; Pham, P.V. Representative 2D-Material-Based Nanocomposites and Their Emerging Applications: A Review. *RSC Adv.* **2021**, *11*, 23860–23880, doi:10.1039/D1RA03425A.
601. Francisco, D.L.; Paiva, L.B.; Aldeia, W. Advances in Polyamide Nanocomposites: A Review. *Polym. Compos.* **2019**, *40*, 851–870, doi:10.1002/pc.24837.
602. Dong, M.; Sun, Y.; Dunstan, D.J.; Young, R.J.; Papageorgiou, D.G. Mechanical Reinforcement from Two-Dimensional Nanofillers: Model, Bulk and Hybrid Polymer Nanocomposites. *Nanoscale* **2024**, *16*, 13247–13299, doi:10.1039/D4NR01356E.

603. Rafiee, R.; Shahzadi, R. Mechanical Properties of Nanoclay and Nanoclay Reinforced Polymers: A Review. *Polym. Compos.* **2019**, *40*, 431–445, doi:10.1002/pc.24725.
604. Pinto, G.M.; Cremonezzi, J.M.O.; Ribeiro, H.; Andrade, R.J.E.; Demarquette, N.R.; Fechine, G.J.M. From Two-dimensional Materials to Polymer Nanocomposites with Emerging Multifunctional Applications: A Critical Review. *Polym. Compos.* **2023**, *44*, 1438–1470, doi:10.1002/pc.27213.
605. Alexandre, M.; Dubois, P. Polymer-Layered Silicate Nanocomposites: Preparation, Properties and Uses of a New Class of Materials. *Mater. Sci. Eng. R: Rep.* **2000**, *28*, 1–63, doi:10.1016/S0927-796X(00)00012-7.
606. Chiu, C.-W.; Huang, T.-K.; Wang, Y.-C.; Alamani, B.G.; Lin, J.-J. Intercalation Strategies in Clay/Polymer Hybrids. *Prog. Polym. Sci.* **2014**, *39*, 443–485, doi:10.1016/j.progpolymsci.2013.07.002.
607. Usuki, A.; Kawasumi, M.; Kojima, Y.; Okada, A.; Kurauchi, T.; Kamigaito, O. Swelling Behavior of Montmorillonite Cation Exchanged for o) -Amino Acids by e-Caprolactam. *J. Mater. Res.* **1993**, *8*, doi:10.1557/JMR.1993.1174.
608. Kiliaris, P.; Papaspyrides, C.D. Polymer/Layered Silicate (Clay) Nanocomposites: An Overview of Flame Retardancy. *Prog. Polym. Sci.* **2010**, *35*, 902–958, doi:10.1016/j.progpolymsci.2010.03.001.
609. Ma, J.; Zhang, S.; Qi, Z. Synthesis and Characterization of Elastomeric Polyurethane/Clay Nanocomposites. *J. Appl. Polym. Sci.* **2001**, *82*, 1444–1448, doi:10.1002/app.1982.
610. Naseem, S.; Wießner, S.; Kühnert, I.; Leuteritz, A. Layered Double Hydroxide (MgFeAl-LDH)-Based Polypropylene (PP) Nanocomposite: Mechanical Properties and Thermal Degradation. *Polymers* **2021**, *13*, 3452, doi:10.3390/polym13193452.
611. de Goes, M.A.; Woicichowski, L.A.; da Rosa, R.V.V.; Santos, J.P.F.; Carvalho, B. de M. Improving the Dispersion of MWCNT and MMT in PVDF Melts Employing Controlled Extensional Flows. *J. Appl. Polym. Sci.* **2021**, *138*, doi:10.1002/app.50274.
612. La Mantia, F.P.; Ceraulo, M.; Mistretta, M.C.; Botta, L. Effect of the Elongational Flow on Morphology and Properties of Polypropylene/Graphene Nanoplatelets Nanocomposites. *Polym. Test.* **2018**, *71*, 10–17, doi:10.1016/j.polymertesting.2018.08.016.
613. Wu, T.; Huang, Z.X.; Wang, D.Z.; Qu, J.P. Effect of Continuous Elongational Flow on Structure and Properties of Short Glass Fiber Reinforced Polyamide 6 Composites. *Adv. Ind. Eng. Polym. Res.* **2019**, *2*, 93–101, doi:10.1016/j.aiepr.2019.06.003.
614. Dintcheva, N.Tz.; Arrigo, R.; Morreale, M.; La Mantia, F.P.; Matassa, R.; Caponetti, E. Effect of Elongational Flow on Morphology and Properties of Polymer/CNTs Nanocomposite Fibers. *Polym. Adv. Technol.* **2011**, *22*, 1612–1619, doi:10.1002/pat.1648.
615. La Mantia, F.P.; Dintcheva, N.T.; Scaffaro, R.; Marino, R. Morphology and Properties of Polyethylene/Clay Nanocomposite Drawn Fibers. *Macrom. Mater. Eng.* **2008**, *293*, 83–91, doi:10.1002/mame.200700204.
616. Baldi, F.; Franceschini, A.; Bignotti, F.; Tieghi, G.; Riccò, T. Rheological Behaviour of Nano-Composites Based on Polyamide 6 under Shear and Elongational Flow at High Strain Rates. *Rheol. Acta* **2009**, *48*, 73–88, doi:10.1007/s00397-008-0315-y.

617. Jalal Uddin, A.; Araki, J.; Gotoh, Y. Toward "Strong" Green Nanocomposites: Polyvinyl Alcohol Reinforced with Extremely Oriented Cellulose Whiskers. *Biomacromolecules* **2011**, *12*, 617–624, doi:10.1021/bm101280f.
618. Bumm, S.H.; White, J.L.; Isayev, A.I. Breakup of Silica Agglomerates in Corotating Twin-Screw Extruder: Modeling and Experiment. *J. Elastomers Plast.* **2014**, *46*, 527–552, doi:10.1177/0095244313476508.
619. Eken, A.E.; Tozzi, E.J.; Klingenberg, D.J.; Bauhofer, W. Combined Effects of Nanotube Aspect Ratio and Shear Rate on the Carbon Nanotube/Polymer Composites. *Polymer* **2012**, *53*, 4493–4500, doi:10.1016/j.polymer.2012.07.045.
620. Lertwimolnun, W.; Vergnes, B. Effect of Processing Conditions on the Formation of Polypropylene/Organoclay Nanocomposites in a Twin Screw Extruder. *Polym. Eng. Sci.* **2006**, *46*, 314–323, doi:10.1002/pen.20458.
621. Villmow, T.; Kretzschmar, B.; Pötschke, P. Influence of Screw Configuration, Residence Time, and Specific Mechanical Energy in Twin-Screw Extrusion of Polycaprolactone/Multi-Walled Carbon Nanotube Composites. *Compos. Sci. Technol.* **2010**, *70*, 2045–2055, doi:10.1016/j.compscitech.2010.07.021.
622. Huang, Z.-X.; Meng, C.; Zhang, G.; Qu, J.-P. Manufacturing Polymer/Clay Nanocomposites through Elongational Flow Technique. *Mater. Manuf. Process.* **2017**, *32*, 1409–1415, doi:10.1080/10426914.2017.1339316.
623. Lee, S.H.; Kim, S.Y.; Youn, J.R. Rheological Behavior and Theoretical Modeling of Uniaxial Elongational Flow Properties of Polypropylene/Layered Silicate Nanocomposites. *Polym. Compos.* **2009**, *30*, 1426–1436, doi:10.1002/pc.20707.
624. Xu, Z.; Deng, J.; Lai, Y.; Chen, J.; Chen, Y.; Huang, S.; Chen, A.; Zhang, J.; Lei, C. Study on the Exfoliation Mechanism of Graphene Nanoplatelets in the Polypropylene/Graphene Nanoplatelets Composites under the Elongational Flow Generated by Convergent-Divergent Channels. *J. Mater. Sci.* **2022**, *57*, 5467–5481, doi:10.1007/s10853-022-07005-1.
625. Socher, R.; Krause, B.; Müller, M.T.; Boldt, R.; Pötschke, P. The Influence of Matrix Viscosity on MWCNT Dispersion and Electrical Properties in Different Thermoplastic Nanocomposites. *Polymer* **2012**, *53*, 495–504, doi:10.1016/j.polymer.2011.12.019.
626. Arrigo, R.; Malucelli, G. Rheological Behavior of Polymer/Carbon Nanotube Composites: An Overview. *Materials* **2020**, *13*, 2771, doi:10.3390/ma13122771.
627. Sumita, M.; Abe, H.; Kayaki, H.; Miyasaka, K. Effect of Melt Viscosity and Surface Tension of Polymers on the Percolation Threshold of Conductive-Particle-Filled Polymeric Composites. *J. Macromol. Sci., Part B: Phys.* **1986**, *25*, 171–184, doi:10.1080/00222348608248036.
628. Svoboda, P.; Zeng, C.; Wang, H.; Lee, L.J.; Tomasko, D.L. Morphology and Mechanical Properties of Polypropylene/Organoclay Nanocomposites. *J. Appl. Polym. Sci.* **2002**, *85*, 1562–1570, doi:10.1002/app.10789.
629. Gupta, R.K.; Pasanovic-Zujo, V.; Bhattacharya, S.N. Shear and Extensional Rheology of EVA/Layered Silicate-Nanocomposites. *J. Non-Newton. Fluid Mech.* **2005**, *128*, 116–125, doi:10.1016/j.jnnfm.2005.05.002.
630. Pasanovic-Zujo, V.; Gupta, R.K.; Bhattacharya, S.N. Effect of Vinyl Acetate Content and Silicate Loading on EVA Nanocomposites under Shear and

Extensional Flow. *Rheol. Acta* **2004**, *43*, 99–108, doi:10.1007/s00397-003-0324-9.
631. Okamoto, M.; Nam, P.H.; Maiti, P.; Kotaka, T.; Hasegawa, N.; Usuki, A. A House of Cards Structure in Polypropylene/Clay Nanocomposites under Elongational Flow. *Nano Lett.* **2001**, *1*, 295–298, doi:10.1021/nl0100163.
632. Grover, C.A.; Bernal, C.B.; Sargin, I.; Beckman, S.P.; Gozen, B.A. Composition-Rheology Relationships of Polymer Composite-Type Precursors. **2023**, doi:10.21203/rs.3.rs-3380097/v1.
633. Mao, N.; Zhou, C.H.; Tong, D.S.; Yu, W.H.; Cynthia Lin, C.X. Exfoliation of Layered Double Hydroxide Solids into Functional Nanosheets. *Appl. Clay Sci.* **2017**, *144*, 60–78, doi:10.1016/j.clay.2017.04.021.
634. Jagadeesh, P.; Puttegowda, M.; Mavinkere Rangappa, S.; Siengchin, S. Influence of Nanofillers on Biodegradable Composites: A Comprehensive Review. *Polym. Compos.* **2021**, *42*, 5691–5711, doi:10.1002/pc.26291.
635. Bhattacharya, M.; Bhowmick, A.K. Polymer–Filler Interaction in Nanocomposites: New Interface Area Function to Investigate Swelling Behavior and Young's Modulus. *Polymer* **2008**, *49*, 4808–4818, doi:10.1016/j.polymer.2008.09.002.
636. Pradhan, S.; Costa, F.R.; Wagenknecht, U.; Jehnichen, D.; Bhowmick, A.K.; Heinrich, G. Elastomer/LDH Nanocomposites: Synthesis and Studies on Nanoparticle Dispersion, Mechanical Properties and Interfacial Adhesion. *Eur. Polym. J.* **2008**, *44*, 3122–3132, doi:10.1016/j.eurpolymj.2008.07.025.
637. Ku, X.; Lin, J. Motion and Orientation of Cylindrical and Cubic Particles in Pipe Flow with High Concentration and High Particle to Pipe Size Ratio. *Journal of Zhejiang University-SCIENCE A* **2008**, *9*, 664–671, doi:10.1631/jzus.A071463.
638. Peng, C.; Yang, H.; Tang, W. Study on the Flammability, Crystal Behaviors and Mechanical Performance of Polyamide 11 Composites by Intercalated Layered Double Hydroxides. *IJMS* **2022**, *23*, 12818, doi:10.3390/ijms232112818.
639. Wang, Q.; Zhang, X.; Wang, C.J.; Zhu, J.; Guo, Z.; O'Hare, D. Polypropylene/Layered Double Hydroxide Nanocomposites. *J. Mater. Chem.* **2012**, *22*, 19113, doi:10.1039/c2jm33493c.
640. Tabuani, D.; Ceccia, S.; Camino, G. Nylon-6 Nanocomposites, Study of the Influence of the Nanofiller Nature on Morphology and Material Properties. *J. Polym. Sci., Part B: Polym. Phys.* **2009**, *47*, 1935–1948, doi:10.1002/polb.21795.
641. Ke, K.; Yue, L.; Shao, H.; Yang, M.-B.; Yang, W.; Manas-Zloczower, I. Boosting Electrical and Piezoresistive Properties of Polymer Nanocomposites via Hybrid Carbon Fillers: A Review. *Carbon* **2021**, *173*, 1020–1040, doi:10.1016/j.carbon.2020.11.070.
642. La Mantia, F.P.; Mistretta, M.C.; Scaffaro, R.; Botta, L.; Ceraulo, M. Processing and Characterization of Highly Oriented Fibres of Biodegradable Nanocomposites. *Compos. B: Eng.* **2015**, *78*, 1–7, doi:10.1016/j.compositesb.2015.03.054.
643. Yamamoto, Y.; Inoue, Y.; Onai, T.; Doshu, C.; Takahashi, H.; Uehara, H. Deconvolution Analyses of Differential Scanning Calorimetry Profiles of β-Crystallized Polypropylenes with Synchronized X-Ray Measurements. *Macromolecules* **2007**, *40*, 2745–2750, doi:10.1021/ma062784s.